Controlling Growth and Electronic Properties of Transition Metal Disulphide Layers *via* Molecular Beam Epitaxy

Inaugural-Dissertation
zur
Erlangung des Doktorgrades
der Mathematisch-Naturwissenschaftlichen Fakultät
der Universität zu Köln

vorgelegt von
M. Sc. Joshua Hall
aus Kleve

Köln 2019

Erster Berichterstatter: Prof. Dr. Thomas Michely
Zweiter Berichterstatter: Priv. Doz. Dr. Daniel Bürgler

Vorsitzender der Prüfungskommission: Prof. Dr. Klas Lindfors
Tag der mündlichen Prüfung: 18.09.2019

Abstract

Transition metal dichalcogenides are an emergent class of layered materials with a broad range of properties that make them interesting for fundamental studies and applications ranging from nanoelectronics, to optoelectronics and spintronics. The weak van der Waals interaction present between successive sheets allows isolation of single layers of the material and grants access to their thickness-dependent properties.

The incompatibility of sulphur powder with ultra-high vacuum conditions creates a lack of *in situ* growth methods, which produce single to few-layer samples of sulphur based transition metal dichalcogenides that grow epitaxially and maintain their intrinsic, freestanding properties. Investigations have been conducted either on *ex situ* grown samples – those are inevitably exposed to ambient conditions – or on layers that are supported on metallic substrates – which alter the pristine properties of the materials through doping and hybridisation.

Here, we introduce a two-step molecular beam epitaxy based synthesis, where we supply elemental sulphur by thermal decomposition of FeS_2, a solid-state compound which is compatible with use in ultra-high vacuum. As a substrate, we use high-quality graphene on Ir(111), which only interacts *via* weak van der Waals forces.

Using the example of semiconducting $2H\text{-}MoS_2$, we demonstrate that the transition metal disulphide layers remain in their pristine state. A large band gap of (2.53 ± 0.08) eV and the ability to move flakes with the scanning tunnelling microscope tip both document the weak interaction of $2H\text{-}MoS_2$ with its substrate. This is corroborated by angle-resolved photoemission spectroscopy displaying the absence of hybridisation with the substrate. Further, Raman spectroscopy indicates independent thermal expansion, and finally, photoluminescence is observed despite the metallic substrate.

Since growth studies on transition metal disulphides are rare, we use the potential of molecular beam epitaxy to systematically study the growth process. Using scanning tunnelling microscopy and low-energy electron diffraction we investigate the influence of the single synthesis parameters and provide insight into the growth and annealing mechanisms. We further study the effect of repeated growth cycles, which we find to facilitate keeping epitaxial alignment at high coverages. Finally, the detrimental effect of inadvertent sulphur intercalation underneath graphene on the growth quality of $2H\text{-}MoS_2$ is considered.

The method also works for the synthesis of other transition metal sulphides, and in the following part of the thesis, we investigate layers of metallic $V_{1+x}S_2$. Since the system vanadium-sulphur has many stable phase equilibria, the structural scanning tunnelling microscopy investigations reveal three distinct single-layer phases and multilayer phases. The single-layer phases include stoichiometric 1T-VS_2 which neither in scanning tunnelling microscopy shows signs of a charge density wave nor of magnetism in circular x-ray dichroism. By thermal annealing, we induce irreversible transformations into two phases with increasing sulphur depletion. The first phase develops upon annealing to 600 K and shows an ordered superstructure, which we interpret as an array of sulphur vacancies. The second sets in when the sample is annealed to temperatures above 800 K and shows a reconstructed surface with a 3×1 superstructure. Atomic models describing the arrangement of the top sulphur layer are given for both phases.

We introduce ways to tune the growth to multilayer morphologies of VS_2, on which two superstructures are found. The superstructures spatially exclude themselves and by comparing the appearance of the occupied and unoccupied states in scanning tunnelling microscopy we resolve their origin. The 2×2 superstructure is ascribed to self-intercalation of V atoms in the van der Waals gap, which cause local stoichiometry $V_{1+x}S_2$. The $(\sqrt{3} \times \sqrt{3})$R30° superstructure shows clear indications of a charge density wave present at room temperature.

Finally, we investigate the charge density wave phase of 2H-TaS_2. For the pristine monolayer, scanning tunnelling microscopy shows a periodicity close to 3×3 and scanning tunnelling spectroscopy determines the partial charge density wave energy gap to be (32 ± 9) meV. Quasiparticle interference patterns and angle-resolved photoemission spectroscopy in tandem determine parts of the occupied and unoccupied band structure and make a precise tight-binding fit to the experimental data possible. The absence of hybridisation is documented and a carrier concentration of (1.10 ± 0.02) electrons per unit cell is determined.

Exposure to Li vapour causes a $(\sqrt{7} \times \sqrt{7})$R19.1° adatom superstructure, presumably accompanied by intercalation. Removing the adatoms with the STM tip reveals a 2×2 superstructure, which together with a reduced energy gap of (18 ± 9) meV implies the presence of a 2×2 charge density wave in *n* doped 2H-TaS_2.

Bilayer 2H-TaS_2 also shows a 2×2 charge density wave which, however, is of poor order compared to the monolayer case. A theoretical analysis based on density functional theory, density functional perturbation theory and many-body perturbation theory provides insight into phonon renormalisation as a function of doping and hybridisation with the substrate. This enables us to present a phase diagram of the charge density wave as a function of these parameters and to infer how they affect lattice dynamics and stability. Our theoretical considerations are consistent with the experimental work presented and shed light on previous experimental and theoretical investigations of related systems.

Deutsche Kurzzusammenfassung *(German Abstract)*

Die aufstrebende Klasse der geschichteten Übergangsmetalldichalkogenide weist ein weites Spektrum physikalischer Eigenschaften auf, welches diese Materialien für Anwendungen in der Nanoelektronik, Optoelektronik und Spintronik interessant macht. Die nur schwach durch van der Waals Kräfte gebundenen Lagen machen es möglich, einzelne Schichten dieser Materialien zu isolieren und gewährt Zugang zu deren schichtdickenabhängigen Eigenschaften.

Da elementares Schwefelpulver nicht mit den Bedingungen des Ultrahochvakuums zu vereinbaren ist, gibt es ein Defizit an *in situ* operierenden Wachstumsmethoden, die freistehende, epitaktisch orientierte, ein- und mehrlagige, schwefel-basierte Übergangsmetalldichalkogenide herstellen können. Bisherige Untersuchungen fanden entweder an *ex situ* gewachsenen Proben statt – diese werden unausweichlich dem Umgebungsdruck ausgesetzt – oder an solchen, die auf metallischen Substraten aufgebracht sind – und diese verändern die Eigenschaften der Materialien durch Dotierung oder Hybridisierung.

In dieser Arbeit wird eine zweistufige Synthesemethode vorgestellt, die auf der Molekularstrahlepitaxie beruht. Elementarer Schwefel wird dabei durch thermische Zersetzung von Pyrit (FeS_2) gewonnen, was mit dem Ultrahochvakuum verträglich ist. Als Substrat wird hoch qualitatives Graphen auf Ir(111) genutzt, welches nur schwach über van der Waals Kräfte wechselwirkt.

Am Beispiel von halbleitendem 2H-MoS_2 wird gezeigt, dass die Schichten von Übergangsmetalldichalkogeniden in ihrer reinen Form bewahrt bleiben. Die schwache Wechselwirkung mit dem Substrat wird hierbei durch mehrere Methoden belegt. Zum einen lassen sich einzelne Flocken mithilfe der Rastertunnelmikrokopspitze bewegen und innerhalb der Rastertunnelspektroskopie zeigt das 2H-MoS_2 eine große Bandlücke von (2.53 ± 0.08) eV. Außerdem wird mithilfe winkelaufgelöster Photoemissionsspektroskopie die Abwesenheit von Bandhybridisierung gezeigt. Raman-Spektroskopie indiziert unabhängige thermische Expansion und zuletzt ist Photolumineszenz trotz des metallischen Substrates zu beobachten.

Da Wachstumsstudien an Übergangsmetallsulphiden selten sind, nutzen wir das Potential der Molekularstrahlepitaxie und studieren den Wachstumsprozess in systematischer Weise. Hierbei wird der Einfluss der einzelnen Wachstumsparameter mithilfe von Rastertunnelmikroskopie und niederenergetischer Elektronenbeugung untersucht und ein Einblick in die Wachstums- und Ausheilmechanismen gegebenen. Des Weiteren untersuchen wir den Effekt von wiederholten Wachstumszyklen und finden, dass diese es erleichtern, bei hoher Bedeckung eine epitaktische Orientierung zum Sub-

strat zu wahren. Zuletzt berücksichtigen wir weiterhin den Effekt von Schwefelinterkalation unter das Graphen, was sich nachteilhaft auf die Qualität des 2H-MoS_2 auswirkt.

Die Wachstumsmethode lässt sich auch auf andere Übergangsmetallsulphide ausweiten und in einem weiteren Teil dieser Arbeit untersuchen wir Schichten von metallischem $V_{1+x}S_2$. Das System Vanadium-Schwefel prägt sich durch vielzahlige stabile Phasengleichgewichte aus, was sich auch in unseren Untersuchungen niederschlägt. Mittels Rastertunnelmikroskopie werden drei distinkte einlagige und ebenso mehrlagige Phasen identifiziert. Die einlagigen Phasen beinhalten stöchiometrisches 1T-VS_2, welches weder in der Rastertunnelmikroskopie Anzeichen einer Ladungsdichtewelle noch des Magnetismus im zirkularen Röntgendichroismus zeigt. Durch thermisches Ausheilen können irreversible Übergänge zu zwei schwefelverarmten Phasen erzeugt werden. Die erste Phase stellt sich nach dem Ausheilen zu 600 K ein und zeigt eine geordnete Überstruktur, welche als eine Anordnung von Schwefelfehlstellen interpretiert wird. Die zweite Phase setzt durch Ausheilen zu Temperaturen oberhalb von 800 K ein und zeigt eine 3×1 Überstruktur auf einer rekonstruierten Oberfläche. Es werden atomare Modelle für beide Phasen gezeigt.

Es werden Wege aufgezeigt, das Wachstum zu einer mehrlagigen Morphologie zu bewegen, wobei die Oberfläche der Multilagen zwei Überstukturen aufweist. Die Überstrukturen grenzen sich räumlich voneinander ab und werden mittels eines Vergleichs des Erscheinens der besetzten und unbesetzten Zustände innerhalb der Rastertunnelmikroskopie auf ihren Ursprung untersucht. Die 2×2 Überstruktur wird in der van der Waals Lücke selbst-interkalierten Vanadium Atomen zugeschrieben, und die $(\sqrt{3} \times \sqrt{3})R30^\circ$ Überstruktur zeigt klare Indizien einer Ladungsdichtewelle bei Raumtemperatur.

Zuletzt untersuchen wir die Ladungsdichtewellephase von 2H-TaS_2. Die Rastertunnelmikroskopie zeigt bei 5 K für das reine einlagige Material eine Periodizität die nahe einer 3×3 Überstruktur liegt und mithilfe der Rastertunnelspektroskopie wird eine Energielücke von (32 ± 9) meV gemessen. Quasiteilchen-Interferenzmuster werden zusammen mit winkelaufgelöster Photoemissionsspektroskopie genutzt, um Teile der besetzten und unbesetzten Bandstruktur zu vermessen und auf Basis dessen einen präzisen Tight-Binding-Fit an die Messdaten zu erstellen. Dieser zeigt eine Ladungsträgerkonzentration von (1.10 ± 0.02) Elektronen pro Einheitszelle.

Das Verdampfen von Li resultiert in einer $(\sqrt{7} \times \sqrt{7})R19.1^\circ$ Adatom Überstruktur, welche vermutlich mit Interkalation einhergeht. Ein Abtragen der Adatome zeigt eine 2×2 Überstruktur, die mit einer verringerten Energielücke von (18 ± 9) meV ein starkes Indiz für eine veränderte Ladungsdichtewelle darstellt.

Die Bilage 2H-TaS_2 zeigt ebenfalls eine 2×2 Überstruktur, welche allerdings gegenüber der Monolage von minderer Ordnung ist. Theoretische Analysen, die auf der Dichtefunktionaltheorie, der Dichtefunktional-Störungstheorie und der Mehrteilchen-Störungstheorie basieren bieten Einsicht in die Phononenrenormalisierung als Funktion der Dotierung und der Hybridisierung. Dies ermöglicht es uns ein Phasendiagramm der Ladungsdichtewelle als Funktion dieser Parameter anzugeben. Unsere theoretischen Überlegungen sind konsistent mit den experimentellen Befunden und tragen aufklärend zur Diskussion vorhergehender experimenteller und theoretischer Arbeiten an verwandten Systemen bei.

Frequently used Symbols and Abbreviations

1D - one-dimensional
2D - two-dimensional
3D - three-dimensional
ARPES - angle-resolved photoemission spectroscopy
BL - bilayer
BZ - Brillouin zone
CVD - chemical vapor deposition
CDW - charge density wave
DFT - density functional theory
DFPT - density functional perturbation theory
(L)DOS - (local) density of states
FS - Fermi surface
FT - Fourier transformation
Gr - graphene
h-BN - hexagonal boron nitride
L - Langmuir, $1\ \mathrm{L} = 1 \times 10^{-6}\ \mathrm{Torr} \cdot \mathrm{s} \approx 1.33 \times 10^{-6}\ \mathrm{mbar} \cdot \mathrm{s}$
LEED - low-energy electron diffraction
MBE - molecular beam epitaxy
ML - monolayer
MTB - mirror twin boundary
PLD - periodic lattice distortion
PL - photoluminescence
QPI - quasi-particle interference
STM - scanning tunnelling microscopy
STS - scanning tunnelling spectroscopy
TB - tight-binding
TMDC - transition metal dichalcogenide
TMDS - transition metal disulphide
UHV - ultra-high vacuum
vdWE - van der Waals epitaxy
XAS - x-ray absorption spectroscopy
XMCD - x-ray magnetic circular dichroism

Contents

PART I

Introduction

Triggered by the acclaimed isolation of graphene – a single sheet of carbon atoms [1,2] – an entirely new field of material physics rapidly emerged. Though layered systems, in which individual layers are loosely bound to each other by van der Waals forces, are a relatively old field of physics [3–10], the revelation of newly emerging phenomena ascribed to the two-dimensional nature of an isolated single-layer material has set off the field of two-dimensional materials research. In this field, transition metal dichalcogenides are on the ascent and, owing to a vast portfolio of physical properties, provide a new platform for exploring internal quantum degrees of freedom and their potential for new applications.

Despite them all sharing a rather similar structure, the family of transition metal dichalcogenides embodies the probably widest spectrum of properties amongst two-dimensional materials [11]. Besides generic characteristics ranging from insulators, to semiconductors, to metals – which is a consequence of the existence of non-bonding *d* bands and their filling with electrons – the scope of correlation phenomena hosted in these systems is also broad, and includes superconductivity [12–15], charge density waves [16, 17] and Mott insulators [18–20]. Even Weyl semimetals, where ramifications of topologically protected states become important, may be found amongst the material class under concern [21, 22].

The transition metal dichalcogenides distinguish themselves not only through their diverse properties but also by their manipulability. The electronic properties can be deliberately tailored and tuned by varying the number of layers, inducing strain or admixing foreign elements.

In semiconducting transition metal dichalcogenides such as 2H-WSe$_2$ and 2H-MoSe$_2$, the reduction of layer number results in an increase of band gap size and finally at monolayer thickness in an indirect to direct band gap transition [23], which renders the material class important for (opto-)electronic applications and technological advancement. Consequently, the first field-effect transistor based on 2H-MoS$_2$ was quick to come [24] and further technologies such as photodetectors based on 2H-MoS$_2$/graphene heterostructures are being investigated [25].

In metallic transition metal dichalcogenides, correlation phenomena such as superconductivity and charge density waves also show layer number dependent properties, namely through variation of transition temperatures into the respective phase. In that regard, 2H-TaS$_2$ has been found to exhibit an increase of the superconducting transition temperature [13, 14], while 2H-NbSe$_2$ has been found to have a tremendous increase in charge density wave transition temperature [26], both when thinned down to the monolayer regime.

Though long thought to remain an elusive dream, also two-dimensional magnetic materials have been recently discovered [27, 28] and amongst the transition metal dichalcogenides, monolayers of VX$_2$ (X = S, Se) are predicted to show magnetic behaviour [29].

Practical control of these properties is a precondition for exploiting quantum phases and may be achieved, for example, by external stimuli such as electrical gating. In 1T-TaS$_2$, the charge density wave state has been shown to be controllable by electrical gating [30,31] and a first voltage-controlled charge density wave oscillator has been achieved [32]. Another way of controlling material properties is to employ refined synthesis techniques and thus to directly tailor electrical character.

However, most of the recent investigations have been performed on bulk samples or exfoliated layers from geological sources or chemical vapour transport grown crystals. While these approaches are *per se* valuable to the 2D research community, they are neither suitable for controlling electronic properties, nor for the scale-up required for industrial applications. Methods capable of producing large-scale samples with growth control include atomic-layer deposition, chemical vapour deposition and molecular beam epitaxy. While chemical vapour deposition is comparably inexpensive and uncomplicated and is therefore performed more commonly, molecular beam epitaxy holds several advantages over the other techniques. Since it operates *in situ* and under ultra-high vacuum conditions, it provides ultimate cleanliness and the availability of *in situ* investigation, without any exposure to ambient conditions. It furthermore offers precise growth control, firstly of layer thickness and secondly of admixing foreign elements.

Unfortunately, the high vapour pressure of sulphur makes it incompatible with ultra-high vacuum conditions and consequently, transition metal disulphides are less often subject to *in situ* studies. One solution is to use a metallic substrate, which can catalytically dissociate a sulphur-containing precursor molecule such as H_2S. This, however, brings along a metallic support for the transition metal disulphides, which alters their properties through doping and hybridisation [33–36].

In this thesis, we introduce an ultra-high vacuum compatible *in situ* synthesis approach using inert and decoupling substrates. The technique can be used for the controlled growth of epitaxial transition metal disulphide monolayers, as well as thin multilayers, which maintain their intrinsic, freestanding properties. We circumvent the above-mentioned difficulties by evaporating sulphur from FeS_2 and employing van der Waals epitaxy – a molecular beam epitaxy based technique in which the two reactants are *in situ* supplied from their gas phase on only van der Waals interacting substrates [37–40]. As a principle substrate we use graphene on Ir(111), a substrate that is readily prepared as a single-crystal with a very low defect density [41, 42] and is expected to interact only weakly with the epilayer through van der Waals interactions.

To the structure of this thesis: in **Part II**, we first of all introduce the fundamentals of the material class transition metal dichalcogenides (**Chapter 1**) and the experimental approaches (**Chapter 2**) we use to study said class.

Part III, presents the results achieved in this work. In **Chapter 3**, we present the newly developed synthesis approach on the example of the archetypal transition metal dichalcogenide material 2H-MoS_2, demonstrating the ultra-high quality, cleanliness and quasi-freestanding nature of the as-grown layers by a large array of surface science techniques [43–45]. We employ scanning tunnelling microscopy and low-energy electron diffraction to investigate the structure of the semiconducting 2H-MoS_2, utilise scanning tunnelling spectroscopy to measure the size of the band gap and show that it resembles that of the freestanding case. Angle-resolved photoemission spectroscopy measures the occupied band structure and documents the absence of hybridisation between epilayer and its substrate, allowing determination of the large splitting of the K valleys which arises in the monolayer due to spin-orbit coupling. The decoupling of 2H-MoS_2 and graphene is further corroborated by Raman spectroscopy, which measures independent thermal expansion in the two layers. Finally, despite the metallic substrate, the sound decoupling allows photoluminescence to be maintained in the heterostructure.

Based on this synthesis method, we explore the growth kinetics and dynamics of van der Waals epitaxy in a systematic manner (still focussing on 2H-MoS_2) in **Chapter 4**. In contrast to conventional epitaxy, van der Waals epitaxy makes use of the substrate and the epilayer having inert surfaces with no dangling bonds [46], which is why conventional growth models such as Frank-van-der-Merve, Stranski-Krastanov and Volmer-Weber growth do not suitably describe the growth energetics and instead concepts such as ad- and desorption, nucleation and (edge-)diffusion become important. We systematically investigate the influence of the synthesis parameters on these quantities and thereby give insights on the growth mechanisms.

We close the topic of MoS_2-based investigations by introducing experimental progress enabled through the newly developed technique, ranging from exotic fundamental one-dimensional physics incorporated in metallic mirror twin boundaries [47], to trapped one-dimensional states that are caused by band bending, to showing ways towards experimental control and tailoring of electrical properties of the two-dimensional material.

After having gained an understanding of the growth complexity, we tackle the challenging growth of the metallic transition metal dichalcogenide 1T-VS_2 in **Chapter 5**. The material is a prototypical d^1 system and a candidate for strongly correlated physics [48]. Being both a charge density wave material [49,50] and a candidate for two-dimensional magnetism [29,51] with layer-dependent properties [52], it represents an exciting laboratory to study correlation phenomena. The promising diversity comes with a challenging downside: the complex V-S phase diagram shows plentiful stable phase equilibria and bulk 1T-VS_2 is even only a metastable compound [53]. This prevents simple exfoliation and consequently, physical properties are disputed [54] and monolayer investigations rare [55]. We aim to provide some clarity, investigating both novel two-dimensional phases of vanadium sulphides concerning their structural and magnetic properties, and showing that bulk 1T-VS_2 indeed exhibits a charge density wave.

Finally, in **Chapter 6** we investigate the influence of environmental embedding on the charge density wave phase in 2H-TaS_2, the existence of which is undisputed in the literature [56, 57]. While the material shows layer-dependent superconducting properties [13, 14], the 3×3 charge density wave phase persists apparently unchanged when epitaxially grown on graphene/6H-SiC(0001) [58]. In our molecular beam epitaxy grown 2H-TaS_2/graphene/Ir(111) samples, angle-resolved photoemission spectroscopy determines the occupied band structure, which is complemented by quasi-particle interference measurements detecting parts of the unoccupied states. This proves the absence of hybridisation and allows a tight-binding fit for the band structure of the 2H-TaS_2. In line with the freestanding nature, we observe a 3×3 charge density wave in the monolayer, while Li doping shifts the periodicity to a 2×2. Unexpectedly, the bilayer also displays a distorted 2×2 charge density wave. Calculations of the phonon dispersions based on a combination of density-functional theory, density-functional perturbation theory, and many-body perturbation theory enable us to provide phase diagrams for the 2H-TaS_2 charge density wave as functions of doping, hybridisation and interlayer potentials, and offer insight into how they affect lattice dynamics and stability.

PART II

Fundamentals

CHAPTER 1

Transition Metal Dichalcogenides

Structural Properties, Electronic Correlations and Synthesis Approaches

A tremendous diversity of physical properties renders the family of two-dimensional (2D) transition metal dichalcogenides (TMDCs) extremely popular, setting off extensive fundamental research progress and giving high hopes for widespread fields of applications such as (opto-)electronics, energy storage and conversion, catalysis, biomedicine, and sensors. The group of TMDCs includes a variety of about 60 compounds, of which about two-thirds assume layered structure (most of group IVB – VIIB TMDCs, see below) and will be introduced here. Concerning the properties of bulk TMDCs, Wilson and Yoffe have offered a seminal review [59], which has been complemented recently by Kolobov and Tominaga with a focus on TMDCs in their 2D form [11]. Triggered by their technical exploitability, many topical reviews focussing on semiconducting TMDCs have been published, concerning their chemical [60], electronic [61], optoelectronic [62] and phase transition properties [63]. Recently, also the metallic TMDCs have been reviewed [64].

In this chapter, the reader is given a brisk overview of the TMDC related fundamentals important for this thesis. We start by introducing the structural phases and layer dependent electronic band structure of TMDCs, examining in particular their charge density wave states, and possible magnetic phases. We then examine the methods that can be used to synthesize these materials and introduce van der Waals epitaxy (vdWE). Finally, we introduce the substrates used in our synthesis, namely graphene (Gr) and hexagonal boron nitride (h-BN) both epitaxially grown on Ir(111).

1.1 Crystal Structure

Layered TMDCs consist of sheets of metal atoms from group IVB – VIII[1] denoted as M atoms, sandwiched between two sheets of chalcogen atoms (S, Se or Te) denoted as X atoms, hence showing a stoichiometry of MX_2.

As schematically illustrated in Fig. 1.1 (a) and (b), there are two main phases in which single-layer TMDCs crystallise[2]. In the first, the metal atom is covalently bonded with the chalcogen X atoms

---

[1] In this work, we focus on group VB (V, Ta), and group VIB (Mo, W) TMDCs.

[2] For completeness sake should we mention that distorted metal coordination and polytypes are known to exist amongst the TMDCs. Some TMDCs develop a periodic distortion of the crystal lattice lifting the hexagonal symmetry by the

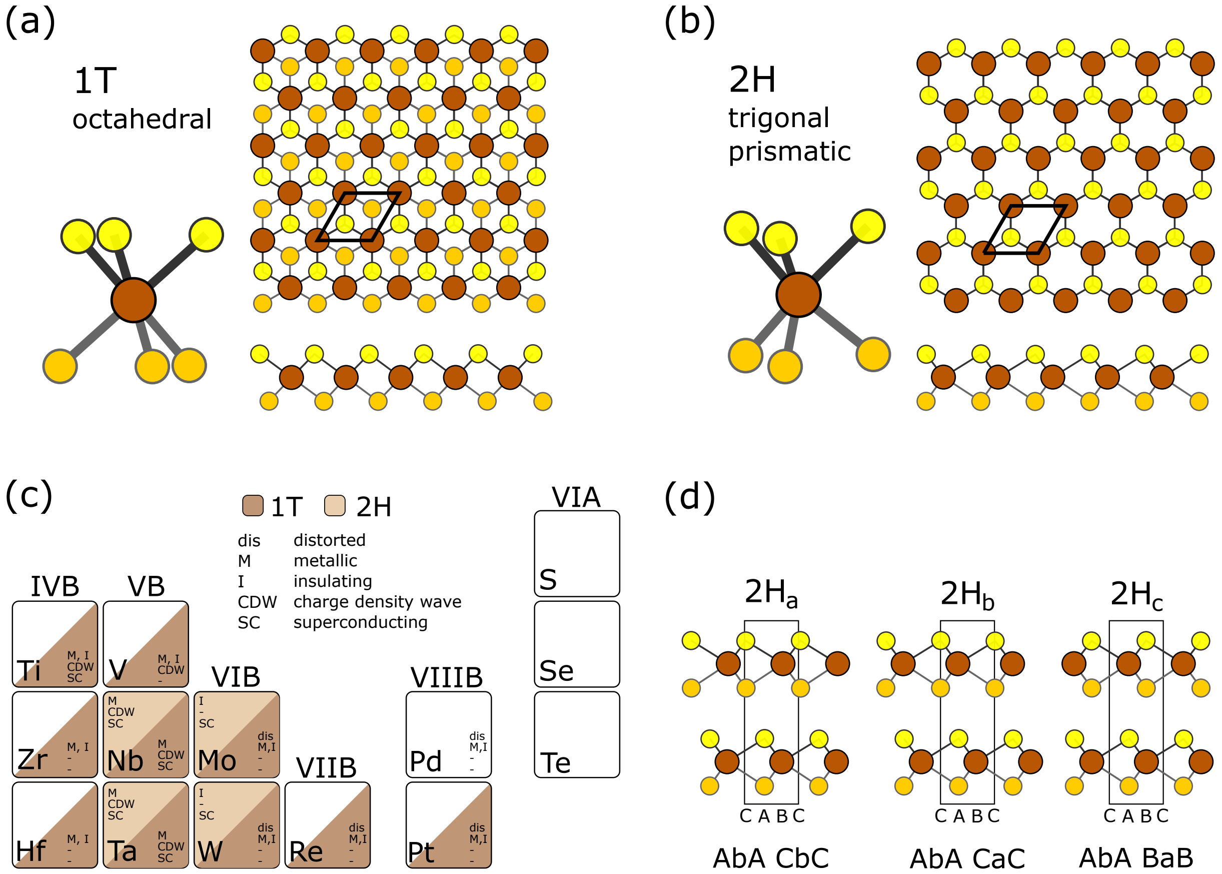

Figure 1.1: Crystal structure of TMDCs: (a) Octahedral 1T phase, visualised in perspective, top and side view. The 2D unit cell is indicated. (b) Trigonal prismatic 2H phase, visualised in perspective, top and side view. The 2D unit cell is indicated. (c) 'Periodic table' of layered TMDCs indicating selected properties and crystal structure (1T, 2H or other, as in the case of Pd-based TMDCs) based on the transition metal element involved. (d) Different stacking types of 2H phase. Figures adapted partially from Ref [59] and Ref. [61].

in 6-fold octahedral coordination (T-phase), and in the second in trigonal prismatic coordination (H-phase). The oxidation states of metal and chalcogens are 4+ and -2, respectively. The preferred phase is mainly determined by the transition metal *d*-electron count [11] and an illustrative overview is given in Fig. 1.1 (c). TMDCs containing metal atoms from group IVB are d^0 systems (the four electrons in the *d* orbitals are involved in the covalent bonding with the chalcogens) and can be found predominantly in octahedral coordination. Group VB TMDCs are d^1 systems and both trigonal prismatic and octahedral coordination may be thermodynamically stable, and in group VIB TMDCs (d^2 systems) the dominant coordination is trigonal prismatic. In each specific case, however, also the relative size of the atoms has to be taken into account.

In their three-dimensional (3D) form, multiple weakly interacting van der Waals (vdW) layers are stacked on top of each other giving rise to different polytypes. The most typical are 1T, 2H and 3R,

---

formation of metal atoms into zig-zag chains. This 1T'-phase called structure is adopted by WTe_2, for example, but is not relevant for this thesis.

where integer and letter indicate the number of layers needed to build up the 3D unit cell and crystal symmetry (T – trigonal, H – hexagonal, R – rhombohedral), respectively[3].

Due to the staggered chalcogen planes in the 1T polytype, stacking in the 1T polytype is trivial and in adjacent layers, metal atoms lie on top of each other. The stacking sequence is thus AbC AbC, where capital and lower case letters denote chalcogen and metal atoms, respectively.

In the 2H case, stacking is not trivial, giving rise to three different sub-polytypes $2H_a$, $2H_b$ and $2H_c$, which are depicted in Fig 1.1 (d). 2H-TMDCs with transition metals from group VB (Nb, Ta) are found in the $2H_a$ polytype with AbA CbC stacking (in simple words: adjacent layers rotated by 180°, metal on top of metal), while group VIB (Mo, W) 2H-TMDCs exhibit the $2H_c$ type with stacking sequence AbA BcB (in simple words: adjacent layers rotated by 180°, metal on top of chalcogen). Non-stoichiometric compounds $M_{1+x}X_2$, where additional metal atoms are located in an octahedrally coordinated site in the vdW gap, which is termed self-intercalation, take on the $2H_b$ polytype with stacking AbA CaC (in simple words: adjacent layers not rotated, metal on top of chalcogen) [65].

We note that the intercalation is not limited to self-intercalation and the intercalant does not need to be the same element as in the host material, offering chances to manipulating the system. The intercalation of TMDC compounds is an established field [66] of still active research as it gives a large lever to tune electronic properties. For example, Cu or Pd intercalation induces superconductivity in 1T-$TiSe_2$ [67, 68], whereas substitutional doping by Pt leads to insulating behaviour [69]. In 2H-TaS_2, Cu intercalation leads to both an increase of the superconducting transition temperature and a change in CDW periodicity [70]. Also, the magnetic properties may be influenced by doping, and both anti- and ferromagnetic behaviour may be induced in the metallic TMDCs [71, 72].

1.2 Layer Dependent Electronic Structure

The large number of possible combinations of transition metal and chalcogens and the variety of structural phases results in a broad range of electronic properties. A systematic understanding of the electronic structure and origin of the properties of TMDCs has been achieved and reviewed for both bulk materials [10], monolayer forms [11], and several TMDC bilayer heterostructures [73]. Here, we restrict ourselves to a phenomenological introduction and follow the outline of description by Wilson and Yoffe [59] and Huisman *et al.* [74], who – in terms of empirical electronic band structure – described the TMDCs first.

The physical properties of TMDCs are mainly dependent on the ligand field splitting of the metal *d* orbitals and again the *d*-electron count. In both the 1T and the 2H structures, the atomic *d* levels transform into narrow *d* bands because of the reduced overlap between metal atoms in the compound relative to that in the pure metal. In a simple tight-binding (TB) picture, the non-bonding *d* bands lie in between the broad valence and conduction bands. The valence band is based primarily on the

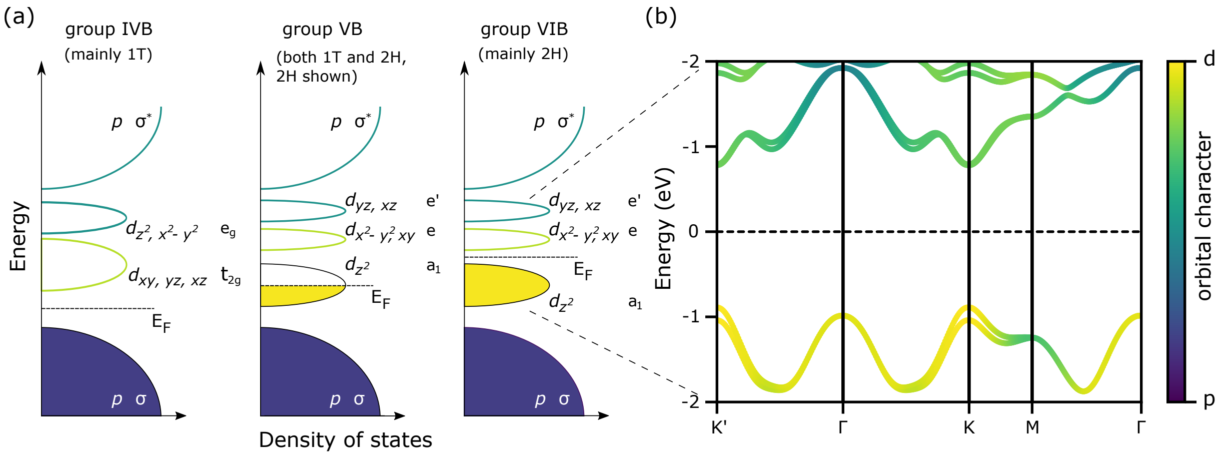

Figure 1.2: Electronic structure of TMDCs: (a) Schematic band structure of group IVB – VIB TMDCs. (b) Tight binding fit of the band structure of monolayer 2H-MoS_2. Figure adapted from Ref. [11] and TB fit from Ref. [75].

chalcogen *p* wave functions (σ, bonding states) and the conduction band arises from mainly *s* and *p* orbitals of the metal (σ^*, anti-bonding states); features we illustrate in Fig. 1.2.

As depicted in Fig. 1.2 (a), in the 1T octahedral coordination the metal *d* band is split into two degenerate orbitals e_g (d_{z^2}, $d_{x^2-y^2}$) and t_{2g} (d_{xy}, d_{yz} and d_{xz}), whereas in the 2H trigonal prismatic case the band is split into three groups: a_1 (d_{z^2}), e (d_{xy}, $d_{x^2-y^2}$) and e' (d_{xz}, d_{yz}) [76]. Please note that the orbital splitting determines which bands are lower in energy. Here, the d_{z^2} in the 2H structure is lowest in energy.

On the basis of this model, a rigid band approach to the electrical properties of the group IVB, VB, and VIB materials (found predominantly in octahedral coordination, both trigonal prismatic and octahedral coordination, and trigonal prismatic coordination, respectively) would predict insulating, metallic, and semiconducting behaviour with 0, 1, or 2 electrons in the *d* band respectively, resulting in the schematic densities of states shown in Fig. 1.2 (a). This range is experimentally found to be valid reaching from insulating behaviour[4], found in HfS_2, over semiconducting materials, such as MoS_2 and WS_2, to metallic properties in NbS_2 and VSe_2 [59].

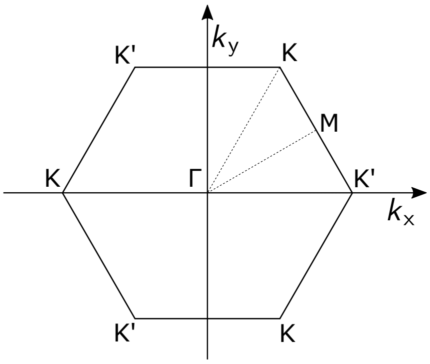

Figure 1.3: Hexagonal Brillouin zone of TMDCs. High symmetry points are indicated.

One of the intriguing features of TMDCs is the ability to tune their physical properties as a function of layer thickness. For example, several semiconducting 2H-TMDCs like MoS_2 or $MoSe_2$ display a widening of their band gap together with a transition from an indirect to a direct band gap when reducing the thickness from bulk material to the

---

[3] Further polytypes are known but not relevant for this thesis. Interested readers are referred to the literature [65].

[4] HfS_2 is generally assumed to be an insulator, owing to its low electron mobility. Nonetheless, recent studies have found HfS_2 based transistors to show electronic performances suitable for 'ultra-low-power applications' [77].

monolayer [78,79]. Fig. 1.2 (b) shows the electronic band structure of monolayer MoS_2 *via* a TB fit[5]. Opposed to the bulk, in monolayer MoS_2, the valence band maximum and the conduction band minimum are both located at the K point (see also Fig. 1.3), yielding a direct band gap. The transition from indirect to direct band gap was recently directly visualised through angle-resolved photoemission spectroscopy (ARPES) for high-quality $MoSe_2$ grown by molecular beam epitaxy (MBE) [23][6].

Additionally, the breaking of inversion symmetry in monolayer 2H-MoS_2 (and other group VIB 2H-TMDCs) together with strong spin-orbit coupling leads to opposite spin polarisation in the spin-split valence band valleys at the K and K' points of the hexagonal Brillouin zone (BZ, see Fig. 1.2 (b) and Fig. 1.3) – an effect that is absent for the bulk material [76, 83, 84]. This is commonly referred to as spin-valley coupling and makes semiconducting TMDCs attractive for their use in spintronics and valleytronics[7], even though they are usually non-magnetic [86].

With the change of band structure come also changed optical properties in the semiconducting TMDCs, such as enhanced photoluminescence (PL) [79, 87], and a change in Raman signal [88, 89]. These dependencies can be utilised to quickly investigate the number of layers in exfoliated samples.

In the metallic TMDCs, correlation phenomena such as superconductivity, CDW, or magnetism also display a clear dependence on the thickness of the TMDC layer. These phenomena will be introduced in the following.

1.3 Charge Density Waves

In regular metals, the electron density is usually highly uniform and the equilibrium positions of the ions form a periodic lattice. When lowering temperature, this configuration may become energetically unfavourable, and a transition into a state in which the charge density is spatially periodically modulated may occur. These charge density wave (CDW) phases are a consequence of electronic instabilities due to strong electron-phonon or electron-electron interaction [90]. Though CDWs are a relatively old topic [91–93] and a basic understanding of the mechanisms explaining CDW nature has been achieved, a full microscopic picture capable of explaining the origin of their formation in different materials has remained elusive to date and prevents reliable quantitative predictions of CDW properties.

In the TMDCs, CDWs occur mainly in the metallic d^1 systems with group VB transition metals due to strong electronic correlations and have a long-standing history of interest [9, 94]. Around the 1980s, CDW formation mechanisms used for explaining their occurrence in bulk TMDC systems were based on a picture offered by Peierls for a one-dimensional (1D) metallic chain, which he noted to be unstable against structural deformation [91]. In the course of renewed interest in 2D materials in their monolayer form, also TMDC CDW materials have been revisited [95, 96] and simple Fermiology has often not sufficed to explain the experimental findings.

---

[5] The Hamiltonian and the parameters used in the TB fit are taken from Ref. [80].

[6] A little ahead of their time Klein *et al.* demonstrated this transition already in 2000 in vdWE-grown WS_2/graphite, but remained largely unnoticed [81, 82].

[7] In valleytronics, the valley pseudospin, which labels the degenerate energy extrema in momentum space is exploited as a binary quantum degree of freedom for future electronics [85].

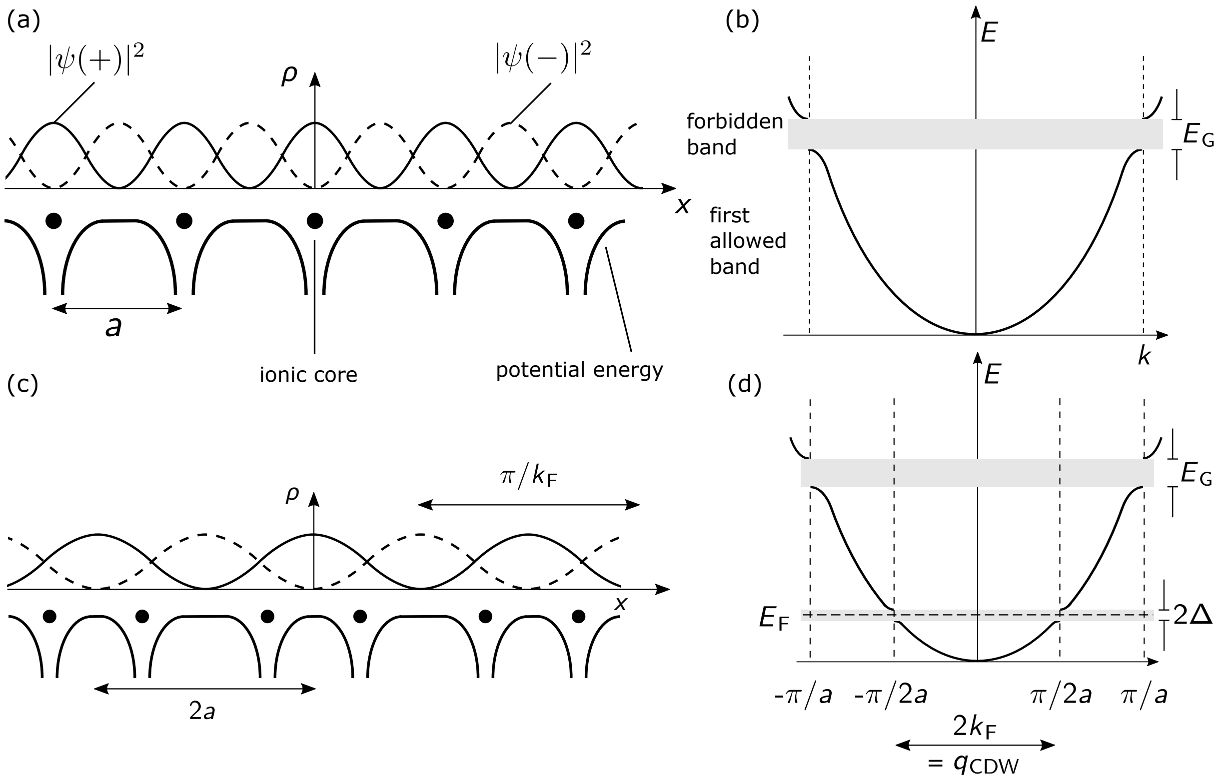

Figure 1.4: Electrons in a periodic potential and Peierls instability: (a) Probability density ρ of electrons in a periodic potential of ion cores. The probability density $|\psi(+)|^2 \propto \cos^2 \pi x/a$ leads to an increase of charge density around the ionic cores and therefore reduces the average potential energy. *Vice versa*, $|\psi(-)|^2 \propto \sin^2 \pi x/a$ increases the average potential energy. (b) Band gap opening of size E_G at the edge of the first BZ. (c) Visualisation of periodic lattice distortion, which leads to a dimerisation of the monoatomic chain. The consequent charge density modulation has a periodicity of π/k_F. (d) CDW energy gap 2Δ opening around the Fermi energy E_F. Figures adapted from Ref. [96] and Ref. [97].

Here, we introduce a qualitative understanding of CDW formation (loosely following Ref. [96]), which may be achieved by a simple energetics consideration in the 1D Peierls instability. We furthermore introduce the limits of the Peierls instability and in the end discuss peculiarities and layer number dependence of 2D TMDC CDW systems.

Peierls Instabilty

The basic idea of the Peierls instability is that in a monoatomic chain, a periodic lattice distortion (PLD, which costs deformation energy) will open up a band gap at the Fermi level E_F, by which the total energy of the system may be lowered. If the energy gain through band gap formation exceeds the deformation energy, the system will transform into the CDW state.

We consider a 1D metal chain with lattice spacing a, compare Fig. 1.4 (a). The nearly-free electrons in this weak periodic potential of the ionic cores may be described by Bloch wavefunctions, which will be reflected at the Brillouin zone (BZ) boundary fulfilling the Bragg condition. By superposition of the incoming and the reflected waves, standing waves will form, where, due to the periodicity of the system, two solutions are allowed. One of these solutions $|\psi(+)|^2$ will reduce and the other one $|\psi(-)|^2$ will increase the total energy of the system, which opens up a band gap, see Fig. 1.4 (b). Though this consideration is basic to solid-state physics, it is helpful for the following to note that the states above and below this band gap are located at the same wave vector, but are antiphase in real space, see Fig. 1.4 (a).

When introducing a static PLD, see Fig. 1.4 (c), the spacing of the Bravais lattice in real space is increased and the BZ is decreased accordingly. Following the above line of thought, this opens up a band gap at the new BZ boundary, see Fig. 1.4 (d). If the Fermi energy E_F lies inside the band gap, an electronic energy gain is achieved by lowering the energy of the occupied states and increasing the energy of the unoccupied states. It is here interesting to note that depending on the filling of the band, different PLD/CDW periodicities may lead to the specific energy gain needed for the PLD. At last, the conduction electrons will follow the distorted ionic potential and thus a periodic charge modulation occurs; by definition a charge density wave.

In order to specify under which conditions the CDW state is energetically favourable, we describe the coupling of a free-electron gas to the underlying lattice through electron-phonon coupling in a mean-field approach in the weak-coupling limit, which shall be defined by the condition that the PLD is significantly smaller than the lattice constant; a condition which is usually fulfilled in the TMDCs. The Fröhlich Hamiltonian then reads [90]:

$$\mathcal{H} = \sum_{\mathbf{k}} \epsilon_{\mathbf{k}} \, a^\dagger_{\mathbf{k}} \, a_{\mathbf{k}} + \sum_{\mathbf{q}} \hbar \omega_{\mathbf{q}} \, b^\dagger_{\mathbf{q}} \, b_{\mathbf{q}} + \frac{1}{\sqrt{N}} \sum_{\mathbf{k},\mathbf{q}} g_{\mathbf{q}} \, a^\dagger_{\mathbf{k}+\mathbf{q}} \, a_{\mathbf{k}} (b^\dagger_{-\mathbf{q}} + b_{\mathbf{q}}), \tag{1.1}$$

where the first term describes the free electron gas with $a^\dagger_{\mathbf{k}}$ and $a_{\mathbf{k}}$ being the creation and annihilation operators of the electron state $\mathbf{k}$ with energy $\epsilon_{\mathbf{k}}$. Similarly, in the second term, which describes the lattice vibrations, $b^\dagger_{\mathbf{q}}$ and $b_{\mathbf{q}}$ are the creation and annihilation operators for phonons with wave vector $\mathbf{q}$ and energy $\hbar\omega_{\mathbf{q}}$. The last term describes the electron-phonon coupling with a $\mathbf{q}$-dependent (but $\mathbf{k}$-independent) coupling constant $g_{\mathbf{q}}$.

When considering the effect of a perturbation (the PLD may be interpreted as such) on the electronic system in a linear response theory, the interaction of the electron liquid with an external potential induces a charge density, the strength of which is determined by the density response function or electron susceptibility of the system. In a nearly free electron gas model, this response function can be calculated *via* the Lindhard approximation [98], which includes both the response to the external potential as well as the potential produced by the density response itself [99]. Although the Lindhard response function is generally a complex function, in the static limit (the frequency of the external perturbation is zero, which may be assumed for a static PLD) the imaginary part vanishes and we arrive at [100]:

$$\chi_0(\mathbf{q}) = \frac{1}{L} \sum_{\mathbf{k}} \frac{f(\epsilon_{\mathbf{k}+\mathbf{q}}) - f(\epsilon_{\mathbf{k}})}{\epsilon_{\mathbf{k}} - \epsilon_{\mathbf{k}+\mathbf{q}}}, \tag{1.2}$$

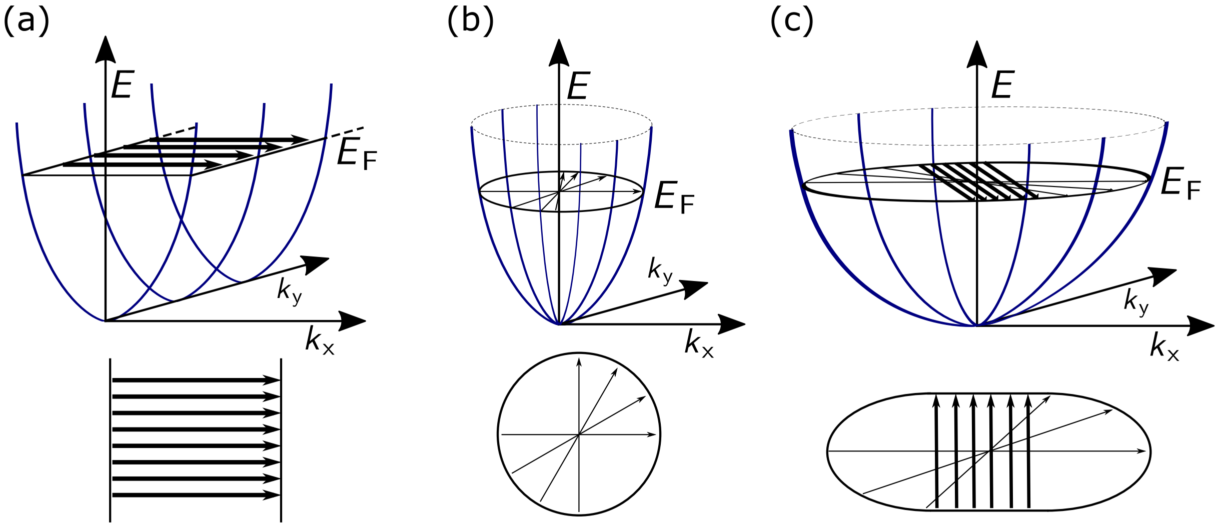

Figure 1.5: Fermi surface nesting: (a) For quasi 1D systems, the 2D Fermi surface is built up by parallel lines that can be connected by a single scattering vector. (b) For a free-electron like 2D dispersion, the nesting condition is not fulfilled. (c) When the 2D Fermi surface has parallel segments, partial nesting can be achieved. The thickness of the arrows indicates how strongly they contribute to nesting.

with $f(\epsilon_{\mathbf{k}})$ the Fermi distribution at energy $\epsilon(\mathbf{k})$, L the length of the chain and the sum running over the first BZ. It is instructive to understand the action of the Fermi surface (FS) topology on the electron susceptibility. The numerator in the expression of $\chi_0(\mathbf{q})$, becomes non-zero when occupied states can be coupled to unoccupied states by a wave vector $\mathbf{q}$ and the biggest contributions to $\chi_0(\mathbf{q})$ require a small denominator, hence states close to the Fermi energy. When the FS is formed such that one $\mathbf{q}$ can connect multiple states, contributions to $\chi_0(\mathbf{q})$ increase drastically. This is given for parallel segments of the FS, where so-called nesting is achieved, see Fig. 1.5.

In Fig. 1.5 (a), we illustrate this situation for the ideal 1D case. The Fermi surface is here built up of two parallel lines, and one single nesting vector can connect infinitely many states. This is called perfect nesting and consequently, the susceptibility $\chi_0(\mathbf{q})$ diverges as shown in Fig. 1.6 (a). In higher dimensions, the nesting condition cannot always be fulfilled. Fig. 1.5 (b) illustrates that for a free-electron like 2D dispersion no nesting is achieved and consequently, also the susceptibility decreases [see. Fig. 1.6 (a)]. If the Fermi surface is formed such that partially parallel segments evolve, like in Fig. 1.5 (c), partial nesting can be achieved.

The Peierls picture draws also a connection to the phonon dispersion: since in Eq. (1.1) we explicitly find electron-phonon coupling, also the phonon system reacts to the electronic perturbation. The associated Kohn anomaly [101] - a strong anomaly in the phonon dispersion - is usually considered a consequence of the divergence of the susceptibility function and is illustrated in Fig. 1.6 (b). This may

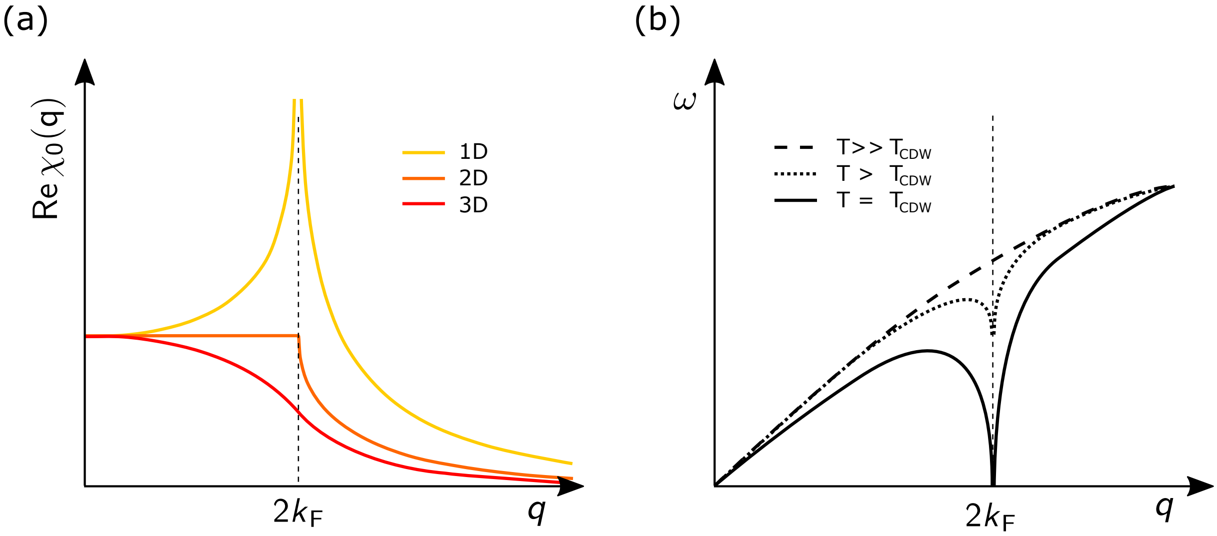

Figure 1.6: (a) Real part of Lindhard response function for a free electron gas in 1D, 2D, and 3D. Phonon energy of a 1D atomic chain at different temperature showing a Kohn anomaly. Adapted from [90].

be understood by noting that solving the Hamiltonian in Eq. (1.1) results in a phonon renormalisation

$$\tilde{\omega}_{\mathbf{q}}^2 = \omega_{\mathbf{q}}^2 \left(1 - \frac{4\,g_{\mathbf{q}}^2}{\hbar\,\omega_{\mathbf{q}}} \chi_0(\mathbf{q})\right). \tag{1.3}$$

For non-zero electron-phonon coupling $g_{\mathbf{q}}$ and if the nesting condition at $\mathbf{q}_{\mathbf{CDW}}$ is fulfilled, the susceptibility function diverges, and the renormalised energy of the phonon becomes imaginary $\tilde{\omega}_{\mathbf{q}_{\mathrm{CDW}}}^2 < 0$. Imaginary phonon frequencies are associated with a complete softening of the phonon mode, meaning that a static lattice distortion appears. This PLD then has a wavelength $\lambda_{\mathrm{CDW}} = 2\pi/q_{\mathrm{CDW}} = \pi/k_{\mathrm{F}}$, as indicated in Fig. 1.4 (c).

The question if a system is unstable against CDW formation may be determined by the criterion that the lattice deformation energy $\delta E_{\mathrm{lattice}}$ is smaller than the distortion-induced band energy gain δE_{band}. Noting that $\delta E_{\mathrm{lattice}} \propto \omega_{\mathbf{q}}$ and $\delta E_{\mathrm{band}} \propto -g_{\mathbf{q}}^2\,\chi_0(\mathbf{q})$, and including Coulomb interaction U_{q} and exchange interactions V_{q}, we arrive at [102]:

$$\frac{4\,g_{\mathbf{q}}^2}{\hbar\,\omega_{\mathbf{q}}} - 2\,U_{\mathrm{q}} + V_{\mathrm{q}} > \frac{1}{\chi_0(\mathbf{q})}. \tag{1.4}$$

Concluding, the 1D Peierls transition stresses the requirements for CDW formation: large electron-phonon and electron-electron exchange interactions (g_{q} and V_{q}), small Coulomb interaction and lattice strain energy (U_{q} and ω_{q}), and large electronic susceptibility $\chi_0(\mathbf{q})$ facilitate the electronic instability.

Limits of the Peierls Picture

The 1D Peierls picture helpfully illustrates the main dependencies for CDW formation and introduces commonly employed criteria for a CDW such as a periodic lattice distortion, an electronic band gap, Fermi surface nesting, a sharp peak in the electronic response function, and a Kohn anomaly. However, in real materials and especially in 2D and 3D, these need not all be fulfilled [103] due to the following reasons.

In the above considerations the first simplification is to assume each g_q, U_q, and V_q to be $\mathbf{k}$-independent. Another approximation which not needs be fulfilled in real materials is the static limit needed to reduce the description to the real part of the susceptibility function. Experimentally, ARPES can be utilised to measure the occupied electronic structure and calculate both the imaginary and the real part from the electronic bands [104]. Furthermore, we quietly implied the harmonic, adiabatic and independent electron approximations. Even though the first two are frequently used and may suffice to describe many systems, the independent electron approximation may not hold in strongly correlated systems. In this case, the non-interacting Lindhard function $\chi_0(\mathbf{q})$ cannot properly describe the properties of the electronic system and the interacting susceptibility $\chi(\mathbf{q}, \omega)$ should be used, which is not experimentally accessible, however. All these approximations explain that even though the Peierls picture predicts 1D metallic chains to always form a CDW, they might, in fact, be stable [105].

Charge Density Waves in 2D Transition Metal Dichalcogenides

Though the TMDCs are prone to CDW formation, experimental observations are often contradictory and no thorough understanding of their CDW properties has been achieved, let alone a full microscopic theory. Also, the layer number dependency of TMDCs and CDW properties adds a parameter, which is often not fully understood. In the following, we discuss selected layer dependent properties of the metallic TMDCs, which includes, in particular, their transition temperatures. A comprehensive overview of group VB TMDCs and their CDW and superconducting phases is given in Fig. 1.7.

To start with, in the group VB TMDCs, CDW properties seem to depend strongly on the transition metal coordination. In bulk 2H-TMDCs, periodicities close to a 3×3 superlattice are typically observed, while in the 1T polytype, a star-of-David distortion is typical (see below).

Considering the 2H polytype, 2H-TaSe$_2$ first undergoes a transition into a non-commensurate CDW at $T_\mathrm{NC-CDW} = 122$ K, to eventually fully lock-in with the underlying lattice at $T_\mathrm{C-CDW} = 90$ K [94, 115], well above the superconducting transition temperature $T_\mathrm{C} = 0.2$ K [120, 124]. When thinning down the layer thickness to monolayer, CDW order has been shown to persist, despite a significant change in band structure as observed by ARPES and STM [123].

On the other hand, bulk 2H-NbSe$_2$ transitions into a non-commensurate CDW state close to 3×3 at $T_\mathrm{NC-CDW} = 33$ K [115] and stays incommensurate in its CDW ground state as confirmed by electron diffraction [125], nuclear magnetic resonance [126], and scanning tunnelling microscopy (STM) [127]. In bulk it further exhibits superconductivity below $T_\mathrm{C} = 7.5$ K [116]. At monolayer

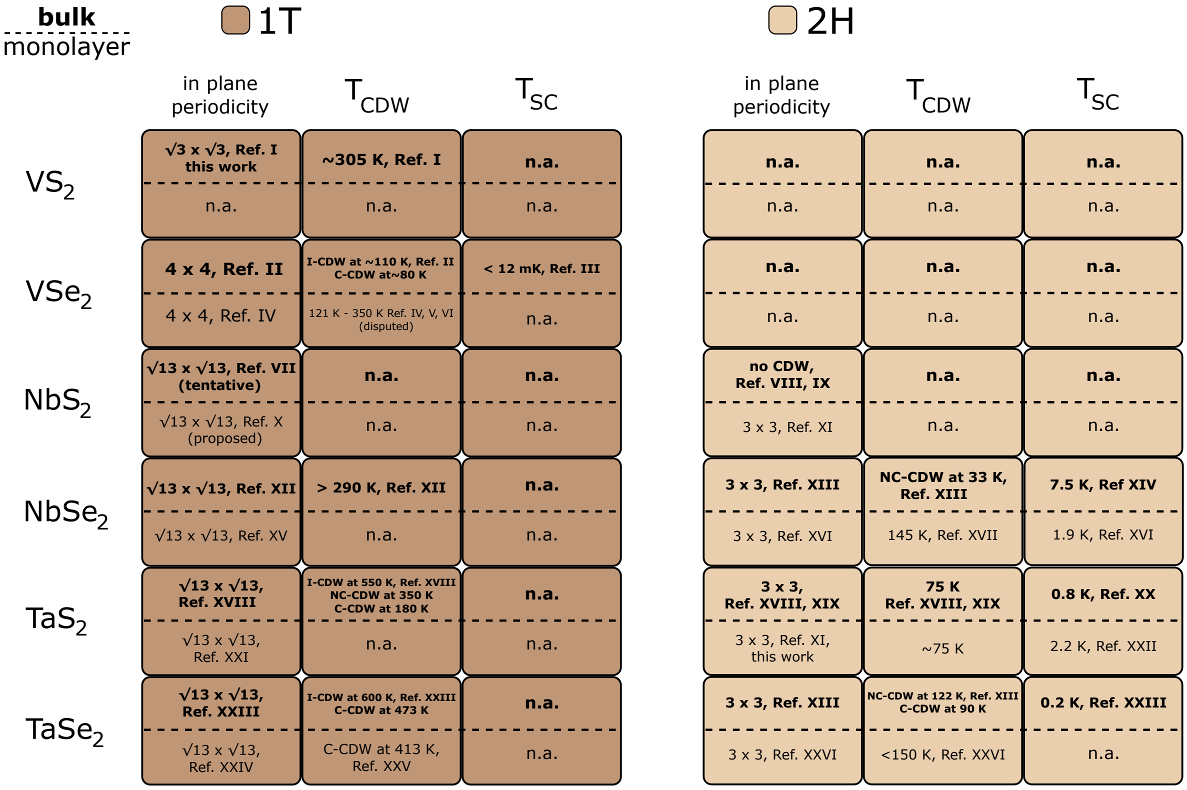

bulk
monolayer

	1T			2H		
	in plane periodicity	T_{CDW}	T_{SC}	in plane periodicity	T_{CDW}	T_{SC}
VS_2	**√3 x √3, Ref. I this work** n.a.	**~305 K, Ref. I** n.a.	**n.a.** n.a.	**n.a.** n.a.	**n.a.** n.a.	**n.a.** n.a.
VSe_2	**4 x 4, Ref. II** 4 x 4, Ref. IV	**I-CDW at ~110 K, Ref. II C-CDW at~80 K** 121 K - 350 K Ref. IV, V, VI (disputed)	**< 12 mK, Ref. III** n.a.	**n.a.** n.a.	**n.a.** n.a.	**n.a.** n.a.
NbS_2	**√13 x √13, Ref. VII (tentative)** √13 x √13, Ref. X (proposed)	**n.a.** n.a.	**n.a.** n.a.	**no CDW, Ref. VIII, IX** 3 x 3, Ref. XI	**n.a.** n.a.	**n.a.** n.a.
$NbSe_2$	**√13 x √13, Ref. XII** √13 x √13, Ref. XV	**> 290 K, Ref. XII** n.a.	**n.a.** n.a.	**3 x 3, Ref. XIII** 3 x 3, Ref. XVI	**NC-CDW at 33 K, Ref. XIII** 145 K, Ref. XVII	**7.5 K, Ref XIV** 1.9 K, Ref. XVI
TaS_2	**√13 x √13, Ref. XVIII** √13 x √13, Ref. XXI	**I-CDW at 550 K, Ref. XVIII NC-CDW at 350 K C-CDW at 180 K** n.a.	**n.a.** n.a.	**3 x 3, Ref. XVIII, XIX** 3 x 3, Ref. XI, this work	**75 K Ref. XVIII, XIX** ~75 K	**0.8 K, Ref. XX** 2.2 K, Ref. XXII
$TaSe_2$	**√13 x √13, Ref. XXIII** √13 x √13, Ref. XXIV	**I-CDW at 600 K, Ref. XXIII C-CDW at 473 K** C-CDW at 413 K, Ref. XXV	**n.a.** n.a.	**3 x 3, Ref. XIII** 3 x 3, Ref. XXVI	**NC-CDW at 122 K, Ref. XIII C-CDW at 90 K** <150 K, Ref. XXVI	**0.2 K, Ref. XXIII** n.a.

Figure 1.7: Thickness-dependent phase transition temperatures and CDW periodicities of group VB TMDCs. The colours indicate the polytype, bulk properties are in bold font, monolayer properties are in regular font, 'n.a.' denotes not available. Ref.I [50], Ref.II [47], Ref.III [106], Ref.IV [107], Ref.V [108], Ref.VI [109], Ref.VII [110], Ref.VIII [111], Ref.IX [112], Ref.X [113], Ref.XI [58], Ref.XII [114], Ref.XIII [115], Ref.XIV [116], Ref.XV [19], Ref.XVI [17], Ref.XVII [16], Ref.XVIII [117], Ref.XIX [56], Ref.XX [118], Ref.XXI [119], Ref.XXII [13], Ref.XXIII [120], Ref.XXIV [121], Ref.XXV [122], Ref.XXVI [123].

thickness, a considerable enhancement of the CDW transition temperature $T_{\mathrm{NC-CDW}} = 145$ K has been reported [16]. This, however, has not been confirmed by other authors who documented a 3×3 CDW in the monolayer [17]. Still, there is a consensus that the superconducting transition temperature decreases with reducing thickness [17, 26, 128].

A similar behaviour holds for 2H-TaS_2, which has its bulk CDW transition temperature to a non-commensurate (close to 3×3 periodicty) at $T_{\mathrm{NC-CDW}} = 75$ K [56] and also stays incommensurate [57, 115]. In monolayer 2H-TaS_2, a persistent 3×3 CDW has been reported [58], and in contrast to 2H-$NbSe_2$, alongside an increase of the superconducting transition temperature [13].

Surprisingly, in the bulk compound 2H-NbS_2, CDW order seems to be absent [111, 112]. However, recent findings have shown traces of CDW order [110], and further to this 2H-NbS_2 has been argued to be susceptible to self-intercalation and that CDW order is suppressed in non-stoichiometric $Nb_{1+x}S_2$ for $x > 0.07$ [129]. In the monolayer regime, on the other hand, 2H-NbS_2 has been shown to exhibit a 3×3 CDW [58], in accordance with DFT calculations [130], which also show possible spin density wave instabilities [131].

What all the above TMDCs have in common is that the 1D Peierls picture does not suffice to describe their CDW formation properly. In 2D, the FS is generally not planar and the new BZ edge formed in the CDW phase might only partly coincide with the FS, which is where the energy gain comes from. This results in only partial gapping of the FS and at certain locations in the BZ the density of states (DOS) at E_F being non-zero, ruling out a Peierls picture metal-to-insulator transition. Consequently, all the above materials are observed to remain metallic in their CDW state.

Additionally, the role of the electronic susceptibility seems to be strongly diminished as the FS does not need to show indications for nesting (as *e.g.* in $NbSe_2$ [132–134]). As the non-interacting response function strongly depends on the dimensionality of the system [see Fig. 1.6 (a)], in 2D the logarithmic divergence of χ_0 with temperature evolves into a smooth peak, which is also reflected in experimental data [135]. Accordingly, the Kohn anomalies are not as strong and generally, stronger electron-phonon coupling is required to foster CDW formation [136, 137].

In contrast to the 2H TMDCs, the octahedrally coordinated 1T polytypes behave substantially different, and in the CDW ground state, the electron-electron interaction strongly affects the electronic structure [96, 138]. This may lead to Mott [139], Slater, or magnetic-insulating states [140] and even to spin liquids [20]. Along with other non-commensurate phases, a star-of-David distortion can be found in the materials 1T-$TaSe_2$ [141], 1T-$NbSe_2$ [19, 142], and 1T-TaS_2 [94]. In 1T-NbS_2, the star-of-David CDW phase has recently been proposed [113]. See Fig. 1.7 for more information.

As indicated, CDW characteristics are non-trivial and very material-specific. In Chapter 5 and Chapter 6, we will investigate the materials 1T-VS_2 and 2H-TaS_2 concerning their CDW properties.

1.4 Magnetism in Two-Dimensional Systems

Even though layered magnetic crystals have been investigated and available since the 1970's [143, 144], for a long time magnetism in 2D materials had remained an elusive dream. Only recently, magnetic properties have been observed experimentally in 2D CrI_3 and $Cr_2Ge_2Te_6$ [27, 28]. The magnetic properties of 2D materials and their heterostructures have been reviewed in Ref. [145] which serves as a foundation for the following.

Whether long-range magnetic order may be established or not depends on a delicate interplay. On the one hand, the exchange interaction between neighbouring spins tends to favour specific relative orientations between them and on the other hand, thermal fluctuations tend to misalign magnetic moments with increasing temperature. While in 3D, magnetic order may always be present at finite temperature, long-range order in 1D is only possible at $T = 0$ K [146]. In 2D, the Mermin-Wagner theorem predicts the absence of long-range magnetic order due to thermal fluctuations at any finite temperature if the spin dimensionality[8] is isotropic, thus $n = 3$ [147, 148]. In a basic picture, the generalised Heisenberg spin Hamiltonian reads [145]:

$$\mathcal{H} = -\frac{1}{2}\sum_{i,j}(J\,\mathbf{S_i}\cdot\mathbf{S_j} + \Lambda S_i^z S_j^z) - \sum_i A(S_i^z)^2, \tag{1.5}$$

where J is the exchange coupling constant between neighbouring spins $\mathbf{S_i}$ and $\mathbf{S_j}$ [favouring either ferromagnetic ($J > 0$) or antiferromagnetic ($J < 0$) order], and A and Λ are the on-site and intersite (or exchange) magnetic anisotropies, respectively. If A and Λ are zero, the Hamiltonian describes the isotropic Heisenberg model, whose solution includes gapless long-wavelength excitations (spin waves) that have a finite DOS in 2D and can thus be easily excited at any finite temperature, which prohibits long-range order.

If A and Λ are non-zero, the magnetic anisotropy lowers the spin dimensionality which opens a gap in the spin wave spectrum, and thereby long-range order may also be stabilised in 2D. Thus, if not for magnetic anisotropy, magnetism is not *a priori* guaranteed to be maintained in monolayer thickness, even when starting from bulk magnetic materials.

In real systems, the magnetic anisotropy may originate from strong spin-orbit coupling (magneto-crystalline anisotropy) as in CrI_3 [149] or may be induced by applying external magnetic fields [28].

Magnetism in 2D Transition Metal Dichalcogenides

Though usually, the family of TMDCs is non-magnetic – aside from edges [150, 151], grain boundaries [152, 153], vacancies [154], strain [29], or other impurities – recently VS_2 and VSe_2 compounds have attracted major attention because of their magnetic properties. Besides plentiful theroretical contributions predicting magnetic behaviour [29, 48, 51, 52, 155, 156], experimental findings also indicate magnetic order in these materials.

From a theoretical perspective, in both VS_2 and VSe_2 ferromagnetism is predicted from a difference in spin-up and spin-down DOS at E_F. By the projected DOS, it is inferred to stem mainly from the V-atoms, whereas S or Se atoms, contribute weakly to the total magnetic moment [29].

Experimentally, indications for room-temperature ferromagnetism were first found in ultrathin VS_2 nanosheets [157, 158]. For VSe_2, two studies found indications for magnetism in MBE-grown single-layer VSe_2 on HOPG [108, 159]. In the rather ambiguous first, peaks in the dI/dV spectrum were attributed to magnetic characteristics [159], while in the second, clear indications for ferromagnetism in both VSe_2 on HOPG and on MoS_2 were found by magneto-optical Kerr measurements with a Curie-temperature above room-temperature [108]. By contrast, bulk VSe_2 is paramagnetic [160]. It

---

[8] The spin dimensionality is the order of the dimensional degree of freedom in which the spins are allowed to align in. Consider spins on a square lattice; if the spin is only allowed to point out-of or in the plane (strong uniaxial anisotropy), the spin dimensionality is $n = 1$ and the spin Hamiltonian describes the Ising model. If the spins may align in a given plane (easy-plane anisotropy), it is $n = 2$ and the Hamiltonian would describe the XY model. For $n = 3$ there is no constraint on the spin direction and the Hamiltonian describes the isotropic Heisenberg model.

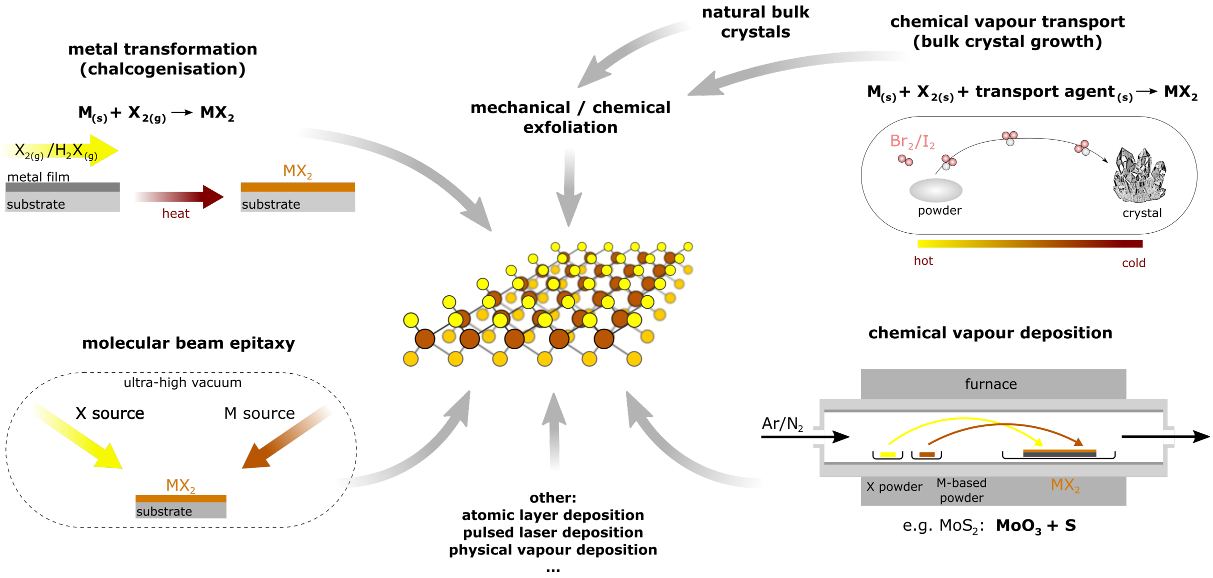

Figure 1.8: Summary of primary synthesis techniques for the formation of monolayers of TMDCs. These methods include exfoliation from natural or chemical vapour transport grown bulk crystals, chemical vapour deposition, molecular beam epitaxy and others. Figure partially adapted from Ref. [168].

has been pointed out that this discrepancy might be explained by a change in band structure and a comparably higher DOS at E_F in the monolayer case then fulfilling the Stoner criterion[9] [29,145,162].

Magnetic 2D materials are important for spintronics applications, in which the spin degree of freedom is used for information processing. In this regard, for example magnetic tunnel junctions are proposed on the basis of VSe_2/MoS_2 heterostructures [163], and the heterostructure VS_2/MoS_2 is proposed to function as a spin-filter with variable Schottky barrier heights [164]. In Chapter 5, we will investigate the magnetic properties of VS_2 layers grown on Gr/Ir(111).

1.5 Synthesis

This section aims to embed the synthesis approach used in this thesis in a bigger framework and briefly introduces common techniques (see Fig. 1.8 for an overview) and their assets and drawbacks. Approaches to the experimental fabrication of 2D materials can be divided into two categories: top-down techniques in which already existing 3D crystals are exfoliated into few-layer structures, and bottom-up approaches, in which single to few-layer systems are grown *e.g.* by molecular beam epitaxy (MBE) or chemical vapour deposition (CVD). In the following, in-depth information will be only given for MBE; we refer to the literature for reviews on exfoliation [165] and CVD [166] and crystal growth [167].

---

[9] Within the Stoner criterion the energy gain via a spin splitting of the band which crosses E_F is compared with the kinetic energy cost produced by displacing minority-spin electrons into a higher-energy majority-spin band and only when a net energy reduction can be achieved, the system may become spontaneously magnetic [161].

Mechanical exfoliation is one of the most successful techniques for obtaining high crystalline quality [1, 169] of 2D materials in monolayer or few-layer form. In this simple approach, thin flakes of TMDCs are peeled off from the bulk crystal by micromechanical cleavage and are put on target substrates. Though the crystal quality is excellent, the number of layers in the structure fabricated is not controllable and the method is not suitable for the fabrication of large-area TMDC films required for practical applications. For fundamental research, on the other hand, also the ability to form heterostructures is of concern and the ease with which they are mechanically formed underlines the importance of mechanical exfoliation [170].

Liquid [171], chemical [87] and thermal exfoliation [172] are valuable variants of exfoliation, which nonetheless lack the ability of thorough growth controllability; a requirement which is essential for the investigation of the above-mentioned layer number dependent properties.

Methods capable of growth control on the atomic level are bottom-up techniques including CVD and MBE.

Nowadays, CVD is the mainstream approach for large-scale fabrication of 2D materials. In CVD, a target substrate is exposed to volatile precursor molecules which react or decompose to produce the desired deposit. For TMDC growth, different approaches to CVD exist, including pre-deposited metal chalcogenisation [173] or admittance of both metal and chalcogens through precursors [174]. Though CVD has advanced to yield high-quality, uniform layers of controllable thickness and size, the synthesis in ambient conditions impedes the preservation of pristine materials properties, and oxidation and degradation are likely to happen [175].

To avoid these obstacles and to enable close connection to *ab initio* predictions, a growth method needs to operate *in situ* and under ultra-high vacuum (UHV) conditions. Here, we distinguish between three different approaches:
(I) One elegant version is the growth of single-layer TMDCs by direct chalcogenisation of a transition metal single crystal as performed in the growth of $PtSe_2$/Pt(111) [176]. In this way, single-crystalline monolayer $PtSe_2$ was grown for the first time, showing a moiré of 3×3 $PtSe_2$ unit cells on 4×4 Pt(111) unit cells. This method is obviously very limited in the flexibility of TMDC growth.
(II) Rather than obtaining the desired transition metal from the substrate, it can be supplied externally during the growth process. Originally first employed for the synthesis of small MoS_2 clusters on Au(111) in the context of catalysis research [177, 178], a successful, very low pressure *in situ* CVD approach using a catalytically active metallic substrate to support the decomposition of a chalcogen containing precursor molecule has been developed using simultaneous supply of Mo and H_2S. In the recent past, the technique was extended to yield large islands and full monolayer coverage on Au(111) [179, 180] and even single-crystalline monolayer MoS_2 was achieved [181]. Using the same approach, the synthesis of high-quality WS_2 [34], NbS_2 [36], TaS_2 [35] and VS_2 [55] has been demonstrated.

Though the epitaxy of TMDCs on metal (111) surfaces is excellent and enables high-quality ARPES experiments [176, 182, 183], the interaction of the TMDCs with the metal substrate is considerable. It lifts the Au(111) herringbone reconstruction [179, 180], causes a band broadening and distortion, band gap narrowing [184], doping, a suppression of CDWs, and impedes spectroscopic analysis of the intrinsic TMDC properties [33, 35, 179]. One approach to solve this problem is the post-growth intercalation of atoms or molecules, which decouple the epilayer from the substrate, which has been recently shown for WS_2 on Ag(111) intercalated by Bi atoms [185].

van der Waals Epitaxy

(III) A method that can fulfil the above requirements of thickness controllability and cleanliness with the asset of low substrate interaction is van der Waals MBE [37, 38, 40], *ab hinc* shortened as van der Waals epitaxy (vdWE). In vdWE, the two reactants are supplied from the vapour phase under UHV conditions onto an inert substrate, with which the interaction of the growing TMDC is only of van der Waals type, but strong enough to impose orientation. Recent reviews on progress in the growing field of vdWE can be found in Ref. [46, 186].

Building on the pioneering work of Koma and his group [37, 38, 40], vdWE has grown into an active field of growth-related research. Notably, it holds some considerable advantages over its fellow growth techniques, also by making use of the fact that *in situ* growth allows *in situ* analysis:

Firstly, the use of high purity sources and a UHV growth environment minimises the impurity concentration and the comparably lower growth temperatures justify the inherent ability to grow vertical heterostructures with minimal degradation [187]. This enables high experimental flexibility, and even allows monolayers normally unstable under ambient conditions to be synthesised and analysed [188].

The lack of covalent bonding between the substrate and epilayer [37] allows to grow highly lattice-mismatched heterostructures without strain [189]. This has been documented in several systems using methods including reflection high-energy electron diffraction [37], low energy electron diffraction (LEED) [190], STM [191–193], and Raman spectroscopy [194].

Even if the substrate-epilayer interaction is low, it is not absent as indicated by two factors:
(i) As usually indicated by LEED and STM, well established epitaxial orientation of the epilayer with the substrate has been shown in a variety of systems such as $MoSe_2$ thin films on SnS_2 [39], $MoSe_2/HfSe_2$ [195], $TaSe_2/MoSe_2$ [187], WTe_2 on different substrates such as MoS_2 or Bi_2Te_3 [190], and $SnSe_2/WSe_2$ [196].
(ii) Selected systems show a moiré pattern, such as in monolayer WSe_2 on monolayer MoS_2 on graphite [197, 198], WSe_2/graphite or graphene [199, 200], $WS_2/MoTe_2$ [201], $MoSe_2$/BLG [202], VSe_2/MoS_2 [108], which opens up possibilities of achieving new system properties [203].

Precise thickness control of the vdWE-grown layers is indicated by transmission electron microscopy and low energy electron loss spectroscopy which are used to monitor atomically sharp interfaces [39].

All this enables investigations of unique precision, including measurement of band gap renormalization [202], detection of charge density waves [204], and spin-charge separation in one-dimensional metallic twin boundaries of $MoSe_2$ and MoS_2 monolayers [47, 205].

In addition, vdWE is an ideal growth approach to study fundamental nucleation and growth mechanisms, which we will make use of in this thesis. Unfortunately, growth models used to describe conventional epitaxy, such as Frank-van-der-Merwe-growth, Stranksi-Krastanow-growth, and Volmer-Weber-growth are not suitable for characterising vdWE. These models apply when out-of-plane bonding is of comparable size to in-plane bonding; an assumption which is not true for vdWE, where interlayer interaction is weaker than in-plane interaction. While the conventional models are based on equilibrium thermodynamics, for vdWE growth kinetic quantities such as adsorption, desorption, surface- and edge-diffusion, and nucleation and attachment are important [206].

Theoretical modelling can help understanding of growth processes to gain improved control over structural properties such as nucleation density, grain sizes, point defects, layer number, and surface roughness. However, owing to the seldom-practised nature of vdWE in contrast to conventional epitaxy, theoretical modelling and simulations are still rare in the field [207–211].

1.6 Substrates

Although in vdWE the substrate interaction is generally low, the choice of substrate still plays an important role. Besides the above-mentioned moiré superlattices, which are a strong indicator for substrate-epilayer interaction, certain substrates have a distinct influence on their adlayers' properties. For example, $MoSe_2$ grown on HOPG shows a giant band gap renormalisation – that affects its optoelectronic properties – compared to $MoSe_2$ on bilayer graphene on SiC [202]. Furthermore, while the $MoSe_2$ band structure has been shown to resemble that of the freestanding case on graphitic substrates, for $MoSe_2/MoS_2$ and $MoSe_2/WSe_2$ signs for hybridisation have been reported [212,213].

From a growth perspective, the substrate may also influence the balance of the competition on the thermodynamic stability between the single-layer and the multilayer [210], which will be shown later in this work to be manipulable by intercalating the substrate prior to the growth of the TMDC (see Chapter 6).

In this section, we will shortly introduce the substrates used in this thesis. The main substrate is Gr/Ir(111), while in some experiments a layer of h-BN/Ir(111) is used.

Graphene on Ir(111)

The structural and electronic properties of graphene (Gr) have been reviewed many times. Here, we restrict to a brief, fundamental introduction and more detailed information can be found in Ref. [214].

Gr is a 2D sp^2 hybridised allotrope of carbon and forms a honeycomb lattice. The hexagonal Bravais lattice is built up by unit cells with two carbon atoms denoted A and B forming two sublattices. The hexagonal first BZ shows the same high symmetry points Γ, M, K, and K' as in the TMDCs (cf. Fig. 1.3), where K and K' are again inequivalent due to the two sublattices in the Bravais lattice.

Gr's band structure consists of a valence band derived from π-states and a π^*-states derived conduction band. The two bands meet at the six Dirac points which are located at the K and K' points, around which the dispersion relation is linear forming so-called Dirac cones.

Owing to the delocalised π electrons, graphene is chemically inert [215] and only non-covalent physisorption on the basal plane is practically possible [216].

In this thesis, single-crystalline Gr is *in situ* epitaxially grown on Ir(111), the method is described in Section 2.6. Due to a lattice mismatch between Gr ($a_{Gr} = 2.46$ Å) [217] and Ir(111)

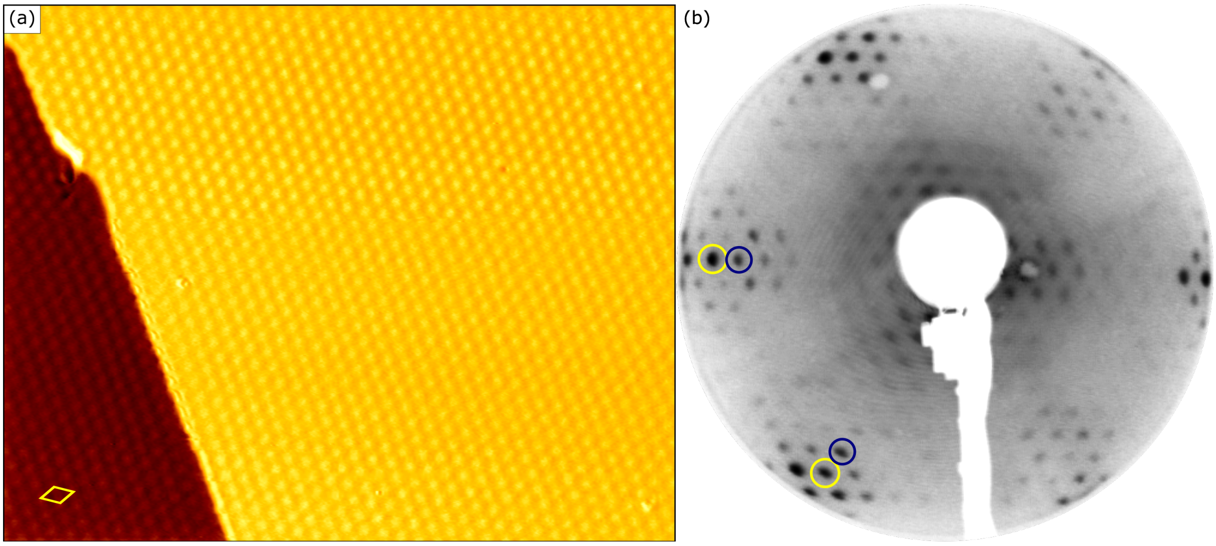

Figure 1.9: Structure of Gr on Ir(111): (a) STM topograph of Gr on Ir(111). A step edge crosses the image from top left to bottom right. The moiré unit cell is indicated. (b) LEED pattern of Gr on Ir(111) at 75 eV. The position of the Gr and Ir(111) spots are indicated, the residual diffraction spots originate from the moiré. Image information (image size, sample bias, tunnelling current): (a) 100×80 nm^2, -2 V, 1 nA.

($a_{Ir} = 2.715$ Å) [218], the system shows a moiré superlattice of 25.3 Å periodicity. This is illustrated in Fig. 1.9. In (a), an STM topograph illustrates the moiré superlattice, which is also reflected in the LEED data in panel (b).

Gr on Ir(111) is only weakly interacting; it is only physisorbed with a low binding energy of 50 meV per carbon. The weak bonding is reflected in its adsorption height of $h = 3.38$ Å and $\Delta h \approx 0.6$ Å corrugation [219]. In ARPES, the Dirac cone of Gr on Ir(111) resembles that of the freestanding case but is shifted slightly above the Fermi energy, yielding *p*-doping by about 100 meV [220].

Hexagonal Boron Nitride on Ir(111)

Hexagonal boron nitride (h-BN) is another vdW substrate used in this thesis. Structurally, h-BN is very similar to Gr. It is formed by a superposition of two triangular sublattices each containing B and N atoms, respectively. The lattice constant is 2.48 Å [221]. The first BZ is also hexagonal, showing the same high symmetry points. Electronically, h-BN is an insulator with a large band gap of about 5 eV [222].

Monolayer h-BN is grown similarly to Gr and experimental growth details can be found in Section 2.6. Due to the lattice mismatch between h-BN and Ir(111), the system shows a moiré superlattice with a periodicity of 29.1 Å [221].

Due to a stronger interaction between h-BN and Ir(111) compared to Gr/Ir(111), h-BN has a strong corrugation. In x-ray standing wave measurements, the mean adsorption height in strongly chemisorbed valleys is 2.20 Å, where weakly physisorbed hills show a height of 3.71 Å [221].

CHAPTER 2

Methods

Experimental Methods, Procedures and Theoretical Calculations

This chapter introduces the basic concepts of the experimental methods and the typical procedures used in this thesis. These include mainly scanning tunnelling microscopy (STM) and -spectroscopy (STS) and low-energy electron diffraction (LEED), which will be introduced in the first two sections. After this, we introduce the here less frequently employed techniques angle-resolved photoemission spectroscopy (ARPES) and x-ray circular dichroism (XMCD) in section three and four.

We will use section five to shortly introduce the experimental setups including both home labs and beamlines. Based on these fundaments we introduce typical procedures including a technical description of the sample preparation in section six.

Finally, in section seven, we introduce the basics of the theoretical calculations that corroborate our experimental findings.

2.1 Scanning Tunnelling Microscopy / Spectroscopy

Scanning tunnelling microscopy (STM) is a surface science technique used for imaging surfaces down to the atomic level. Since its Nobel prize awarded development in 1982 by Binning and Rohrer [223], the technique became ubiquitous in nano- and surface science and has been reviewed numerous times. Notable detailed introductions to the field can be found in Chen's book [224] and in the more recent book of Voigtländer [225].

The basic principle of the technique is to probe the local topography and electronic structure of a conducting surface using a sharp metallic tip, which is scanned across the surface. An applied bias between the sample and the tip leads to a net current which flows between the two even if they are not in mechanical contact but only in very close proximity. The current is explained by quantum mechanical tunnelling and exponentially depends on the tip-surface distance, which gives the technique a high spatial resolution.

In a theoretical description of the tunnelling current, we follow Bardeen's formalism [226] – in which the tunnelling problem is separated for the two subsystems tip and sample – and assume a 1D barrier.

From Fermi's golden rule, the probability w of an electron tunnelling from a state ψ_s inside the sample to a state ψ_t inside the tip and thus the amplitude of electron transfer between the two subsystems is determined by the overlap of their respective wave functions:

$$w(\psi_s \rightarrow \psi_t) = \frac{2\pi}{\hbar} |M|^2 \, \delta(E_{\psi_s} - E_{\psi_t}). \tag{2.1}$$

Here, M is the tunnelling matrix element. Summing over all states and noting the density of states (DOS) to read $\rho(E) = \sum_k \delta(E_k - E)$ gives the total tunnelling current expressed as a convolution of the DOS of the sample ρ_s and tip ρ_t [227, 228]:

$$I \propto \int_{-\infty}^{+\infty} |M|^2 \, [f(E_\mathrm{F} - eU + E) - f(E_\mathrm{F} + E)] \, \rho_s(E_\mathrm{F} - eU + E) \, \rho_t(E_\mathrm{F} + E) \, dE \tag{2.2}$$

Here, $f(E) = [1 + \exp((E - E_\mathrm{F})/kT)]^{-1}$ is the Fermi-Dirac distribution, which at low temperatures (i.e. for all measurements at 5 K) can be approximated as a step function, and the above equation condenses to:

$$I \propto \int_{0}^{eU} |M|^2 \, \rho_s(E_\mathrm{F} - eU + E) \, \rho_t(E_\mathrm{F} + E) \, dE \tag{2.3}$$

If we further evaluate the tunnelling matrix element assuming a 1D barrier in the Wentzel-Kramers-Brillouin approximation, the matrix element can be approximated by the transmission probability [225]:

$$|M|^2 = T(\phi, d) \propto \exp(-2\kappa d) = \exp\left(-2d\sqrt{2m\bar{\phi}/\hbar^2}\right) \tag{2.4}$$

Where $\bar{\phi} = (\frac{\phi_s + \phi_t}{2} + eU - E)$ is the average barrier height between tip and sample and ϕ_s (ϕ_t) is the work function of the sample (tip). The exponential dependence of the tunnelling probability on the tip-sample distance is the key factor to the high spatial resolution. Summarising, an STM topograph is a superposition of the topography and the local density of states (LDOS).

While in STM, the topography of a sample is probed, in scanning tunnelling spectroscopy (STS) the aim is to measure the density of states of the sample. This is achieved through differential conductance dI/dV curves, which are in first approximation proportional to the DOS:

$$dI/dV \propto \rho_t(0)\rho_s(eU)T(eU, U, d) \tag{2.5}$$

In the simplest approximation, both the DOS of the tip and the transmission probability are considered to be bias independent and hence the differential conductance is directly proportional to the energy-dependent DOS of the sample:

$$dI/dV \propto \rho_s(eU) \tag{2.6}$$

Quasiparticle Interference

A variation of STM/STS, which is even capable of directly measuring band dispersion utilises standing wave patterns of the LDOS. These modulations of the LDOS are termed quasiparticle-interference (QPI) patterns and can be measured by differential conductance maps in low-temperature STM. The first observation of QPI by STM was by Crommie on Cu(111) [229] and shortly after by Hasegawa on Au(111) [230], where standing wave patterns were observed at step edges and point defects. Today, QPI is an important tool and gave insight on scattering mechanisms in TMDCs, including monolayer WSe_2 [231, 232], MoS_2 [233], and $NbSe_2$ [234]. QPI in unconventional 2D systems has been reviewed recently [235].

Since the technique is not at the very fundaments of STM, we introduce it phenomenologically in a little more detail. A theoretical treatment needed to simulate the modulation patterns includes electronic scattering theory in terms of T-matrix theory or the joint density of states approximation, exceeds what is relevant for this thesis, and may be read up *e.g.* in Ref. [236] and references therein.

Analogous to long-range Friedel oscillations of the charge density, which occur in a solid due the continuum electrons screening a local potential perturbation caused *e.g.* by a defect [237], sources of disorder can introduce modulations of the LDOS on the surface of metals. The impurities cause elastic scattering of different eigenstates of a system, and due to energy conservation, this mixes states of different $\mathbf{k}$, but the same $\epsilon(\mathbf{k})$, hence some which lie on a constant energy contour (CEC) in k-space. The superposition of states $\mathbf{k_i}$ and $\mathbf{k_f}$ results in a standing wave in the quasiparticle wavefunction $\psi_\mathbf{k}$ of wave vector $(\mathbf{k_f} - \mathbf{k_i})\,/\,2$. The LDOS[1] is proportional to the absolute square $|\psi_\mathbf{k}|^2$ and hence will be modulated by a pattern of wave vector $\mathbf{q} = (\mathbf{k_f} - \mathbf{k_i})$ and wavelength $\lambda = 2\pi\,/\,q$.

Interesting insight is gained when considering Fermi's golden rule [238]:

$$w(i \to f) \propto \frac{2\pi}{\hbar}\,|V_\mathbf{q}|^2\,\rho_i(E_i,\mathbf{k_i})\,\rho_f(E_f,\mathbf{k_f}), \tag{2.7}$$

where $E_i = E_k$ for elastic scattering, $\mathbf{q} = (\mathbf{k_f} - \mathbf{k_i})$, $V_\mathbf{q}$ is the Fourier component of the scattering potential at wave vector $\mathbf{q}$, and ρ_i, ρ_f are the density of the initial and final states.

Equation 2.7 makes plain that if the CEC contains a large joint DOS (JDOS) of $\mathbf{k}$-pairs which may be connected by a particular $\mathbf{q}$, this wave vector will dominate the QPI at energy E. This condition is fulfilled in two cases:

(i) The first is the case of Fermi surface nesting, where two parallel segments of the Fermi surface (and hence many states) may be connected by one wave vector. In this view, the charge density oscillations may also be interpreted as a direct consequence of a singularity of the Lindhard susceptibility $\chi_0(\mathbf{q})$ at wave vector $2k_\mathrm{F}$ [239] and – in simple words – a Fourier transformation (FT) of the QPI pattern directly images the FS contour [240].

(ii) Another reason for large JDOS may arise from flat regions in k-space, where DOS(E) $\propto$

---

[1] The LDOS is defined as $\rho(E,\mathbf{r}) = \sum_k \delta(E_k - E)\,|\psi_k(\mathbf{r})|^2$

$1/\left|\nabla_k\left(E\right)\right|$ is large. In the extreme case of a van Hove singularity – an extreme case of increased DOS – the scattering processes combining the $\mathbf{k}_{\mathrm{VHS}}$ momenta with k points close to a CEC are dominant (because the van Hove singularity has large JDOS with all other CEC) and give rise to a FT QPI image which essentially represents a map of all of the CEC at a given energy [241].

2.2 Low-Energy Electron Diffraction

Complementary to structural characterisation of real space using STM, low-energy electron diffraction (LEED), uses the wave nature of the electron to investigate periodic structures on surfaces in reciprocal space. The technique was the first proof of the wave nature of electrons in 1927 [242] and has become a standard technique in UHV surface science and an introduction can be found in Ref. [243].

In LEED, monochromatic low-energy electrons are accelerated towards a target surface at which they scatter[2]. As their energy is in the range $20 - 500$ eV, the technique is highly surface sensitive with a small penetration depth of about 1 nm. From the backscattered electrons only the elastically scattered ones are accelerated towards a fluorescent screen at which they display a diffraction pattern.

The underlying physical properties of LEED are essentially the same as in other forms of crystalline diffraction, except for its high surface sensitivity. This leads to momentum conservation only in the sample plane and the treatment becomes two-dimensional. Therefore, the Laue condition reads [244]:

$$\mathbf{k}_{\mathrm{out}} = \mathbf{k}_{\mathrm{in}} + \mathbf{G}_{hk}, \tag{2.8}$$

with

$$\mathbf{G}_{hk} = h\,\mathbf{a}^{*} + k\,\mathbf{b}^{*} \tag{2.9}$$

the reciprocal lattice vector and $\mathbf{a}^{*}$, $\mathbf{b}^{*}$ the primitive translation vectors of the reciprocal lattice.

2.3 Angle-Resolved Photoemission Spectroscopy

Angle-resolved photoemission spectroscopy (ARPES) is a widely practiced experimental technique to directly probe the electronic band structure of materials using the photoelectric effect [245, 246]. The method has advanced considerably in the recent three decades and a dense review focussing on ARPES on ‘quantum materials’ – which includes TMDCs – can be found in Ref [247].

In ARPES, electrons are excited by an incident light beam (usually from a synchrotron or gas lamp) to energies above the vacuum level, so that they can escape the solid (in all directions).

---

[2] The de Broglie wavelength $\lambda = h/\sqrt{2mE}$ of low-energy electrons is on the order of a few Ångstrom and hence satisfies diffraction conditions.

The photoelectrons are collected by an electron analyser with angular resolution that measures their kinetic energy E_{kin} and momentum $\mathbf{q}_{||}$. When neglecting the photon's momentum[3], and noting the momentum conservation in the *xy*-plane, the momentum of the measured photoelectron $\mathbf{q}_{||}$ is equal to the *xy*-component of the electron's quasimomentum in the solid $\mathbf{k}_{||}$:

$$\mathbf{q}_{||} \;=\; \hbar\mathbf{k}_{||} \;=\sqrt{2mE_{\text{kin}}}\sin\theta \tag{2.10}$$

Further, energy conservation reads

$$E_{\text{kin}} = h\nu - E_{\text{bind}} - \phi, \tag{2.11}$$

where ϕ is the work function of the material. The relation between the binding energy E_{bind} and the quasimomentum $\mathbf{k}_{||}$ is the electron dispersion relation, which determines many physical properties of the material.

The photoemission process is usually phenomenologically described in a three-step model, which includes the absorption of the photon and an excitation into a final state in the bulk, the travel and possible scattering to the surface, and finally the transmission through the surface [248].

2.4 X-ray Absorption Spectroscopy and Magnetic Circular Dichroism

X-ray magnetic circular dichroism (XMCD) is used to investigate the magnetic properties of a sample. The technique denotes the difference in absorption of right and left circularly polarised light and is in turn based on x-ray absorption spectroscopy (XAS), which we shortly introduce first. A review on XMCD can be found in Ref. [249].

Absorption

XAS is used to determine the unoccupied electronic energy levels of atomic orbitals. *Via* the absorption of incident x-ray beams, electrons from a core-shell are optically excited into the unoccupied valence states; a transition which has to obey quantum mechanical selection rules.

While the absorption may be measured in several modes, such as transmission, fluorescence yield or total electron yield, here we restrict to the latter, since it displays the highest surface sensitivity. When using soft x-rays, the decay of the core-level hole-pocket proceeds predominantly *via* an Auger process, during which electrons are emitted from the sample. The secondary charge compensating for this loss (the sample is grounded) is measured and is thus a direct measure for the absorption.

The absorption process is characterised by the absorption edge (corresponding to element-specific

---

[3] At 100 eV, the momentum of a photon is $2\pi\lambda^{-1} = E/\hbar c = 0.05$ Å^{-1}, that is about 2% of the typical size of the irreducible BZ of TMDCs. The photon energies used in this thesis are in the range $20 - 50$ eV, hence produce even smaller deviations in the above considerations.

binding energies of core electrons), which for the TMDCs limits to the *L*-edge, *i.e.* transitions from $2p$ to unoccupied $3d$ levels.

Magnetic Circular Dichroism

In magnetic materials, the absorption probability becomes spin-dependent and the absorption spectra differ for the different helicities of circularly polarised light. The magnetic circular dichroism (XMCD) signal is thus the difference in the absorption spectra μ^+ and μ^- of the different helicities:

$$\mu^{\text{XMCD}} = \mu^+ - \mu^- \tag{2.12}$$

2.5 Experimental Setups

The aforementioned experimental techniques are employed either at STM apparatuses located at the University of Cologne or at beamlines located at different synchrotrons.

Home Labs

The STM/STS and LEED investigations are performed both in a home-built variable temperature (VT-STM) and a commercial low-temperature (LT-STM) STM chamber. Both have been described in detail elsewhere and information on the systems can be found in Ref. [250] for the VT-STM and Ref. [251] for the LT-STM, respectively.

In brief, the VT-STM 'TuMA II' has a single-chamber design, in which both sample synthesis and investigation are performed. The UHV base pressure of about 1×10^{-10} mbar allows storing the inert 2D layers for more than one day without visible degradation. The sample is non-transferably fixed on the uniaxial manipulator which is used to access the instrument sites. The fixed mounting allows fixed thermocouples, which reliably measure the (e-beam heated) temperature of the sample. In the middle of the chamber, several evaporators including a multiple-pocket e-beam evaporator and an effusion cell, are mounted at a distance of $7 - 15$ cm from the sample, alongside a gas inlet. For analysis, a commercial three-grid LEED and a home-build beetle-type STM with a PtIr tip and a mass spectrometer are present. Upon cooling of the sample with liquid helium a lowest temperature of around 30 K is reached.

The commercial LT-STM 'TSTM' consists of three chambers, which are connected by gate valves. The system contains a load-lock for sample transfer, a preparation chamber and an STM chamber in which the sample is cooled to 5 K inside a bath cryostat. The preparation chamber contains equal equipment as the VT-STM, however, LEED has a multichannel plate, which amplifies the signal. For STS, we use a W-tip and standard lock-in technique with modulation frequency of 777 Hz and modulation amplitudes $V_{\text{mod}} = 4\ \text{mV}_{\text{rms}}$. For point spectra and constant height topographs U_{stab} and I_{stab} of stabilisation are indicated in the respective figure caption.

For STM analysis and data processing the software *WSxM* [252] was used.

Beamlines

APRES experiments on MoS_2 have been carried out at BaDElPh beamline at ELETTRA synchrotron in Trieste, Italy [253]. The beamline is equipped with a preparation chamber including a load-lock and an analysis chamber for LEED and ARPES. Sample preparation was performed *in situ* at the beamline and subsequently checked with LEED for quality. ARPES on MoS_2/Gr/Ir(111) was carried out with linear s- and p- polarisation at $h\nu = 31$ eV photon energies at temperatures of 20 K.

Regarding ARPES on TaS_2, the samples were grown in Cologne in the group of Alexander Grüneis and checked with LEED for quality. They were transported and transferred in a vacuum-tight container without air exposure to the Forschungszentrum Jülich and the SOLEIL synchrotron in Saint-Aubin, France, respectively. In Jülich, ARPES data were taken at about 40 K using 21 eV photon energy, while in SOLEIL the KM direction was taken at about 100 K and 50 eV photon energy.

Finally, XMCD measurements have been conducted by F. Huttmann and S. Kraus at the beamline ID32 of the ESRF in Grenoble, France. The central part of the soft x-ray beamline is a high-field magnet, capable of up to 9 T. The $V_{1+x}S_2$ samples were grown *in situ* inside the preparation chamber and checked with LEED and STM before XAS. To be surface sensitive, the XAS measurements were conducted in the total electron yield mode under normal incidence and at 5 K. The spectra were recorded at the $L_{3,2}$-edges, *i.e.* the dipole allowed transition from $2p$ states into the $3d$ shell generating the magnetism.

2.6 Procedures and Sample Preparation

Substrate Preparation

The Ir(111) substrate is cleaned by grazing incidence 4.5 keV Xe^+ ion erosion and short annealing of the crystal to 1500 K. Since the crystal usually remains in UHV, only a few layers need to be sputtered. The cleanliness of the crystal is checked with LEED, in which clean Ir(111) displays sharp hexagonal diffraction spots.

A closed monolayer of single-crystalline Gr on Ir(111) is grown in a two-step approach [42]. In the first step, at temperatures below 400 K, the substrate is exposed to about 5 L ethylene which ensures full saturation. The substrate is then quickly annealed to 1500 K without ethylene background. This causes the adsorbed ethylene to thermally decompose and results in a low coverage of well-oriented Gr islands. In the second step, the islands are grown to a complete layer through exposure to 200 L ethylene at 1200 K. The quality of Gr/Ir(111) is checked in LEED and should resemble Fig. 1.9 (b). For S intercalation experiments, samples with about 0.95 ML Gr coverage were prepared by limiting the ethylene dosage to 100 L in the second step.

For single experiments, Gr was intercalated by either Eu or Li. For self-limiting Eu intercalation, a closed layer Gr/Ir(111) is exposed to Eu vapour from a Knudsen cell at about 770 K. The sample is kept at 700 K to ensure re-evaporation of excess Eu. Full Eu intercalation is confirmed by a $(\sqrt{3} \times \sqrt{3})$R30° intercalation pattern with respect to Ir in LEED. Further intercalation phases are known but not relevant for this thesis [254].

With the sample held at 500 K, Li is evaporated from commercial getter sources until full saturation and is indicated by a weakening of moiré diffraction spots [255].

For some experiments, a monolayer of hexagonal boron nitride was grown instead of Gr through a 200 L borazine exposure at 1200 K [221].

Preparation of Transition Metal Dichalcogenides

The physics of the TMDC growth method will be the topic of Chapter 3, here a technical description is given, which is summarised in Table 2.1.

For TMDC growth, Gr/Ir(111) is exposed to a metal atom flux F_{metal} from an e-beam evaporator for a growth time t^{g} (the reference value is $t^{\mathrm{g,ref}} = 120\,\mathrm{s}$), simultaneously with a sulphur vapour flux out of a Knudsen cell filled with $\mathrm{FeS_2}$ at a growth sample temperature in the range of $100\ \mathrm{K} \leq T^{\mathrm{g}} \leq 500\,\mathrm{K}$ (the reference value is $T^{\mathrm{g,ref}} = 300\,\mathrm{K}$).

The sulphur vapour flux is characterised by a sulphur growth pressure $P^{\mathrm{g}}_{\mathrm{sulphur}}$ measured distant from both the Knudsen cell and the sample with an ion gauge. For a distance of 9 cm between the crucible and sample and with the shutter open we estimate an S flux at the sample location higher by a factor of 10 compared to the measured $P^{\mathrm{g}}_{\mathrm{sulphur}}$. The measured reference sulphur pressure is $P^{\mathrm{g,ref}}_{\mathrm{sulphur}} = 5 \times 10^{-9}$ mbar.

The metal flux onto the sample is obtained through STM-based area determination of pseudomorphic monolayer islands on Ir(111) and varies for the particular materials. For $\mathrm{MoS_2}$, the reference value is $F^{\mathrm{ref}}_{\mathrm{Mo}} = 2.9 \times 10^{16}$ atoms $\mathrm{m^{-2}\,s^{-1}}$, while for $\mathrm{VS_2}$ and $\mathrm{TaS_2}$ the reference values are $F^{\mathrm{ref}}_{\mathrm{V,Ta}} = 2.5 \times 10^{16}$ atoms $\mathrm{m^{-2}\,s^{-1}}$.

Subsequently, the sample is annealed at an annealing temperature T^{a}, where the reference value varies for each material. For $\mathrm{MoS_2}$, the reference is $T^{\mathrm{a,ref}} = 1050\,\mathrm{K}$, for $\mathrm{VS_2}$ $T^{\mathrm{a,ref}} = 800\,\mathrm{K}$ and for $\mathrm{TaS_2}$ $T^{\mathrm{a,ref}} = 1000\,\mathrm{K}$.

Annealing is performed in an annealing sulphur pressure $P^{\mathrm{a}}_{\mathrm{sulphur}} < P^{\mathrm{g}}_{\mathrm{sulphur}}$ (the reference value is $P^{\mathrm{a,ref}}_{\mathrm{sulphur}} = 2 \times 10^{-9}$ mbar) for a time interval t^{a} (reference value is $t^{\mathrm{a,ref}} = 300\,\mathrm{s}$). In our system, sulphur release from $\mathrm{FeS_2}$ becomes measurable at a Knudsen cell temperature of 470 K. Mass spectrometric measurements (see Appendix A.1) show the absence of iron release and support the sulphur vapour over $\mathrm{FeS_2}$ to consist primarily of diatomic sulphur, in agreement with literature [256–258].

The resulting deposited coverage θ of the TMDS is measured in monolayers (ML, where one ML refers to the one-unit-cell triple layer (S-Mo-S) of $\mathrm{MoS_2}$ which contains 1.16×10^{19} Mo atoms $\mathrm{m^{-2}}$).

Table 2.1: Reference synthesis parameters.

Growth Step

Material	Substrate Temperature $T^{\mathrm{g,ref}}$ in K	Sulphur Pressure $P^{\mathrm{g,ref}}_{\mathrm{sulphur}}$ in mbar	Metal Flux $F^{\mathrm{ref}}_{\mathrm{metal}}$ in atoms $\mathrm{m}^{-2}\,\mathrm{s}^{-1}$	Deposition Time $t^{\mathrm{g,ref}}$ in s
MoS_2	300	5×10^{-9}	2.9×10^{16}	120
VS_2	300	5×10^{-9}	2.5×10^{16}	120
TaS_2	300	5×10^{-9}	1.8×10^{16}	300

Annealing Step

Material	Substrate Temperature in K	Sulphur Pressure $P^{\mathrm{a,ref}}_{\mathrm{sulphur}}$ in mbar	Time $t^{\mathrm{a,ref}}$ in s
MoS_2	1050	2×10^{-9}	300
VS_2	800	2×10^{-9}	300
TaS_2	1000	2×10^{-9}	300

2.7 Density Functional Theory

All density functional theory (DFT) and density functional perturbation theory (DFPT) calculations have been carried out by Jan Berges and Eric van Loon under supervision of Tim Wehling in Bremen using Quantum ESPRESSO [259, 260].

DFT is a quantum mechanical modelling method for investigating the electronic structure of a many-body system. To avoid having to solve the many-body Schrödinger-equation, the ground state is calculated based on the electron density of the system. The foundation of DFT is the Hohenberg-Kohn theorem stating that the electron density $\rho(\mathbf{r})$ is a unique functional that is minimised in the ground state. Further, the Kohn-Sham equations are used to simplify the many-body Schrödinger-equation for interacting particles in a static potential to a system of non-interacting particles that generate the same density as any given system of interacting particles in an effective potential. The effective potential includes both the external potential as well as Coulomb, exchange and correlation interactions between the electrons.

In this thesis, the generalised gradient approximation (GGA) by Perdew, Burke and Ernzerhof (PBE) [261, 262] is applied. Further, optimised norm-conserving Vanderbilt pseudo-potentials [263] from the PseudoDojo pseudo-potential table [264] at a plane-wave cutoff of 70 Ry are used. Monkhorst-Pack meshes of 18×18 $\tilde{k}$ and 6×6 $\tilde{q}$ points are combined with a Gaussian occupation smearing of 10 mRy. Spin-orbit coupling and van-der-Waals interactions are taken into account, the latter *via* Grimme's DFT-D3 method [265].

The modification that is required for constrained DFPT is described in detail in Ref. [266]. For the transformation of the electronic energies and electron-phonon coupling to the Wannier basis, we used Wannier90 [267] and the EPW code [268, 269].

PART III

Results

CHAPTER 3

Growing Transition Metal Disulphides on Inert Substrates

This chapter contains contributions from ***J. Hall****, N. Ehlen, C. Murray, B. Pielić, W. Jolie, B. V. Senkovskiy, M. Hell, G. di Santo, L. Petaccia, C. Busse, M. Kralj, A. Grüneis and T. Michely. Much of this chapter is already published in Ref. [43–45]. Ref. [43] concentrates on the growth technique for the TMDCs, Ref. [44] on optical properties of the* MoS_2 *layers and in Ref. [45] a detailed description of the band structure of* MoS_2 *is given.*

I *developed the synthesis technique and analysed the data, including all STM and LEED measurements at* TuMA II *with the initial help of B. Pielić.* ***I*** *transferred the recipe and performed the synthesis at the low-temperature system* $_{\text{T}}$STM, *where C. Murray and W. Jolie performed STS measurements.* ***I****, furthermore, performed the sample synthesis at the BaDElPh beamline at ELETTRA synchrotron, Trieste. There, ARPES was taken mainly by N. Ehlen,* ***me****, and B. V. Senkovskiy and in parts by M. Hell. G. di Santo and L. Petaccia instructed how to operate the system. The ARPES data were analysed by N. Ehlen and B. V. Senkovskiy. N. Ehlen and B. V. Senkovskiy measured and analysed Raman spectroscopy and Photoluminescence. A. Grüneis supervised the optical measurements, whereas STM/STS/LEED measurements were supervised by T. Michely.*

All data were discussed by ***me****, N. Ehlen, C. Murray, B. Pielić, W. Jolie, B. V. Senkovskiy, C. Busse, M. Kralj, A. Grüneis and T. Michely.*

I *wrote the manuscript of Ref. [43] and finalised it in close collaboration with T. Michely. N. Ehlen wrote the main part of the manuscript of Ref. [44],* ***I*** *wrote the parts of the manuscript which deal with STM and LEED. The manuscript was finalised together with T. Michely and A. Grüneis. C. Murray wrote the manuscript of Ref. [45], which was finalised together with T. Michely.* ***I*** *contributed to the discussion.*

3.1 Motivation: Sulphur in Molecular Beam Epitaxy

To investigate TMDC layer dependent material properties experimentally and to enable close connection to *ab initio* predictions, a growth method yielding epitaxial films of controlled thickness, low defect density, negligible substrate interaction, and ultimate cleanness is necessary. A method that can fulfil all of these requirements is van der Waals epitaxy (vdWE) [37, 38, 40] introduced in Section 1.5. In this respect, considerable progress has been achieved in the recent years for the growth of transition metal diselenides and ditellurides [188, 202, 204, 205, 270–275]. For these materials, even scalable approaches have been presented, which makes TMDC growth by MBE available for industrial applications [276, 277].

For the transition metal disulphides (TMDSs) the situation for MBE is less promising, as one immediately encounters the 'sulphur problem': The vapour pressure of sulphur is already 10^{-6} mbar at room temperature or 2.5 mbar at a typical bakeout temperature of 200 °C [278], and thus incompatible with UHV based MBE growth. Though the use of sulphur-containing precursor molecules may solve this problem on metallic substrates, this approach is unsuitable for vdWE. Due to the lack of the metallic substrate, defects appear to be necessary for the nucleation of MoS_2 islands using H_2S gas, and neither a phase pure system nor one with a well defined epitaxial relation could be realised [182, 279, 280]. In another approach, valved sulphur cracker sources may be employed and yield high-quality samples [281], but present costly experimental approaches.

We overcome these difficulties by adopting an approach that has already been developed in the 1990s [256, 282–284] in vdWE. Instead of using precursor molecules, we use a solid-state sulphur compound as a sulphur source, namely pyrite (FeS_2), which has a marginal vapour pressure even at UHV bakeout temperatures but provides a sufficient vapour pressure in the 10^{-9} mbar range at well accessible Knudsen cell temperatures.

As a principal substrate we use Gr on Ir(111) (cf. Section 1.6), a substrate that is readily prepared as a single crystal with a very low defect density [41, 42] and is expected to interact only weakly with the TMDS through van der Waals interactions.

We introduce the growth technique in the second section of this chapter using the example of MoS_2 and demonstrate the resulting single layers to be clean, phase pure and excellently epitaxially ordered. We furthermore directly compare this growth approach to the use of precursor molecules, which we find to be detrimental for sample quality.

in the third section, we illustrate the layers of tunable coverage to be electronically well decoupled from their substrate through a multitude of techniques. While the freestanding nature will be highlighted *via* STM/STS by the ability to move flakes with the STM tip and a large band gap of MoS_2, ARPES indicates the absence of hybridisation of the epilayer with electronic states from the substrate. Further evidence of the loose bonding comes from temperature-dependent UHV Raman spectroscopy that displays the thermal expansion of Gr and MoS_2 to be independent of each other. Finally, the weak MoS_2-Gr interaction enables PL to be observable, despite the metallic substrate.

We use section four to show that this synthesis approach is extremely versatile and is neither restricted to MoS_2 as an epilayer nor Gr as a substrate. We will demonstrate the synthesis of WS_2, TaS_2 on Gr and also use h-BN as a growth substrate.

Finally, we discuss the assets and drawbacks of the new synthesis technique. We compare both with the synthesis of TMDSs on metallic substrates and with the use of H_2S on vdW substrates and emphasise what are important imminent tasks.

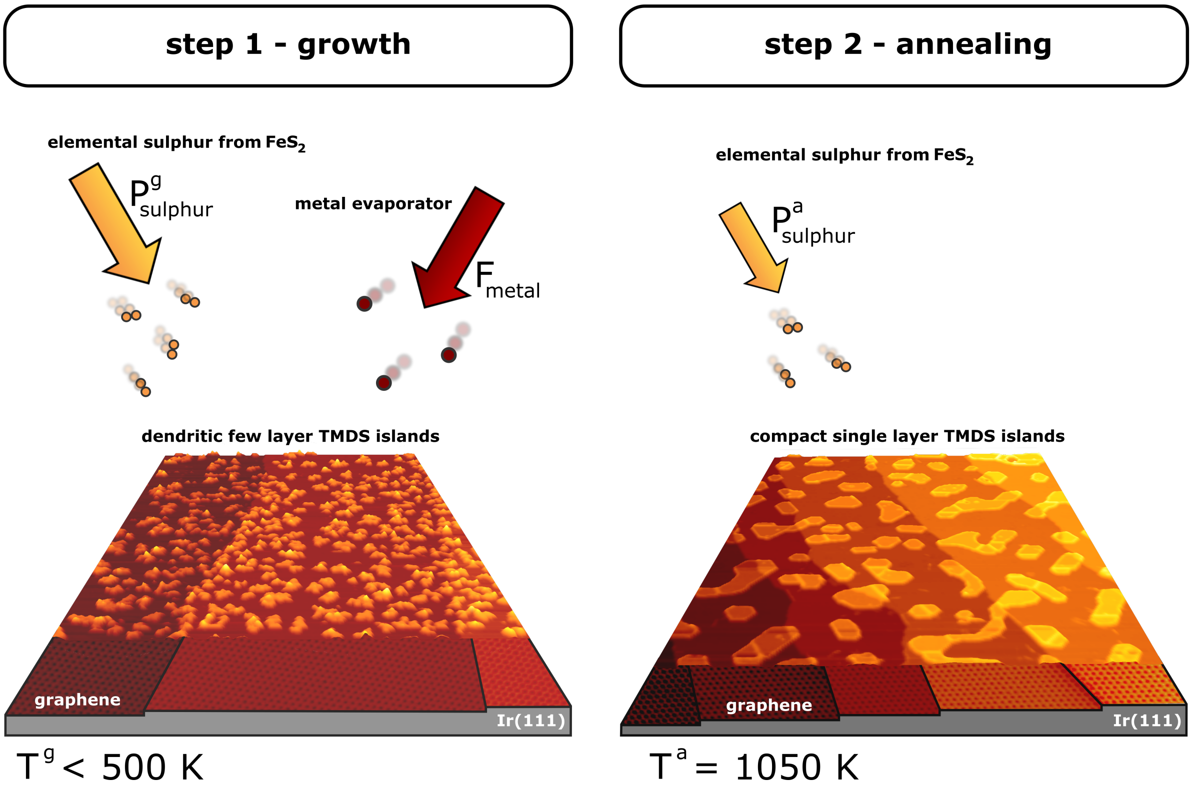

Figure 3.1: Schematics of the two-step synthesis of the TMDS: (a) Metal and elemental sulphur are co-evaporated in UHV onto Gr/Ir(111) held at a growth temperature $T^{\mathrm{g}} \leq 500\,\mathrm{K}$. (b) The sample is annealed to a high temperature $T^{\mathrm{a}} = 1050\,\mathrm{K}$ in a background of sulphur vapour.

3.2 The Method

The procedure we employ for the growth of TMDSs consists of a two step synthesis, which we explain on the example of $\mathrm{MoS_2}$:

(i) The growth step [cf. Fig. 3.1 (a)] characterised by a substrate temperature T^{g}, a metal flux F_{metal}, a sulphur pressure $P^{\mathrm{g}}_{\mathrm{sulphur}}$ and the growth time t^{g}. Since at 300 K the residence time τ of unreacted sulphur on Gr is only of the order of milliseconds[1], while that of the metal is infinite, growth is conducted in sulphur excess. For the same reason, the growth rate is determined by F_{metal} rather than $P^{\mathrm{g}}_{\mathrm{sulphur}}$. The resulting deposited coverage θ of the TMDS is measured in monolayers (ML, where one ML refers to the one-unit-cell triple layer (S-Mo-S) of $\mathrm{MoS_2}$ which contains 1.16×10^{19} Mo atoms $\mathrm{m^{-2}}$).

(ii) In the annealing step [cf. Fig. 3.1 (b)] the sample is quickly heated up to T^{a} where it remains for a time interval t^{a} in a sulphur vapour pressure $P^{\mathrm{a}}_{\mathrm{sulphur}}$ until the heating is switched off.

---

[1] Assuming an adsorption energy of 0.5 eV [285] and a standard prefactor of $\nu_0 = 5 \times 10^{-12}\,\mathrm{s^{-1}}$, the desorption rate is $\nu = \nu_0 \exp(500\mathrm{meV}/25\mathrm{meV}) \approx 400\,\mathrm{s^{-1}}$ and the residence time $\tau \approx 2\,\mathrm{ms}$.

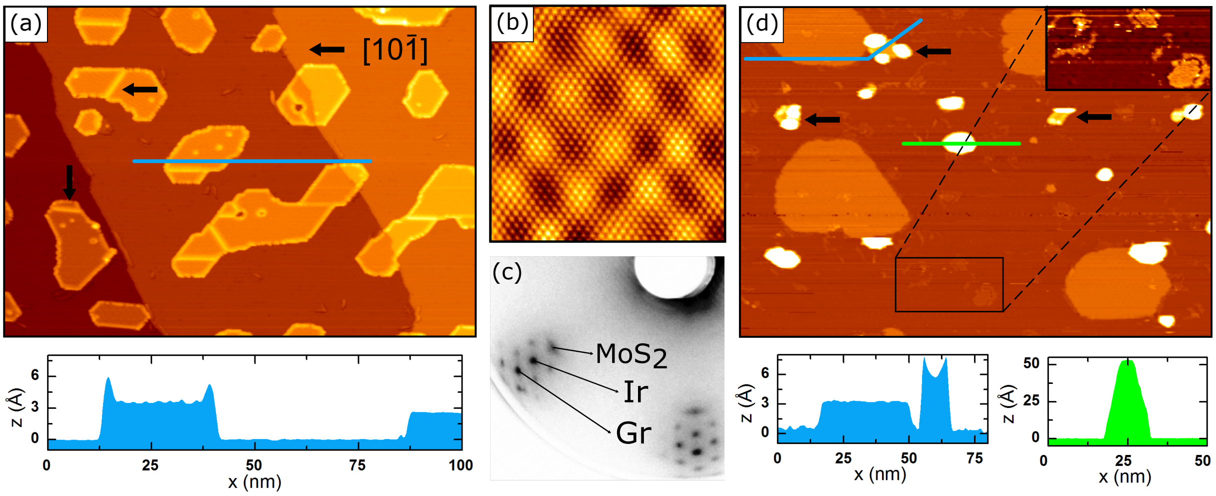

Figure 3.2: Overview of the two step TMDS synthesis: (a) Upper panel: STM topograph after growth of MoS_2 islands with the reference parameters (see section 2.6) on Gr/Ir(111), resulting in a coverage of 0.3 ML. Arrows on the left-hand side highlight mirror twin boundaries in MoS_2 islands. The $\left[10\bar{1}\right]$ Ir substrate direction is indicated by a black arrow on the right-hand side. Lower panel: height profile along the blue line in the upper panel. (b) Atomically resolved topograph of an MoS_2 island. (c) Section of a corresponding 80 eV LEED pattern. The first order reflections of MoS_2, Ir(111) and Gr are indicated. (d) Upper panel: STM topograph after synthesis with growth parameters identical to (a), except using H_2S with a higher pressure instead of elemental sulphur. Black arrows indicate small MoS_2 islands. Contrast enhanced inset in upper right highlights sulphur intercalation. Lower panel: The blue height profile corresponding to the blue line in the upper panel crosses a Mo intercalated patch and a small MoS_2 bilayer island, which becomes clear by comparison with the height indicated in the blue line profile in (a). The green height profile corresponds to the green line in the upper panel and crosses a cluster of unreacted Mo.
Image information (image size, sample bias, tunnelling current): (a) 200×140 nm^2, -1.5 V, 50 pA, (b) 9×9 nm^2, -0.5 V, 60 pA, (d) 200×140 nm^2, -1.5 V, 50 pA.

In anticipation of our findings below (see Section 4.2), we point out that a two-step growth process is necessary for optimum results, since:

(a) After growth at temperatures up to 500 K the orientation of the islands is scattered, the shapes are non-compact, and bilayer (BL) islands are frequent. Only during the annealing step the islands become epitaxial, compact and small BL islands dissociate, leaving ML MoS_2 on the sample.

(b) Growth at sufficiently high temperatures that would allow creating islands of optimised epitaxy, shape and flatness in one step is hampered in UHV conditions since with increasing temperature the residence time τ of sulphur on the sample drops dramatically. When using pressures in the range $1 \times 10^{-9} - 5 \times 10^{-9}$ mbar during the growth step, the drop impedes the reaction between metal and sulphur to the TMDS and due to this, substantial metal intercalation under Gr takes place. In Section 6.6, we will demonstrate that at high substrate temperatures a significantly higher growth sulphur pressure may be used to compensate for this.

General Overview of Molecular Beam Epitaxy Grown MoS_2

Figure 3.2 (a) presents an STM topograph of the synthesis outcome using the reference values specified in Section 2.6, resulting in a coverage $\theta = 0.3\,\mathrm{ML}$ of MoS_2. The substrate displays two monoatomic steps of 2.2 Å height [compare line profile Fig. 3.2 (a)] crossing the topograph from top to bottom, which result from Ir(111) steps overgrown by Gr. Irrespective of these substrate steps, ML MoS_2 islands with linear dimension of the order of 20 nm are distributed rather homogeneously over the sample, extending occasionally over a substrate step without visible influence of it.

In STM, the apparent height of semiconducting MoS_2 is bias-dependent. In this topograph, the islands are of 3.5 Å apparent height [compare line profile Fig. 3.2 (a)] and bound by bright edges about 1.5 Å higher. The apparent island height is considerably smaller than the ML thickness of 6.15 Å [59] in MoS_2 bulk, but in line with a broad range of bias dependent apparent ML MoS_2 heights reported in the literature [182, 194]. The bright edges of apparently larger height are attributed to metallic island edge states as described by Bollinger *et al.* [286]. Straight, bright lines are found in some of the islands which we identify as metallic states in mirror twin boundaries (MTBs) [compare black arrows in the left part of Fig. 3.2 (a)]. Though the islands are generally of irregular shape, it is obvious that extended portions of their edges are aligned with respect to the dense-packed Ir(111) substrate directions, of which the $\left[10\bar{1}\right]$ direction is indicated in Fig. 3.2 (a).

An atomically resolved zoom into one MoS_2 island is shown in Fig. 3.2 (b). The MoS_2 lattice does not display any defects, and within the limits of error, the atomic periodicity agrees with the literature value for the in-plane, bulk MoS_2 lattice constant of 3.15 Å [287]. Besides the atomic structure, a large scale periodicity of 25 Å is visible, which is due to moiré corrugation of Gr with the underlying Ir substrate [217] adapted by the MoS_2 island.

The 80 eV LEED pattern of Fig. 3.2 (c) makes the epitaxial relations between Ir, Gr, and MoS_2 obvious. All three materials display a hexagonal lattice with the first order reflections aligned, but at different separations from the (0,0) reflection. This implies the dense-packed rows of Ir(111), of Gr, and of the ML MoS_2 lattice are aligned but keep independent lattice parameters. Additional reflections due to the moiré of Gr with Ir(111) are visible [217] which surround the first order reflections. Calculating the real space in-plane lattice parameter of MoS_2 from the positions of the first order reflections of MoS_2 with respect to the first order reflections of Ir(111) yields (3.13 ± 0.03) Å, in good agreement with the literature value of 3.15 Å [287] for the bulk material. Additionally, the LEED data show that the first order MoS_2 reflections are radially slightly elongated. This implies a scatter of $\pm\ 2^\circ$ for the MoS_2 island orientations.

The results of our LEED analysis make also clear that the straight step segments in the MoS_2 island edges, as seen in Fig. 3.2 (a), are dense-packed steps. Due to the only threefold symmetry of MoS_2 there are two types of dense-packed steps named Mo- and S-steps by Lauritsen *et al.* [288]. Compared to the frequent triangular MoS_2 island shapes [177, 194], our more hexagonal form indicates a lower sulphur chemical potential during MoS_2 island shaping [288–290] consistent with the low sulphur fluxes applied here during growth and annealing.

All six MoS_2 related first order reflections in the LEED pattern of Fig. 3.2 (c) display a uniform variation in intensity with energy (not shown), despite the threefold symmetry of MoS_2. This is a strong indication that on the sixfold symmetric Gr substrate two different twin orientations of the threefold symmetric MoS_2 islands grow in equal proportion. Where differently oriented islands join with their dense-packed edges, an MTB results. MTBs in $MoSe_2$ carry a metallic edge state and shine brightly, *i.e.* possess a larger apparent height in STM [204, 205, 291, 292]. By structural similarity it is plausible that this is the case for MoS_2 as well. Together with the same hexagonal lattice in the same orientation observed on both sides of the defect line, this reasoning makes our assignment of the bright lines highlighted by arrows in the islands of Fig. 3.2 (a) to MTBs conclusive. More details on MTBs in MoS_2 will be given in Section 4.4.

Comparison of FeS_2 with H_2S

To compare our MBE growth method to low-pressure CVD using H_2S, we conducted also a growth experiment leaving all parameters identical except for replacing the pressure of elemental sulphur during growth and annealing by a pressure of H_2S. Since Gr is catalytically inactive, and in order to give the H_2S experiment a chance, we used a pressure of H_2S exceeding P^{g}_{sulphur} by a factor of 150 during growth and P^{a}_{sulphur} by a factor of 10 during annealing. The resulting morphology is represented by the STM topograph in Fig. 3.2 (d).

We identify four morphological features:
(I) Large flat islands of 2.5 Å height [compare blue line and height profile in Fig. 3.2 (d)] which are attributed to intercalated Mo. This assignment is based on experiments that show the same feature after Mo deposition and annealing on Gr/Ir(111) in the absence of any sulphur compound. See Appendix A.2.
(II) Bright bumps of up to 50 Å height [compare green line and height profile in Fig. 3.2 (d)] which are attributed to Mo clusters *on* Gr. As for (I), the assignment is based on the observation of the same features for experiments after Mo deposition on Gr/Ir(111), but in the absence of sulphur supply. See Appendix A.2.
(III) Tiny flat areas with attached high Mo clusters marked in Fig. 3.2 (d) by black arrows. The blue line in Fig. 3.2 (d) is crossing such an island. From the corresponding height profile we assign these islands to be MoS_2. They display a bias dependent height with the characteristic bright edges and seem to be of bilayer thickness.
(IV) Through enhanced contrast, the zoomed inset in the topograph of Fig. 3.2 (d) makes a second intercalation structure visible that we tentatively attribute to intercalated S. Irrespective of any assignment, the experiment results in four different phases and the output of MoS_2 is at most marginal. Thus, MBE using elemental sulphur yields clearly superior results on the inert Gr substrate as compared to low-pressure CVD using H_2S.

Though our data provide clear evidence for Mo and S intercalation, we are unable to pinpoint

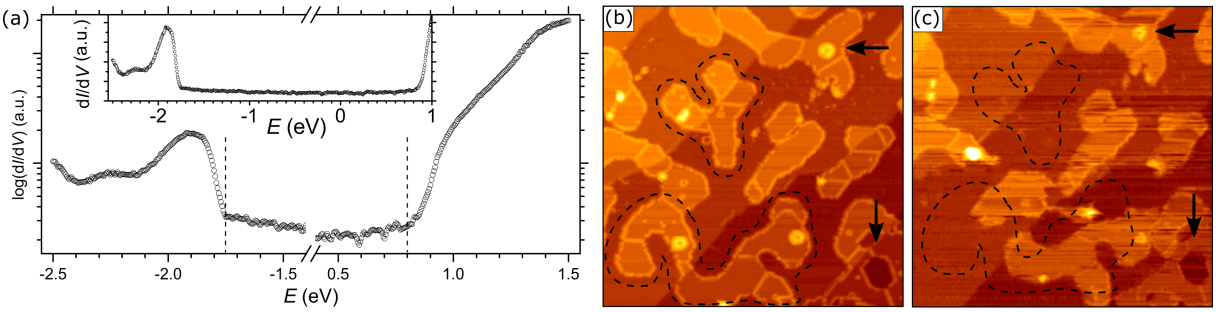

Figure 3.3: Low substrate interaction between MoS_2 and Gr: (a) Logarithmic scale constant height STS spectrum of MoS_2/Gr/Ir(111) taken at 5 K. Inset: linear scale, but same data. (b),(c) Two STM topographs with MoS_2 islands (coverage 0.5 ML) taken one after another at the same position. Black arrows mark unchanged locations, dashed lines locations where MoS_2 islands were displaced due to scanning.
Image information: (a) Set point voltage 1.5 V, set point current 100 pA. (b) and (c) (image size, sample bias, tunnelling current) 160×160 nm^2, -1.0 V, 600 pA.

the intercalation mechanisms unambiguously – a situation that seems to be rather general for this intricate problem. Considering Mo intercalation, we speculate intercalation *via* reactive passage of Mo by defect formation in Gr at elevated temperatures. This speculation is based on the fact that Mo intercalation does not occur at room temperature and takes place at several locations on otherwise perfect terraces (see Appendix A.2). The same mechanism has been proposed also for intercalation of other metals under Gr [254,293,294]. As for S intercalation, we find S intercalation to be fostered, when Mo intercalation had taken place. This observation leads us to speculate that S intercalates at defects in the Gr layer that were created by the reactive passage of Mo during intercalation. Information on the structure of S under Gr/Ir(111) is given in Appendix A.3.

3.3 Low Substrate Interaction

The following section emphasises the freestanding nature of the layers of MoS_2 – which we recall to be a direct band gap semiconductor, in which the valence band maximum (VBM) is located at the K point – using STM, STS, ARPES, Raman spectroscopy and PL.

Scanning Tunnelling Microscopy and Spectroscopy

Figure 3.3 (a) displays a constant height dI/dV spectrum taken at 5 K on top of a ML MoS_2 island, distant from edges and MTBs. The main panel shows the spectrum in logarithmic scale, while in the inset a linear scale is used. The MoS_2 band gap is obvious from the flat spectrum between -1.75 eV and 0.80 eV. The gap is intuitively measured to be $E_g = (2.55 \pm 0.05)$ eV. However, as states from the BZ edge exhibit a large parallel momentum $k_{\|}$ and a consequent small decay length, these may go undetected in constant height STS, influencing the measured band gap. "Comprehensive STS", in other words the comparison of constant height STS, constant current STS and measurements of the inverse decay constant κ allows to infer deeper understanding of the band structure by STS and determines a ML band gap of (2.53 ± 0.08) eV for MoS_2/Gr/Ir(111). Details concerning the band structure, as measured by comprehensive STS of mono-, bi- and trilayer MoS_2 epitaxially grown on Gr/Ir(111) can be found in Ref. [45].

Depending on the interaction strength with the substrate, substrate screening, and the presence of excited charge carriers, the ML MoS_2 band gap is substantially reduced (renormalised) [280] compared to the GW calculations based theoretical predictions ranging from $2.76-2.97$ eV [295–297]. To name a few, the gap of ML MoS_2 measured by STS in the literature is 1.74 eV on Au(111) [184], 2.0 eV on epitaxial Gr on SiC [194], 2.15 eV on graphite [270, 298], 2.17 eV on fused quartz [299], 2.20 eV on Gr/Au substrates [300], and 2.40 eV again measured on graphite [298]. When grown on inhomogeneous substrates, the MoS_2 may locally be decoupled and large band gaps of 2.65 eV [301] and 2.7 eV [302] have been reported.

We interpret the large band gap of 2.55 eV measured here to result from the absence of adsorbates, the marginal screening through the Gr substrate, and the absence of binding of the MoS_2 islands to Gr beyond van der Waals interaction.

The weak binding of the MoS_2 islands to the Gr substrate is strikingly confirmed through two consecutive STM topographs displayed in Figs. 3.3 (b) and (c). It is apparent that MoS_2 islands were displaced or even disappeared from the scanning area. Such displacement events become likely at comparatively low tunnelling resistance, when the tip comes close to the MoS_2 islands.

Angle-Resolved Photoemission Spectroscopy

The results of ARPES scans on the system MoS_2 on Gr/Ir(111) are illustrated in Fig. 3.4. In panel (a), a spectrum taken along the high symmetry directions of the hexagonal BZ is shown. Bands originating from MoS_2 and Gr and both the Γ and the respective K points of MoS_2 and Gr are indicated. The K_{Gr} point of Gr is at ≈ 1.7 Å^{-1}, while the K_{MoS_2} point of MoS_2 is at ≈ 1.3 Å^{-1}. The observed band structure indicates the ML thickness and the trigonal prismatic nature of the grown MoS_2 through two distinct features: (i) the VBM is found at the K point. (ii) The splitting of the VB at K_{MoS_2} due to spin-orbit interaction is clearly seen in the high-resolution scan shown in the inset of Fig. 3.4. A fit to an energy distribution curve going through K_{MoS_2} reveals a band splitting of 144 meV, which is shown in Fig. 3.4 (b). By contrast, bilayer MoS_2 has its VBM at the Γ point and does not show a splitting of the bands at K_{MoS_2} as visualised in Appendix A.4.

Besides small doping of Gr, which is indicated by the Dirac cone binding energy being shifted from 0.1 eV in the pristine Gr/Ir(111) case to 0.25 eV in the MoS_2/Gr/Ir(111) case, ARPES does not indicate any interaction between the two van der Waals coupled layers, in particular, hybridisation is absent.

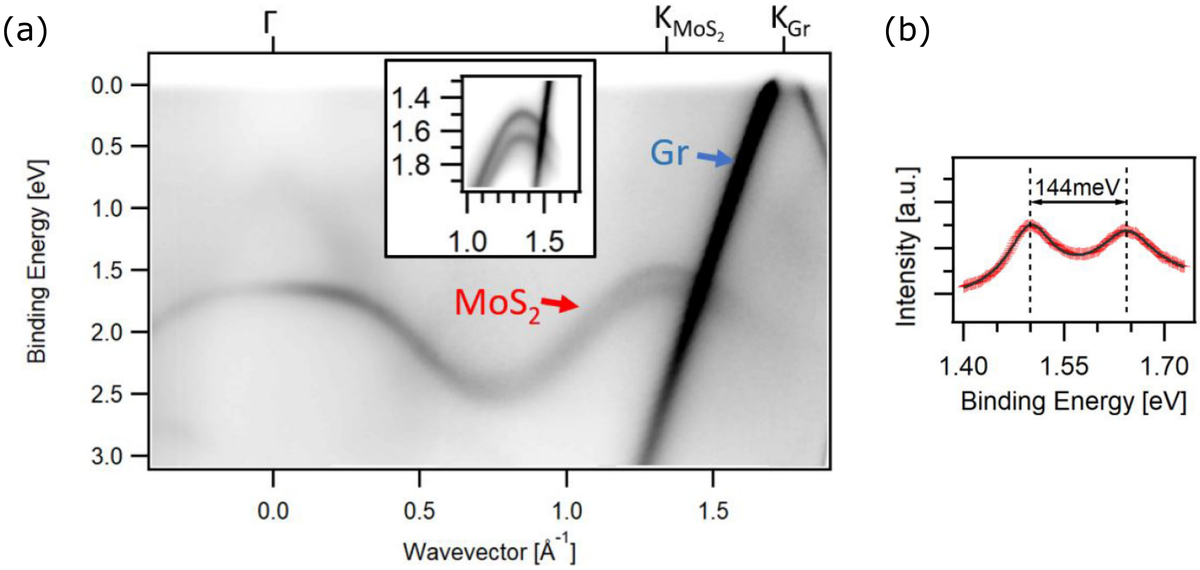

Figure 3.4: ARPES of ML MoS_2 on Gr/Ir(111): (a) ARPES data taken along the high symmetry directions of the hexagonal BZ. The Γ and the respective K points of MoS_2 and Gr are indicated. The inset shows the region around the MoS_2 K point in high-resolution. (b) Energy distribution curve (EDC) cut of that data at the K point of MoS_2 (labelled by K_{MoS_2}). The extracted spin-orbit splitting is 144 meV.
Image information: The ARPES spectra were taken with p - polarised light at $h\nu = 31$ eV and $T = 20$ K.

Raman Spectroscopy and Photoluminescence

Further evidence for the freestanding nature of MoS_2 grown on Gr/Ir(111) is provided by optical investigations by Ehlen *et al.*, details can be found in Ref. [44]:

(A) Performing UHV Raman spectroscopy allows investigating temperature-induced changes in bond length and strain through a change of the frequency of the Raman active modes. If for example, two materials are strongly coupled to each other, their thermal expansion is expected to be similar, while for two decoupled layers the thermal expansion may be independent.

For the system MoS_2/Gr/Ir(111), temperature-dependent Raman investigations show that the thermal expansion of MoS_2 and Gr are independent of each other indicating loose bonding. This is inferred by analysis of the phonon hardening of the MoS_2 modes when reducing the temperature from room temperature to 4 K. The phonon hardening is clearly better described by the freestanding case in comparison to MoS_2 strongly bound to Gr/Ir(111) [44].

(B) Finally, despite the metallic substrate it has been possible to observe PL at low temperatures. Normally, exciton quenching by either Förster or Dexter transfer processes is expected [44], which would impede the observation of PL. Förster-type energy transfer describes energy transfer mediated by long-range dipole-dipole coupling [303], whereas Dexter-type energy transfer refers to a transfer of excited electrons in the limit of orbital overlap between donor and acceptor systems (and is therefore short-range) [304].

The observation of PL in the present system is interpreted as a result of an efficient decoupling of the MoS_2 from its substrate Gr/Ir(111). The narrow measured peak width of 18 meV indicates a large exciton binding energy, which is estimated to be 480 meV [44].

3.4 Universality of Method

The applicability of the MBE growth with elemental sulphur for TMDS synthesis is neither limited to MoS_2 nor to Gr/Ir(111) as a substrate. In Fig. 3.5 (a) and (b), STM topographs after syntheses of monolayer WS_2 and TaS_2 islands are presented, while Fig. 3.5 (c) displays MoS_2 islands on a monolayer of h-BN on Ir(111).

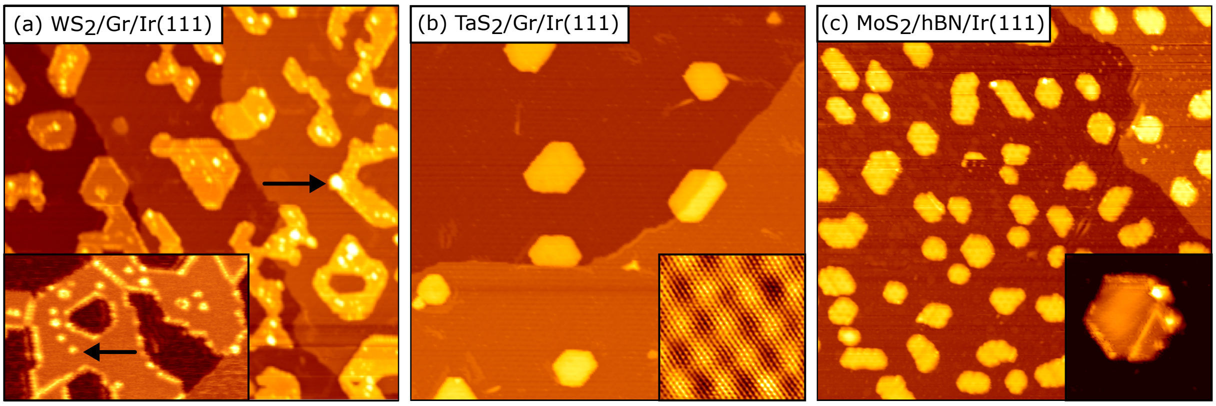

Figure 3.5: Different TMDS grown by the MBE based two step synthesis: (a) STM topograph of WS_2 islands on Gr/Ir(111). Growth with reference values of Section 2.6, except $F_W = 1.9 \times 10^{14}$ atoms $m^{-2}\,s^{-1}$ and $t^g = 300\,s$ yielding a coverage of 0.3 ML. Arrow in the main topograph points to W clusters. Inset highlights edge states and domain boundaries at tunnelling voltage within the band gap. Arrow suggests point defects. (b) STM topograph of TaS_2 islands on Gr/Ir(111). Growth with reference values, except $F_{Ta} = 0.5\,F_{Ta}^{ref} = 8.8 \times 10^{15}$ atoms $m^{-2}\,s^{-1}$ and $t^g = 60\,s$. Coverage is 0.05 ML. The inset displays atomic resolution of the TaS_2 lattice in the interior of an island, superimposed with the moiré corrugation. (c) STM topograph of MoS_2 islands on a monolayer of h-BN on Ir(111). Growth with reference values, except $F_{Mo} = 1.3\,F_{Mo}^{ref} = 3.8 \times 10^{16}$ atoms $m^{-2}\,s^{-1}$ and $t^g = 60\,s$. The measured coverage is 0.2 ML. Image information (image size, sample bias, tunnelling current): (a) $150 \times 150\,nm^2$, -2.3 V, 20 pA, inset $50 \times 30\,nm^2$ -1.0 V, 10 pA, (b) $150 \times 150\,nm^2$, -0.5 V, 100 pA, inset $9 \times 9\,nm^2$, -0.2 V, 600 pA, (c) $150 \times 150\,nm^2$, 2.0 V, 60 pA, inset $20 \times 20\,nm^2$ 0.9 V, 40 pA.

Since WS_2 is a semiconductor similar to MoS_2 [59], the ML islands in Fig. 3.5 (a) also display metallic edge states and bright domain boundaries [compare also inset of Fig. 3.5 (a)]. Island distribution, sizes and heights are similar to the MoS_2 case as well. An increased number of bright spots [see inset of Fig. 3.5 (a)] on the islands is visible, which we interpret as small W clusters (see arrow in the main topograph) and point defects (see arrow in inset). Growth parameter optimisation, in this case an increase of S pressure, which has not been conducted for WS_2, promises to reduce these defects substantially.

TaS_2 is a metallic TMDS and therefore no specific contrast between edges, domain boundaries and the island itself is expected, consistent with the homogeneous appearance of the TaS_2 islands in Fig. 3.5 (b). Despite the lack of growth of optimisation, the inset displays a perfect, hexagonal, defect-free lattice of monolayer TaS_2 with the moiré of Gr and Ir(111) superimposed. Close inspection of Fig. 3.5 (b) reveals a certain amount of S intercalation, which probably could be mitigated by reducing T^{a} or $P^{\mathrm{a}}_{\mathrm{sulphur}}$ slightly. Further results on TaS_2/Gr/Ir(111) will be presented in Chapter 6.

Instead of Gr, a monolayer of h-BN can be grown epitaxially in excellent quality on Ir(111) [221, 305]. The resulting substrate is inert and withstands high temperature. Despite its more strongly corrugated unit cell [221], it may be considered as a suitable substrate for TMDS growth through MBE with elemental sulphur. Figure 3.5 (c) displays MoS_2 islands grown on h-BN with the growth parameters specified in the figure caption. Well-developed ML islands are visible, which are present in higher density and consequently smaller size compared to growth on Gr. Through the insulator h-BN, the islands are much better insulated from the substrate metal and consequently rather hard to image by STM. The inset highlights an island with a bright MTB.

Finally, the growth recipe has been successfully applied to the growth of VS_2 as well. However, since the system vanadium-sulphur exhibits a manifold of stable phases, we discuss this separately in Chapter 5.

3.5 Discussion

The MBE based two-step technique serves as a UHV compatible synthesis approach for sulphur based TMDCs. Taking advantage of the low vapour pressure of FeS_2, the method fills in a gap in the MBE community and provides the possibility of synthesising these materials on weakly interacting substrates. In comparison to using precursor molecules such as H_2S as a sulphur source, the usage of S vapour from FeS_2 is superior in vdWE as the substrates lack the catalytic activity of a noble metal surface. The use of FeS_2 allows keeping very low chalcogen pressures and results in particularly clean samples. Using the right synthesis parameters, the method yields uniformly distributed sub-ML films with a low defect density which are epitaxially well oriented. On the downside, in comparison with the synthesis of TMDCs on strongly coupling substrates, a small orientational scatter seems inevitable. On the upside, the low substrate interaction present in vdWE allows the TMDC to keep its pristine material properties as indicated by a broad range of experimental surface science techniques including STM, STS, ARPES, Raman and PL. This combination of low interaction with the substrate, low defect density and high cleanliness is key to yielding unambiguous results, even useful for benchmarking theoretical modelling.

The method proves to be extremely versatile as it is applicable to both several TMDS epilayers and multiple substrates. Using Gr/Ir(111) as a substrate comes with both assets and drawbacks. On the upside, the substrate brings a very high-quality and inertness alongside tremendous experimental flexibility, such as the possibility of intercalation before TMDC growth. We will make use of this in Section 6.6. This is an elegant experimental lever as it allows tuning of the epilayer's properties without direct contact of it with the dopant. On the downside, reactants may inadvertently intercalate beneath Gr and alter its and the TMDCs properties. We will investigate the direct influence of S intercalation on MoS_2 growth in Section 4.3.

The deposition at comparably low temperatures (300 - 500 K) thus enables cleanliness in two ways: firstly, by directly allowing low growth pressures in the range of 10^{-9} mbar and secondly, by reducing the intercalation to a minimum. However, the problem with growth at low temperatures is a high nucleation density. The low temperature limits surface diffusion and as a consequence, many small and slightly misaligned grains together with a high density of domain boundaries evolve. When considering *e.g.* MoS_2 as a potential material for (opto-)electronic or valleytronic applications, a high density of grain boundaries is detrimental to mobility and general device performance.

To overcome these challenges it is therefore important to fully understand the possibilities and limits of the technique through performing growth studies and to achieve an understanding of the microscopic mechanisms. In this thesis, we will provide detailed growth studies on MoS_2 in Section 4.2, where we restrict ourselves to a very low-pressure UHV regime. In Section 6.6, we relax this constraint and explore how to enable large grain sizes of TaS_2 by increasing the substrate temperature, which necessitates higher S pressures.

3.6 Conclusion

In conclusion, MBE synthesis of transition metal disulphides with elemental sulphur is a straightforward, UHV compatible, and widely applicable method. It consists of a low-temperature growth step, enabling one to keep the applied sulphur pressure low, and a high-temperature annealing step improving epitaxial orientation, enlarging island size and yielding compact structures. It was exemplified for the growth of three transition metal disulphides and two inert substrates. For the example of MoS_2 on Gr/Ir(111) the method was shown to result in quasi-freestanding monolayer islands with weak substrate interaction and large band gap. The method provides extremely clean, well oriented and almost defect-free islands and layers, which allow *in situ* characterisation of pristine material properties.

Based on the obtained insight, we speculate that in the future with MBE using elemental sulphur it will be possible to grow pure and alloyed transition metal disulphides on a variety of substrates that were not previously synthesised as monolayers and thus not accessible for investigation.

CHAPTER 4

Molybdenum Disulphide: Understanding van der Waals Epitaxy

This chapter contains contributions from ***J. Hall****, B. Pielić, W. Jolie, C. Murray, P. Valerius, C. Busse, M. Kralj, and T. Michely. The part of this chapter that concerns the growth mechanisms of a single synthesis cycle is already published in Ref. [43].*

I *performed the growth study and analysed the data, including STM and LEED at* TuMA II *with the initial help of B. Pielić. The data were discussed by* **me***, B. Pielić, M. Kralj, and T. Michely.* ***I*** *wrote the manuscript of Ref. [43] and finalised it in close collaboration with T. Michely.*

I *extended the studies towards growth cycles, measured and analysed the data and investigated the growth on S intercalated Gr. Part of the images on point defects were taken by C. Murray and W. Jolie. T. Michely supervised all measurements.*

At the end of Section 4.4, ***I*** *introduce projects that were enabled through the new synthesis technique and* ***I*** *was involved in. In particular, three projects are introduced: (i) Electrons which are confined in 1D mirror twin boundaries exhibit Tomonaga-Luttinger-liquid behaviour. This is already published in Ref. [306]. W. Jolie took the leading part in this project under the supervision of C. Busse and T. Michely.* ***I*** *synthesised the sample at* $_{\mathrm{T}}$STM*, measured the room temperature data that is presented in Appendix D of Ref. [306] and took part in the discussions. (ii) The electronic band bending caused by additional charge inside a mirror twin boundary traps a 1D hole gas. This is unpublished. C. Murray took the leading part in this project under the supervision of T. Michely.* ***I*** *guided the synthesis and took part in the discussions. (iii) Ion beam irradiation can cause full amorphisation of* MoS_2 *alongside a semiconductor-to-metal transition. This can be reversed by annealing in sulphur. This is unpublished. P. Valerius took the leading part in this project under the supervision of T. Michely.* ***I*** *prepared the sample at* TuMA II*, instructed how to use the system, assisted the ion beam irradiation experiment, took part of the data and contributed to the discussions.*

4.1 Motivation: MoS_2, the Archetypal TMDC

Today often regarded as the archetypal TMDC with broad technological potential, MoS_2 was long time overlooked. Though the first publication on suspended monolayer MoS_2 dates back to 1986 [307], only within the recent 15 years it came to full bloom[1]. By now, notable figures of merit of semicon-

---

[1] According to the online database ‘Web of Science’ 90 % of roughly 25.000 publications including the word ‘MoS_2’ were published in the years 2005 - 2019.

ducting MoS_2 are a tunable band gap size when reducing thickness [45, 298] or choosing dielectric embedding [308] and a high carrier mobility [24] in the ML. The transition from an indirect to direct band gap semiconductor when reaching ML thickness makes it suitable even for optoelectronic applications. In addition, broken inversion symmetry in the monolayer leads to coupled spin-valley physics, a field that exploits the valley degree of freedom for possible technical applications [76, 309].

Though nothing short of a promising material, still, most of the experimental investigations are performed on exfoliated or CVD-grown samples, which inevitably includes ambient conditions. In turn, the preservation of pristine material properties is often difficult and alteration of surface properties have been documented plentiful [310–315]. On the other hand, in the MBE community, where particularly clean samples may be achieved, a lack of proper understanding of the growth processes impedes the development of large scale fabrication of single-crystalline material with a low defect density.

Since systematic growth studies for TMDCs are rare in the field of 2D materials with few exceptions [188, 206, 281], in this chapter we exploit the potential of MBE using co-evaporation of sulphur from FeS_2 and Mo in a systematic manner in order to provide a sound basis for future work.

In the second section, we will investigate the influence of selected growth parameters such as the annealing temperature and the influence of S background pressure and provide insight into the growth mechanisms in vdWE. After the growth step at comparably low temperatures, we observe fractal grain morphologies, which document growth far from equilibrium and justify the necessity of post-growth annealing. Only after high temperature, the grain morphologies are turned into thermodynamically favoured compact forms. During the growth step, a sufficiently high S supply is needed to ensure full conversion of the reactants. During the annealing step, high S pressures influence the growth mode and foster bilayer growth.

After having laid a fundamental understanding of the growth processes, we consider possible side effects that influence the growth in the third section. Intercalation of S below Gr is the most frequently observed imperfection in our two-step synthesis and we investigate its effect by deliberately growing MoS_2 on S intercalated Gr/Ir(111). Though we find a detrimental effect on the growth quality, the electronic properties seem to remain largely unchanged.

A stronger effect on the physical properties comes from defects, and we use the forth section to introduce the typical types encountered in MBE-grown MoS_2. Finally, we briefly discuss recent experimental progress on MoS_2 on Gr/Ir(111) – enabled through the newly developed technique.

4.2 Dependence of MoS_2 Growth on Synthesis Parameters

In this section, we will provide some insights into the growth mechanisms, by analysing the effect of selected synthesis parameters on structure and growth morphology of MoS_2. We, furthermore,

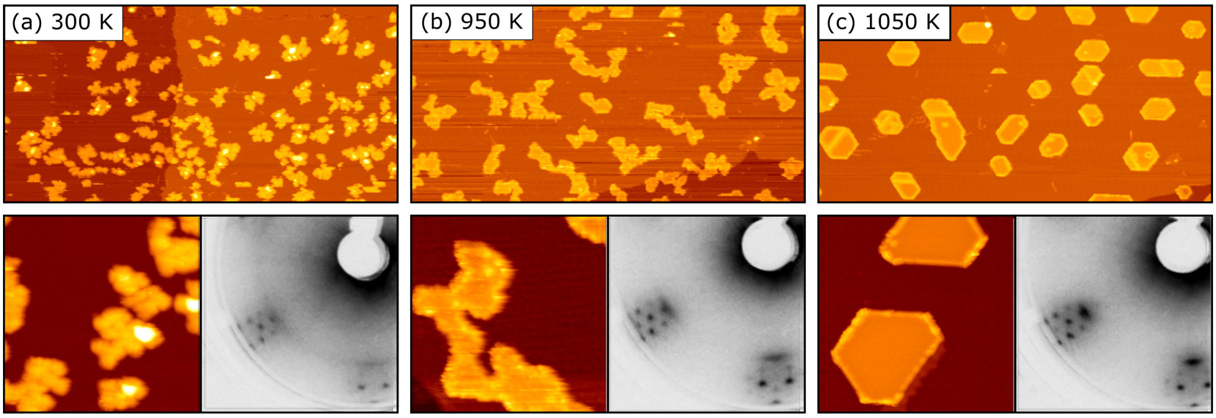

Figure 4.1: STM topographs and LEED patterns after growth with identical synthesis parameters, but variation of annealing temperature T^{a} as indicated. For synthesis the reference values (see Section 2.6) were chosen, except $t^{g} = 60\,s$ and $F_{Mo} = 3.8 \times 10^{16}$ atoms $m^{-2}\,s^{-1}$. Insets to the lower left are zooms highlighting island shapes, insets to lower right are 70 eV LEED patterns.
Image information (image size, tunnelling bias, tunnelling current): (a) 150×300 nm^2, -1.8 V, 20 pA, (b) 150×300 nm^2, -1.9 V, 40 pA, (c) 150×300 nm^2, -2 V, 20 pA, insets 40×40 nm^2.

consider the result of repeated growth cycles, which on the one hand promotes second layer growth, while on the other hand, it allows maintaining epitaxial alignment.

Annealing Temperature T^{a}:

The STM topograph in Figure 4.1 (a) displays the morphology after the growth step without any additional annealing, *i.e.* with $T^{a} = 300\,K$. A high density of small, dendritic islands of ML height, with occasional second layer nuclei [compare STM inset of Fig. 4.1 (a)], has formed upon growth. The LEED pattern in Fig. 4.1 (a) displays a diffuse diffraction ring with an enhanced intensity in the orientation of the first order diffraction spots of Gr and Ir(111). We conclude that already upon room temperature deposition of elemental S and Mo the reaction to form MoS_2 takes place. Growth is preferential within the ML plane of MoS_2 resulting in a predominance of ML islands. The rough, irregular island edges and their dendritic shapes imply that diffusion along step edges, detachment of small species (Mo, S, or MoS_x), and their exchange between islands must be absent. The island orientation scatters widely but displays already a preference for the epitaxial orientation established after annealing. The faint appearance of the diffraction ring can be traced back to the small size of the diffracting structures.

Upon annealing to $T^{a} = 950\,K$, as visualised in Fig. 4.1 (b), the island number density decreases substantially, the island branches become larger, the island edges straighter, second layer nuclei almost disappeared, and the metallic edge has started to develop [see the STM image of Fig. 4.1 (b)]. In LEED [compare LEED inset of Fig. 4.1 (a)], the diffraction ring of MoS_2 is broken up. Instead, we find slightly broadened diffraction spots, with an angular scatter of $\pm 4°$ width that are aligned with the first order spots of Ir(111) and Gr. The reshaping of the island most likely took place through island diffusion and aggregation (Smoluchowski ripening) and limited step edge diffusion. The still

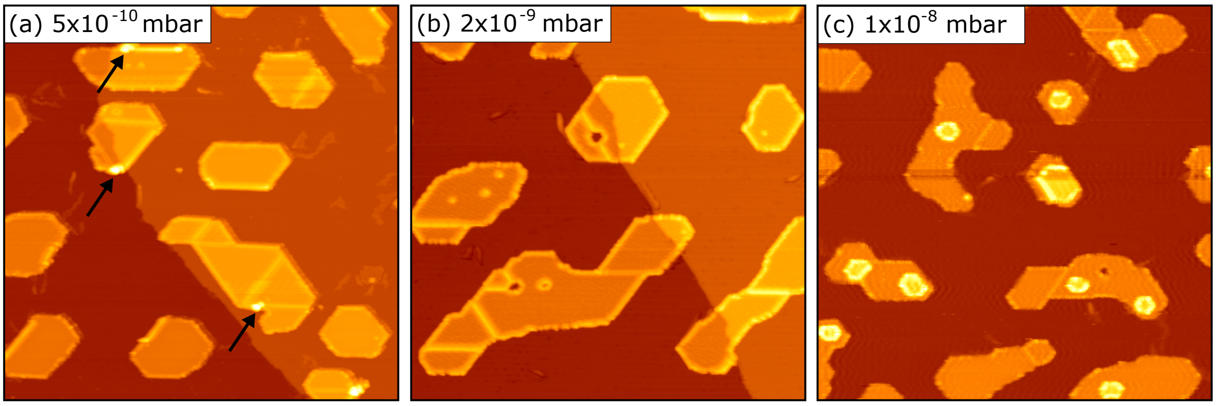

Figure 4.2: STM topographs after growth with identical synthesis parameters, but variation of annealing S pressure $P^{\mathrm{a}}_{\mathrm{sulphur}}$ as indicated. For synthesis the reference values (see Section 2.6) were chosen. Arrows in (a) indicate Mo clusters.
Image information (image size, tunnelling bias, tunnelling current): (a) $120 \times 120\,\mathrm{nm}^2$, -1.7 V, 10 pA, (b) $120 \times 120\,\mathrm{nm}^2$, -1.5 V, 50 pA, (c) $120 \times 120\,\mathrm{nm}^2$, -1 V, 10 pA.

branched and elongated shapes would be hard to reconcile with Ostwald ripening (detachment and reattachment of small species). The disappearance of second layer nuclei is thus most likely a consequence of island mobility, of which the integration into the larger ML islands is energetically favourable.

Figure 4.1 (c) displays the situation after annealing to $T^{\mathrm{a}} = 1050\,\mathrm{K}$. The island number density is nearly the same compared to the 950 K case. Compact islands, with straight and well-oriented steps and almost no second layer islands, have formed. Furthermore, a well-developed edge state [illustrated in the STM inset of Fig. 4.1 (c)], and MTBs are present within some islands. The LEED spots of $\mathrm{MoS_2}$ [compare LEED inset of Fig. 4.1 (b)] are sharpened and display a reduced angular spread of $\pm 2^\circ$. Though the large islands are presumably unable to diffuse over extended distances, small rotations optimising their binding and epitaxial orientation are apparently possible. Since the island number density remains nearly constant, reshaping of the islands happens presumably primarily through edge diffusion. Reshaping through detachment and reattachment of small species should have also affected the island number density, which is apparently not the case. Compact island shapes are energetically preferred to branched ones, simply because of reduced edge length. Likewise, the straight dense-packed S- and Mo-edges that developed are evidently energetically preferred under the given conditions of S chemical potential.

Annealing to even higher temperatures around 1150 K initiates rapid degradation through decomposition of $\mathrm{MoS_2}$, resulting in frequent metallic Mo clusters at the edges of $\mathrm{MoS_2}$ islands and Mo intercalation. This is shown in Appendix A.5.

Annealing Sulphur Pressure $P^{a}_{sulphur}$:

Based on the arguments used until now, one might assume that the MoS_2 islands are perfectly stable at the annealing temperature of 1050 K, such that an additional annealing S pressure $P^{a}_{sulphur}$ would be obsolete.

Figure 4.2 (a) refutes this assumption. Annealing in the residual S pressure around 5×10^{-10} mbar, which is still present in the first minutes after the growth process, results in a significant number of bright spots at the edges of MoS_2 islands. Some of these spots are highlighted by black arrows in Fig. 4.2 (a). They display a height of the order of 20 Å. We interpret them to be elemental Mo which result from the gradual decomposition of MoS_2 islands at their edges. While the S desorbs (or intercalates), Mo atoms aggregate to clusters.

Fig. 4.2 (b) shows the sample morphology after annealing in 2×10^{-9} mbar S pressure. The islands edges show uniform bright contrast without additional spots. Apparently, to compensate for the slight loss of S, $P^{a}_{sulphur} = 2 \times 10^{-9}$ mbar is sufficient.

A comparably high S pressure of 1×10^{-8} mbar applied during annealing fosters the formation of second layer MoS_2 island nucleation. The reason for the second layer formation due to annealing in a high $P^{a}_{sulphur}$ is not clear. We speculate that the residence time of arriving S-dimers is higher on the MoS_2 islands compared to Gr. Therefore, liberated Mo atoms from the island edge and S arriving on the island top could initiate nucleation and cause subsequent growth of these nuclei.

Annealing Time t^{a}:

The variation of annealing time t^{a} was probed within in the span from of 60 s to 1200 s and did not show a significant effect on the morphologies. The edges of the islands become straighter and better oriented along the dense-packed directions for extended t^{a}. Fig. A.7 in Appendix A.5 shows an image which was annealed for 1200 s instead to the reference annealing time of 300 s.

Growth Temperature T^{g}:

The growth temperature acts twofold on the resulting growth morphology. Firstly, it influences how strongly branched and dendritic the MoS_2 islands grow, an effect that still can be recognised after annealing, and secondly, due to the strong temperature dependence of the residence time τ of S on Gr it influences the availability of S for the reaction to MoS_2.

After growth at 100 K, the STM topograph in Fig. 4.3 (a) displays a percolation network of MoS_2. The LEED pattern shown in the inset of Fig. 4.3 (a) displays an almost closed diffraction ring with an enhanced intensity in the orientation of the first order diffraction spots of Gr and Ir(111), similar to the LEED inset of Fig. 4.1 (a). In Fig. 4.3 (a) also some S intercalation (thin stripes) is visible. The interpretation is as follows: At 100 K both, Mo and S stick to the sample, the latter being present in large excess. Either already at 100 K or during heating the reaction of Mo with S takes place, resulting in a small scale percolation network. During the annealing step the percolation network

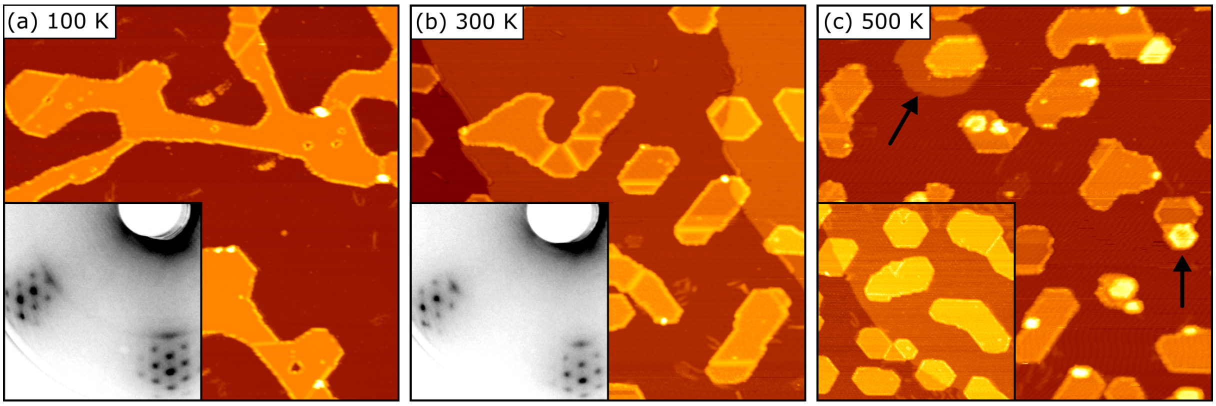

Figure 4.3: STM topographs after growth with identical synthesis parameters, but variation of growth temperature T^{g} as indicated. For clarity, please note that the annealing temperature T^{a} was the same for the respective data shown. For synthesis the reference values (see Section 2.6) were chosen. Insets in (a) and (b) display 80 eV LEED patterns. Arrows in (c) highlight an Mo intercalation island (upper left) and a second layer MoS_2 island (right-hand side). Inset in (c) represents growth with synthesis parameters as for the experiment represented by the main topograph, but with $P^{\mathrm{g}}_{\mathrm{sulphur}} = 1 \times 10^{-7}$ mbar.
Image information (image size, tunnelling bias, tunnelling current): (a) 150×150 nm^2, -1.2 V, 10 pA, (b) 150×150 nm^2, -1.5 V, 50 pA, (c) 150×150 nm^2, -0.9 V, 10 pA, inset 150×150 nm^2, -0.9 V, 30 pA.

coarsens by step edge diffusion, but the connectivity of the network is still preserved to a certain extent. As in a percolation network the differently oriented patches are connected to each other, reorientation is hampered and largely suppressed compared to free islands, thus giving rise to the inferior orientation order as observed in LEED.

The comparison of Fig. 4.3 (b) with (a) underlines the significant differences in the growth process (single, non-percolated and well-oriented islands) as already discussed in the context of Fig. 4.1.

When the T^{g} is lifted to 500 K, STM topographs as the one shown in Fig. 4.3 (c) display a failure of the growth process. Large intercalated islands of Mo are present, one of which is *under* an MoS_2 island and highlighted in Fig. 4.3 (c) by an arrow. Moreover, a substantial number of second layer islands have grown. The LEED pattern (not shown) is nearly identical to that obtained after growth at 300 K. While the lifetime of S is of the order of milliseconds at 300 K, it is about 5 orders of magnitude shorter at 500 K, if a standard prefactor of $5 \times 10^{12}\, s^{-1}$ is assumed for desorption. Although the lateral diffusion will certainly be also enhanced because of the higher temperature, it is plausible that due to an S deficit not all Mo can be reacted to MoS_2, resulting in Mo intercalation and Mo clusters. In the subsequent annealing step, the Mo clusters are apparently seeds for second layer MoS_2 islands (black arrows). If this reasoning is correct, an increase of $P^{\mathrm{g}}_{\mathrm{sulphur}}$ should be able to compensate for the reduced τ at 500 K. The inset of Fig. 4.3 (c) displays the morphology resulting from growth at 500 K with the same parameters, but at $P^{\mathrm{g}}_{\mathrm{sulphur}}$ enhanced by a factor of 20. As visible, Mo intercalation and BL formation are suppressed, confirming our interpretation.

Furthermore, the growth at higher substrate temperature and higher S pressure yields a decrease in nucleation density and an accompanying increase in lateral island size. While after growth at 300 K,

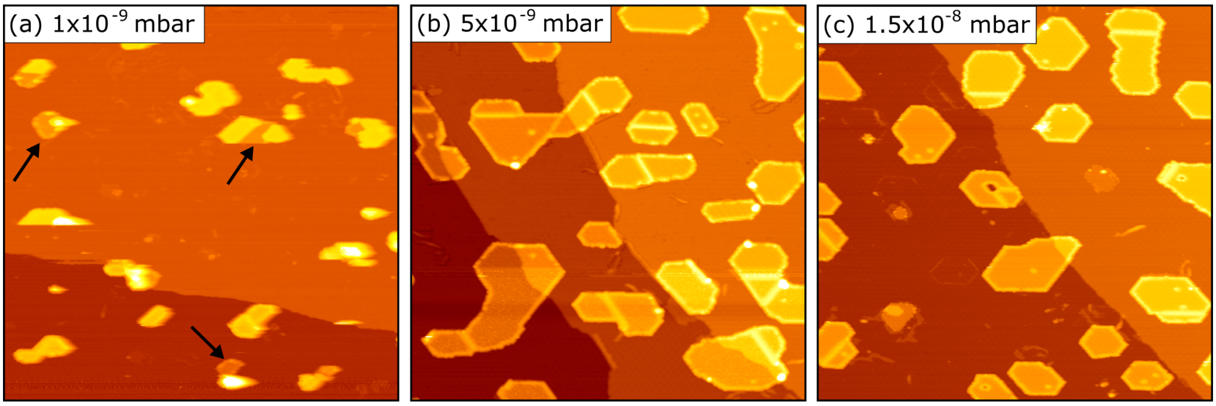

Figure 4.4: STM topographs after growth with identical synthesis parameters, but variation of growth S pressure P^{g}_{sulphur} as indicated. For synthesis the reference values (see Section 2.6) were chosen. Arrows in (a) indicate monolayer MoS_2 islands.
Image information (image size, tunnelling bias, tunnelling current): (a) 150×150 nm^2, -1 V, 10 pA, (b) 150×150 nm^2, -1.5 V, 50 pA, (c) 150×150 nm^2, -1.5 V, 50 pA.

the lateral dimensions are about 20 nm, this increases to roughly 40 nm for 500 K substrate temperature. In Section 6.6, we further investigate this issue using TaS_2 and increase lateral dimensions to up to 70 nm.

Growth Sulphur Pressure P^{g}_{sulphur}:

Figure 4.4 displays the effect of S pressure variation during the growth step with reference synthesis parameters. Variation of the S pressure during growth has little effect on the resulting morphology, as long as P^{g}_{sulphur} is large enough to react all Mo. In Fig. 4.4 (a) the morphology upon growth at too little S pressure is shown. Here, BL MoS_2 islands dominate, whereas ML MoS_2 is rare and highlighted in Fig. 4.4 (a) with black arrows. Also, a high amount of bright structures, which we interpret as Mo clusters appear frequently on the edges of the islands. Upon increase of the S growth pressure, ML growth is restored as visible in Fig. 4.4 (b). Increasing the S pressure further seems to not alter the morphology substantially. Figure 4.4 (c), shows very much the same compact growth morphology and nucleation density of the islands in comparison to Fig. 4.4 (b). However, the amount of intercalation structures increases.

It thus seems that the dominating condition for ML growth is an S growth pressure high enough such that all Mo can react and the stoichiometry is met. Otherwise, Mo clusters form since Mo does not wet Gr. These clusters subsequently form BL structures after annealing. Furthermore, it does not seem favourable to exceed the necessary amount of S extensively, since intercalation intensifies.

Growth Metal Flux F^{g}_{metal}:

Varying the metal flux on the scale of $F_{\text{Mo}} = 10^{16}\,\text{atoms}\,\text{m}^{-2}\,\text{s}^{-1}$ does not have a significant influence on the morphology. Since it is decisive that at a given growth temperature all Mo metal is

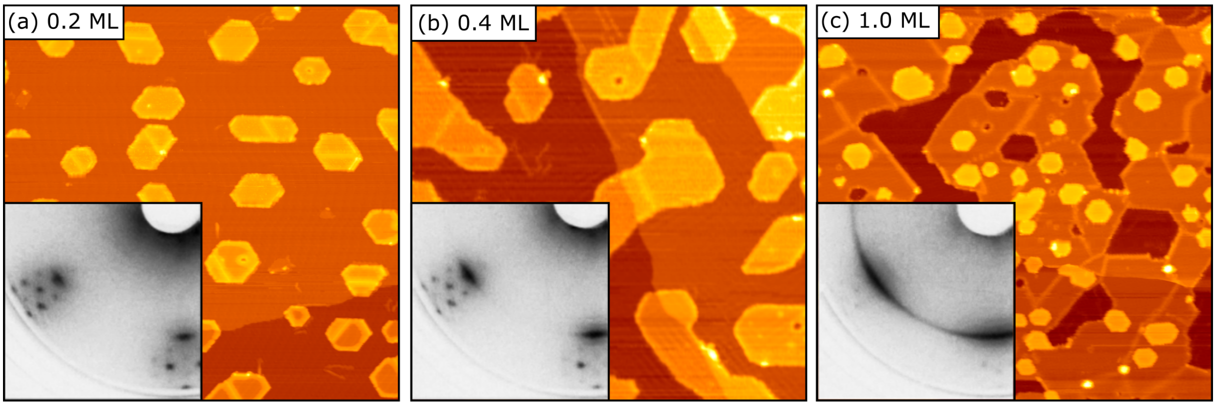

Figure 4.5: STM topographs after growth with identical synthesis parameters, but variation of growth time t^{g} resulting in variations of the deposited amount θ as indicated. For synthesis the reference values (see Section 2.6) were chosen, except of $F_{\mathrm{Mo}} = 3.8 \times 10^{16}\,\mathrm{atoms\,m^{-2}\,s^{-1}}$ and $t^{\mathrm{g}} = 60\,\mathrm{s}$ in (a), $t^{\mathrm{g}} = 120\,\mathrm{s}$ in (b) and $t^{\mathrm{g}} = 300$ in (c). Insets display 70 eV LEED patterns.
Image information (image size, tunnelling bias, tunnelling current): (a) $200 \times 200\ \mathrm{nm}^2$, -2 V, 20 pA, (b) $200 \times 200\ \mathrm{nm}^2$, -2 V, 40 pA, (c) $200 \times 200\ \mathrm{nm}^2$, -2 V, 40 pA.

reacted to MoS_2, what matters is the ratio of sulphur flux to metal flux onto the sample. Therefore variation of $F^{\mathrm{g}}_{\mathrm{metal}}$ is reciprocal to the variation of $P^{\mathrm{g}}_{\mathrm{sulphur}}$. However, at too high Mo fluxes, not all Mo is reacted in the growth step to MoS_2 with similar consequences as mentioned above for a too low $P^{\mathrm{g}}_{\mathrm{sulphur}}$: Mo intercalation islands, Mo clusters, and MoS_2 BL islands are observed after annealing.

Growth Time t^{g}:

The variation of the growth time t^{g} implies, with all other parameters left identical, a variation of coverage. In Fig. 4.5 this parameter is tuned from 0.2 ML to 1.0 ML.

Figure 4.5 (a) displays an STM topograph taken after growth of 0.2 ML. Compact, hexagonal MoS_2 islands bound by dense-packed, straight steps are predominant. As indicated by the LEED inset, the island orientation with respect to the substrate is excellent.

After deposition of 0.4 ML, the situation is changed as visualised in Fig. 4.5 (b). The islands form elongated structures reminiscent of the network formed after growth at 100 K [compare Fig. 4.3 (a)]. Due to the large coverage, the resulting structures formed in the growth step are more branched and extended and, upon annealing, are not able to reshape to perfect hexagons. This implies also the presence of step portions that are not dense-packed. The LEED inset indicates still a good orientation order, but slightly inferior to Fig. 4.5 (a).

Figure 4.5 (c) illustrates the situation after the growth of a full ML. The first layer is almost closed. At the same time nucleation of second layer MoS_2 islands took place making up 0.15 ML. As we might have expected based on previous knowledge, the LEED inset rather displays a diffraction ring, as opposed to spots found at lower coverages. The reason is simply that the formation of a full ML

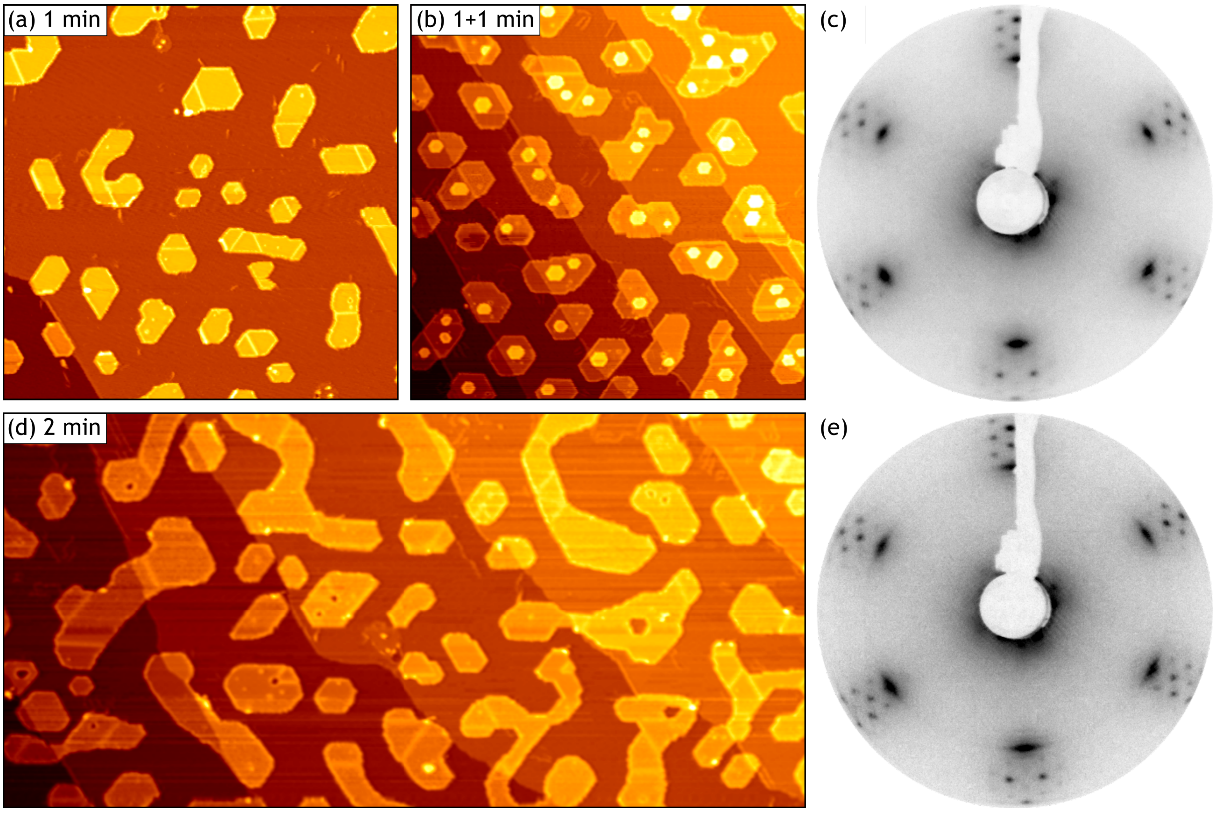

Figure 4.6: Cycled synthesis in comparison to all-in-one-go: For synthesis reference values (see Section 2.6) were chosen, except of $F_{\text{Mo}} = 3.8 \times 10^{16}$ atoms $\text{m}^{-2}\,\text{s}^{-1}$ and varying times t^{g} for the different panels. (a) STM topograph after one cycle with $t^{\text{g}} = 60\,\text{s}$ resulting in 0.2 ML MoS_2. (b) Sample topography after two successive equivalent cycles with $t^{\text{g}} = 60\,\text{s}$ each. (c) Corresponding LEED data at 70 eV. (d) Synthesis outcome after one cycle with $t^{\text{g}} = 120\,\text{s}$ at otherwise constant parameters. (e) Corresponding LEED data at 70 eV.
Image information (image size, sample bias, tunnelling current): (a) $250 \times 250\,\text{nm}^2$, -2 V, 20 pA, (b) $250 \times 250\,\text{nm}^2$, -2 V, 30 pA, (d) $500 \times 250\,\text{nm}^2$, -2 V, 40 pA.

already at low temperature impedes the rotations of the misoriented MoS_2 patches as they are fixed within the layer.

Repeated Synthesis Cycles

After having investigated the influence of the parameters of one synthesis cycle, we now evaluate the influence of repeated synthesis cycles, where one cycle includes as well the growth step and the annealing step. We will find this to be an additional route of controlling growth mode and layer number.

Figure 4.6 illustrates the effect of growing in cycles opposed to growing in a single-cycle approach. In panel (a), the sample morphology after a first reference step – using growth parameters stated in the figure caption – is displayed. Comparable to Fig. 4.5 (a), the 0.2 ML MoS_2 arrange in compact hexagonal ML islands scattered homogeneously over the sample surface. After an equivalent second growth cycle in Fig. 4.6 (b), the lateral island size did only slightly increase, but a large fraction of second layer islands have formed. The sample is now covered by 0.35 ML which arrange in the first layer and 0.05 ML can be found in the second layer. Considering the corresponding LEED pattern in (c), we note excellent ordering and an azimuthal spread of about 2°.

In comparison to the cycled growth, Fig. 4.6 (d) shows the synthesis outcome after the direct deposition of 0.4 ML. Here, no BL has formed and the observed forms are not as compact anymore, giving rise to many island edges not being aligned with dense-packed rows of the substrate. This decreased ordering can also be observed in the LEED data in panel (e) showing an azimuthal scatter of about 4° through elongated MoS_2 spots.

The comparison shows that the cycled growth approach allows keeping a better epitaxial relation on the expense of formation of BL MoS_2 islands. This behaviour might be interpreted as follows: after the first full cycle, compact highly oriented TMDC islands are present on the sample. As a rule of thumb, the lower the deposited amount, the better the alignment. Within the second growth cycle, these islands are precursors for the newly deposited material, which attaches at them presumably already during growth which thus results in good alignment. Furthermore, if during the growth step of the second cycle some reactants agglomerate on top of the first layer, these lack the mobility to diffuse step-down – even in the annealing step – which causes second layer formation.

Maintaining Epitaxial Relations at High Sample Coverages

Finally, we consider a variant of the above approach, which allows maintaining a well established epitaxial relation, without increasing the number of second layer islands at higher coverages. We investigate the possibility of a low coverage seeding growth cycle, which will result in epitaxially orientated islands, followed by a second growth cycle again at lower temperatures in which we deposit the residual MoS_2. Fig. 4.7 shows the effect of this technique by a direct comparison of two samples - one grown in a single cycle, the other with a seeding step.

The STM topograph in Fig. 4.7 (a) displays the morphology of the sample, which was grown in a single cycle. The total deposited amount is about 0.75 ML, of which about 0.1 ML are found in the second layer. The residual 0.65 ML arrange in the first layer, form a branched network, which shows a lot of grain boundaries. In panel (b), the LEED diffraction pattern displays rather a full ring instead of diffraction spots. Even though a clear preference towards the first order spots of Gr and Ir is visible, a well-defined alignment is lacking. Overall, considering both STM and LEED the sample is similar to the one shown in Fig. 4.5 (c), except that the coverage is lower.

In Fig. 4.7 (c) and (d), the result of seeded growth is displayed. Here, the sample is grown in two cycles. In the first cycle, a small amount of less than 0.05 ML MoS_2 is deposited and annealed to high temperatures. This results in highly aligned compact islands [cf. Fig. 4.5 (a)]. After the

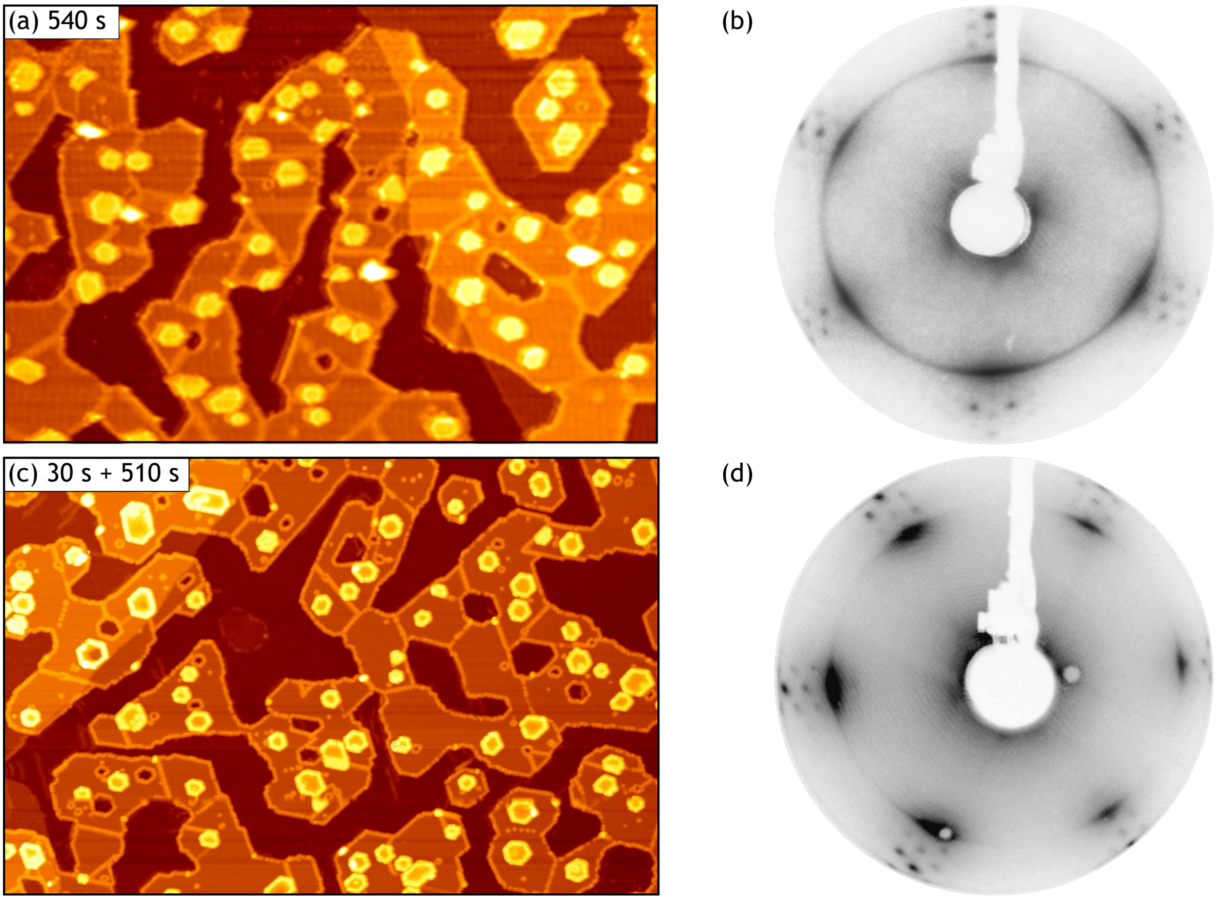

Figure 4.7: Growth of MoS_2 *via* seeding: (a) STM topograph after usual growth with reference parameters (see Section 2.6) except for $F_{\mathrm{Mo}} = 0.5\,F_{\mathrm{Mo}}^{\mathrm{ref}} = 1.5 \times 10^{16}$ atoms $\mathrm{m}^{-2}\,\mathrm{s}^{-1}$ and $t^{\mathrm{g}} = 540$ s. (b) Corresponding LEED data at 70 eV. (c) STM topograph after synthesis consisting of two cycles. In the first cycle, a small amount of about 0.05 ML is deposited in the time t_1^{g} and quickly flash-annealed to 1050 K. When the temperature has again dropped to about 350 K, the residual amount is grown in a second cycle with time t_2^{g}. The growth parameters follow the reference values except for $F_{\mathrm{Mo}} = 0.5\,F_{\mathrm{Mo}}^{\mathrm{ref}} = 1.5 \times 10^{16}$ atoms $\mathrm{m}^{-2}\,\mathrm{s}^{-1}$ and $t_1^{\mathrm{g}} = 30$ s and $t_2^{\mathrm{g}} = 510$ s. (d) Corresponding LEED data at 70 eV.
Image information (image size, sample bias, tunnelling current): (a) $300 \times 200\ \mathrm{nm}^2$, -2 V, 20 pA, (c) $300 \times 200\ \mathrm{nm}^2$, -1.6 V, 60 pA.

temperature has dropped to about 350 K, the residual amount is grown in a second cycle with the parameters stated in the figure caption.

In STM, the morphologies of Fig. 4.7 (a) and (c) compare well and it is hard to make out any qualitative difference. In both, a first layer network is visible and the island edges are not substantially straighter in one of the images. Regarding the second layer, also here coverage and nucleation density are similar in both samples. However, the LEED data in Fig. 4.7 (d) are in stark contrast to the LEED data in Fig. 4.7 (b). In the seeded sample, the diffraction ring has broken up and the intensity condenses in the Gr and Ir direction establishing a clear defined epitaxial relation.

Thus, the seeding step enabled high coverage samples to maintain their epitaxial relation with their substrate without an increase of second layer islands. This is again possible through highly oriented precursors which are already existing in the growth step of the second cycle.

In conclusion, we demonstrated the influence of the growth parameters within the two-step synthesis and gave insights into the growth mechanisms. We further extended the two-step synthesis consisting of one cycle towards multiple cycles, in which we find that it is easier to maintain epitaxial orientation at higher coverages.

4.3 MoS_2 on S Intercalated Gr/Ir(111)

A comprehensive understanding of the MBE synthesis does not only concern the pristine growth processes, but also possible side effects. Here, intercalation of the educts under Gr is the most probable outcome of an imperfect synthesis, which may be related to defected Gr or inadequate synthesis parameters. Since the growth is conducted in S excess, S intercalation is observed more frequently than Mo intercalation. The structures of two possible S intercalation phases – $(\sqrt{3} \times \sqrt{3})R30^\circ$ and the denser 4×2 phase – under Gr are discussed in Appendix A.3. Two main results are important for the subsequent growth of a TMDC on top: (i) preliminary ARPES and STS investigations indicate that doping of Gr is small if not negligible; (ii) the suppressed moiré signal in LEED shows that S intercalation decouples Gr from Ir(111).

In this section, we will discuss the influence of S intercalation under Gr on the growth of MoS_2. As a starting point, a sample with partial Gr/Ir(111) coverage is exposed to about 5 L S vapour at 800 K, resulting in $(\sqrt{3} \times \sqrt{3})R30^\circ$ superstructure formation comparable to Fig. A.4 (a), see Appendix A.3. The sample has been checked in STM and homogeneous intercalation with a coverage of about 95% of the sample surface was found. On this sample the MoS_2 was subsequently grown.

Since we already assume S to decrease the interaction strength of Gr and Ir(111), a reduced epitaxial orientation of the TMDC is to be expected. In order to maintain some epitaxial relation, the above-introduced seeding technique is applied.

Fig. 4.8 (a) and (b) display the result of MoS_2 growth after a first cycle, in which a little amount of MoS_2 was deposited with synthesis parameters stated in the figure caption. Both the STM results in (a) and LEED data in (b) illustrate the consequence of the decreased interaction with the substrate. In the STM topograph, the 0.15 ML MoS_2 arrange in elongated islands which display a significant portion of the island edges to deviate from the dense-packed direction of the substrate and show a high defect density. In stark contrast to this, we recall the 0.2 ML on pristine Gr shown in Fig 4.5 (a) to form compact defect-free islands, with hexagonal shapes and epitaxial orientation of the island edges.

The same comparison holds for LEED: though the low coverage should enable highly epitaxially ordered growth, Fig. 4.8 (b) displays poor ordering at an azimuthal spread of about 8° for the S intercalated sample, while the LEED data of MoS_2 on pristine Gr in Fig 4.5 (a) show excellent

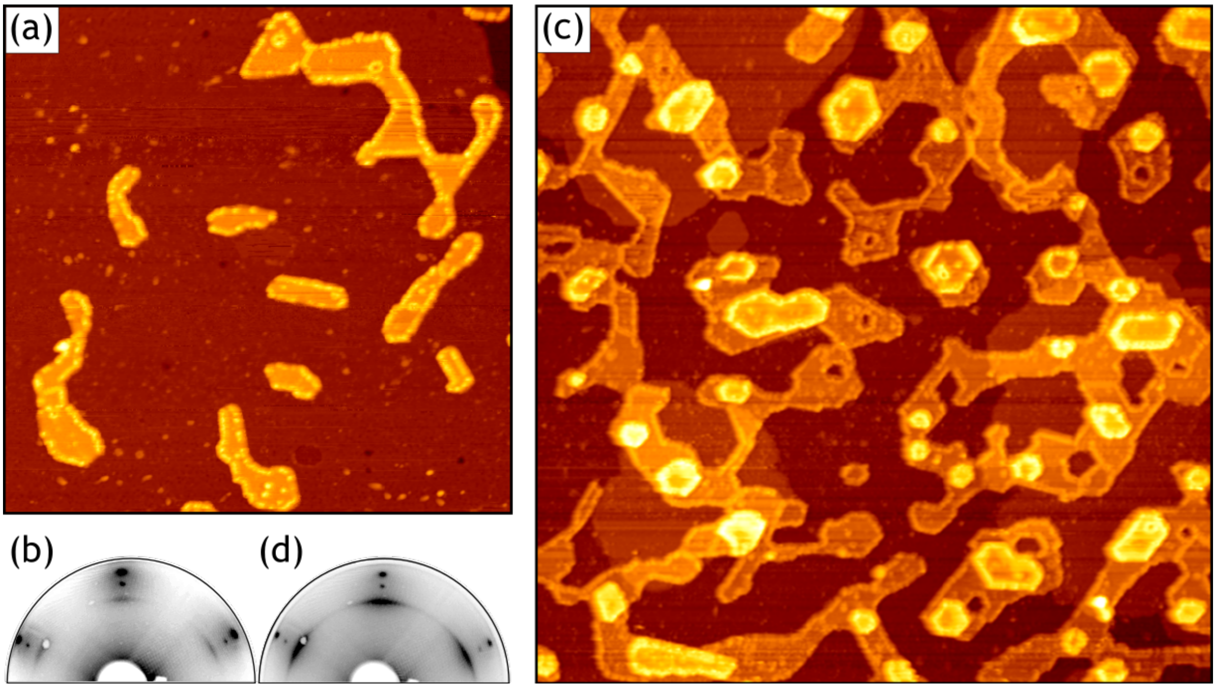

Figure 4.8: MoS$_2$ on S intercalated Gr/Ir(111): (a) STM topograph of 0.15 ML MoS$_2$ on Gr/S/Ir(111), for synthesis reference parameters were chosen except for $F_{\mathrm{Mo}} = 0.5\,F_{\mathrm{Mo}}^{\mathrm{ref}} = 1.5 \times 10^{16}$ atoms m^{-2} s^{-1} and $t^{\mathrm{g}} = 120$ s. (b) Corresponding LEED data at 65 eV (c) STM topograph after a second cycle with the same metal flux as before, but additional $t^{\mathrm{g}} = 600$ s. The total deposited amount is 0.9 ML of which about 0.45 ML reside in the first layer. Additional 0.1 ML are found in the second layer and a high amount of 0.35 ML is found in Mo intercalation structures. (d) Corresponding LEED data at 65 eV.
Image information (image size, sample bias, tunnelling current): (a) 150 × 150 nm^2, −0.2 V, 30 pA, (c) 200 × 200 nm^2, −1.0 V, 10 pA.

epitaxial ordering. We note that the moiré contrast has not significantly decreased from before to after MoS$_2$ growth (data not shown), but that the $(\sqrt{3} \times \sqrt{3})$R30° diffraction spots related to S ordering are not visible anymore. Since the low coverage of MoS$_2$ will not be able to suppress the signal of a hypothetically still ordered S phase, the absence of diffraction spots indicates a high level of disorder introduced by the MoS$_2$ growth. In line with this, the $(\sqrt{3} \times \sqrt{3})$R30° phase could not clearly be resolved by STM after MoS$_2$ growth.

The result of continuing the growth *via* a second cycle with the same parameters, but prolonged deposition, is shown in Fig. 4.8 (c). In STM, the branched elongated growth continues and a thin network of irregular shapes appears. While the first layer seems strongly affected by the S intercalation – opposed to growth on pristine Gr as *e.g.* in Fig. 4.7 thin structures evolve – the second layer appearance has not considerably changed. Both the nucleation density and the size of the islands is roughly comparable to a similar experiment on pristine Gr in Fig. 4.7, when accounting for the slightly different coverage. However, both the first and the second layer show a high defect density after S intercalation. The total deposited amount in Fig. 4.8 (c) amounts to roughly 0.9 ML,

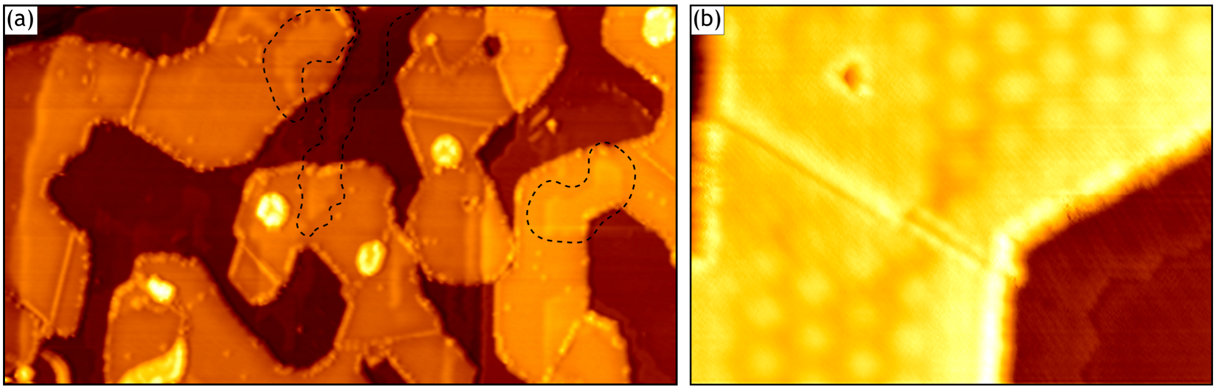

Figure 4.9: S intercalation under MoS_2: (a) STM topograph allowing S intercalation below Gr to be visible through MoS_2 (b) The moiré contrast of Gr/Ir(111), which is also seen on the MoS_2 is decreased by S intercalation.
Image information (image size, sample bias, tunnelling current): (a) $150 \times 80\ \mathrm{nm}^2$, 0.9 V, 80 pA, (d) $25 \times 20\ \mathrm{nm}^2$, -2 V, 0.1 nA,.

of which about 0.45 ML reside in the first layer. Additional 0.1 ML are found in the second layer and a high amount of 0.35 ML is found in Mo intercalation structures.

In LEED, which is shown in Fig. 4.8 (d) the orientation scatter increased, but the cycled approach prevented a complete loss of alignment. Compared to the low coverage LEED data in panel (b), the spread has about doubled and now amounts to about 15°.

Though the intercalation of S under Gr has obvious influence on the synthesis outcome, this must not directly imply S to be present under MoS_2 – after all, an interaction of the MoS_2 layer with the S intercalation is obvious through the decreased order indicated by the absence of $(\sqrt{3} \times \sqrt{3})R30^\circ$ spots in LEED. Furthermore, STM data usually do not show the continuity of S intercalation patterns below the TMDC islands, but the contrast of the intercalation ends at the edge of the flake. Fig. 4.9 (a) clears this issue by displaying unambiguous continuity of S intercalation patterns under MoS_2. Furthermore, Fig. 4.9 (b) also clearly illustrates a decreased moiré contrast in an area which is intercalated by S. It is therefore plausible that though MoS_2 growth interferes with the S intercalation, it does not repel it from under the islands.

We summarise that though S intercalation is detrimental for epitaxial ordering and sample quality, it does not directly disable the growth. The fact that key features such as the metallic edge state are still present underlines that doping cannot be strong and that still 2H-MoS_2 is grown. However, the increased amount of defects may also alter the material's properties, which we consider in the next section.

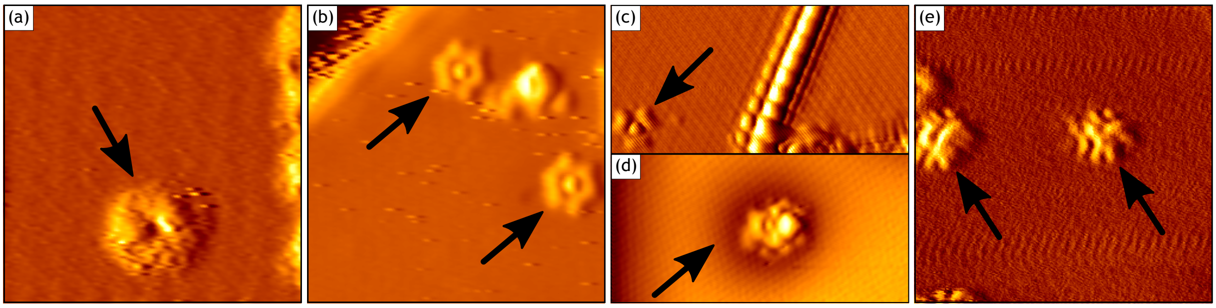

Figure 4.10: Point defects in MoS_2 grown on Gr/Ir(111): (a) A point defect with a depression in the middle is marked by a black arrow. (b) Two point defects with flower-like appearance are marked. (c) Point defect of clover-like triangular symmetry and a protrusion in the middle. (d) Point defect lacking symmetry. (e) Bias dependent point defect.
Image information (image size, sample bias, tunnelling current): (a) 10×10 nm^2, -0.9 V, 60 pA, (b) 10×10 nm^2, -1.5 V, 0.1 nA, (c) 10×5 nm^2, 0.4 V, 1 nA (d) 10×10 nm^2, 1 V, 50 pA, (e) 10×10 nm^2, 1.2 V, 10 pA.

4.4 Defects in Molecular Beam Epitaxy Grown MoS_2

In this section, we will introduce defects and impurities which are common in MBE-grown MoS_2. Typical defects include vacancies, antisite atoms, substitutional atoms, and adatoms, which in 2D have a strong effect on electronic properties. For example, considering semiconducting materials, even single defects might introduce states localised in the band gap [316–318] or act as dopants [319, 320]. Usually, defects are detrimental to electron mobility and limit performance in possible device applications. However, they also create an experimental lever for tuning the electronic properties and the field of defect engineering has recently been reviewed [321]. In addition, in extended line defects that are frequently encountered in MBE-grown layers, they may also host exotic physical phenomena [306, 322]. The two-step MBE-grown MoS_2 on Gr/Ir(111) has enabled high precision STS investigations on sulphur based systems, which we will briefly introduce at the end of the section.

Point Defects

Regarding the archetypal TMDC MoS_2, the study of (point) defects has largely been influenced by usage of transmission electron microscopy and scanning transmission electron micorscopy [323–327], and theoretical contributions [317, 328], while STM studies on defects only recently increased in number [329–334] with few numbered theoretical support [334, 335].

Fig. 4.10 summarises a non-complete list of the most frequently observed point defects when investigating the two-step-grown MoS_2 on Gr/Ir(111) by STM. The first type of defects in Fig. 4.10 (a) appears as a bright protrusion with threefold symmetry and a depression in the middle. Top layer chalcogen vacancies have been reported to have the least formation energy [316, 317] and are frequently observed as depressions [329,331,334], suggesting the same interpretation here. Fig. 4.10(b) illustrates the second defect type, which is sixfold symmetric and has a flower-like appearance. By comparison with DFT calculations, we speculate this defect to be a bottom layer S vacancy [334]. STM simulations give reason to speculate the origin of type three - threefold symmetric with a protrusion in the middle - shown in Fig. 4.10 (c) to be an S divacany [335]. Defect type four in Fig. 4.10 (d) is characterised by the lack of symmetry and a surrounding decrease in apparent height in STM. Structurally similar findings have been made in the literature and have been interpreted as adsorbed impurities accompanied by a surrounding electron depletion [329, 331]. The last kind of point defect can be found frequently and is illustrated in Fig. 4.10 (e). The fingerprint of this defect is its bias dependency, upon which the structure changes, but mostly maintains threefold symmetry. Bias dependent bright protrusions of threefold symmetry have been interpreted as interstitial atoms [331, 333, 334, 336]. Whether native metal or chalcogen atoms occupy these interstitial sites is an active debate. Additionally, it has been discussed that substitutional O might be the origin of these kinds of point defects [337, 338].

Grain Boundaries

Another structural type of defects are grain boundaries, which form upon coalescence of differently oriented grains. Special interest was dedicated to mirror twin boundaries (MTB), which can be described by containing a mirror-plane along the grain boundary and have been reviewed recently [339].

Owing to the crystal structure of 2H-TMDCs, different kinds of MTBs can be formed [292]. The ones observed in MBE-grown MoS_2/Gr/Ir(111) are summarised in Fig. 4.11. In (a) a 4|4P MTB consisting of fourfold rings sharing a point at the chalcogen site [292] is shown. In STM, these MTBs appear as a double line of bright contrast, which is assigned to their extra charge. As a consequence of strong electronic correlations, a beating pattern which is close to three times MoS_2 lattice constant is observed and briefly discussed below. A sketch of their structure is shown in Fig. 4.11 (b). DFT suggests these MTBs to be chalcogen-deficient and it was proposed that they form due to low formation energies of MTBs in comparison to the isolated chalcogen vacancies [340].

Another type of MTB observed in MoS_2/Gr/Ir(111) is a 4|4E MTB, again containing fourfold rings but sharing an edge between them [292], see Fig. 4.11 (c). Their STM fingerprint is a single line of bright contrast which exhibits a beating pattern close to double the atomic spacing, again discussed below. Panel (d) illustrates the structure schematically. Though for MoS_2 the formation energy is calculated to be smaller for 4|4P (0.38 eV) than for 4|4E (0.48 eV) [339], in the system MoS_2/Gr/Ir(111), 4|4E MTBs are more frequently observed.

For the semiconducting TMDCs, the special hallmark of MTBs is the possible generation of 1D dispersing bands localising states in the band gap of the 2D material. If this band crosses the Fermi level, a one-dimensional metallic state is embedded in an otherwise insulating matrix giving rise the above-mentioned beating arising from strongly correlated physics.

In this instance, it is not *a priori* obvious what kind of physical behaviour evolves and investigations on metallic 4|4P MTBs in $MoSe_2$ on vdW substrates yield partially conflicting results regarding their

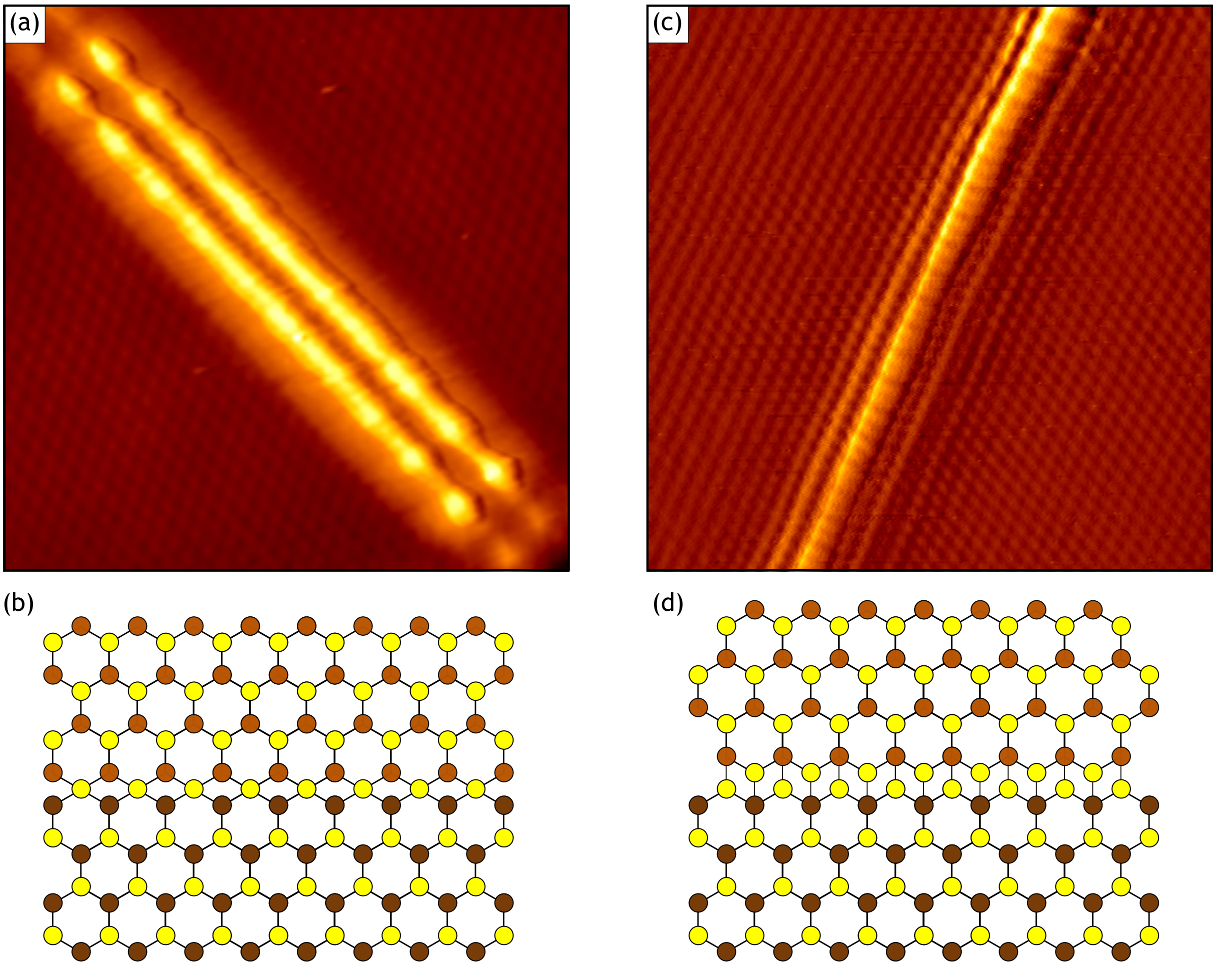

Figure 4.11: Mirror twin boundaries in MoS_2 on Gr/Ir(111): (a) STM of 4|4P type MTB. (b) STM of 4|4E type MTB. (c) Scheme of 4|4P. (d) Scheme of 4|4E.
Image information (image size, sample bias, tunnelling current): (a) $10 \times 10\ \mathrm{nm}^2$, -0.7 V, 20 pA, (b) $10 \times 10\ \mathrm{nm}^2$, -0.5 V, 60 pA.

electronic nature. The interpretations of the experimental findings reach from quantisation effects due to the finite length of the MTB [271], over Peierls type CDW phases [204] up to Tomonaga-Luttinger-liquid behaviour [205]. The latter theory is based on the assumption that the concept of single-particle fermionic excitations, which describes electrons in 2D- or 3D systems sufficiently well, breaks down in 1D. There, electrons are expected to become a strongly correlated quantum liquid with elementary excitations of bosonic nature, in which spin- and charge-degree of freedom fractionalise. This is known as a Tomonaga-Luttinger-liquid (TLL) [341–343].

The high quality and weak interaction of MBE-grown MoS_2 with its substrate Gr/Ir(111) has allowed Jolie *et al.* to perform STS investigations of the metallic 4|4E MTB with unprecedented precision to unambiguously reveal their electronic structure [306]. Low temperature dI/dV curves taken along the MTB reveal a spectrum with discrete states which are confined in the large band gap of MoS_2. Indeed, DFT predicts a 1D hole-like band to cross the Fermi-level, but a simple particle in a 1D box model fails to describe the experimental spectrum. On the other hand, a model based on TLL theory successfully describes the spectrum providing unambiguous evidence of spin-charge separation in real space. In addition, a CDW origin was also excluded, as it does not describe the spectrum sufficiently.

Though such exotic physics are interesting for fundamental research, from the perspective of electronic applications, defects and grain boundaries are usually regarded as shortcomings.

In this regard, line defects introduce electronic states which are located in the band gap. As these get populated, additional charge transfer from the substrate leads to considerable band bending between the semiconducting MoS_2 and the metallic defect [344]. For CVD-grown MoS_2 on graphite, asymmetric upward bending in the conduction and valence band has been reported leading to a decreased band gap at the grain boundary [298, 331]. In contradiction, further publications indicate the possibility of band gap broadening in the same system [345]. Within these studies, the structure of the grain boundary is often unclear and the discrepancies are further partially attributed to ill-defined samples through local impurities such as adsorbates, which come with the CVD synthesis.

Similarly here, current investigations by Murray *et al.* on band bending in MBE-grown MoS_2 on Gr/Ir(111) enjoy Ångstrom-scale accuracy due to the low interaction and clean system [322]. The investigations concern the well-defined 4|4E MTB and observe sizable upward bending of about 0.8 eV in the valence band, while the conduction band bends 0.5 eV. Furthermore, the MTB is found to act as a tunnel barrier to the charge carriers in the valence band. The holes become trapped in the resultant potential well, creating a 1D hole gas perpendicular to the MTB. The structurally different 4|4P MTB is observed to be less charged and consequently shows weaker band bending. These findings underline the importance of well-defined and decoupled systems to unambiguously investigate the local electronic landscape of defects in 2D materials.

Not only line defects introduce energy barriers, but when considering the implementation of 2D materials in functional devices, also the metal contacts bring in additional Schottky barriers. The energy barriers in these non-Ohmic contacts hinder the efficient injection into the device channel and consequently. *e.g.* in two-terminal MoS_2 devices, a large portion of the applied bias drops across the increased contact resistance and leads to performance degradation.

The Schottky barrier could be partially circumvented by a gradual transition from the semiconductor to a metal. This can be realised through deliberate local defect production which reduces the band gap. Theoretical simulations show that through choosing suitable ion beam parameters selective top layer sputtering without substantial harm to the MoS_2 lattice may be achieved [346].

Here, Valerius *et al.* make use of the high experimental flexibility of *in situ* grown MoS_2 on Gr/Ir(111) [347]. By low energy ion beam treatment, a complete amorphisation of the MoS_2 is achieved and indicated by LEED. This is accompanied by a semiconductor-to-metal transition, in which the metallic state is indicated by STS through the closing of the band gap. The process is fully reversible by subsequent annealing in vapour from FeS_2 as both the crystallinity and the band gap are fully recovered.

In conclusion, we introduced typical point and line defects in MBE-grown MoS_2 on Gr/Ir(111), briefly discuss their implications and report on recent progress enabled through the two-step MBE synthesis.

4.5 Discussion

Our presented growth study gives insight into the growth and annealing mechanisms of sulphur based TMDCs in vdWE. It is indicated that the TMDC already forms at room temperature, though the limited diffusion rate causes the islands of dendritic shapes to exhibit nearly random alignment with the crystallographic axes. This necessitates a second annealing step, in which the island reshape, become flat and compact, and epitaxially aligned. The parameters in the annealing step are crucial as they influence the outcome heavily. Annealing needs to be performed at high enough temperatures to ensure alignment and transition to compact forms, but in turn causes degradation of the islands through decomposition. At about 1050 K this decomposition can be compensated by an S background pressure, which prevents rapid degradation. If the annealing temperature is too high (1150 K), the high decomposition rate inevitably causes the synthesis to fail and only metallic clusters are left on the surface. A simple increase of the S background pressure during annealing is not advisable since it causes the growth mode to change in favour of multilayer growth.

At suitable growth parameters, the technique yields stable results and is able to grow almost closed layers with only a small amount of second layer. When simply prolonging the deposition time however, the overall alignment of the epilayer with the substrate, quickly worsens when exceeding about 0.5 ML coverage. This difficulty can be overcome by cycled growth. Here, we introduce two approaches.

In the first, equivalent growth steps can tune the growth towards epitaxially well-oriented BL growth, through which thickness-dependencies may be investigated. Since it is found that annealing in higher S pressure further enables multilayer growth, these two levers should be used simultaneously.

In the second, a first seeding cycle, in which only a small amount of highly oriented first layer islands is deposited, enables maintaining alignment at high ML coverages.

When the growth parameters are not chosen well, the growth quality is quickly lowered. In this chapter, we restrict to low S pressures in the range of $1 \times 10^{-9} - 1 \times 10^{-8}$ mbar which on the one hand facilitates the choice of growth parameters and allows us to grow particularly clean samples, but on the other hand, limits the highest growth substrate temperatures to below 500 K. When exceeding this growth temperature, the reduced S residence time has to be accounted for and requires increased S pressures. We will consider this route in Chapter 6, where we lift the restriction of low S pressures and explore the influence of high substrate temperature during growth. We foreclose that with the higher temperature the stoichiometry balance is not easily maintained and we observe the rate of intercalation to upscale quickly.

Fortunately, in the case of S intercalation under Gr, this is not inherently problematic, since S intercalation underneath Gr does not show signs for a strong electronic influence and does not significantly change the doping level of Gr, but only decouples further from Ir(111). Though this obviously decreases the growth quality in our above investigations, one has to account for different effects. There are effects which should be attributed to the S intercalation, those caused by the cycling approach and those that are caused by only partially covered Gr (which during the usual synthesis is not the case, but done here to especially allow for strong S intercalation).

It seems obvious to attribute the decreased epitaxial alignment indicated in LEED to the reduced interaction of Gr with Ir(111). Since the interaction between MoS_2 and Gr is weak, the epitaxial relation is reduced accordingly. The fact that the island shapes are elongated and thin is not obviously attributed to S intercalation. If only epitaxial ordering would be decreased, one would still expect compact shapes (with a high density of grain boundaries). This is in fact observed in the system MoS_2/Gr/Eu/Ir(111) [348]. In general, (edge-)diffusion plays an important factor in how efficient initially formed (dendritic) grain morphologies are turned into thermodynamically favoured ones such as compact forms. How this is affected by S intercalation remains unclear. Furthermore, a tremendously problematic result of the above synthesis is the high intercalation rate of MoS_2 in Fig. 4.8 in the second cycle on S intercalated Gr. It is hard to pinpoint the reason for this, but we assume the partial coverage of Gr to facilitate the intercalation. To certainly relate this to S intercalation, further investigations are needed. A closely related question is how the MoS_2 growth affects the $(\sqrt{3} \times \sqrt{3})R30^\circ$ ordering which is no longer observed after growth. Also here, further investigations have to clear the speculations.

4.6 Conclusion

Through a systematic variation of growth parameters, we provided insight into the growth and annealing mechanisms. Coarsening, reshaping, reorientation and formation of compact islands are due to island diffusion and coalescence as well as step edge diffusion. Though transition metal disulphide decomposition through S detachment and evaporation can be counterbalanced to some extent through an applied S pressure, eventually it limits the accessible temperatures for the annealing step of the synthesis.

We investigated the influence of S intercalation and find this to degrade sample quality, however, without substantial electronic changes.

Finally, we introduced defects which are common in MBE-grown MoS_2 and discussed recent progress through the presented growth technique.

CHAPTER 5

Vanadium Sulphides: Stoichiometric VS$_2$ and Sulphur Depleted Phases

*This chapter contains contributions from **J. Hall**, T. Wekking, F. Huttmann, S. Kraus, K. Ollefs, L.M. Arruda, N. Brookes, G. Schönhoff, J. Berges, K. Kummer, T. Wehling, W. Kuch, H. Wende, and T. Michely. The content of the chapter is unpublished, but parts can be found in T. Wekkings master's thesis.*

***I** developed the growth recipe and performed the growth studies, including STM and LEED measurements with the assistance of T. Wekking. **I** analysed and interpreted the data and developed the atomic models for the different monolayer phases. **I** analysed the multilayer phases and investigated the charge density wave properties. The data were discussed by **me**, T. Wekking and T. Michely.*

*Using **my** recipe, F. Huttmann and S. Kraus grew the vanadium sulphide sample during the beamtime at the ESRF, Grenoble and measured XMCD. K. Ollefs, L.M. Arruda, N. Brookes, K. Kummer, W. Kuch and H. Wende were involved in the XMCD measurements.*

T. Michely supervised all measurements.

*G. Schönhoff, J. Berges and T. Wehling contributed to a discussion (with **me**, T. Wekking and T. Michely) on the striped reconstruction of the monolayer $V_{1+x}S_2$ that was initially thought to be of charge density wave origin.*

5.1 Motivation: Interplay of Charge Ordering and Magnetism

Physical phenomena caused by strongly correlated systems, such as charge density waves [349], and high-temperature superconductivity in transition metal oxides [350] are in the focus of contemporary physics. This is in part because these systems afford an exceptional venue to uncover the behaviour of quasi-particles that cannot be described in terms of non-interacting entities, and next, because of technical exploitability as *e.g.* in colossal magneto-resistive effects [351].

In the TMDCs, metallic VX$_2$ (X = S, Se) serves as a complex laboratory for the investigation of both charge ordering phenomena (*e.g.* CDW), magnetic behaviour, and their largely unexplored interplay. VX$_2$ materials are model d^1 systems, in which their 3d electrons are significantly more localised than the 4d or 5d electrons of NbS$_2$ or TaS$_2$, rendering them candidates to host exotic correlation phenomena [48]. Although theoretical calculations indicate that the 2H structure is the thermodynamic ground state at temperatures below room temperature [52,352], experimental reports on the 2H structure remain absent while the bulk version of VS_2 and VSe_2 occur only in the 1T polytype [53, 158, 353].

In the 1T form, both materials are susceptible to structural instabilities making them attractive for the investigation of electronically ordered phases. While in VSe_2 the occurrence of a CDW phase is undisputed [47, 354–356], and even its thickness-dependence has been investigated [107, 357, 358], the situation for VS_2 is more controversial. Several contributions find experimental indications for a $(\sqrt{3} \times \sqrt{3})$R30° CDW transition at around 305 K [49, 50, 53, 359, 360]. In these studies bulk VS_2 has been prepared by deintercalation of 1T-Li_xVS_2, which has been argued to possibly affect the CDW transition by doping through residual Li. In addition, the $LiVS_2$ system has been theorised to show an ordering phase transition at 305 K [361]. In line with these arguments, CVD-grown samples and powder samples prepared under high pressure show no CDW transition at 305 K [54, 362]. Nevertheless, anomalies in the resistance vs. temperature curve were found around $120 - 150$ K and 25 K [54, 362]. Interestingly, within DFT Gauzzi *et al.* find a phonon instability at a wave vector corresponding to the aforementioned $(\sqrt{3} \times \sqrt{3})$R30° CDW [54], which is again supported by other DFT calculations [48].

The situation becomes more complicated due to the intricate V-S phase diagram, which contains various intermediate compounds (V_3S_4, V_5S_8, VS_2, and more) [363, 364] that can be easily transformed into each other by thermal annealing [365]. In a study on CVD-grown VS_2, several superstructures were found and partially attributed to V atoms self-intercalated into the vdW gap [366]. Though the study also finds $(\sqrt{3} \times \sqrt{3})$R30° superstructures in some areas, no relation to a CDW is drawn. On the other hand, peculiar extrema in resistance vs. temperature measurements around 106 K and 25 K are again associated with phase transitions related to electronic ordering [366]. It has further been demonstrated that self-intercalation of V atoms in the $V_{1+x}S_2$ compounds is sufficient to suppress CDW formation even for a small fraction x [367].

Regarding magnetic properties, both VX_2 materials show interesting phenomena. Bulk, VSe_2 is paramagnetic [160, 368, 369], and it has been argued that possible ferromagnetism is suppressed by its CDW [162], while VS_2 shows ferromagnetism [370]. When reducing the sample thickness down to a monolayer, both materials have been predicted to show magnetic behaviour [48,51]. This has indeed been confirmed for VSe_2 [108, 159], while magnetic measurements for monolayer VS_2 remain absent. However, magnetisation *versus* magnetic field curves in ultrathin VS_2 nanosheets measured with a superconducting quantum interference device revealed small hysteresis loops at room temperature [157].

The lack of measurements for VS_2 at monolayer thickness is owed to the difficulty in synthesis, and the situation does not seem promising: bulk VS_2 is a metastable material with no thermodynamic stable polymorph [53], preventing easy exfoliation; and it is further chemically unstable under ambient conditions. Hence, publications on both bulk VS_2 and its monolayer form are comparably rare.

Furthermore, bulk phase equilibria of different stoichiometric compounds have been found plentiful, suggesting this diversity to be maintained down to the monolayer limit.

Recently, monolayer vanadium sulphides have been fabricated using a well-established synthesis method on Au(111) [55]. Although a stoichiometric monolayer VS_2 phase has been achieved, this phase is thermally unstable, and readily transforms to sulphur-depleted phases when heated inside UHV without any additional sulphur supply. Two novel vanadium-sulphide phases have been grown in this way. The most sulphur deficient one displays a striped appearance and has been explained by an ordered sulphur vacancy row array. Due to the strong interaction with the metallic substrate, neither a CDW phase nor magnetic behaviour was observable. A very similar striped pattern has been recently found in isotypic monolayer VSe_2/HOPG [371]. In both VS_2/Au and VSe_2/HOPG systems, the striped pattern was shown to be transformable to a non-chalcogen-deficient phase by low-temperature annealing in chalcogen vapour.

Only the growth of stoichiometric monolayer VS_2 on weakly interacting substrates can give unambiguous results on CDW phases and the magnetic properties of the material. Here, we make use of the two-step MBE synthesis developed in this thesis and grow layers of vanadium sulphides on the inert Gr/Ir(111) substrate and aim to clarify some of the above mentioned issues. We will demonstrate that the growth is indeed challenging and that a multitude of mono- and multilayer stoichiometric VS_2 and non-stoichiometric phases can be stabilised. If the stoichiometry of the grown phase is unclear or unimportant for that matter we refer to general vanadium sulphides as $V_{1+x}S_2$ to indicate the close connection to the parent material VS_2.

In the second section, we consider monolayer $V_{1+x}S_2$, for which three stable phases including stoichiometric VS_2 and two with certain levels of sulphur depletion are observed and explained by atomic models. The most sulphur depleted phase also shows striped patterns and it is discussed in detail. In neither of the phases, we find indications for a CDW.

Depending on the synthesis parameters, we find a sharp transition between mono- and multilayer morphology, and also possible tuning to 1D structures, which we document in section three. The multilayer VS_2 is detailed in the fourth section and shows a $(\sqrt{3}\times\sqrt{3})$R30° CDW phase transition at around room temperature, and is locally influenced by 2×2 self-intercalation, that occurs at elevated temperatures. In the fifth section, we discuss preliminary XMCD results that do not show indications for magnetic behaviour in the prepared samples. The possible reasons for this are discussed.

5.2 Monolayer Vanadium Sulphides

Similar to VS_2/Au(111), the synthesis of stoichiometric VS_2 on Gr/Ir(111) is challenging and the system turns out to exhibit numerous stable phases of different stoichiometry. After the usual second step of the synthesis - *i.e.* annealing - when the sample is exposed to elevated temperatures, phase transitions between $V_{1+x}S_2$ polymorphs occur. Three stable crystalline monolayer phases have been observed. We first follow the evolution of the observed structures with increasing temperature in

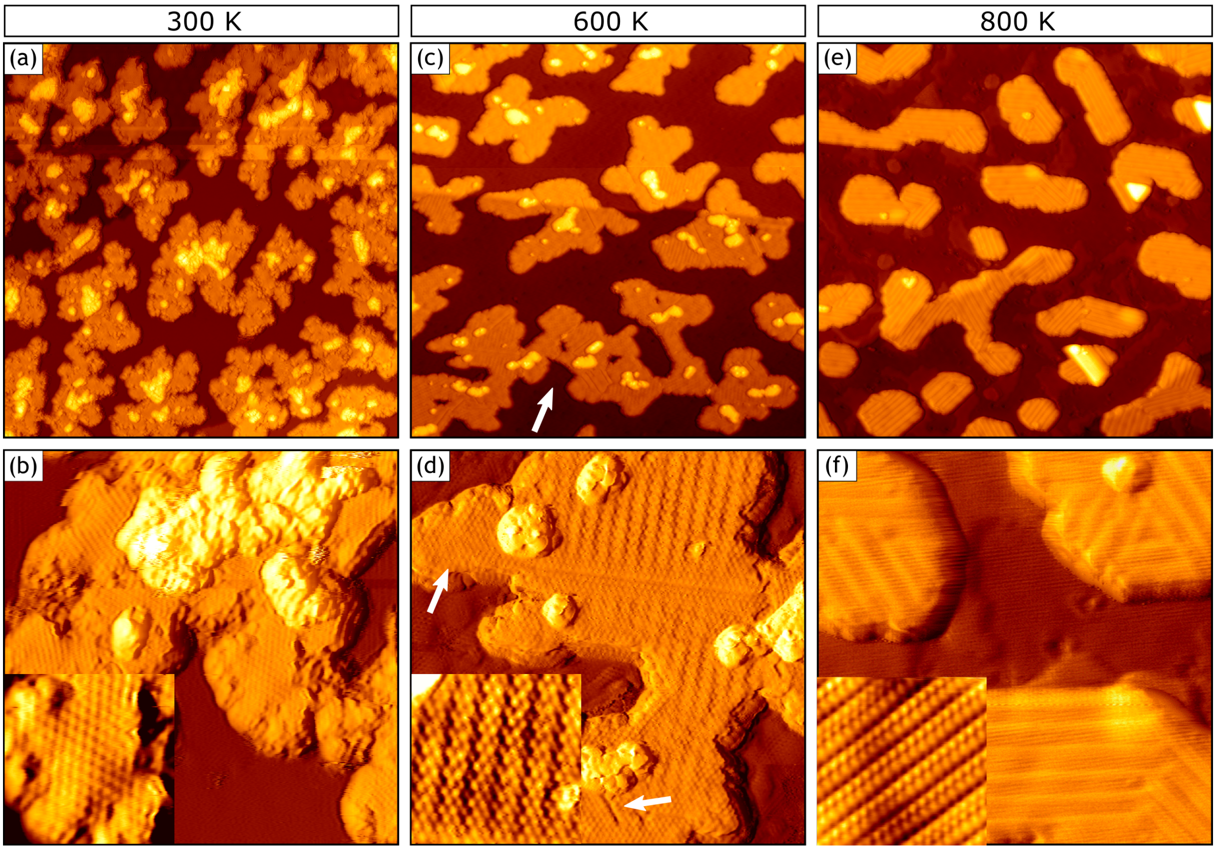

Figure 5.1: Evolution of $V_{1+x}S_2$ phases with temperature: (a) Sample morphology directly after deposition at 300 K. (b) STM close-up showing ML islands with hexagonal lattice (increased in inset) and ill-defined second layer. (c) After annealing to 600 K regular superstructures can be found in certain areas. Arrow in (c) marks islands connected to a network. (d) Close-up of one island showing partially superstructure-free areas (arrow on the left) large superstructured parts (increased in inset). Arrow at the bottom marks a dark row along close-packed row. (e) Annealing to 800 K causes a striped phase to develop. (f) Close-up showing domains of stripes on islands (increased in inset) The images are each a superposition of STM topographs and their derivative to enhance the visibility of atomic structures while keeping topographic information.
Image information (image size, sample bias, tunnelling current): (a) $80 \times 80\ \text{nm}^2$, -1 V, 0.2 nA, (b) $20 \times 20\ \text{nm}^2$, -0.8 V, 0.2 nA, (c) $80 \times 80\ \text{nm}^2$, -1 V, 0.1 nA, (d) $20 \times 20\ \text{nm}^2$, -0.8 V, 0.5 nA, (e) $80 \times 80\ \text{nm}^2$, -1.2 V, 10 pA, (f) $20 \times 20\ \text{nm}^2$, -1.2 V, 10 pA, insets $6 \times 6\ \text{nm}^2$ are zooms.

Fig. 5.1, and afterwards discuss each structure in greater detail, especially elaborating on the striped pattern.

The sample morphology directly after the growth step, *i.e.* without any annealing, is displayed in Fig. 5.1 (a) and (b). As we will justify below, we interpret the observed structures to be stoichiometric VS_2. The large scale image in (a) shows the VS_2 of about 60 % surface area coverage[1] and height 7 Å to exhibit dendritic island shapes similar to the ones observed for MoS_2 (cf. section 4.2) directly after

---

[1] The coverage will be grossly overestimated by the STM due to the fractal geometry of the island. When annealing to 600 K, the islands become more compact and the coverage is determined to be 50 %.

deposition. Besides extended monolayer parts, also second layer heights of 14 Å are apparent, and can be found on about every island. Their coverage amounts to about 10 % surface area. Although the dendritic VS_2 islands can be found uniformly scattered over the sample surface, they appear to align with the substrate step edges as it is visible in the bottom right corner of Fig. 5.1 (a).

Figure 5.1 (b) shows a close-up of an island. On the atomic scale, which is shown in the inset at enhanced contrast, the monolayer shows extended parts with hexagonal ordering of periodicity (3.4 ± 0.2) Å, which compares well with the lattice parameter of bulk 1T-VS_2 [353,366] and justifies the assignment of the observed hexagonal lattice to stoichiometric ML VS_2. At this stage no point defects are visible and the island edges appear noisy. This may be related to adsorbed excess sulphur. The second layer does not display a uniform height, appears cloudy and does not show atomic resolution.

After annealing to 600 K, see the overview in Fig. 5.1 (c), the monolayer islands become more roundish (cover around 50 % of surface area), but are still without straight edges or hexagonal forms. In some parts, a monolayer network starts to form, which is indicated by the white arrow. Already in the large scale image, local disturbances of the monolayer surface are recognisable. Both the area of the second layer islands and their number density have decreased and now cover around 5 % of the sample surface in more compact shapes.

On the atomic level, which is illustrated in Fig. 5.1 (d), the structure changed considerably and we note four distinct features.
(i) On the far left-hand side still intact hexagonal ordering can be seen marked by a white arrow. Noting that the periodicity again amounts to (3.4 ± 0.2) Å, we ascribe this to stoichiometric VS_2.
(ii) Moving to the right, a pattern consisting of parallel beats covers the upper part of the island and is enhanced in the inset. The lines have average (non-equidistant) spacing of about (8.0 ± 0.2) Å and the dots of about (5.5 ± 0.2) Å. We will refer to this phase as *'parallel-beats-phase'*.
(iii) Below that, a horizontal line crosses the island, under which the parallel beats continue. The nature of the horizontal line is hard to pinpoint and a grain boundary or a dislocation are possible causes.
(iv) At the bottom of the island, an arrow marks a dark line following one close-packed direction of the hexagonal lattice, which we interpret as a sulphur vacancy row being the herald of the phase fully encountered at 800 K.

Further annealing to 800 K changes the sample morphology as depicted in Fig. 5.1 (e). On the large scale, the islands become compact, but often remain elongated and hexagonally oriented edges start to form. The surface coverage amounts to 40 %. On the monolayer, a striped pattern evolves and often more than one orientation of these stripes can be found on one island. The average periodicity of the stripes amounts to (10.6 ± 0.2) Å. We will refer to this phase as *'striped phase'*. Regarding the second layers, we note that a large fraction of second layer islands have vanished and the remaining ones (about 1 % surface area) epitaxially orient with their respective first layer. Also, a high amount of intercalated structures can be found around and below the islands, which we reason to be the cause of the decreased surface coverage of the sample.

On a closer look, in Fig. 5.1 (f), the striped pattern often shows irregular spacing, though preferred widths are observable. Point defects are not visible anymore and resolving the atomic structure allows recognising atomic rows with hexagonal ordering separated by seemingly missing rows. The details of this structure will be discussed in a separate section.

On the discussion of the origin of the observed superstructures: considering our findings of Section 3.3, in which we demonstrate the quasi-freestanding nature of TMDC islands on Gr/Ir(111), we, first of all, do not consider strain as an origin of the superstructures. The possibilities we consider are:
(A) Thermal decomposition of the islands and a consequent regular pattern of sulphur vacancies similar to the findings in the systems VS_2/Au(111) and VSe_2/HOPG.
(B) The annealing causes the metal V to self-intercalate in regular patterns. This might still go along with sulphur deficiency and thermal decomposition.
(C) The metastable 1T-VS_2 has been transformed to a thermodynamically more stable phase similar to a distorted 1T' polymorph.
(D) The patterns observed do not have a pure structural origin, but rather are a consequence of electronic effects such as a CDW.

(D) Noting that the images are all taken at 300 K and that the temperature-induced superstructures differ only depending on the highest annealing temperature, we regard a purely electronic origin of the superstructures as unlikely. For the parallel-beats-phase, it is unlikely to observe a CDW in some areas of the sample whilst it is absent in other defect-free areas. Regarding the striped phase, it is also unlikely to observe a CDW which develops irregularly spaced stripes. (C) We consider a simple distorted 1T' structure as the reason for the superstructures questionable. Concerning the parallel-beats phase, a varying dimerisation - trimerisation transition is needed to explain the non-equidistant rows. If not for additional influences, this scenario seems thermodynamically unlikely. As for the striped phase, although a di- or trimerisation of metal rows in a distorted 1T' structure could locally explain the irregular striped pattern, more than a simple uniform distortion is needed to explain the random transition of line spacings. (B) Regarding self-intercalation: although self-intercalation is known to happen in $V_{1+x}S_2$[2], this is ruled out as the sole origin of the superstructures due to precise calibration experiments, in which the amount of deposited V corresponds to the expected area covered by unintercalated VS_2 in samples which are completely in the striped phase. It is further noted that: firstly, the apparent height measured in STM deviates only slightly for the three monolayer phases, and secondly, the moiré of Gr/Ir(111) is always visible, while in intercalated systems, the height is generally expected to increase and the moiré corrugation to decrease. (A) We, therefore, interpret the temperature-induced phase transitions mainly as a result of thermal decomposition of the islands and the stability of a large number of phase equilibria in the V-S system. This, however, does not categorically exclude the possibility of consequential lattice deformation or local V self-intercalation.

---

[2] The bulk polymorph V_5S_8 can, for example, be interpreted as VS_2, in which additional V atoms are arranged in a 2×2 superstructure inside the vdW gap separating two VS_2 layers.

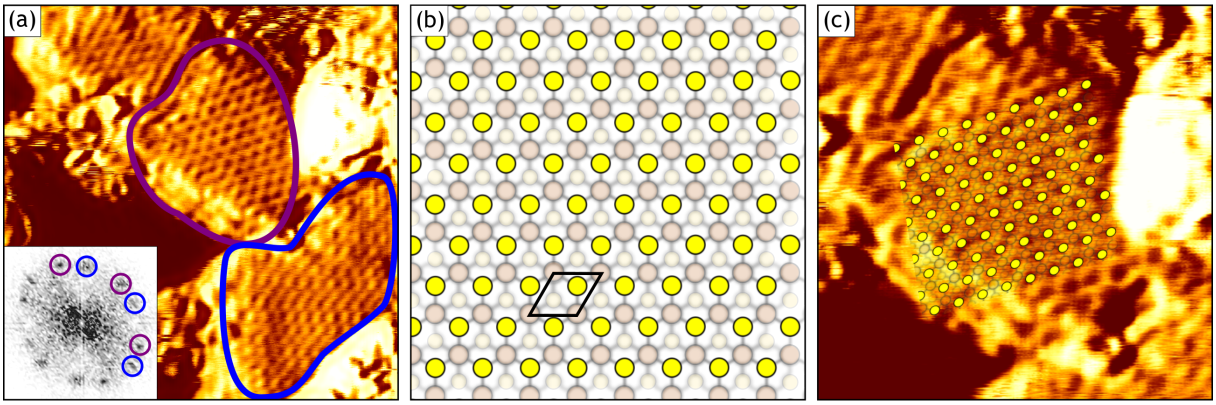

Figure 5.2: Stoichiometric monolayer VS_2: (a) STM topograph showing rotated domains, which are marked by colours. Inset: corresponding FT with colour coded circles indicating peaks corresponding to the different grains. (b) Model of the 1T phase. The unit cell is indicated. The bottom and top sulphur layers are illustrated by faint and full yellow circles, while V atoms are depicted faintly in red. (c) Model superimposed on enlarged STM topograph.
Image information (image size, sample bias, tunnelling current): (a) 10×10 nm^2, -1 V, 0.1 nA, (c) 6×6 nm^2, zoom of (a).

Stoichiometric VS_2

Directly after deposition at 300 K stoichiometric monolayer VS_2 is present on the sample, which is illustrated in Fig. 5.2. The islands are not large and only small patches of hexagonal ordering with a periodicity of (3.4 ± 0.2) Å can be identified as shown in panel (a). In the STM topograph, in the upper grain the contrast shows pronounced dark depressions, whereas in the structure on the right-hand side, the contrast is dominated by bright protrusions. This inverted contrast points to very roughly oppositely oriented grains. The Fourier transformation (FT) in the inset illustrates that the grains are rotated by about 150° and shows no reliable indications for any superstructure.

The question, if the monolayer comes in the 1T or 2H polytype cannot be answered by STM alone. Several aspects give reason to believe that in the MBE-grown layers the 1T structure is adopted: the bulk counterpart only exhibits the 1T phase, and no experimental indications for the 2H phase, neither in bulk nor in ML have yet been published. When grown on Au(111) by a similar growth approach, also the 1T structure is observed [55]. Additionally (though not as strong an argument), DFT calculations show that the 2H polytype tends to have a smaller lattice constant of about $3.16 - 3.21$ Å compared to the 1T structure of about $3.17 - 3.33$ Å [372], while we measure (3.4 ± 0.2) Å. Due to these reasons, we illustrate this phase in Fig. 5.2 (b). In (c), the schematic lattice is placed on top of a close-up of (a).

We note that the monolayer VS_2 does not show reliable indications of a CDW phase, which is observed in bulk VS_2 below 305 K [50]. Reasons for the absence of a CDW phase in ML VS_2 may be a thickness-dependent decrease of the CDW transition temperature or poor sample quality. We note that after mild stepwise annealing to 400 K and 500 K, when slow conversion of the dendritic islands to more compact shapes is observed, no CDW is identifiable.

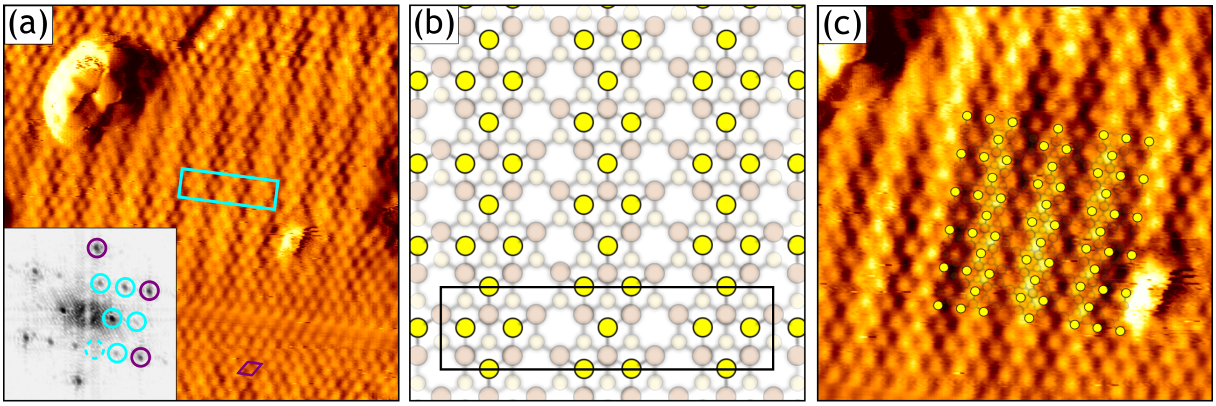

Figure 5.3: Regular superstructure in monolayer VS_2: (a) Derivate of STM topograph illustrating the pattern. The atomic lattice and superstructure unit cells are indicated in violet and turquoise, respectively. Inset: corresponding FT, with circles indicating peaks to the colour-corresponding unit cell. Dashed circles indicate symmetry expected peak positions, even though the intensity is small. (b) Model of the pattern forming the observed $7 \times \sqrt{3}$ superstructure. (c) Overlay of the model on the STM data from (a). Image information (image size, sample bias, tunnelling current): (a) $10 \times 10\ \text{nm}^2$, -1 V, 1 nA, (c) $6 \times 6\ \text{nm}^2$, zoom of (a).

Vacancy Beats

When exposing the sample to elevated temperatures the surface develops superstructures. Already after 400 K the first small patches are introduced, and after 600 K a regular pattern evolves over large parts of the sample surface, which is illustrated in Fig. 5.3. The nature of the pattern is ambiguous and we will describe it first geometrically. At a larger scale the pattern resembles parallel beats which are separated by about (8.0 ± 0.2) Å and have an in-line periodicity of (5.5 ± 0.2) Å.

The structure is shown in high-resolution in panel (a), the inset shows the FT. In the interior of the structure, a peculiar contrast is present in which single atomic sulphur sites are imaged at lower apparent height encircled by a dark surrounding. Interestingly, going toward the horizontal defect line at the bottom of the image, the contrast fades and rather smoothly turns into non-superstructured hexagonal ordering. The sites making up the superstructure arrange in a rectangular pattern with a large $7 \times \sqrt{3}$ unit cell, which is indicated in the model in panel (b). Here, a regular 1T structure with a vacancy superstructure is shown. The unit cell stoichiometry reads $V_{14}S_{23}$ and is undocumented in the literature. In (c), this model is placed on top of the STM data and reproduces the pattern well.

As mentioned above, the nature of the superstructure remains ambiguous. As the moiré is still visible we exclude the possibility of extended V atom intercalation. The introduction by thermal annealing and the fact that the structure is locally formed, while other areas remain stoichiometric, points to the possibility of vacancy ordering. As indicated in the model, the vacancy creation causes under-coordinated V trimers to form. Whether they form additional bonds and therefore cause the state visible in STM at the vacancy site remains unclear. It is furthermore not *a priori* clear why the contrast merges continuously into regular hexagonal ordering.

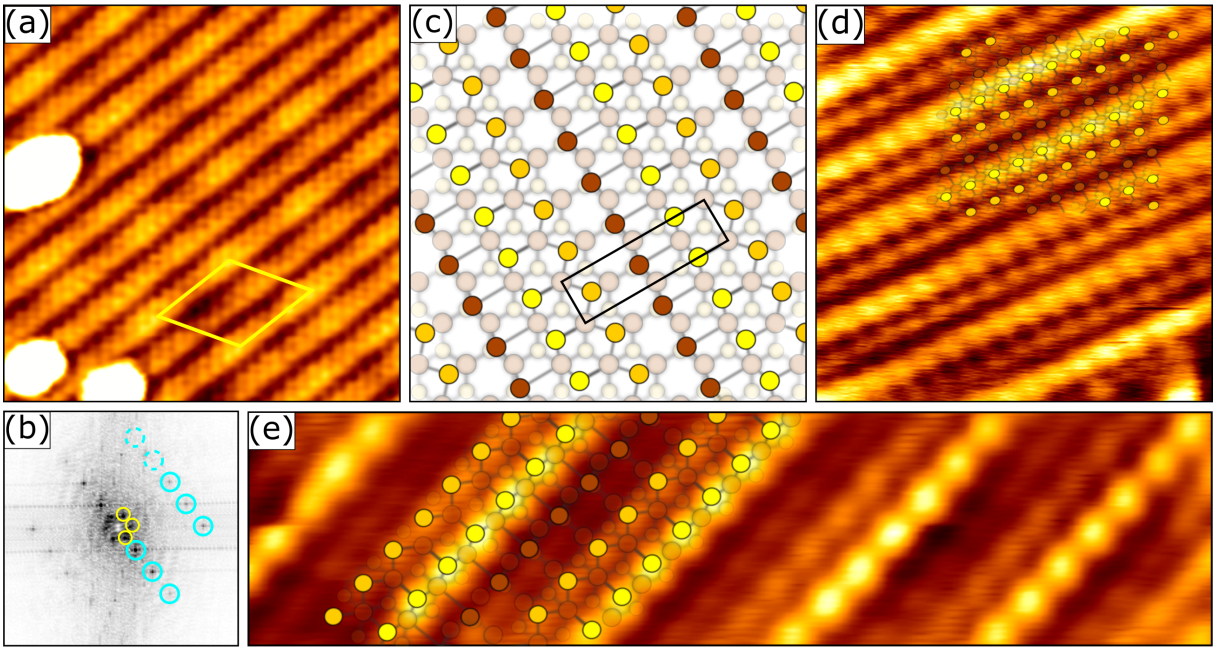

Figure 5.4: Striped reconstruction of monolayer $V_{1+x}S_2$: (a) STM topograph illustrating striped phase. The moiré unit cell is indicated and adsorbates are visible. (b) Corresponding FT, with circles indicating peaks related to the moiré (yellow) and stripes (turquoise). Dashed circles indicate symmetry expected peak positions, even though the intensity is small. (c) Atomic model of the reconstructed surface. Only the top sulphur layer is redrawn, the V atom and bottom S plane are generic to the 1T phase. (d) STM contrast mode only showing two rows with atomic resolution. (e) High-resolution STM topograph showing all three rows and the rectangle formed by neighbouring S atoms in the lowest and second lowest row.
Image information (image size, sample bias, tunnelling current): (a) $10 \times 10\ \text{nm}^2$, -0.3 V, 0.5 nA, (d) $5 \times 5\ \text{nm}^2$, 0.01 V, 2 nA, (e) $7 \times 2\ \text{nm}^2$, -0.1 V, 0.5 nA.

Reconstructed Striped Phase

Above 800 K, the $V_{1+x}S_2$ island surface transforms to a phase presented in Fig. 5.4. In (a), an overview of evenly distributed rows is visible, which form the reconstructed surface of the former VS_2 monolayer. On the left-hand side and bottom corner adsorbates are visible, which often accompany the striped reconstruction. As also visible in the FT in (b), the moiré of Gr/Ir(111) is still visible and the stripes align with it, which is owed to the epitaxial relation between the epilayer and substrate.

This most sulphur depleted stable monolayer phase is interpreted to originate from average desorption of every third sulphur row and an accompanying deformation of the atomic lattice. Fig. 5.4 (c) shows the proposed model of the reconstructed surface with the unit cell indicated. As a result of vacancy row creation, in two particular adjacent rows neighbouring sulphur atoms form a rectangle. This lowers the symmetry of the former hexagonal system, and the unit cell becomes rectangular. By a careful analysis of multiple STM images, and in comparison to the moiré of Gr/Ir(111), the unit cell dimensions are measured to be (3.4 ± 0.1) Å along its short axis and (10.6 ± 0.1) Å along its long axis. Since STM alone is not able to infer reliable geometric information on the V and bottom S atomic plane, in the model these are of generic 1T structure. The reconstruction is nonetheless

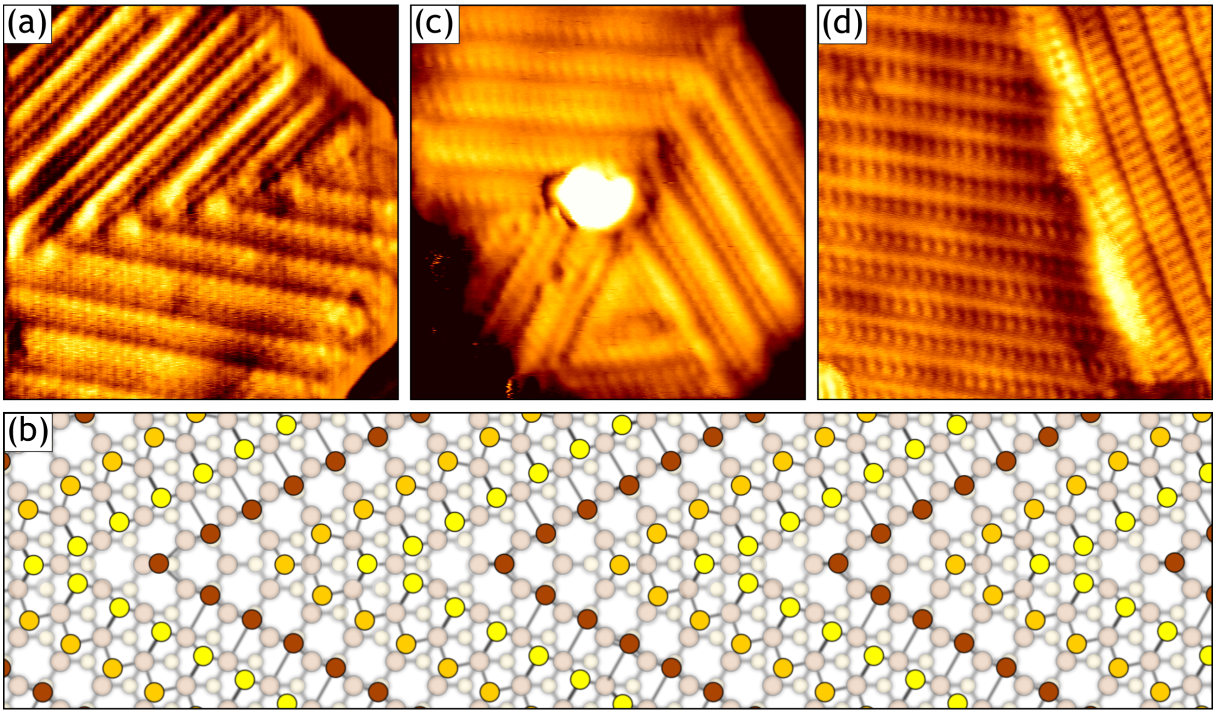

Figure 5.5: Different domains of striped reconstruction of monolayer $V_{1+x}S_2$: (a) STM topograph showing two domains which meet under an angle of 60°. (b) Atomic model of the domain boundary in (a). Note that all S atoms are threefold coordinated, leaving some V atoms under-coordinated. (c) Three domains meeting close to an adsorbate. (d) Two domains meeting under an arbitrary angle due to grain rotation.
Image information (image size, sample bias, tunnelling current): (a) 10×10 nm^2, -900 V, 50 pA, (c) 10×10 nm^2, -900 V, 50 pA, (d) 10×10 nm^2, 0.02 V, 0.4 nA.

assumed to also affect the bottom planes of the lattice. We point out that every sulphur atom is threefold coordinated, which causes some V atoms to be under-coordinated. Since V may also assume an oxidation state of 3+, this structure is still stable. The stoichiometry of this phase amounts to V_4S_7 – a phase which is again undocumented in the literature.

We speculate the apparent height differences in STM, which pronounce the 3×1 superstructure on top of the reconstructed $V_{1+x}S_2$ lattice, to result from both electronic and geometric height modulation. This speculation is supported by AFM scans showing height corrugation in the similar system VSe_2/HOPG [371].

In the STM topograph in (d), the atomic resolution of the rows suggests that the lowest sulphur row remains invisible; an STM contrast mode which is often observed when imaging this $V_{1+x}S_2$ phase. Only rarely, all three sulphur rows are imaged as it is the case in the high-resolution image in (e).

It is interesting to note that within elongated single-crystalline islands, usually an orientation of the stripes along the island is observed. A close look at the reconstructed atomic lattice model in Fig. 5.4 (c) allows to infer this - in a naive simple picture - as a consequence of the under-coordination of the V atoms through S removal. Thus, S row formation parallel to lattice termination seems energetically most favourable due to the least amount of dangling bonds. As the islands grow with promoted epitaxial orientation, the island edges grow mostly straight and both the island edge and the stripes align with the moiré of Gr/Ir(111).

If the symmetry is broken due to defects such as vacancies or adsorbates, different domains of stripes that meet at an angle of 60° are present on one island, which is displayed in Fig. 5.5. In (a), a regular extended domain boundary is shown. In STM, atomic resolution of the domain boundary structure is difficult, which is in part owed to the typical contrast mode only allowing two of the three sulphur rows to be visible. As a consequence, no definite atomic structure has been observed, but a model of the domain boundary is proposed in Fig. 5.5 (b). Every S atom is threefold coordinated, which leaves some V atoms under-coordinated and likely causes the additional charge visible as periodic bright protrusions along the domain boundary in the STM topograph. Fig. 5.5 (c) shows an island where an adsorbate influences the formation of different domains, which meet under symmetric conditions. If the symmetry is further broken and the underlying lattice is not continuous as, for example, in poly-crystalline island structures, stripe domains may meet under arbitrary angles depending on relative grain orientation. This is shown in Fig. 5.5 (d).

A few interesting remarks can be made when discussing how the striped phase can be achieved experimentally, which we do here in two ways:

(i) After the growth step at comparably lower temperatures, the sample can be quickly heated up to about 850 K without any sulphur background. Typically, the synthesis outcome is then well represented by Fig. 5.1 (e), *i.e.* clean islands and strong intercalation structures. We interpret the high intercalation rate as a direct result of the high temperature at low S background: when the sample is exposed to high temperature, the rapid decomposition and re-evaporation of S into the vacuum enables V atoms to intercalate below Gr at a high rate. We speculate this to happen through a reactive passage, *i.e.* the Gr is being defected. The increased defect rate, on the other hand, enables highly mobile S not only to desorb but to also intercalate. These processes repeat themselves and the sample is left with ill-defined strong intercalation.

To prevent the high intercalation rate, annealing to lower temperatures is advisable. This, however, comes at the downside of irregular stripe formation, as often not strictly every third S row is removed, but stochastically only every fourth or fifth, as in the inset of Fig. 5.1 (f). This is obviously detrimental for reproducibility.

(ii) As demonstrated in Section 4.2, in the usual two-step synthesis approach, the sample is annealed at high temperature in a sulphur background pressure to compensate for S loss. In the V-S system, this does not work reliably and the synthesis outcome after sample annealing at 850 K in S vapour is illustrated in Fig. 5.6. In (a), an overview topograph of a sample with purely monolayer thickness and no intercalation is shown. Due to the low growth temperature of 150 K, which facilitates local S excess, the islands connect to a network similar to the case of MoS_2 in Fig. 4.3. The surface of the islands, on the other hand, is not clean but covered in adsorbates, which arrange along domains of

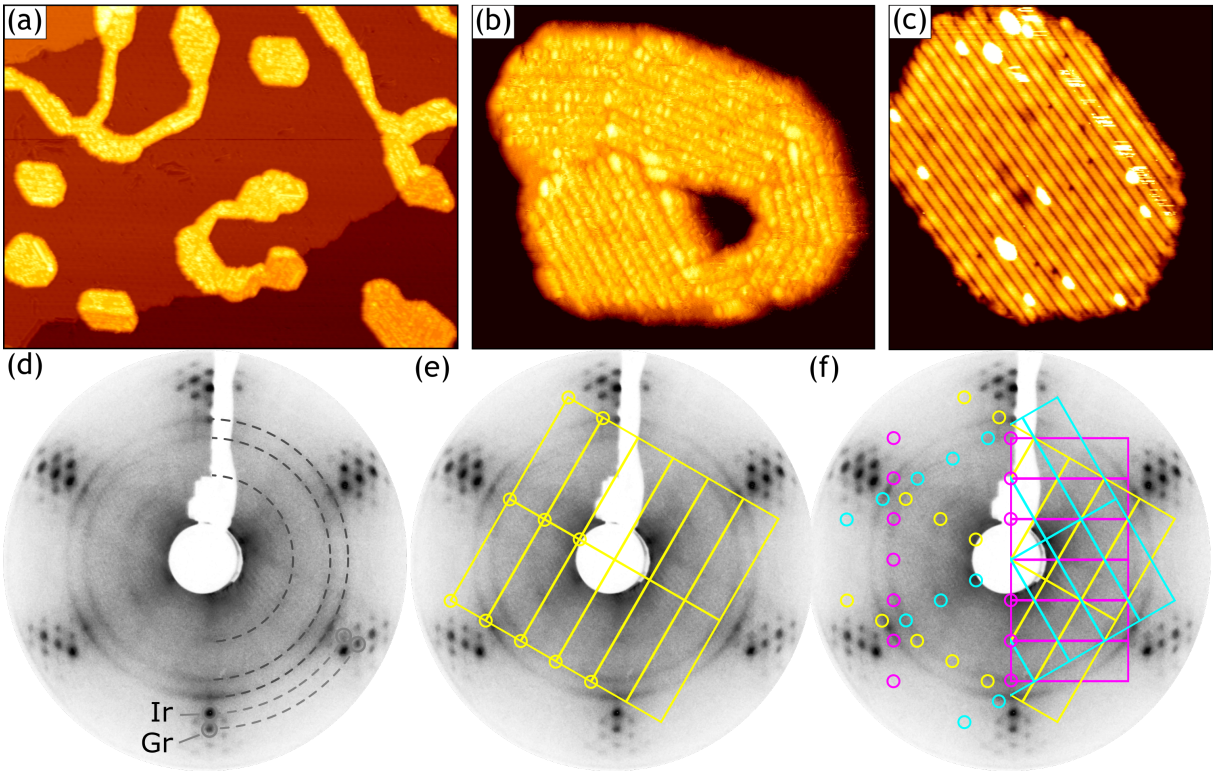

Figure 5.6: Adsorbates on reconstructed $V_{1+x}S_2$: (a) STM overview of ML reconstructed $V_{1+x}S_2$ which are covered in adsorbates from the synthesis. The growth step was performed at low temperature $T^g = 150$ K, which causes the elongated structures. (b) Close up of an adsorbate covered island. (c) Island surface after quick heating to 600 K. Most of the adsorbates have desorbed. (d) LEED pattern of the sample after flash annealing to 600 K. Besides Gr/Ir(111) and its moiré, three rings form the diffraction pattern of the reconstructed $V_{1+x}S_2$ islands. (e) LEED overlaid with the reciprocal lattice of one reconstructed domain. The circles mark the position of the diffraction spots. (f) The entire LEED pattern explained by rotated domains, where on the lefthand side only the circles marking the diffraction spot position are shown for clarity. The LEED pattern is reproduced through overlap of several rotationally misfit domains.
Image information (image size, sample bias, tunnelling current): (a) 160×120 nm^2, -1 V, 50 pA, (b) 35×30 nm^2, -0.5 V, 10 pA, (c) 30×30 nm^2, -0.3 V, 20 pA.

stripes, as shown in (b) in more detail. We conclude that though the additional supply of S prevented strong intercalation, decomposition and reconstruction of the lattice still takes place.

Since the adsorbates arise after annealing in S vapour, it seems obvious to interpret them as adsorbed S atoms or dimers. It seems that the surface is not sufficiently passivated as the surface of 2D materials is usually chemically inert and after usual synthesis of MoS_2 and TaS_2 no S is observed on the surface of the grown TMDCs. On the one hand, this might be exploited *via* functionalisation in patterning [371], on the other hand, it is not a priori obvious, what additional annealing results in. There is firstly the possibility of reincorporation of the S adsorbates into a stoichiometric VS_2 lattice, as shown for VS_2/Au [55] and VSe_2/HOPG [371]. Secondly, simple desorption of the adsorbates may happen resulting in the cleaning of the islands. Thirdly, the metastability of the system might cause another transition into another thermodynamically more stable phase.

When quickly heating the system in Fig. 5.6 to 600 K, the island surface transforms into the one shown in (c). The adsorbates have mostly desorbed from the surface leaving a comparably clean pattern on top of the moiré behind. Additionally, a small amount of point defects becomes visible, and their appearance as dark depressions suggest them to be S vacancies. Notably, no reincorporation of S into the lattice has taken place.

As a consequence of S adsorbate desorption, in electron diffraction a regular pattern becomes visible. Although in the LEED data shown in Fig. 5.6 (d) the low growth temperature is detrimental to the epitaxial relation, clear features can be detected. Going from outside to inside, firstly the Gr and Ir spots and their associated moiré is visible. Following, three rings with increased intensity along epitaxial directions form the diffraction pattern of the reconstructed $V_{1+x}S_2$ islands. Panel (e) illustrates how the pattern evolves from the reciprocal space lattice of a single domain of the reconstructed $V_{1+x}S_2$ and in (e) three principal domains are overlaid on the LEED pattern, which emerges from the rotation of each reciprocal lattice.

We also tried to transform the striped phase back into stoichiometric VS_2 by low-temperature annealing in sulphur vapour, by which the metastability of this phase becomes evident. Instead of stoichiometric monolayer islands, multilayer islands are observed on Gr/Ir(111), which are discussed in detail in Section 5.4.

In conclusion, three monolayer vanadium-sulphur phases have been observed and can be transformed - up to now irreversibly - into each other by thermal annealing. The first is stoichiometric hexagonal VS_2, which does not show indications for CDW formation. The second is $V_{14}S_{23}$, which shows a regular vacancy pattern of centred rectangular symmetry. The third has a stoichiometry V_5S_7 and comes with a reconstruction of the atomic lattice to rectangular symmetry.

5.3 From Monolayer to Multilayer

The diversity of stable phases of $V_{1+x}S_2$ does not restrict itself to monolayer regimes and the influence of growth parameters on the stabilisation of different phases is not well understood. In the following, the influence of selected growth parameters, which have a distinct action on the system of $V_{1+x}S_2$ are presented and a brief overview of non-phase pure systems will be given.

Annealing Temperature: From 2D to 1D

The sulphur loss associated with elevated temperatures leads not only to vacancy superstructures but rather indicates the metastability of the VS_2 phase by a quick transition to a thermodynamically more stable phase. In that regard, the striped sulphur vacancy row phase found in monolayer $V_{1+x}S_2$ is also not stable and readily transforms into elongated crystallites as illustrated in Fig. 5.7 when going to higher temperatures.

In panel (a), an overview over a formerly pure monolayer sample after annealing at 900 K in sulphur vapour is given. Besides the formation of small close to triangular-shaped bilayer islands, elongated

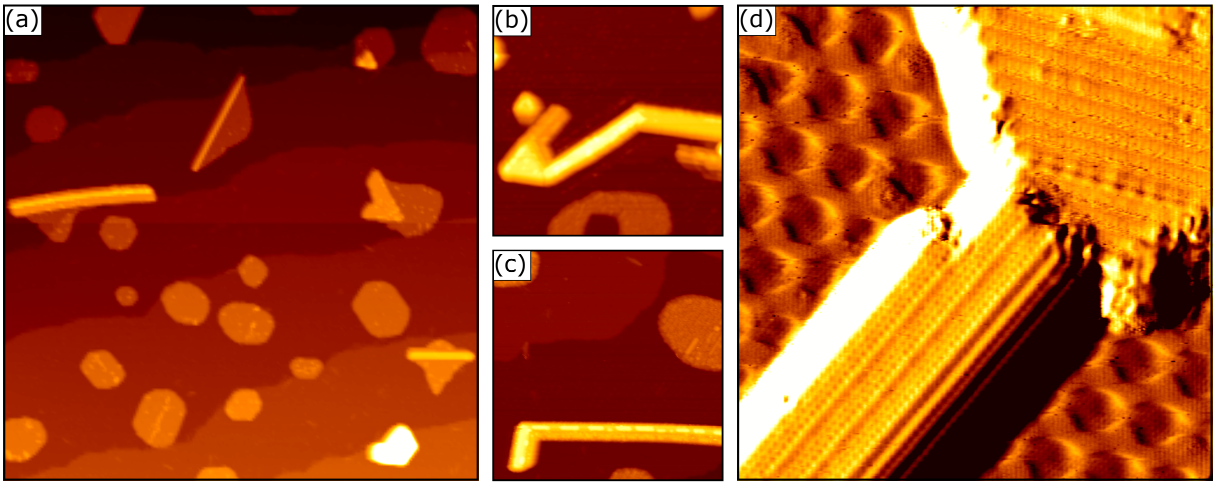

Figure 5.7: 1D crystallites of $V_{1+x}S_2$: (a) After exposure to 900 K, 1D crystallites form at the edges of formerly ML $V_{1+x}S_2$. (b), (c) Solitary 1D structures which show apparent heights of several nm. (d) At the atomic scale again striped reconstructions are visible reminiscent of the striped ML phase.
Image information (image size, sample bias, tunnelling current): (a) $250 \times 250\,\text{nm}^2$, -0.3 V, 20 pA, (b) $80 \times 80\,\text{nm}^2$, -0.4 V, 10 pA, (c) $80 \times 80\,\text{nm}^2$, -1 V, 10 pA, (b) $20 \times 20\,\text{nm}^2$, -0.08 V, 0.4 nA.

bright structures form at the edge of an island strongly resembling rolled-up layers. Owing to their increased height of about $2 - 2.5$ nm (which varies due to adsorbate coverage), but low surface contact area to the Gr, these structures are easily dragged over the surface or picked up by the STM tip under proper tunnelling conditions.

In (b) and (c), single, free-standing crystallites, which are not connected to any residual monolayer are shown. In STM, these structures have an apparent height of up to 3 nm and are again covered in adsorbates, which arrange periodically. This indicates a lattice rearrangement similar to the one observed for ML and may also be resolved atomically as shown in (d). Here, the clean multilayer of 16 nm height shows striped ordering reminiscent of the monolayer analogue.

V/S Ratio and Coverage: From 2D to 3D

Another critical parameter in the synthesis of $V_{1+x}S_2$ on Gr/Ir(111) is the deposition time, which unexpectedly induces a growth mode change, when a certain value is overcome. As we will discuss in the following the critical deposition time is not universal, but related to the remaining synthesis parameters, especially the ratio of V to S flux. In the case shown in Fig. 5.8, the critical deposition time is around $3 - 6$ min, leading to an equivalent critical coverage of $45 - 90\,\%$ monolayer surface coverage.

As visible in panel (a), under reference growth conditions stated in Section 2.6 except for $t^{\mathrm{g}} = 60\,\mathrm{s}$, compact stripe-reconstructed ML islands cover about 15 % of the sample surface.

Enhancing the deposition time to $t^{\mathrm{g}} = 180\,\mathrm{s}$, but keeping all other synthesis parameters the same, causes a sample morphology as illustrated in Fig. 5.8 (b). The total surface coverage is about 20 % and multiple island structure types and heights can be found. As indicated in the line profile at

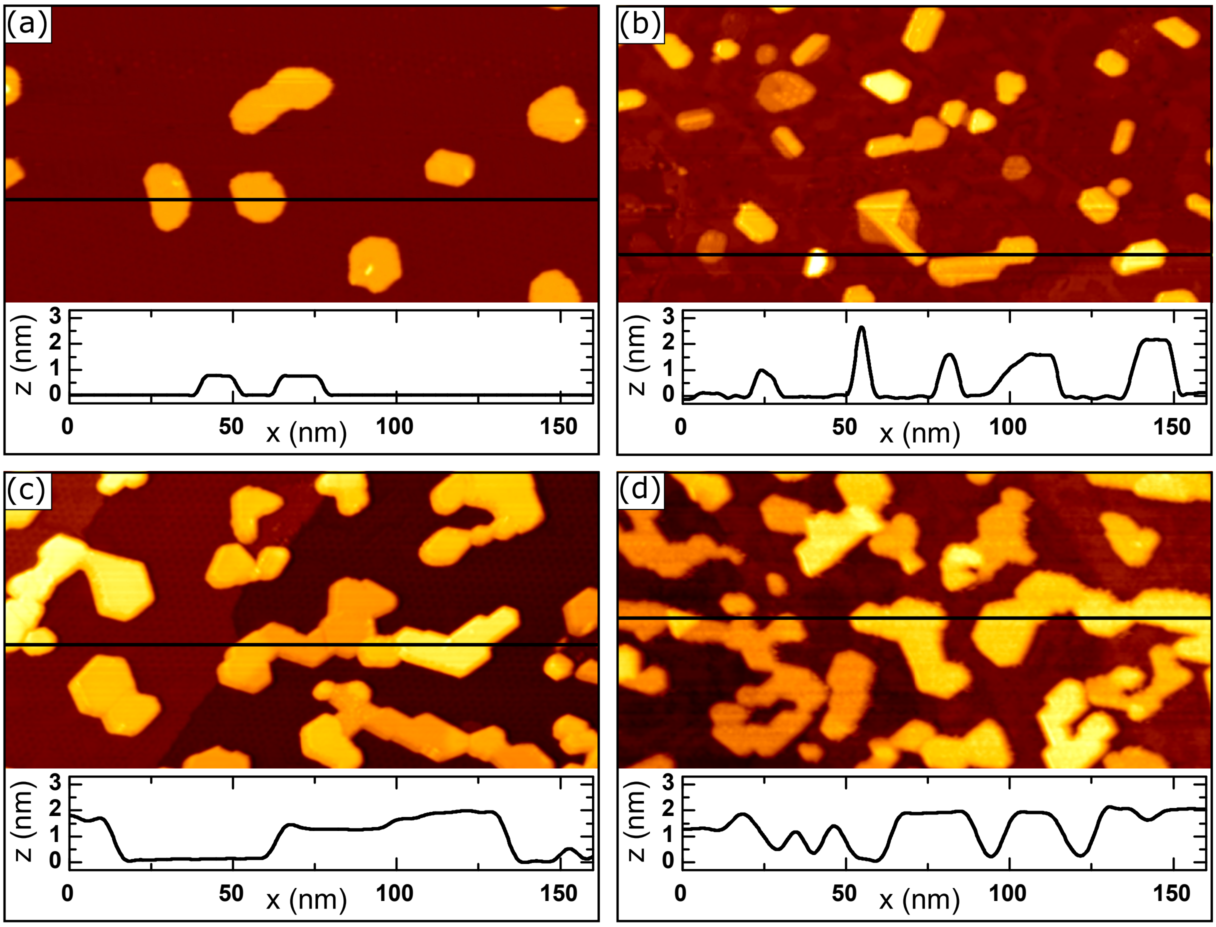

Figure 5.8: Transition from mono- to multilayer growth mode: STM topographs after growth with identical synthesis parameters (see Section 2.6), but variation of deposition time, which unexpectedly results in a change in growth mode. (a) $t^{g} = 60\,\mathrm{s}$ results in 15 % surface coverage, which arrange in monolayer height islands. (b) $t^{g} = 180\,\mathrm{s}$ creates a non phase-pure system of mixed mono- and multilayer heights, which cover 20 % of the surface area. (c) After using $t^{g} = 360\,\mathrm{s}$ no monolayer heights can be found anymore, the surface coverage amounts to 30 %. (d) $t^{g} = 540\,\mathrm{s}$ results in a sample with only multilayer heights and a surface coverage of 45 %.
Image information (image size, sample bias, tunnelling current): (a) $160 \times 80\,\mathrm{nm}^2$, 1.3 V, 20 pA, (b) $160 \times 80\,\mathrm{nm}^2$, −1 V, 1 nA, (c) $160 \times 80\,\mathrm{nm}^2$, −1 V, 0.5 nA, (d) $160 \times 80\,\mathrm{nm}^2$, −0.7 V, 0.1 nA.

the bottom, monolayer and multilayer islands are observed, and very often single grains exhibit one height. This is in contrast to multilayer growth of MoS_2, where small second layer islands are observed on top of a larger first layer, while in $V_{1+x}S_2$ mostly the entire grain exhibits either a monolayer or multilayer growth mode. We note that the presented sample morphology is rarely observed, and the lack of reliable reproducibility underlines the metastability of these phases.

More often a quick transition from (a) to (c) is observed when a certain deposition time is overcome. In (c), the synthesis outcome with $t^{g} = 360\,\mathrm{s}$ illustrates a complete change in sample morphology, and no monolayer heights are anymore observed on the sample. This trend continues when increasing

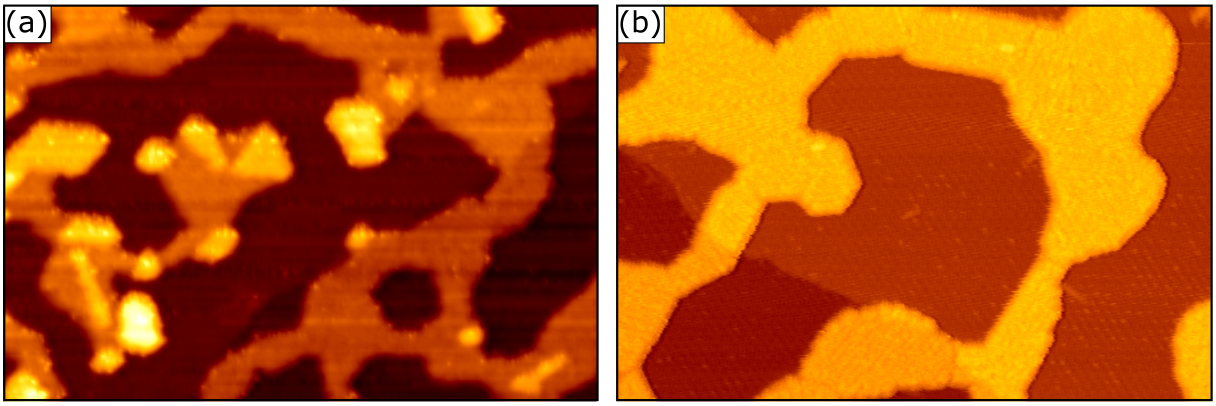

Figure 5.9: Influence of V to S ratio: (a) STM topograph of a $V_{1+x}S_2$ monolayer network which was grown at reference parameters except for $F_V = 3.3\,F_V^{\mathrm{ref}} = 8.3 \times 10^{16}$ atoms m^{-2} s^{-1}, $t^g = 60$ s, $T^g = 150$ K. (b) Lowering the V:S ratio towards S excess enables to grow phase pure ML samples. The growth parameters are as in (a), but $F_V = 1.8\,F_V^{\mathrm{ref}} = 4.4 \times 10^{16}$ atoms m^{-2} s^{-1}, which results in roughly halving the V:S ratio.
Image information (image size, sample bias, tunnelling current): (a) 150×100 nm^2, -0.4 V, 80 pA, (b) 150×100 nm^2, -0.1 V, 10 pA.

the deposition time to $t^g = 540$ s, which is illustrated in (d), where again no monolayer heights are observed.

At first, the reason for this transition from monolayer growth mode to multilayer growth mode seems arbitrary and the lack of any monolayer islands unlikely. In anticipation of results, which are presented in the following Section 5.4, we interpret this transition to result from V atom self-intercalation. We will show the surface of the multilayer islands to regularly show indications of a 2 × 2 superstructure, which regard the multilayer to be rather 3D $V_{1+x}S_2$ with local stoichiometry V_5S_8. This structure is known to be a stable 3D V-S compound, which may be interpreted as bulk VS_2 intercalated by a V(2 × 2) superstructure in the vdW gap and appears to be thermodynamically more stable than pristine VS_2 [373]. Since the intercalation of V inside the vdW gap may be local and some regions might still be unintercalated, this system allows investigating the interplay of pristine VS_2 properties and V self-intercalation with a local probe such as STM.

The self-intercalation rate is substantially influenced by the locally effective ratio of V to S, which may be controlled twofold. While the measured fluxes may be directly controlled, another way is to lower the sample temperature during the growth step, which allows staying at low working pressure. The low temperature causes S to adsorb in multilayers on Gr/Ir(111) and hence facilitates keeping an S excess throughout the synthesis, which fosters monolayer growth. Figure 5.9 illustrates the effect of the V to S ratio. Panel (a) displays a sample morphology after synthesis with the growth step at 150 K and the residual synthesis parameters mentioned in the figure caption. About 40 % of the sample surface are covered by a $V_{1+x}S_2$ monolayer network, which again is locally overgrown with small second layer islands. Staying at 150 K, but improving the V to S ratio even allows to grow phase pure ML samples as shown in panel (b).

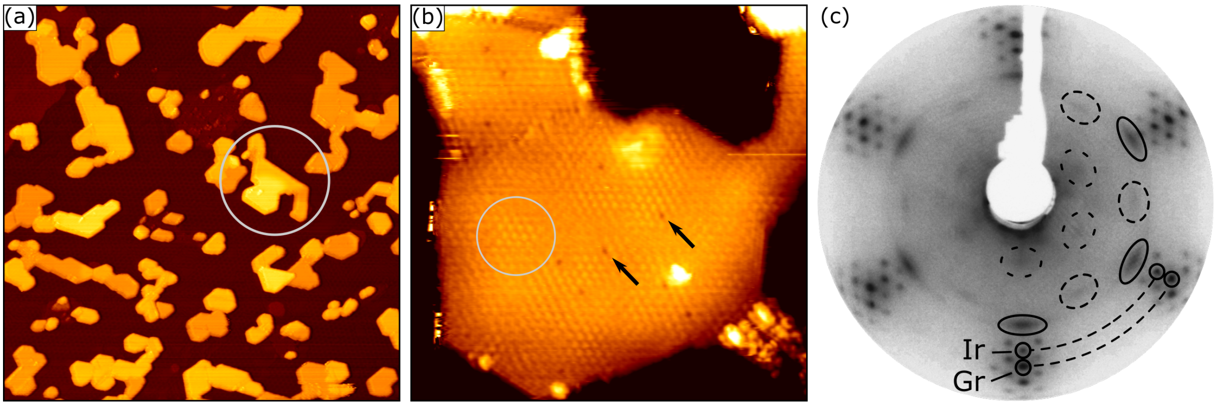

Figure 5.10: Multilayer VS_2: (a) Overview STM topograph of a VS_2 multilayer sample. No monolayer heights are present on the sample. (b) Close up of an island with a height of 14 Å showing disturbed superlattice ordering (marked by circle). Dark depression marked by arrow. (c) Corresponding LEED data at 85 eV showing Gr/Ir(111), moiré, VS_2 spots and a 2×2 superstructure.
Image information (image size, sample bias, tunnelling current): (a) 200×200 nm^2, -1 V, 0.5 nA, (b) 25×25 nm^2, 1 V, 0.5 nA.

The limitation of sample coverage is not observed in the similar system VS_2/Au(111). We interpret this to be a consequence of the low interaction of the TMDC epilayer with its substrate, which consequently cannot serve as a stabilising agent for 2D growth.

We conclude that the synthesis of $V_{1+x}S_2$ is multifaceted and illustrates the metastability of the single phases. We illustrated the influence of certain growth parameters which may be used to tune the growth from 1D over 2D to 3D, and we indicated how to foster high-coverage monolayer growth.

5.4 Multilayer Vanadium Sulphides

Adapting the growth parameters to deliberately tune the growth mode of a material is an important goal in epitaxy and in the case of VS_2 this may be achieved in two ways: as the growth mode appears to favour multilayer VS_2, when the ratio of V to S is high, one route is to deliberately undercut the S pressure needed for ML growth during the synthesis. In another approach, setting the reference synthesis parameters, but overcoming a critical deposition time also fosters multilayer growth. The reasons for this is mainly that through a higher initially deposited amount of material, comparably higher structures are formed since the mobility at growth temperature (300 K or below) is to low to enable strong diffusion. These higher structures tend to result in multilayer growth during the annealing step. The 3D growth is accompanied by V self-intercalation as we will show in the following.

Fig. 5.10 summarises the key features of multilayer VS_2. In (a) a large scale STM topograph illustrates the sample morphology. As shortly stated above, only multilayer heights and no monolayer are observed. The islands assume hexagonal shapes, which align with the substrate orientation.

As visible in the topograph, the structures exhibit several distinct height levels, which often merge continuously into another as highlighted by the circle in the middle of Fig. 5.10 (a).

High-resolution STM images of the multilayer island's surface, Fig. 5.10 (b), reveal distinct morphological features:
(i) Point defects are readily spottable as dark depressions on the surface (see arrows).
(ii) Grain boundaries are visible.
(iii) Although adsorbates are present, compared to the ML islands which were annealed in S, the surface is comparably clean.
(iv) No moiré is visible on the islands, but another structure is visible in large parts of the islands, while it is absent in small areas. Noting that the islands grow epitaxially and therefore island edges terminate in epitaxial directions, a rotation of the superstructure by 30° is apparent and we will show in the following that the periodicity is $(\sqrt{3} \times \sqrt{3})\mathrm{R}30^\circ$.
(v) We foreclose that under suitable tunnelling conditions, also a 2×2 superstructure can be found on the islands, which we will show in Fig. 5.11.

The LEED data in Fig. 5.10 (c) indicate epitaxial growth with small scatter of about 4° and a lattice constant of (3.27 ± 0.01) Å. Additionally, LEED reveals a weak 2×2 superstructure with respect to VS_2 and no sign of a $(\sqrt{3} \times \sqrt{3})\mathrm{R}30^\circ$ phase.

To resolve this discrepancy, and to get information on the nature of the two superstructures, we investigate the behaviour of the two periodicities in the occupied and unoccupied states by switching the polarity of the bias applied to the sample. The expected origins of the two superstructures are self-intercalation of V for the 2×2 and a charge density wave for the $(\sqrt{3} \times \sqrt{3})\mathrm{R}30^\circ$. For intercalation, the switching of polarity should not change the position of a local charge maximum. For a charge density wave, an antiphase behaviour is expected.

In Fig. 5.11, STM close-ups of the occupied and unoccupied states are shown. The data taken allow both the 2×2 and the $(\sqrt{3} \times \sqrt{3})\mathrm{R}30^\circ$ to be visible, though the intensity of the $(\sqrt{3} \times \sqrt{3})\mathrm{R}30^\circ$ is low in the occupied states and the 2×2 signal is weak in the unoccupied states. To enhance the visibility of the respective periodicity, the signal of the other one is filtered out in Fourier space.

In (a) and (b), the behaviour of the 2×2 upon switching the polarity is shown. The circles in (a) and (b) indicate the same positions on the sample, and in both the occupied and unoccupied states encircle charge maxima. This strongly supports the interpretation of V intercalation being responsible for the 2×2 superstructure.

For the $(\sqrt{3} \times \sqrt{3})\mathrm{R}30^\circ$, the situation is different: when comparing occupied and unoccupied states in (c) and (d), we note a change of contrast when switching bias. This is again marked by the circles, this time encircling charge minima and charge maxima, respectively. This indicates the CDW nature of the $(\sqrt{3} \times \sqrt{3})\mathrm{R}30^\circ$ and makes our assignment as such conclusive.

Considering the spatial distribution of the two superstructures, we note that they largely preclude each other. Inside the region enclosed by the three vacancies in Fig. 5.11, the amplitude of the CDW is large, whereas in the region marked by the circles in (a), (b), where the 2×2 intercalation structure is strong, the CDW remains absent. Though there is no strict exclusion, we suggest that

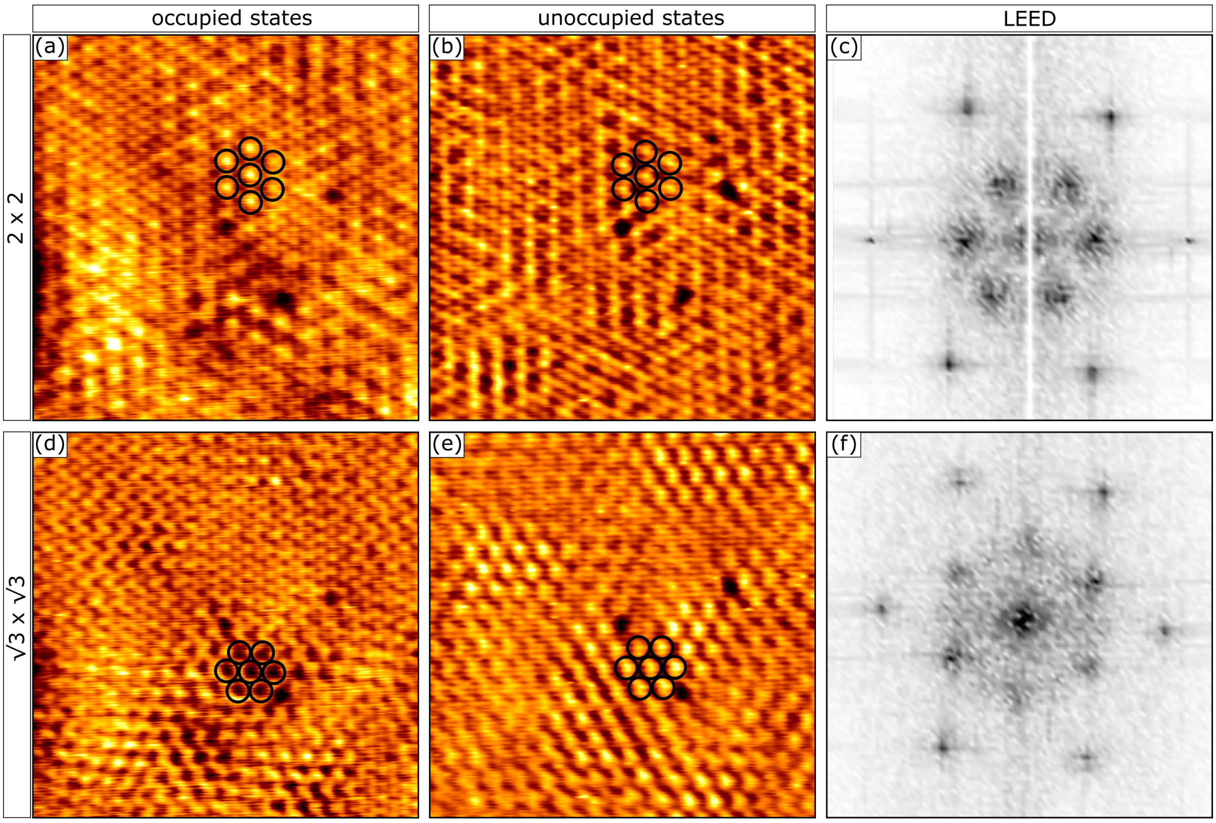

Figure 5.11: Charge ordering and intercalation in multilayer $V_{1+x}S_2$: (a), (b) STM topographs of the occupied states and unoccupied states showing local 2×2 superlattice formation due to intercalation. The circles mark the same atomic positions and underline charge maxima on both sides of the Fermi energy. The signal of the $(\sqrt{3}\times\sqrt{3})R30^\circ$ is filtered in Fourier space to enhance visibility. (c) Corresponding FT supporting the 2×2 structure. (d), (e) Analogous STM topographs for the $(\sqrt{3}\times\sqrt{3})R30^\circ$ charge ordering on opposing sides of the Fermi energy. In the occupied states image, the circles mark local charge maxima. The signal of the 2×2 is filtered in Fourier space to enhance visibility. The sample is at room temperature. (f) Corresponding FT also illustrating the $(\sqrt{3}\times\sqrt{3})R30^\circ$ structure.
Image information (image size, sample bias, tunnelling current): (a), (d) 10×10 nm^2, -1 V, 0.5 nA, (b), (e) 10×10 nm^2, 1 V, 0.5 nA.

the V intercalation (and associated doping) suppresses the CDW and stabilises the lattice. In line with these findings, bulk VS_2 is reported to show a CDW [50], while V_5S_8 not [367].

In conclusion, we grow multilayer $V_{1+x}S_2$ by adapting the synthesis parameters. As multilayer growth is fostered by a higher V:S ratio, the multilayers are often intercalated and display a local stoichiometry of V_5S_8, *i.e.* intercalation by $V(2\times2)$. This intercalation interacts with the $(\sqrt{3}\times\sqrt{3})R30^\circ$ CDW present in pristine multilayer VS_2 and eventually suppresses it at high intercalation density.

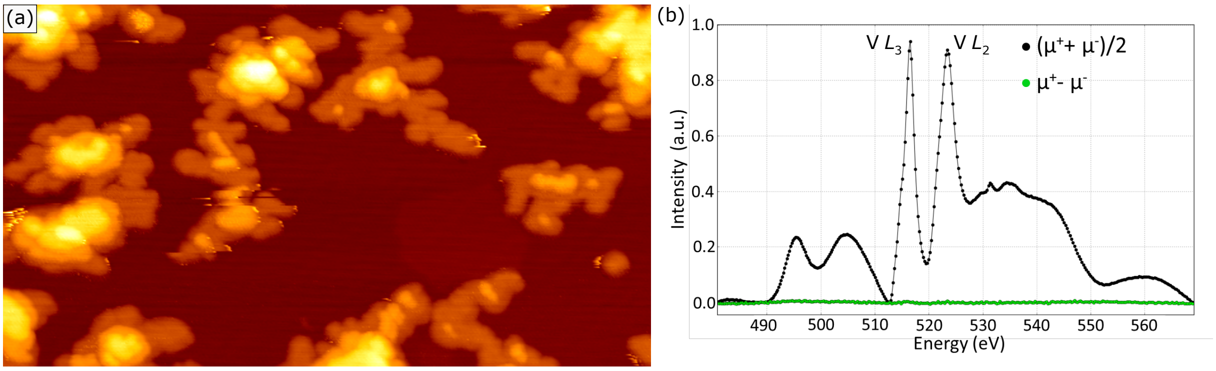

Figure 5.12: Magnetic properties of VS$_2$: (a) STM topograph illustrating the sample morphology. Image size: 100 × 50 nm^2. (b) Average (black) and difference (green) of x-ray absorption spectra taken with right and left circularly polarised light at 5 K in total electron yield mode.

5.5 Magnetic Properties of Vanadium Sulphides

The magnetic properties of V$_{1+x}$S$_2$ on Gr/Ir(111) are investigated employing x-ray absorption spectroscopy (XAS) at the beamline ID32 of the European Synchrotron Radiation Facility (ESFR), Grenoble.

Fig. 5.12 summarises the sample morphology and the XAS measurements. In (a), an STM topograph illustrates the sample morphology and shows the island structure to be dendritic and to extend into 3D. Distinct height levels can be found and indicate at least three layers. By comparison to substrate step edges, the step height is measured to be 7 Å. Due to the dendritic form of the islands, we speculate the highest temperature that the sample has experienced to be below 400 K[3], which allows the assumption of stoichiometric VS$_2$ to be present on the sample, even without atomic hexagonal resolution.

The results of the magnetic measurements are shown in Fig. 5.12 (b). The black curve shows the normalised average of the absorption spectra, recorded with right and left circularly polarised light, respectively. Both, the L_3- and L_2-edge, are visible in the average XAS as indicated. The x-ray magnetic circular dichroism (XMCD) signal – the difference of the absorption spectra – is plotted in green. Apparent is the absence of any XMCD signal in the sample. Hence, no magnetic coupling can be observed and even the magnetic moment of V is suppressed entirely.

In the discussion, why the VS$_2$/Gr/Ir(111) sample does not show any magnetic moment in XMCD, we consider three possible factors:

(i) Although pristine layers of VS$_2$ actually carry a magnetic moment, the poor sample quality impedes the resolution of a magnetic signal. The recipe employed during the beamtime should have yielded epitaxially ordered flat islands; a result which was prevented by a difficult temperature readout. As LEED also did not indicate any ordering (data not shown), the atomic structure may have been ill-defined and consequently, even the magnetic moment of the V atoms is suppressed.

---

[3] The sample was heated resistively with a thermocouple mounted to the heater. The annealing was switched off when the thermocouple read 850 K and was afterwards checked with STM.

(ii) The interaction with the substrate suppresses the magnetic moment in VS_2/Gr/Ir(111). Though the vdW substrate Gr/Ir(111) is inert and substantially decouples the TMDC adlayer from its environment, we cannot exclude the interaction entirely. As introduced in Section 3.3, ARPES indicated a small doping of Gr after MoS_2 growth and in Section 6.2 we will further show TaS_2 to be slightly doped on Gr/Ir(111). The possibility of doping of VS_2 by Gr/Ir(111) and an action on the magnetic properties can therefore not be excluded. (iii) Pristine layers of VS_2 do not show magnetism. Even though multiple calculations indicate the possibility of magnetism, additional influences arising in real systems may suppress the magnetic moments.

In conclusion, dendritic mono- to multilayer islands were probed for their magnetic properties with XMDC, and no indications for magnetic moments were found. We discuss the possible reasons for this.

5.6 Discussion

The V-S system, both in monolayer and in multilayer regime, is complex and exhibits many stable phase equilibria. In the monolayer regime, three stable phases were observed, one stoichiometric VS_2 and two S deficient ones. It proves difficult to grow large-area stoichiometric VS_2 on the inert Gr/Ir(111) substrate, as both handles which allow large area ML growth – elevated temperature and the magnitude of S background pressure – influence the growth mode. Elevated temperatures would be needed to increase surface mobility and edge diffusion in order to foster large area monolayer growth. However, the decomposition of the flakes starts quickly and sulphur deficient phases are readily assumed. Furthermore, at temperatures needed for epitaxial alignment, the decomposition rate is significantly too high and the metastable synthesis ends in a local energy minimum in the striped phase. Also an applied external S pressure does not prevent this but results in the striped islands being covered in adsorbates.

Another scenario is that a sulphur background is admitted at low annealing temperatures, which changes the growth morphology multilayer regime, similar to the synthesis of MoS_2 [cf. Fig. 4.2]. It thus seems that there is only a small window of synthesis parameters that may allow large area stoichiometric ML growth of VS_2. This limitation impedes the investigation of the pristine ML VS_2 properties and even though no indications for a CDW or magnetism were observed, the poor sample quality calls for further investigations before drawing premature conclusions.

Two sulphur deficient monolayer phases were observed. Regarding the lesser S deficient phase, in which S vacancies are arranged in periodic beats, we note that a phase pure stabilisation appears difficult. Although at a temperature range of $500 - 600$ K this phase is dominant, locally, both stoichiometric and other sulphur deficient phases are present. The nature of this phase is not unambiguously determined and needs further investigation. DFT simulations may help to understand whether the observed structure agrees with vacancy ordering in 1T-VS_2 or if one also has to consider lattice distortions and other effects. Adding to this issue, in the related system ML VSe_2 on bilayer graphene, a strikingly similar phase has been observed [109]. At room temperature, Duvjir *et al.* document a questionable metallic 4×1 CDW phase, which does not show strong lattice distortions.

At 79 K, on the other hand, they find additional strong lattice distortions – which match our parallel beats phase observed at room temperature – that are accompanied by a metal-to-insulator transition.

The most sulphur deficient stable monolayer phase appears as stripes on the island surface. The stripes mark a 3×1 superstructure on a reconstructed atomic lattice, which results from average desorption of every third sulphur row. The atomic structure of the V and bottom S layer remains unclear from our STM investigations and further investigations employing XPD, XRD or theoretical approaches such as DFT are needed to fully uncover the structure of the reconstructed lattice. Also, spectroscopic details on the novel phase are missing and could reveal information on the electronic and magnetic structure. At this stage, when only considering the structural characteristics of the surface S layer, we speculate this phase to be interesting for patterning and the investigation of *e.g.* single-atom catalysis.

We observe a sharp transition from monolayer to multilayer growth, which we assign to a stabilisation of the multilayer growth mode through local self-intercalation of V atoms. This also allows concluding the monolayer to be unintercalated (no V atoms between VS_{2-x} and Gr), which is supported by the observability of the moiré on all three kinds of monolayers. We speculate the change in growth mode to originate from charge transfer from V to the V-S layers and propose that the same change should be observed when deliberately doping Gr by intercalation before V_xS_x growth. The understanding of the influence of the charge level in the substrate may allow finding synthesis routes towards stabilised monolayer growth.

The self-intercalation in multilayer $V_{1+x}S_2$ explains the various height levels observed in STM, on the one hand, because of geometric height differences (the interlayer distance in VS_2 is 5.7 Å [353], while in V_5S_8 this increases to 7.91 Å[4] [55]) and on the other hand by possible differences in the DOS. We ascribe the $(\sqrt{3} \times \sqrt{3})R30^\circ$ superstructure on the surface of the multilayer to CDW origin, which is strongly supported by the antiphase behaviour in the occupied and unoccupied states. This, however, needs to be corroborated by additional investigations such as STS, which should indicate a gap in the LDOS around E_F. As we observe the CDW to be absent in regions which are intercalated by $V(2 \times 2)$, we speculate doping to stabilise the atomic lattice, which could be investigated by deliberate doping or theoretical calculations.

5.7 Conclusion

We prepare mono- and multilayer $V_{1+x}S_2$ with different stoichiometries, including both mono- and multilayer VS_2. We follow the thermal evolution of an increasing amount of sulphur deficient monolayer phases and uncover their atomic surface structure. A phase transformation back to a sulphur-rich phase is not possible and induces a growth mode change towards 3D growth. The multilayer $V_{1+x}S_2$ shows indications for local $V(2 \times 2)$ intercalation, which locally suppresses the otherwise present $(\sqrt{3} \times \sqrt{3})R30^\circ$ CDW phase.

---

[4] Please note that V_5S_8 is not a layered material with vdW bonded layers. Therefore the c-axis lattice parameter differs from the interlayer distance of the VS_2 planes. While the c-axis parameter in V_5S_8 measures around 11.3 Å [367], the interlayer distance is smaller.

CHAPTER 6

Tantalum Disulphide: Environmental Control of Charge Density Wave Order

*This chapter contains contributions from **J. Hall**, N. Ehlen, J. Berges, E. van Loon, C. van Efferen, C. Murray, C. Speckmann, M. Rösner, J. Li, B. V. Senkovskiy, M. Hell, M. Rolf, T. Heider, M. C.Asensio, J. Avila, L. Plucinski, T. Wehling, A. Grüneis, and T. Michely. The charge density wave related main results of this chapter are submitted and under review in Ref. [374].*

***I** developed the growth recipe and started the investigations of the charge density wave at the variable-temperature system TuMA II. **I** planned and extended the investigations to the low-temperature STM and STS system* $_{\mathrm{T}}$STM. *The low-temperature data were taken by **me** and C. Murray, who kindly instructed how to operate* $_{\mathrm{T}}$STM. *C. v. Efferen and M. Rolf assisted the measurements. **I** analysed and interpreted the data. T. Michely supervised the STM/STS measurements. N. Ehlen, J. Li, M. Hell and B. V. Senkovskiy measured and analysed ARPES both at the ANTARES endstation of the SOLEIL synchrotron, France (where M. C.Asensio and J. Avila were involved), and at the PGI-6 in Jülich (where T. Heider and L. Plucinski took part). A. Grüneis supervised the ARPES measurements. J. Berges, E. v. Loon and M. Rösner performed the DFT calculations under supervision of T. Wehling.*

*All results were discussed by **me**, N. Ehlen, J. Berges, E. van Loon, C. van Efferen, C. Murray, T. Wehling, A. Grüneis, and T. Michely.*

***I** wrote the manuscript of Ref. [374], which was discussed amongst AG Michely, AG Grüneis and AG Wehling. **I** finalised the manuscript in close collaboration with T. Michely.*

***I**, furthermore, planned and performed the growth studies with the assistance of C. Speckmann, including STM and LEED at the variable-temperature apparatus* TuMA II. ***I** analysed and interpreted the data. T. Michely supervised the measurements.*

6.1 Motivation: Controlling Intricate Phases of Solids

Condensed matter quantum many-body states are often highly sensitive to stimuli such as pressure, temperature, or changes in chemical composition. Therefore, the concurrence of pronounced many-body phenomena in (quasi-) 2D materials [94, 375–377] with advances in synthesis and vertical heterostructuring [378, 379] has fueled hopes for controlling electronic quantum phases on demand [380]. These hopes are supported by experiments revealing electronic phase diagrams of several 2D systems – including Fe-based superconductors [381] and TMDCs [13–17, 31, 290] – to be strongly dependent on dimensionality, thickness, and substrate. However, the microscopic mechanisms behind these dependencies often remain elusive and a thorough understanding of how to tune electronic quantum phases by atomic-scale manipulations is largely lacking to date – although being an inevitable requirement for the implementation of quantum materials into device applications.

Using the example of a prototypical CDW material TaS_2, we experimentally and theoretically explore how CDW order is influenced by the control parameters doping and hybridisation with the substrate. Regarding the latter, this is investigated in ML TaS_2 as well as the case of interlayer interaction in BL TaS_2. These parameters add additional dimensions to the phase diagram of TaS_2 and allow for quantum phase transitions between different kinds of CDW ordered and distorted states. Based on theoretical modelling we identify doping and hybridisation driven phonon self-energy effects as the microscopic origins of the CDW transitions in the ML.

The material under consideration in the present study is the 2H polytype of TaS_2, where the metal atom coordination is trigonal prismatic. As bulk material, it displays a slightly discommensurate 3×3 CDW [57] phase with a partial CDW gap [382–385], a transition temperature of 75 K [56], and a transition to a superconducting phase at around 1 K [386].

In line with related materials [16, 17, 130, 290], the electronic phase diagram of 2H-TaS_2 appears thickness-dependent: when approaching ML regime, the superconducting transition temperature of TaS_2 becomes enhanced as compared to the bulk [13–15, 387, 388]. CDW order turns out to depend on the number of layers too, but the ML limit remains unclear and controversial until now.

Few experimental works addressed charge order in ML 2H-TaS_2 recently. Sanders *et al.* [35] found no CDW when a ML was grown on Au(111) by MBE. Also, Yang *et al.* [14] conclude the CDW for ML 2H-TaS_2 encapsulated in h-BN to be absent, based on transport measurements. In contrast, Lin *et al.* [58] observed a 3×3 superstructure indicative of a CDW for the MBE-grown ML on Gr grown on 6H-SiC(0001). The situation is puzzling and stimulated several theoretical contributions. Freestanding undoped ML 2H-TaS_2 turns out to be dynamically unstable [389] and favours CDW order. Further, DFT studies show that interaction with substrates affects the tendency of ML 2H-TaS_2 towards CDW formation [389, 390].

For a doping level consistent with that derived from ARPES of ML 2H-TaS_2 on Au(111) [35], Albertini *et al.* [389] find the CDW to be suppressed. Shao *et al.* [391] point out that an estimate of the doping level in the ML 2H-TaS_2 on Au(111) based on changes in the FS may severely overestimate the actual charge transfer through non-linear band distortions as a consequence of hybridisation. Correspondingly, Lefcochilos-Fogelquist *et al.* [390] argue that the suppression of the CDW in ML 2H-TaS_2 on Au(111) is primarily a consequence of hybridisation in consequence of strong S-Au interactions, rather than usual charge doping. However, a clear disentanglement of hybridisation and doping effects on CDW order is currently lacking.

In this chapter, we take a close look at this issue and analyse experimentally the absence/presence and properties of CDWs in quasi-freestanding ML 2H-TaS_2 at different doping levels, as well as the situation in the BL of 2H-TaS_2.

In the second section, we present results for the ML 2H-TaS_2, which show unambiguous evidence for a CDW close to a 3×3 periodicity. Using STS, we determine the magnitude of the partial CDW gap. ARPES, complemented by STS for the unoccupied states, makes a TB fit for the band structure of ML TaS_2 possible. As hybridization with substrate bands is absent, the fit yields a precise value for the doping level of the TaS_2 layer.

As we will show in the third section, unexpectedly the bilayer of TaS_2 displays a disordered 2×2 CDW. As we suspect doping to play a role in this transition, we investigate the effect of Li doping on the ML in the forth section, which indeed drives the formerly 3×3 CDW into a 2×2 periodicity.

Results of calculations of the phonon dispersions based on a combination of DFT, DFPT, and many-body perturbation theory are presented in section five. Based on phonon renormalisation, we are able to provide phase diagrams for the TaS_2 CDW as functions of the control parameters doping, hybridisation and interlayer potentials, and offer insight into how they affect lattice dynamics and stability. Our theoretical analysis is not only fully consistent with our experimental results but also resolves apparent discrepancies in previous experimental and theoretical works by clarifying the roles of the aforementioned control parameters for lattice (de-)stabilisation and the formation of CDW states.

On a different note, we use section six to further explore issues related to the growth properties of our *in situ* MBE-grown 2H-TaS_2 on Gr/Ir(111). One problem vdWE suffers from under typical growth conditions is a high nucleation density, and as a consequence, many small grains and limited island sizes appear, alongside a high density of grain boundaries evolving. We offer pathways on how to enlarge lateral grain sizes *via* the influence of the substrate temperature and the deposition rate during growth. Finally, we show how to manipulate the growth mode of TaS_2, once controlling the morphology in a sudden transition to multilayer growth and once controlling the polytype which is grown.

In the end, the possible driving mechanisms for the different transition are discussed, considering both the transition from the 3×3 to 2×2 CDW periodicity and the observed change in growth morphology.

6.2 The 3 × 3 Charge Density Wave in Single Layer TaS_2

Employing the two-step MBE method using the reference parameters stated in Section 2.6 for the growth of TaS_2 readily yields ML 2H-TaS_2. Similar to its bulk counterpart the ML shows a 3×3 CDW at temperatures below about 75 K.

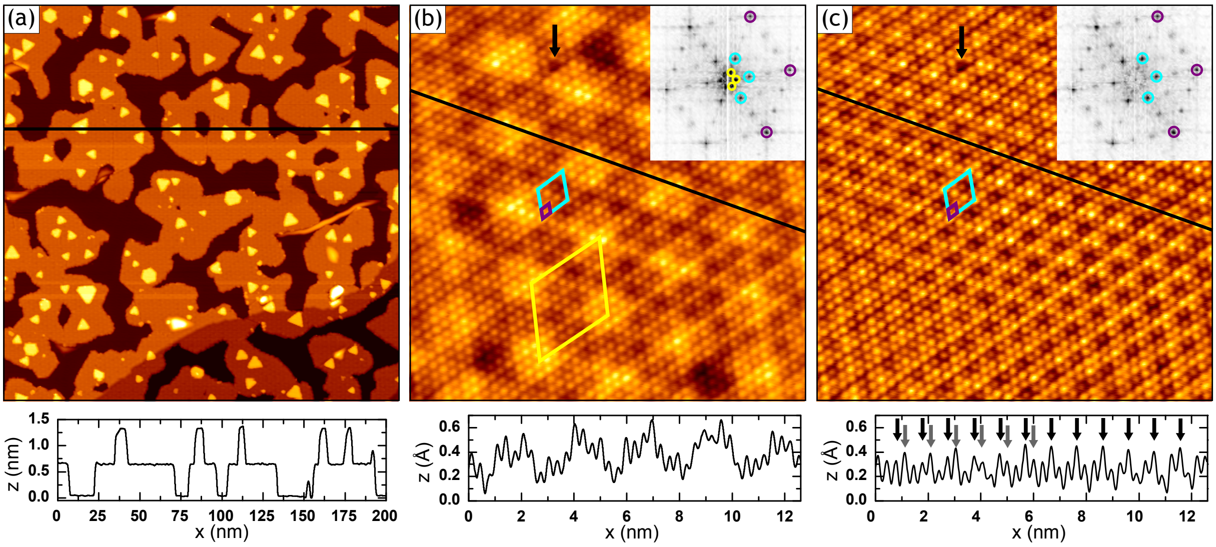

Figure 6.1: STM overview of TaS_2 on Gr/Ir(111) at 5 K: (a) Large scale STM topograph of TaS_2 islands on Gr/Ir(111). The sample was grown with reference growth parameters, except of $F_{\mathrm{Ta}} = 0.25\,F_{\mathrm{Ta}}^{\mathrm{ref}} = 4.5 \times 10^{15}\,\mathrm{atoms\,m^{-2}\,s^{-1}}$ and $t^{\mathrm{g}} = 1500\,\mathrm{s}$. The sample is largely covered with ML TaS_2, on which mostly triangular second layer islands sit. On the right a Gr wrinkle is visible, at the bottom right a step edge. The black line shows the position of the line profile at the bottom. (b) Constant current STM atomic resolution topograph of ML TaS_2. Three periodic structures are indicated, each with its respective unit cell [Gr/Ir(111) moiré yellow, 3 × 3 CDW turquoise, atomic TaS_2 lattice violet]. The arrow marks a point defect. Inset: Fourier transform of the STM image with peaks related to the periodicities circled in same the colour as unit cell rhomboids. (c) Same image as (b), but with the moiré filtered out in Fourier space to enhance the visibility of the CDW. The arrow marks a point defect. Inset: Fourier transform of the STM image. The black line shows the position of the line profile at the bottom, where arrows denote the position of the local charge density maximum.
Image information [image size, sample bias, tunnelling current]: (a) $200 \times 200\,\mathrm{nm}^2$, -1 V, 0.1 nA, (b), (c) $12 \times 12\,\mathrm{nm}^2$, -0.15 V, 0.2 nA.

Key Features of the 3 × 3 Charge Density Wave in Scanning Tunnelling Microscopy

Fig. 6.1 (a) displays a large scale STM topograph of TaS_2 on Gr/Ir(111) taken at 5 K. The geometrical coverage of 0.7 layers of TaS_2 arranges in a network which covers about 65% of the Gr/Ir(111) substrate and readily overgrows a step edge visible in the bottom part of the image. This network is decorated with about 5% coverage of small triangular islands in the second layer. As visible in the line profile along the black line in the topograph, the apparent STM height of ML TaS_2 is 6.5 Å. This compares well to the interlayer distance measured in bulk 2H-TaS_2 of 6.26 Å [392, 393].

In Fig. 6.1 (b) a close-up of the ML TaS_2 surface is shown, along with its Fourier transform in the inset. The surface displays three different periodic structures, each being indicated with its respective unit cell in the STM and its corresponding Fourier peak in the inset, respectively.

The largest structure (yellow rhomboid) in the topograph is the moiré formed by Gr/Ir(111) which is also visible in the TaS_2 layer. Motivated by our above findings, we interpret the lack of an additional moiré between TaS_2 and Gr as a sign for the weak vdW interaction of the TMDC with its substrate Gr/Ir(111).

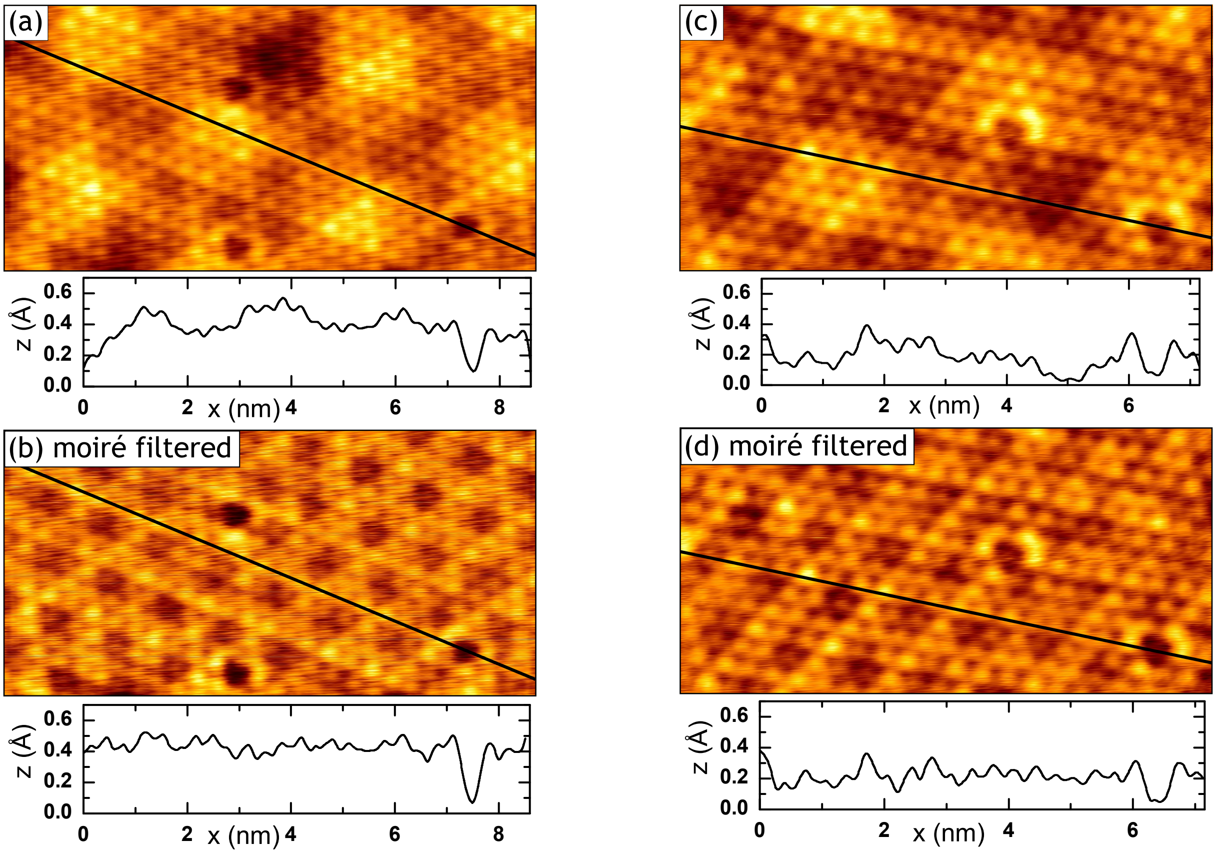

Figure 6.2: Influence of point defects on CDW: (a) STM topograph of TaS_2 on Gr/Ir(111) with point defects. Around the defects an increase in apparent height is visible. (b) Same as (a), but moiré filtered. (c) Further example of defects. The contrast around the defects is even more increased. (d) Same as (c), but moiré filtered.
Image information (image size, sample bias, tunnelling current): (a), (b) 8×4 nm^2, -0.06 V, 0.4 nA, (c), (d) 7×3.5 nm^2, -0.05 V, 0.5 nA.

Due to the low interaction with the substrate, the TaS_2 islands are not perfectly epitaxially aligned. Despite a preferential alignment of the dense-packed TaS_2 and Gr rows, orientation scatter is present. For example, in the STM topograph shown in Fig. 6.1 (b) the orientation mismatch amounts to 4°.

The smallest structure (violet rhomboid) is the atomic lattice of TaS_2, which through comparison with the moiré is determined to be (3.37 ± 0.02) Å. It matches well with the bulk in-plane lattice constant found in the literature [393, 394].

The remaining middle-sized periodic structure can be identified as a 3 × 3 superstructure with respect to the atomic TaS_2 lattice by filtering out the moiré, which is illustrated in Fig. 6.1 (c). The respective unit cells of the atomic lattice and the 3 × 3 superstructure are indicated in violet and turquoise respectively. In analogy to the bulk counterpart, we associate this 3 × 3 superstructure with a CDW phase of ML TaS_2 found at sufficiently low temperatures. We will prove our reasoning below and characterise some of its fingerprints in the following.

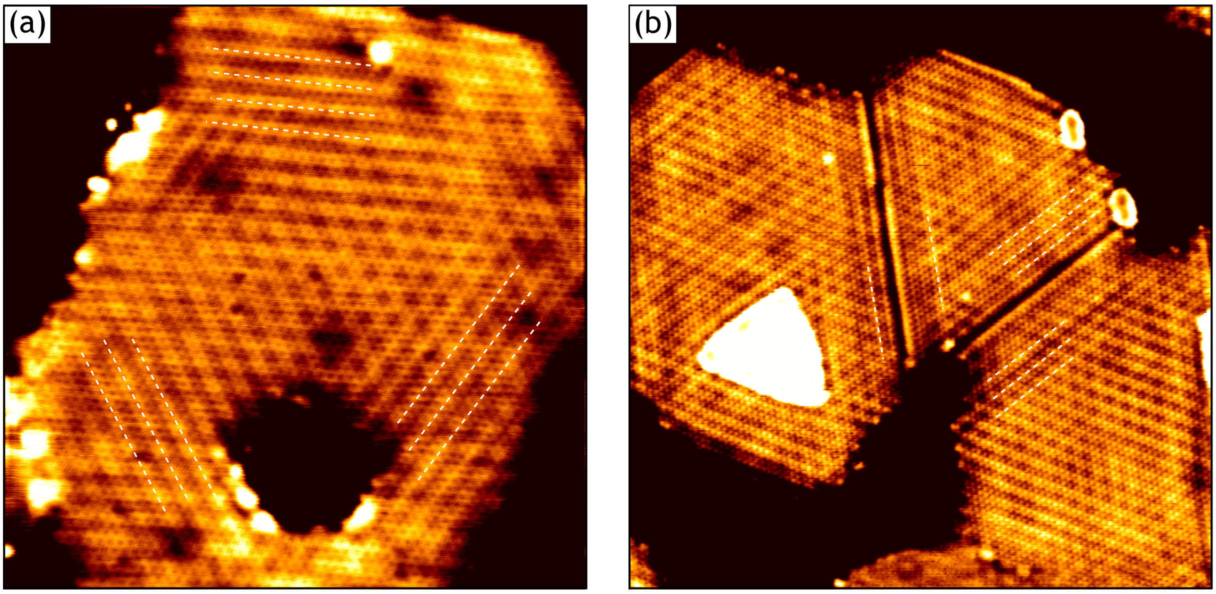

Figure 6.3: Influence of island shape on CDW: (a) Spatial variation of CDW amplitude in a given direction depending on island edges. White dashed lines indicate locally stronger amplitudes. (b) Influence of grain boundaries on CDW amplitude. Image information (image size, sample bias, tunnelling current): (a) 20 × 20 nm^2, −1 V, 0.1 nA, (b) 30 × 30 nm^2, −0.3 V, 0.1 nA.

We first note that it is hard to see any details of the 3×3 CDW from the line profile in Fig. 6.1 (b), as the profile is dominated by the moiré corrugation of about 0.5 Å. Removing the moiré in Fig. 6.1 (c) allows examination of spatial details of the CDW. Following the black arrows marking the position of the highest atom in the line profile from right to left reveals the $3a$ periodicity, where a is the lattice constant of TaS_2. However, on the left-hand side of the line profile, the $3a$ periodicity of the highest atoms is drawn by the position of the grey arrows, which are shifted relative to the black arrows. This indicates a phase shift in the CDW consistent with the absence of strict commensurability [57].

Fig. 6.1 (c) also shows a point defect (marked by arrow), which appears as a dark depression in the atomic lattice which makes an assignment as a vacancy suggestive. Since S vacancies have the least formation energy [395] and appear the most frequent, we reason this also here to be the case. The CDW does not interact, pin or is suppressed by the presence of the defect, which is the typical observation for low concentration S vacancies in our sample. Depending on the tip state, however, additionally an increased apparent height surrounding the vacancy site may be observed and is attributed to states introduced by the defect itself, not pinning of the CDW phase. This is illustrated in Fig. 6.2. In panel (a) and (b), STM topographs of the same location but once with the moiré filtered are shown. In both cases, the increased DOS is apparent and reminiscent of vacancy appearance in MoS_2 (Section 4.4). Panels (c) and (d) show another example, where the defect state is particularly strong. Again, STM topographs both with the moiré and without are shown. The comparison of the line profiles is further indicative of a decreased moiré corrugation in Fig. 6.2 (a)

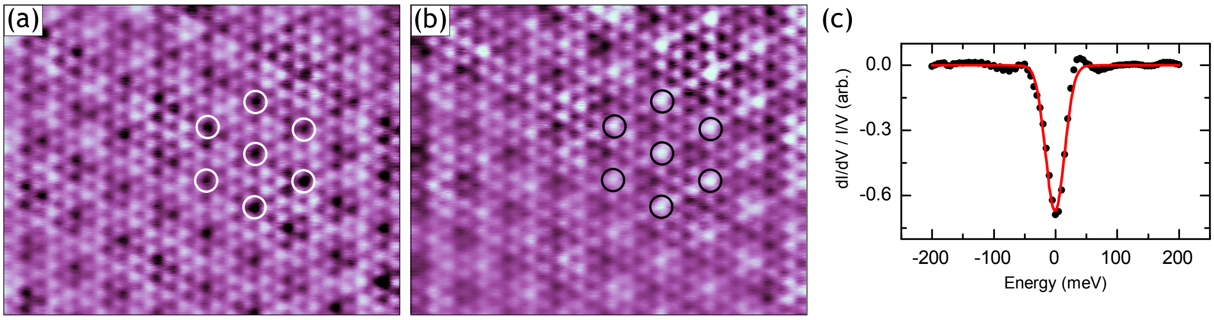

Figure 6.4: The CDW in ML 2H-TaS$_2$ in constant height STM and STS: (a) Constant height STM topograph of ML TaS$_2$/Gr/Ir(111) of occupied states. (b) Corresponding constant height STM topograph of unoccupied states. The circles mark the same positions but either show local maxima or minima of the CDW. (c) Constant height tunnelling spectrum on ML TaS$_2$, treated as in Ref. [47]. The scale is adjusted to be comparable to Fig. 6.7 (f) and Fig. 6.10 (b).
Image information [image size, (stabilisation) sample bias, (stabilisation) tunnelling current]: (a) 7×5 nm^2, -0.02 V, $I_{\text{stab}} = 0.1$ nA, (b) 7×5 nm^2, 0.02 V, $I_{\text{stab}} = 0.1$ nA, (c) $U_{\text{stab}} = -0.3$ V, $I_{\text{stab}} = 0.5$ nA.

and (c) compared to Fig. 6.1 (b) and leads us to rule out different vacancy types as the source of the different behaviour, but rather assign the differences to different tip states.

Fig. 6.3 illustrates the influence of extended defects such as grain boundaries and island edges on the CDW. As illustrated in Fig. 6.3 (a), we observe that the CDW amplitude in a given direction perpendicular to the island termination is increased compared to the remaining closed packed directions. Also at grain boundaries, which are shown in Fig. 6.3 (b), the amplitude perpendicular to the grain boundary is increased. Close to the line defect the lattice and the CDW are in phase and only loose coherence a few nanometers far away from it.

In order to demonstrate the CDW origin of the superstructure, we probe states above and below the Fermi energy by constant height STM and show results in Fig. 6.4 (a) and (b). A contrast inversion takes place upon change of polarity, as highlighted by the black circles in (a) enclosing brightness maxima and the white circles in (b) enclosing brightness minima. Both sets of circles are located around the same atoms. In a CDW, the occupied and unoccupied states above and below the Fermi energy have the same wave vector k_F but different energies, resulting in antiphase behaviour in real space. This behaviour is clearly reproduced in the respective figures.

Performing STS at 5 K reveals a reduction of the LDOS at the Fermi energy [see Fig. 6.1 (c)], which (to our best knowledge) has not been reported before for ML TaS$_2$. We associate this feature with partial gapping of the Fermi surface similar to the bulk case. Following the methodology of Ref. [47, 396], we divide the dI/dV signal by I/V whereby the features in the LDOS become more pronounced (see Appendix A.6). After background subtraction, we find a width of $2\Delta = (32 \pm 9)$ meV, where the scatter reflects the variation of the measured CDW gap due to variations of the tip state. Compared to the data of bulk 2H-TaS$_2$ in which $2\Delta = 100$ meV [383, 384], the

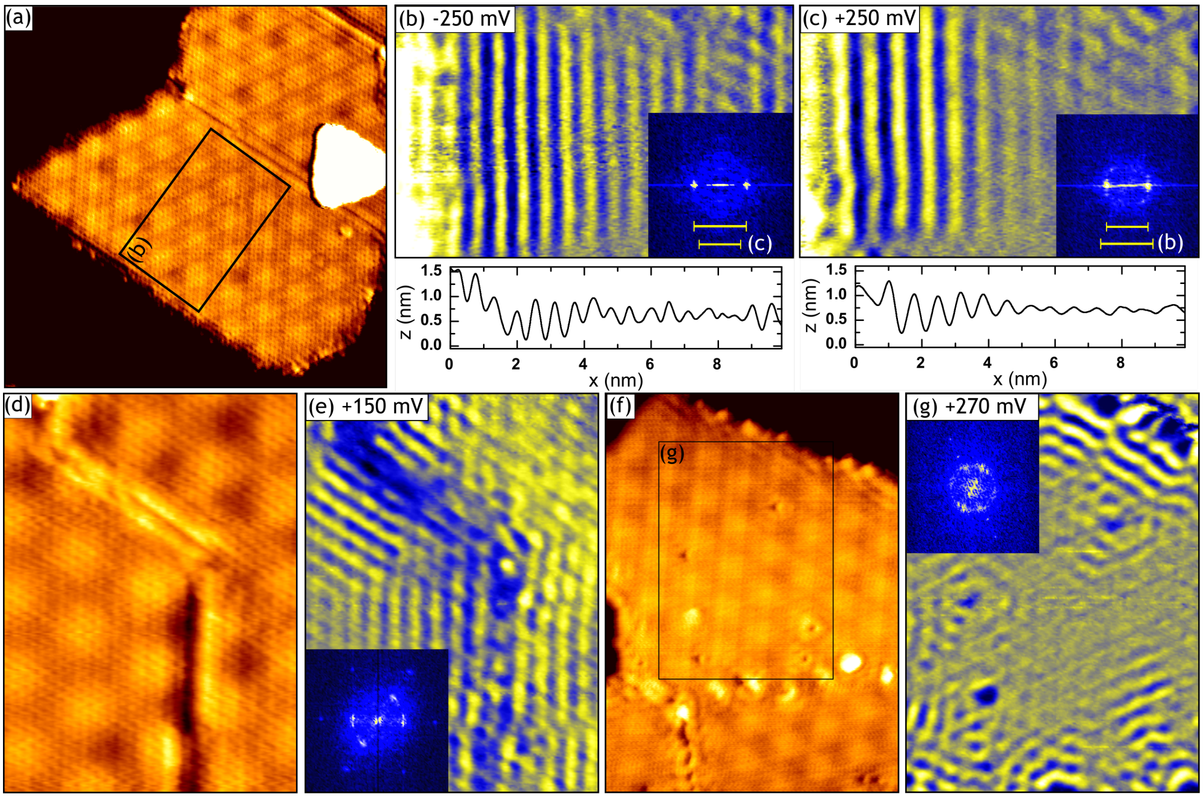

Figure 6.5: Standing wave patterns in the local density of states on the surface of TaS_2: (a) STM topograph of ML TaS_2 on Gr/Ir(111). On the right-hand side of the image a small bilayer island is visible. Please note the grain boundary in the middle of the monolayer island. The black square illustrates the location where (b) and (c) are measured. (b),(c) Constant current dI/dV maps at 5 K showing standing wave patterns on monolayer TaS_2 at -250 meV and 250 meV, respectively. In order to improve visibility of the standing waves, both the moiré and the 3×3 CDW are filtered out in Fourier space. The line profiles along the black lines illustrate the dispersive behaviour with energy, which is also reflected in the FT in the inset. (d), (e) STM topograph and constant current dI/dV map of a region with a kinked grain boundary. The FT in the inset illustrate shows the scattering wave vectors. (f), (g) STM topograph and LDOS map of a region with point defects reflecting the threefold symmetry of the scattering pattern. Image information (image size, sample bias, tunnelling current): (a) 25×25 nm^2, -300 mV, 80 pA, (b) 10×6 nm^2, -250 mV, 0.2 nA, (c) 10×6 nm^2, 250 mV, 0.2 nA, (d) 9×12 nm^2, -150 mV, 0.2 nA, (e) 9×12 nm^2, 150 mV, 0.2 nA, (f) 17×23 nm^2, 270 mV, 0.2 nA, (g) 10×14 nm^2, 270 mV, 0.2 nA

gap here is significantly smaller. Further details of the gap size and comparison with previous data are discussed below.

Both the antiphase behaviour of the occupied and unoccupied states and the partial CDW gap measured in STS make our assignment of the 3×3 as a CDW conclusive.

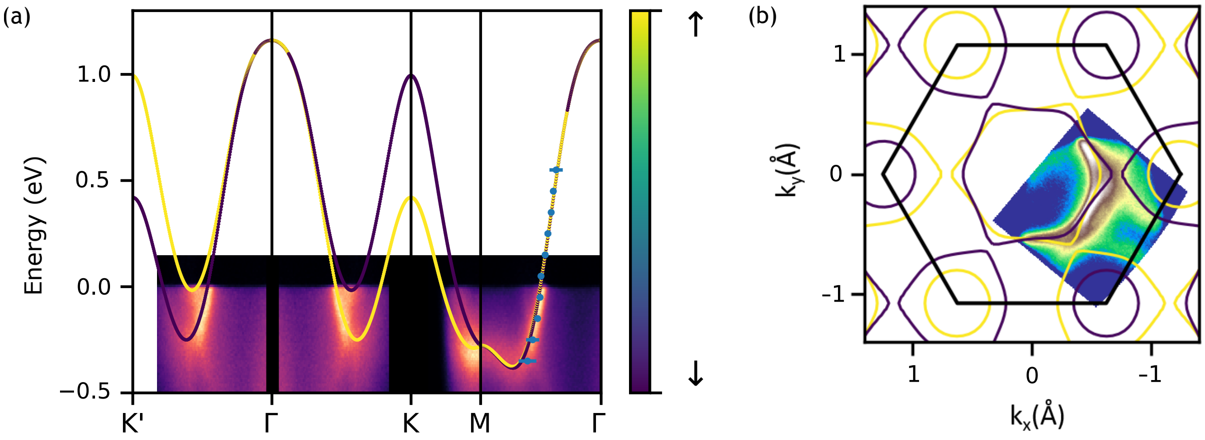

Figure 6.6: Band structure of ML TaS_2: (a) TB fit of the band structure based on experimental ARPES and STS (blue dots) data. The colour of the calculated bands indicates the spin contribution; yellow: spin up, magenta: spin down. The colour scale of the ARPES spectra in the background indicates photoemission intensity from orange (high intensity) to violet (low intensity). (b) Fermi surface as measured with ARPES and TB fit of Fermi surface. Colour scale of the calculated bands as in (a), colour scale of the Fermi surface ARPES data in the background indicates photoemission intensity from white (high intensity) to blue (low intensity). ARPES data was taken at about 40 K using 21 eV photon energy, except for the KM direction which was taken at about 100 K and 50 eV photon energy.

Band Structure Determination by Quasiparticle Interference and Angle-Resolved Photoemission Spectroscopy

The use of STM is not restricted to real space analysis, but can also be employed to obtain momentum space information *via* the scattering patterns visible in differential conductance maps. The dI/dV map is a probe of the LDOS, which is modulated in real space when quasi-particles get scattered by defects creating interference patterns.

Fig. 6.5 shows standing waves on the surface of TaS_2 on Gr/Ir(111). In the upper row, the dispersion of the waves with energy is illustrated. In Fig. 6.5 (a), an STM topograph of the position of panel (b) and (c) is shown. The ML island terminates to the left side and on the right-hand side, a grain boundary acts as a potential scatterer. The dispersion becomes apparent when comparing (b) and (c) and noting their different bias potential of -250 mV and $+250$ mV, respectively. The line profiles further illustrate the difference in wavelength. The FT in the insets of the dI/dV maps show a clear peak, which directly relates to the momentum wave vector of the quasi-particle, and therefore gives a k-position in the band structure.

The bottom row of Fig. 6.5 illustrates patterns formed by the presence of several scatterers. In Fig. 6.5 (d) and (e), both the topography and the LDOS map of an area with grain boundaries are shown and display strong scattering in ΓM direction. The direction is determined by the orientation of the moiré and the epitaxial relation between TaS_2 and Gr/Ir(111). The nearly exclusive propagation of the waves in ΓM direction is underlined in Fig. 6.5 (f) and (g). While (f) displays the topography, (g) shows the LDOS map and surrounding the point defects, clear preferential propagation with threefold symmetry is visible. The direction becomes again obvious in comparison with the moiré shown in (f).

By analysing the QPI patterns [229, 240, 397] in tandem with measuring the occupied band structure *via* ARPES, we quantitatively determine part of the electronic band structure of 2H-TaS_2 on Gr/Ir(111) and the result is plotted in Fig. 6.6.

In Fig. 6.6 (a), ARPES scans in high symmetry directions are shown. The ARPES data indicate a single spin-orbit split band which is attributed to the Ta *d* states, based on literature data for the 2H polytype [385, 398, 399]. The band is composed of a degenerate hole-like pocket around Γ experiencing stronger dispersion towards M than towards the K-direction. The TB fit of the band structure is based on both the ARPES data for the occupied states and the dispersion above and below the Fermi energy obtained by the standing wave pattern analysis around Γ (blue dots). By comparison to the TB fit, the spin-orbit split nature of the band in the ΓK direction and of the hole-like pockets at the inequivalent K points is evident. Overall, the TB fit perfectly reproduces the observed data, and the ARPES data display no hybridisation between the TaS_2 adlayer and its substrate.

Fig. 6.6 (b) displays the Fermi surface of TaS_2/Gr/Ir(111) and the corresponding TB fit. The hexagonal hole pocket around the centre of the BZ and the spin-split hole pockets around the K-points compare qualitatively well with bulk ARPES results [398, 399]. From the relative area of the occupied states enclosed by the Fermi surface we calculate the free charge carrier concentration and find 1.10 ± 0.02 electrons per unit cell, that is an excess or doping of 0.1 electrons per unit cell (in the following denoted as $x = -0.10$) in comparison to half-filling of the band. As the TB band structure is a fit to the experimental band structure, the estimate of the doping level based on it is much more precise than an estimate based on *ab initio* calculations.[1]

In summary, we find slightly doped ML TaS_2 to show a CDW state, with a periodicity close to 3×3. Both the CDW periodicity and the TB band structure we obtain from ARPES and STS are similar to the bulk counterpart.

6.3 A Disturbed 2×2 Charge Density Wave in Bilayer TaS_2

We investigate the layer dependency of the CDW properties of 2H-TaS_2 by adapting the growth conditions to promote bilayer growth, as presented in Section 4.2. Unexpectedly, BL TaS_2 shows a 2×2 CDW, which we analyse and discuss in the following.

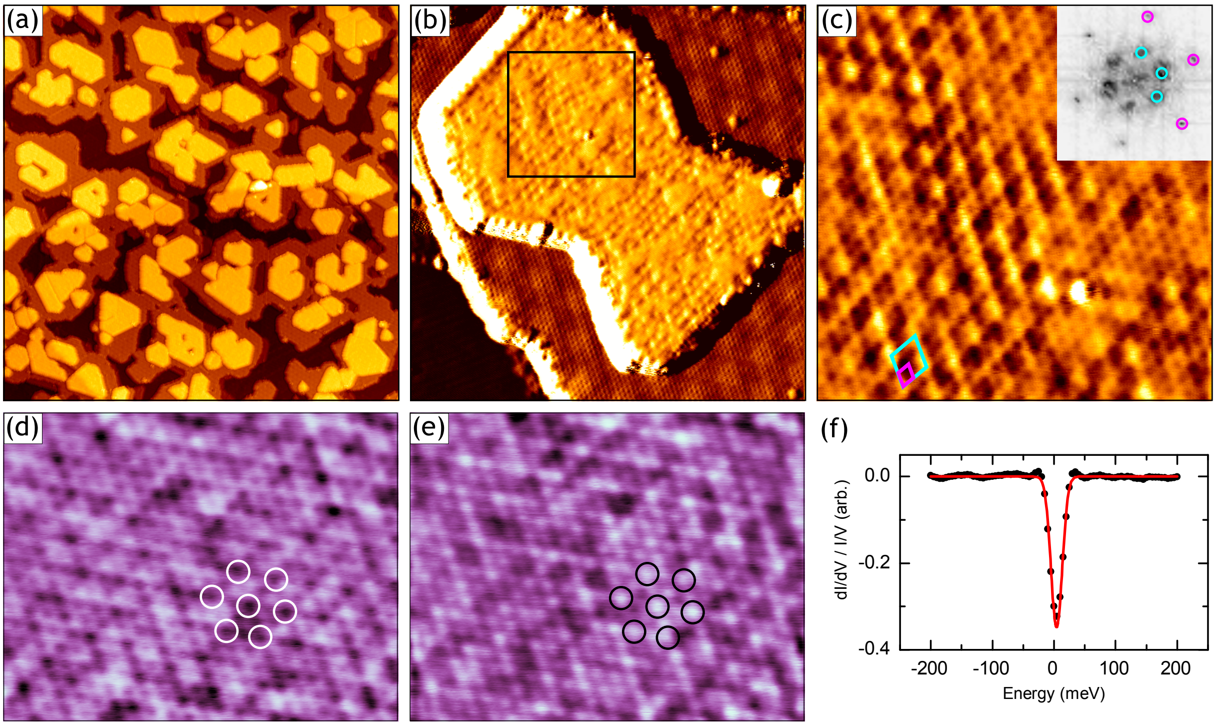

Figure 6.7: STM overview of BL TaS_2/Gr/Ir(111). (a) STM overview topograph. (b) Close up of BL TaS_2 showing a disturbed 2×2 superstructure. The black square indicates the location of panel (c). (c) Constant current STM showing the 2×2 superstructure with atomic resolution on BL TaS_2. The respective unit cells (2×2 CDW turquoise, atomic TaS_2 lattice violet) are shown. Inset: Fourier transform of the STM image with peaks related to the periodicity represented by unit cells circled in same colour as unit cell rhomboids. (d) Constant height STM topograph of the occupied states. (e) Corresponding constant height STM topograph of unoccupied states. The circles mark the same positions but indicate either local maxima or minima of the CDW. (f) normalised constant height STS spectrum on BL TaS_2 [47]. The scale is adjusted to be comparable to Fig. 6.4 (c) and Fig. 6.10 (b).
Image information [image size, (stabilisation) sample bias, (stabilisation) tunnelling current]: (a) $200 \times 200\ \mathrm{nm}^2$, 1.5 V, 0.1 nA, (b) $25 \times 25\ \mathrm{nm}^2$, -1 V, 1 nA, (c) $8 \times 8\ \mathrm{nm}^2$, -1 V, 4 nA (d) $7 \times 5\ \mathrm{nm}^2$, -0.05 V, $I_{\mathrm{stab}} = 0.1$ nA, (e) $7 \times 5\ \mathrm{nm}^2$, 0.05 V, $I_{\mathrm{stab}} = 0.1$ nA, (f) $U_{\mathrm{stab}} = -0.2$ V, $I_{\mathrm{stab}} = 10$ pA.

Key Features of the 2 × 2 Charge Density Wave in Scanning Tunnelling Microscopy

In Fig. 6.7 (a), a large scale STM overview of a sample with substantial BL coverage is shown. The top layer islands grow perfectly aligned to the respective ML TaS_2 bottom layer on Gr/Ir(111). We never find the second layer of TaS_2 with a rotational misalignment relative to the bottom layer. The strict epitaxial relation of the two TaS_2 layers is interpreted as a consequence of a strong interaction between the two layers in the BL case. Evidence is given by the absence of the Gr/Ir(111) moiré in

---

[1] The tight-binding fit was conducted using the quasi-Newton L-BFGS algorithm [400] to minimize the difference in energy between the ARPES peaks of the *d*-type TaS_2 band and the TB result. The TB model is an adapted version of ML MoS_2 models in literature [80] as the atomic structure is the same. As a starting point for the fit, MoS_2 fit parameters were adopted [80] with modified on-site energies to shift the Fermi level inside the *d*-type band.

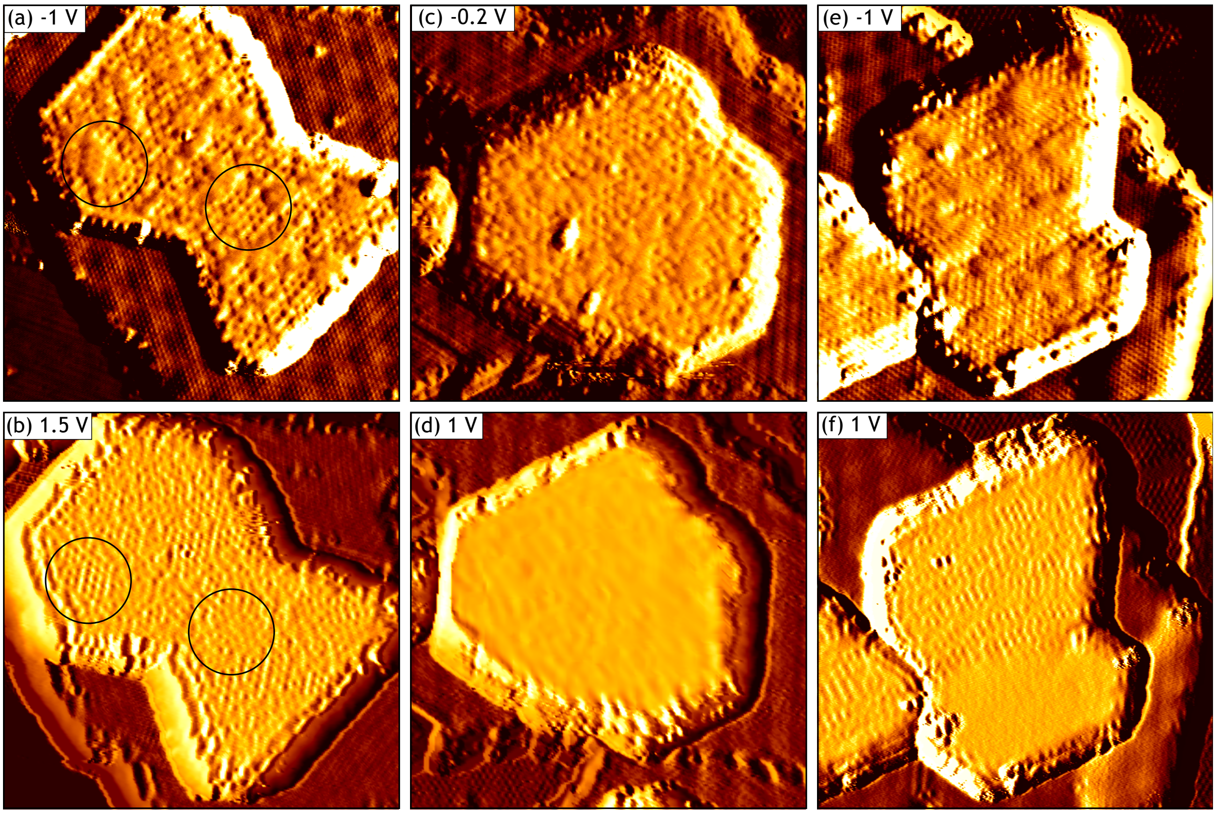

Figure 6.8: Comparison of different apparent topography in bilayer islands of TaS_2 in STM: (a,b) First kind of bilayer. Though a 2 × 2 is always visible, at opposing biases either CDW maxima or minima are visible. Circles mark the same position on the island, but either encircle blurred or clear regions. (c,d) Second kind of bilayer. At negative bias (occupied states) a disturbed 2 × 2 is visible. At positive bias (unoccupied states) internal structure is hardly observable. (e,f) Both kinds of bilayers grown together in one island. All images are an overlay of a topography and its derivative to increase atomic contrast while keeping topographic information.
Image information (image size, sample bias, tunnelling current): (a) 25×25 nm^2, -1000 mV, 1 nA, (b) 25×25 nm^2, 1500 mV, 0.1 nA, (c) 25×25 nm^2, -200 mV, 0.1 nA, (d) 25×25 nm^2, 1000 mV, 0.1 nA, (e) 25×25 nm^2, -1000 mV, 1 nA, (f) 25×25 nm^2, 1000 mV, 0.5 nA.

BL islands, consistent with a stronger interaction of the two TaS_2 layers as compared to the Gr-TaS_2 interaction.

Fig. 6.7 (b) shows one of the BL islands in higher resolution which exhibits internal structure. This is found to be a 2 × 2 superstructure with respect to the atomic lattice of TaS_2 and is of poor order compared to the 3 × 3 case in the monolayer. Though the atomic lattice does not show an increased defect density, the 2 × 2 periodicity is often only preserved over a few periods and may even be absent in small patches, see Fig. 6.7 (c). In (c), the 2 × 2 unit cell and the TaS_2 unit cell are indicated. The 2 × 2 superstructure is also visible in the Fourier transform of Fig. 6.7 (c) shown as an inset.

Analogous to the ML, we investigate the BL superstructure with constant height STM on opposing sides of the Fermi level. A comparison of Fig. 6.7 (d) and (e) illustrates the out-of-phase behaviour of the CDW contrast (the black and white circles again mark the same positions, but are either local CDW maxima or minima). The poorly ordered 2 × 2 thus represents a CDW.

Similar to the ML 3 × 3 CDW, a measurement of the differential conductance shows a reduced LDOS at the Fermi level [cf. Fig. 6.7 (f)], which is interpreted as a partial CDW gap. The numerical value of the BL gap width is $2\Delta = (18 \pm 9)$ meV, when the same analysis as for the ML is used.

General Aspects of Bilayer TaS_2 in Scanning Tunnelling Microscopy and Spectroscopy

It is interesting to note that we find two kinds of BL TaS_2 on the sample, which show distinct apparent STM topography, see Fig. 6.8. In panel (a) and (b), the first kind of BL is shown at opposing polarity. Regardless of the polarity, a disturbed 2 × 2 is always visible. In line with expected CDW behaviour, in the occupied states in (a), the contrast is dominated by dark depressions, while in the unoccupied states in (b), bright protrusions are visible. In addition to this, as indicated by circles, the same position may show a blurred contrast or a clear 2 × 2 depending upon the bias.

The second kind of BL behaves differently. At opposing biases, either a disturbed 2 × 2 or no internal structure, also noteworthy no moiré is visible, when imaged in STM overviews. This is shown in Fig. 6.8 (c,d). When investigating the two kinds of BL at atomic resolution, the 2 × 2 superstructure can be found in both – irrespective of the bias applied.

Rarely, the two kinds can be observed in one island separated by a straight border, as shown in 6.8 (e,f). STM alone cannot distinguish on the stacking order of the two layers, and though 2H-TaS_2 normally assumes $2H_a$ stacking (cf. Fig 1.1), it is not unlikely that MBE favours different growth modes than bulk crystal synthesis approaches. As an example, WSe_2 which usually comes with $2H_b$ stacking has been observed to show $2H_a$ stacking when grown by MBE [46]. We speculate different stacking symmetries to be the origin of the different behaviour in BL 2H-TaS_2 observed in STM.

As argued above, we interpret the interaction between the two TaS_2 layers to be stronger than the interaction of ML TaS_2 with Gr. A strong argument for this is the absence of coherent standing wave patterns on the surface of the BL, as visualised in Fig. 6.9. In (a), an STM topograph illustrates the area of the differential conductance maps shown in (b)-(f), which display a series with varying energy. As a general feature of all images shown, the ML shows strong standing wave patterns which decrease in amplitude towards the interior of the flake. On the BL on the other hand, no such pattern is evident. Although the BL will have more bands crossing the Fermi level and therefore different wavelength could be expectable, we cannot make out any clear dispersing behaviour. The only periodicity we do recognise locally is non-dispersive and fits well to the 2 × 2 CDW in BL TaS_2.

In conclusion, we find BL TaS_2 to show a distorted 2 × 2 CDW. The strict epitaxial relation of the second layer to its respective first layer and the absence of standing wave patterns on the BL surface are indications for stronger interaction, possibly hybridisation and doping.

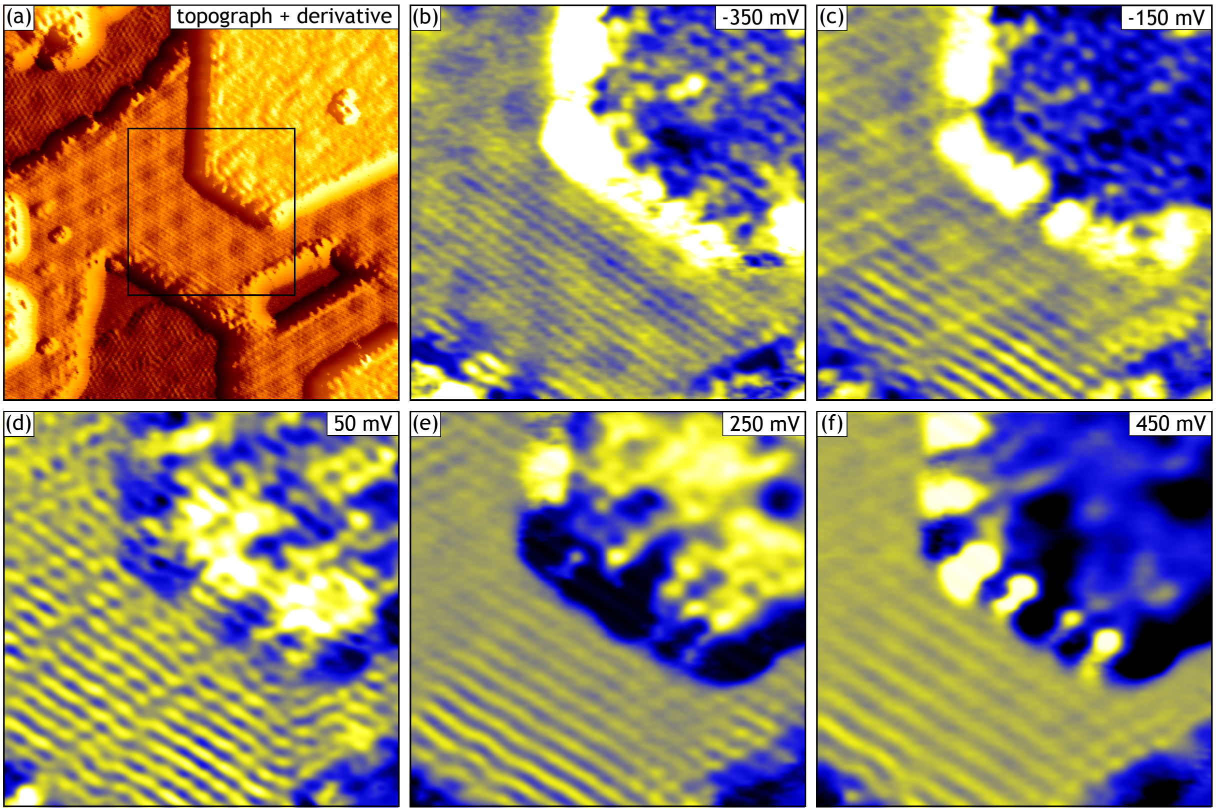

Figure 6.9: No standing waves on BL TaS_2: (a) STM topograph illustrating the area of the following images indicated by the black box. The image is overlaid with its derivative to enhance visibility. (b)-(f) Series of constant current dI/dV maps at 5 K with the applied bias indicated. The dispersion of the standing waves in the LDOS on the ML is obvious. In the BL, the pattern is distorted. The non dispersing feature on the BL corresponds to a 2×2 CDW.
Image information (image size, sample bias, tunnelling current):(a) $30 \times 30\ \mathrm{nm}^2$, -200 mV, 0.1 nA, (b)-(f) $12 \times 12\ \mathrm{nm}^2$, bias indicated, 0.1 nA.

6.4 Doped Monolayer TaS_2

To investigate the influence of doping on the CDW, TaS_2/Gr/Ir(111) at 500 K is exposed to Li vapour. The STM topograph in Fig. 6.10 (a) taken after exposure shows distinct features:
(A) On the ML TaS_2, a regular superstructure is present, which is enlarged in the inset. Relating this structure to the dense-packed TaS_2 directions *via* the TaS_2 lattice allows inference of a $(\sqrt{7} \times \sqrt{7})\mathrm{R}19.1^\circ$ superstructure, which we interpret as a result of ordered Li adatom adsorption.
(B) The moiré of Gr/Ir(111) is no longer visible on the ML TaS_2 islands.
(C) Li intercalation structures can be observed under Gr. These features lead to the interpretation that Li can be found on TaS_2, under Gr, and presumably also in between Gr and ML TaS_2. The indistinct intercalation distribution impedes a precise Li coverage determination. We estimate 0.2 ML $= 2.0 \times 10^{18}$ atoms m^{-1} as a lower bound to the total Li coverage. We further performed DFT calculations that estimate an increase of the doping level through Li adsorption by 0.25 electrons per

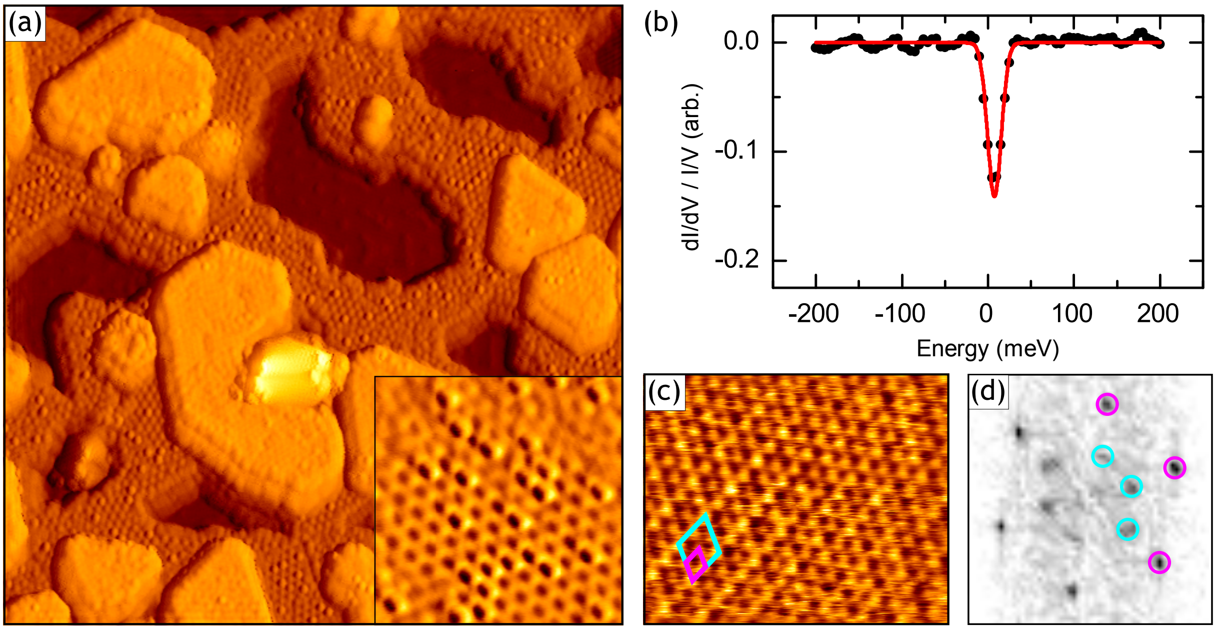

Figure 6.10: Li doped TaS_2: (a) Large scale STM topograph showing the entire sample surface to be covered by Li adatoms. In the inset an ordered $(\sqrt{7}\times\sqrt{7})$R19.1° is visible. (b) Constant height STS spectrum on Li/ML TaS_2/Gr/Ir(111), treated following the methodology of Ref. [47]. The scale is adjusted to be comparable to Fig. 6.4 (c) and Fig. 6.7 (f). (c) Constant current STM taken at 30 K on ML TaS_2 showing atomic TaS_2 resolution and 2×2 indications, both marked with their respective unit cell. (d) Corresponding Fourier transformation.
Image information [image size, (stabilisation) sample bias, (stabilisation) tunnelling current]: (a) 60×60 nm^2, -0.8 V, 0.1 nA, inset: 10×10 nm^2, -0.3 V, 0.1 nA (b) $U_{\text{stab}} = -0.15$ V, $I_{\text{stab}} =$ 0.2 nA, (c) 6×5 nm^2, 0.01 V, 1 nA.

unit cell ($x = -0.25$) at a coverage corresponding roughly to the experimental one. Details are given in the Appendix A.7.

The normalised differential conductance around the Fermi level of the $(\sqrt{7}\times\sqrt{7})$R19.1° superstructure of ML TaS_2 is shown in Fig. 6.10 (b). The partial energy gap of size $2\Delta = (19 \pm 9)$ meV is strong evidence for a remanent CDW. We note that at the spectroscopy temperature of 5 K the STM tip is not able to remove Li. Only by increasing the temperature to 30 K, the Li-adlayer could be removed from the ML TaS_2 with the STM tip, and the atomic lattice of TaS_2 becomes visible. It still exhibits periodic modulations as shown in Fig. 6.10 (c). Both in the STM topography and in the Fourier transform in Fig. 6.10 (d) these modulations relate to a poor 2×2 superlattice ordering.

In the literature, bulk TaS_2 intercalation compounds show a variety of stable intercalation structures [66]. Also, ordered Li intercalation structures were reported [401, 402] and even preliminary data for 2×2 intercalation was mentioned [401]. It can therefore not be excluded that the observed 2×2 superlattice may relate to intercalant ordering under ML TaS_2. Nevertheless, as no other superstructure is present and a partial gap in the density of states at the Fermi level is found, it is plausible that doping changed the CDW periodicity in the ML from 3×3 to 2×2.

We also attempted to remove Li by thermal annealing to 800 K. Unexpectedly, this did not only

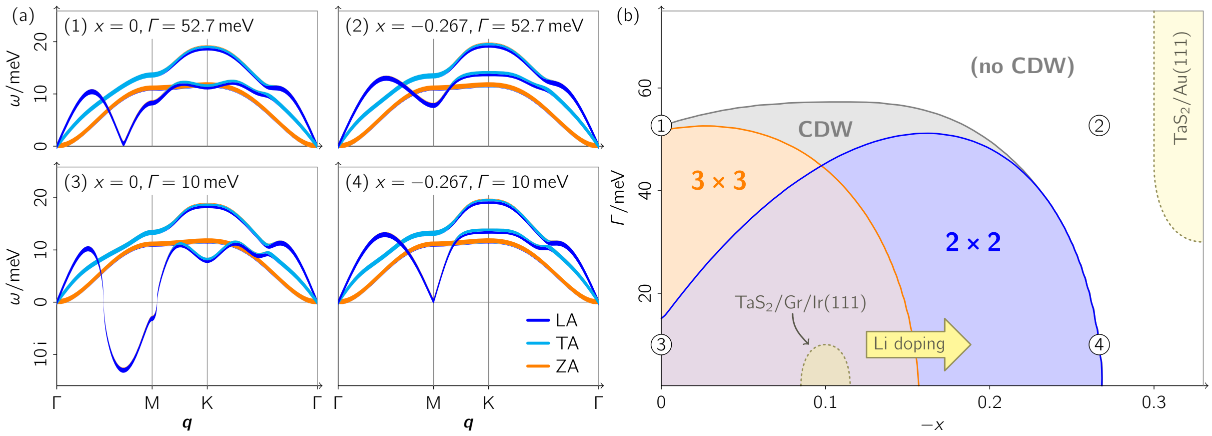

Figure 6.11: Phonon dispersions and lattice instabilities of ML TaS_2 under different electronic conditions at temperature $T = 0$: (a) Acoustic phonon dispersions for different levels of hybridisation with the substrate, Γ (HWHM of the electronic broadening), and charge doping, x in units of electrons per Ta atom. $x < 0$ refers to electron addition. The character of the phonon modes, *i.e.* longitudinal (LA), transverse (TA), or out-of-plane (ZA), is marked in colour. Imaginary phonon mode energies indicate that the lattice is unstable towards corresponding periodic lattice distortions. (b) Phase diagram of lattice instabilities in ML TaS_2. The CDW region is defined by the presence of an imaginary phonon energy at one or more $\mathbf{q}$ points. Regions with instabilities at M for the 2×2 and at $2/3\,\Gamma\mathrm{M}$ for the 3×3 CDW are marked in colour. The experimentally realized situations of pristine ML TaS_2/Gr/Ir(111), as well as Li doped as in this work, and ML TaS_2/Au(111) (Ref. [35, 391]) are located in the phase diagram. Points corresponding to the phonon dispersions shown in (a) are marked with encircled numbers 1–4.

result in Li desorption but in a complete change of morphology of the TaS_2. This topic will be discussed in Section 6.6. We note that no ML islands are left, which prevents investigation of the ML surface.

6.5 Theoretical Analysis of the Charge Density Wave Transition

In order to understand the microscopic origins of the CDW states observed experimentally, we performed calculations of phonon dispersions based on a combination of DFT, DFPT and many-body perturbation theory [266, 403]. We calculated the phonon self-energy, $\Pi_{\mathbf{q}\alpha\beta}$ [see Appendix A.8, Eq. (A.4)], which encodes the renormalisation of the phonon dispersion due to interactions of the phonons with the electrons from the TaS_2 conduction band. On this basis, we analyse how the interplay of several external control parameters, *i.e.* electronic hybridisation with substrates, doping, and interlayer potentials, affects lattice dynamics and stability in TaS_2.

The dependence of the resulting renormalised phonon dispersions in ML-TaS_2 on doping and hybridisation with a substrate is shown in Fig. 6.11 (a). The panels are ordered as in the corresponding phase diagram in Fig. 6.11 (b). That is, the lower-left corner (3) marks the quasi-freestanding case and the strength of doping and hybridisation increases when going to the right and top, respectively. Each panel shows the corresponding phonon dispersion. In the quasi-freestanding case, *i.e.* undoped

($x = 0$) and weakly hybridized ($\varGamma = 10\,\mathrm{meV}$), the longitudinal-acoustic (LA) phonon branch exhibits a strong Kohn anomaly. Phonon modes with imaginary energy imply that the lattice is unstable with respect to corresponding periodic distortions and charge ordering. The density functional theory establishes a local extremum in the Landau energy functional $E(\xi) = E_0 + \frac{1}{2}\omega_{\tilde{q}}^2\xi_{\tilde{q}}^2 + \ldots$. This functional quantifies the energy cost of moving the atoms out of the DFT equilibrium position by some distortion $\xi_{\tilde{q}}$. The square of the phonon energy $\omega_{\tilde{q}}$ is the coefficient of the quadratic contribution to the energy. Therefore, an imaginary phonon frequency implies an energy *gain*, which means that the equilibrium is unstable towards distortions with the corresponding wave vector $\tilde{q}$. This linear response theory reveals the existence of instabilities, but it does not predict the distorted structure (corresponding to the global minimum of the Landau functional). However, the mode with the largest imaginary frequency, also called leading instability is a clear indicator of energetically particularly favourable distortions. In the quasi-freestanding case, the instability region extends over large parts of the Brillouin zone including the wave vectors $\mathbf{q} = 2/3\,\Gamma\mathrm{M}$ and M. At $\mathbf{q} = 2/3\,\Gamma\mathrm{M}$, which is associated with the 3 × 3 CDW in the ML, the lattice instability is particularly strong as indicated by a large imaginary phonon frequency.

When considering the other panels in Fig. 6.11 (a), we see that doping and hybridisation with a substrate can strongly affect the phonon dispersions. In essence, we find that electron doping moves the wave vector of the leading instability, *i.e.* largest imaginary frequency, from $\mathbf{q} \approx 2/3\,\Gamma\mathrm{M}$ to M such that the CDW shifts in wavelength. At electron doping exceeding 0.267 electrons per $\mathrm{TaS_2}$ unit, the lattice becomes dynamically stable, which is in agreement with previous calculations [389]. This situation is depicted in panel (4).

An increase in hybridisation, on the other hand, leaves the wavelength of the leading CDW instability largely unchanged, but weakens the Kohn anomaly and eventually also renders the lattice stable, see panel (1). Thus, both doping and hybridisation trigger a quantum phase transition from CDW to undistorted states of the lattice but *via* different critical wave vectors. The overall relation between lattice instabilities, doping and hybridisation is summarized in the phase diagram shown in Fig. 6.11 (b).

Applied to the experiments performed here, we can state the following: in ML $\mathrm{TaS_2}$/Gr/Ir(111) a doping level of $x = -0.10$ excess electrons per unit cell is measured in ARPES, while no signs of hybridisation are experimentally observed. We, therefore, locate the ML $\mathrm{TaS_2}$/Gr/Ir(111) in the phase diagram of Fig. 6.11 (b) in the region around $x = -0.10$ and $\varGamma \to 0$, which is in line with the 3 × 3 CDW observed in STM. Intercalating Li increases the doping and moves the system towards the right-hand side of the diagram. We estimate $x = -0.25$ based on DFT calculations, see Appendix A.7. This is consistent with the experimental observation of a 2 × 2 CDW in the Li-doped system.

It is important to note that previous experiments [35] on ML $\mathrm{TaS_2}$/Au(111) did not find any charge order down to 4.7 K. A major difference to the experiments reported here, including those with Li intercalation, is the significant hybridisation between $\mathrm{TaS_2}$ and the Au(111) substrate [391]. Our calculations show that hybridisation may effectively prevent charge order. The hybridisation affects

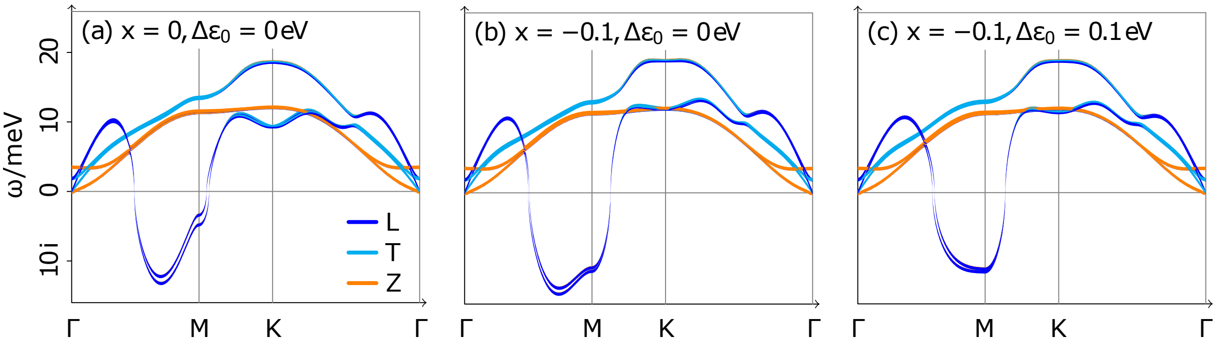

Figure 6.12: Influence of interlayer bias potentials: (a - c) Dispersions of the acoustic phonon branches of BL 2H-TaS$_2$ at different levels of charge doping x and interlayer bias potential $\Delta\epsilon_0$ for a fixed broadening $\varGamma = 1\,\mathrm{meV}$.

the phonon dispersions through the phonon self-energy $\varPi_{\mathbf{q}\alpha\beta}$, Eq. (A.4), and is much more effective in quenching $\varPi_{\mathbf{q}\alpha\beta}$ than thermal broadening (see Appendix A.8). For ML TaS$_2$/Au(111), the hybridisation is energy-dependent [391] and the half-width at half-maximum (HWHM) broadening $\varGamma$ spans a range between 30 meV and 90 meV[2]. Taking also into account the electron (pseudo-)doping [391] in the range between $x = -0.3$ [35] and -0.4 [391] and the hybridisation between $\varGamma = 30\,\mathrm{meV}$ and 90 meV, we are able to place ML TaS$_2$/Au(111) in the phase diagram of Fig. 6.11 (b). Clearly, the interplay of both stabilises the lattice. Lattice relaxation can further support this stabilisation [389, 390].

In Section 6.3, we showed the result of a 2 × 2 CDW in BL 2H-TaS$_2$. In the following, we discuss the mechanisms behind its existence from the point of view of phonon dispersions. In Fig. 6.12 (a), calculated phonon dispersions of freestanding undoped BL 2H-TaS$_2$ are shown. The dispersion and in particular the instability regions in freestanding undoped BL [cf. Fig. 6.12 (a)] are indeed very similar to the corresponding ML case [cf. Fig. 6.11 (a)]. Thus, it is *a priori* unexpected that BL TaS$_2$/Gr/Ir(111) features a 2 × 2 CDW in contrast to the 3 × 3 CDW in ML TaS$_2$/Gr/Ir(111) and also to the 3 × 3 CDW in bulk TaS$_2$.

The question that arises is: what could drive the CDW order in the BL towards 2 × 2? From the knowledge we acquired from the ML case, charge doping is a strong candidate. Since direct interaction in the BL with the substrate is limited to the bottom layer, stronger average charge doping as in the ML due to interaction with the substrate is unlikely. A possible cause of stronger average charge doping could be different defect densities in the monolayer and in the bilayer case. Clearly, in the BL the doping from and hybridisation with the substrate are naturally different for the bottom and top layer. Also, doping due to defects within the layers can be different for each layer due to inequivalent local growth conditions. Such asymmetries between the bottom and top layer might affect CDW formation. In our model, this kind of asymmetries are most simply accounted for

---

[2] We have based our estimate for the electronic broadening on the results of Ref. [391], which contains DFT results for TaS$_2$ with and without Au(111) substrate. A broadening of 30 meV explains the change in spectral weight at the Van Hove singularity, and a broadening of up to 90 meV is needed to describe the transfer of spectral weight into the gap.

in terms of an interlayer bias potential $\Delta\epsilon_0$ (energy gain $-\Delta\epsilon_0/2$ or penalty $+\Delta\epsilon_0/2$ for an electron residing in the bottom or the top layer), the effect of which is illustrated in Fig. 6.12 (b) and (c). We find that the interlayer bias can flatten the phonon dispersion in the regions of the instability and eventually also shift the $\mathbf{q}$ vector of the leading instability from $\mathbf{q} = 2/3\,\Gamma\mathrm{M}$ towards M. Thus, an effective interlayer bias could also explain the observation of the 2×2 CDW in the BL regions.

In conclusion, we theoretically study how doping and hybridisation act on the phonon dispersion of $\mathrm{TaS_2}$. In the pristine case, the lattice dynamics are dominated by a Kohn anomaly around $\mathbf{q} = 2/3\,\Gamma\mathrm{M}$. We have observed that doping shifts the instability region, which is associated with a change in CDW periodicity, resulting in a 2×2 CDW. On the other hand, hybridisation hardly affects the periodicity, but eventually stabilises the lattice. We assign an interlayer bias as a possible driving force for the 2×2 CDW in the BL $\mathrm{TaS_2}$.

6.6 Growth Related

Widening the scope of this chapter, we now consider aspects closely related to the leitmotif of this thesis - growth control of 2D layered materials. In this regard, we tackle two issues reaching out from the basis we have laid in Section 4.2. On the one hand, we explore how to reduce nucleation density in vdWE and thereby enlarge grain sizes; an ability which is key to both furthering fundamental flexibility and enabling industrial applicability. On the other hand, we show how to control growth mode and polytype via the substrate interaction, while leaving the TMDC in its chemically pristine environment.

Enabling Large Grain Size

In theory, there are two key parameters for enabling large grain sizes in vdWE:
(i) A high substrate temperature during growth decreases the nucleation rate, enhances surface diffusion and therefore prevents many small grains to form.
(ii) A low deposition rate also reduces the nuclei count through lowering of the adsorption rate.

Fig. 6.13 illustrates the influence of substrate temperature and deposition rate on the morphology of $\mathrm{TaS_2}$ islands. In panel (a) – (c) STM topographs show the results of synthesis with a deposition rate of $0.5\ \mathrm{ML\,h^{-1}} = 1.4\times10^{15}\ \mathrm{atoms\ m^{-2}\,s^{-1}} \approx 0.1\,F_{\mathrm{Ta}}^{\mathrm{ref}}$ but different growth substrate temperatures as indicated. The total deposited amount of $\mathrm{TaS_2}$ corresponds to 0.95 ML, which in (a) – growth temperature 300 K – divide in 0.7 ML being present in the first layer and 0.25 ML in the second layer. For the growth at 500 K substrate temperature during the growth step in (b), the nucleation density of second layer island goes down by a factor 2, but the total amount of second layer coverage island still measures 0.2 ML. Consequently, about 0.75 ML $\mathrm{TaS_2}$ are present in the first layer. Only when going to sufficiently high temperatures, the second layer is reasonably suppressed. In panel (c), the surface is covered by 0.7 ML first layer island and no second layer islands are present.

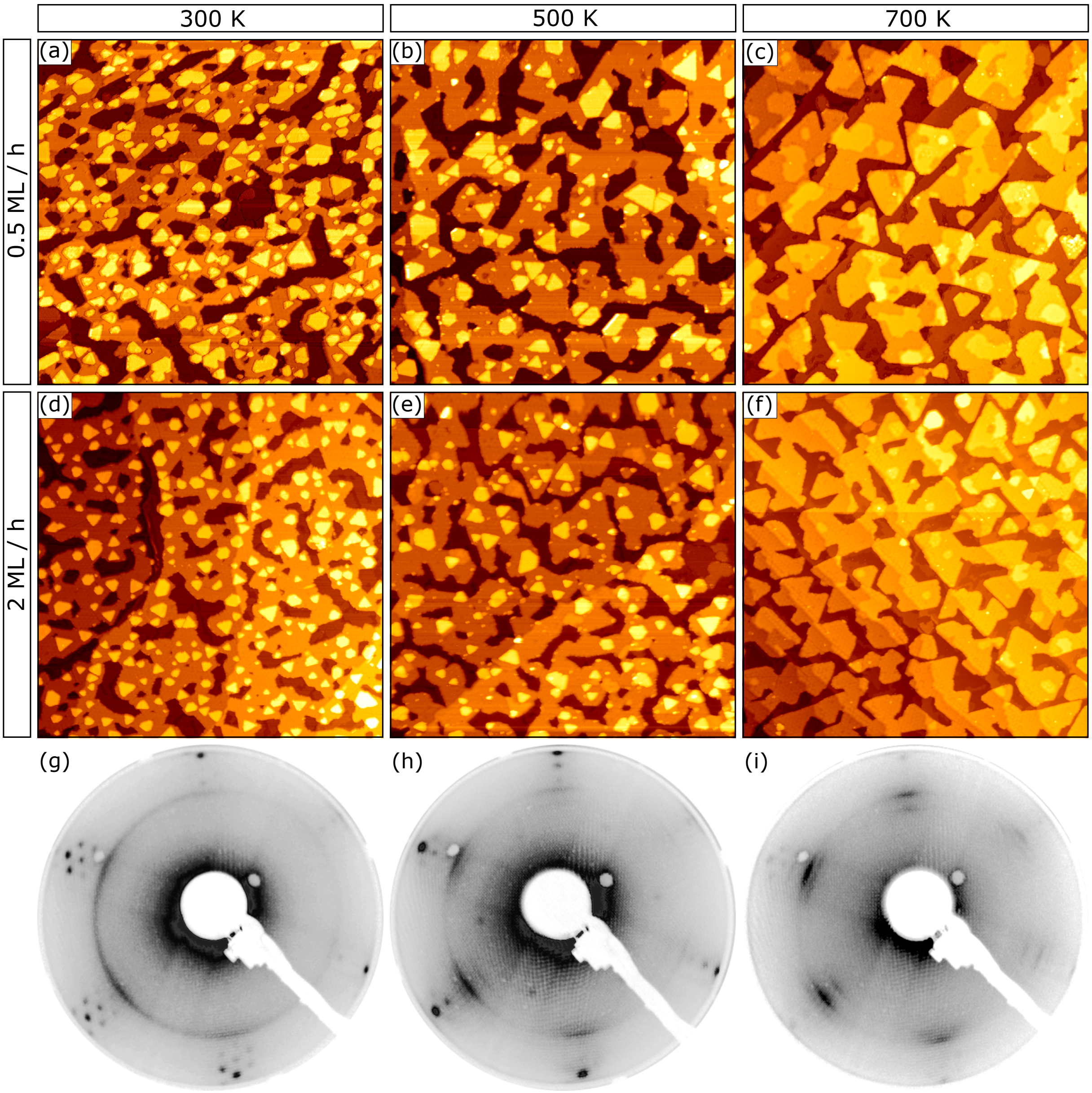

Figure 6.13: STM topographs illustrating the influence of growth temperature and deposition rate on the morphology of TaS_2 after the two-step synthesis: (a) – (c) Growth at 0.5 ML $h^{-1} = 1.4 \times 10^{15}$ atoms $m^{-2} s^{-1} \approx 0.1 F_{Ta}^{ref}$ but different substrate temperatures during the growth step as indicated. For all images $P_{sulphur}^{g} = 1.5 \times 10^{-8}$ mbar were used. The bilayer nucleation density decreases substantially with increasing temperature. (d) – (e) Growth at 2 ML $h^{-1} = 5.6 \times 10^{15}$ atoms m^{-2} $s^{-1} = 0.3 F_{Ta}^{ref}$, but different growth substrate temperature as indicated. For all images $P_{sulphur}^{g} = 2 \times 10^{-8}$ mbar were used. The trend with temperature is the same, and the influence of the deposition rate is best seen when comparing (c) and (f): a lower growth rate enlarges lateral grain size. (g) – (i) LEED pattern of the corresponding temperatures at 68 eV.
Image information: (image size, sample bias, tunnelling current): (a) 200×200 nm^2, -0.9 V, 0.2 nA, (b) 200×200 nm^2, 0.9 V, 0.1 nA, (c) 200×200 nm^2, -0.8 V, 0.5 nA, (d) 200×200 nm^2, -0.6 V, 30 pA, (e) 200×200 nm^2, -1.2 V, 10 pA, (f) 200×200 nm^2, -0.9 V, 0.5 nA.

The increase in substrate temperature comes at the expense of decreased chalcogen residence time (enhanced desorption) on the sample surface and a consequential change in effective Ta : S ratio. If the local chalcogen flux is to low, metal-rich clusters form on the surface, and may subsequently intercalate at high temperature, which explains the additional structures observed in (c).

We also conducted TaS_2 growth directly at the annealing temperature of 1000 K, which corresponds to a one-step synthesis. Though this growth approach yields lateral grain sizes of up to 70 nm with no second layer output, we failed to reliably reproduce the synthesis, because of insufficient S pressures (the maximum growth pressure used was 1×10^{-7} mbar). Appendix A.9 shows a successful synthesis.

The second row in Fig. 6.13 shows how the above situation evolves with a change in deposition rate. The series of topographs in Fig. 6.13 (d) – (f) displays a growth series with a deposition rate of $2\,\mathrm{ML\,h^{-1}} = 5.6 \times 10^{15}\,\mathrm{atoms\,m^{-2}\,s^{-1}} = 0.3\,F_{\mathrm{Ta}}^{\mathrm{ref}}$ and varying substrate temperature as before, which allows direct comparison. Close inspection of the average lateral dimension of the structures reveals the subtle effect of the growth rate: comparing each (a) with (d) and (b) with (e) shows the second layer islands to be larger in the $0.5\,\mathrm{ML\,h^{-1}}$ rate series. The same is true and even more evident for comparison of (c) with (f). In both cases, the surface area coverage is 70 %, but in (c) the lateral dimensions are larger. We further note that in (f) the S pressure used was higher than in (c) resulting in lower intercalation rate.

Noteworthy, an intuitive comparison of the amount of second layer area is misleading and should not be done. As the total amount of deposited TaS_2 is slightly different in the two series, this obviously affects the total amount of second layer islands.

Figures 6.13 (g) – (i), show LEED patterns, in which the influence of the growth rate is not evident. We observe that: while in (g), after growth at 300 K almost a full ring corresponding to the lattice parameter of TaS_2 is shown, the epitaxial relation improves considerably with temperature. Already at 500 K in (h), the diffraction ring is broken up into elongated spots, show an angular spread of about 12° which align with the substrate. Increasing the temperature further for 700 K in (i) reduces the angular misalignment further, which now amounts to about 8°. In (h), we note the $\mathrm{S}(\sqrt{3} \times \sqrt{3})\mathrm{R}30^\circ$ intercalation structure, which is due to the particular synthesis, not general to the temperature.

As shown, the growth substrate temperature and the deposition rate are important factors when controlling the growth morphology. While a growth temperature around 700 K enables exclusive monolayer growth mode, the deposition rate can be used to control lateral grain sizes.

Polytype Transition

The substrate temperature does not only act on the nucleation density and growth morphology but may also allow post-growth polytype transitions. Figure 6.14 illustrates that it is principally possible

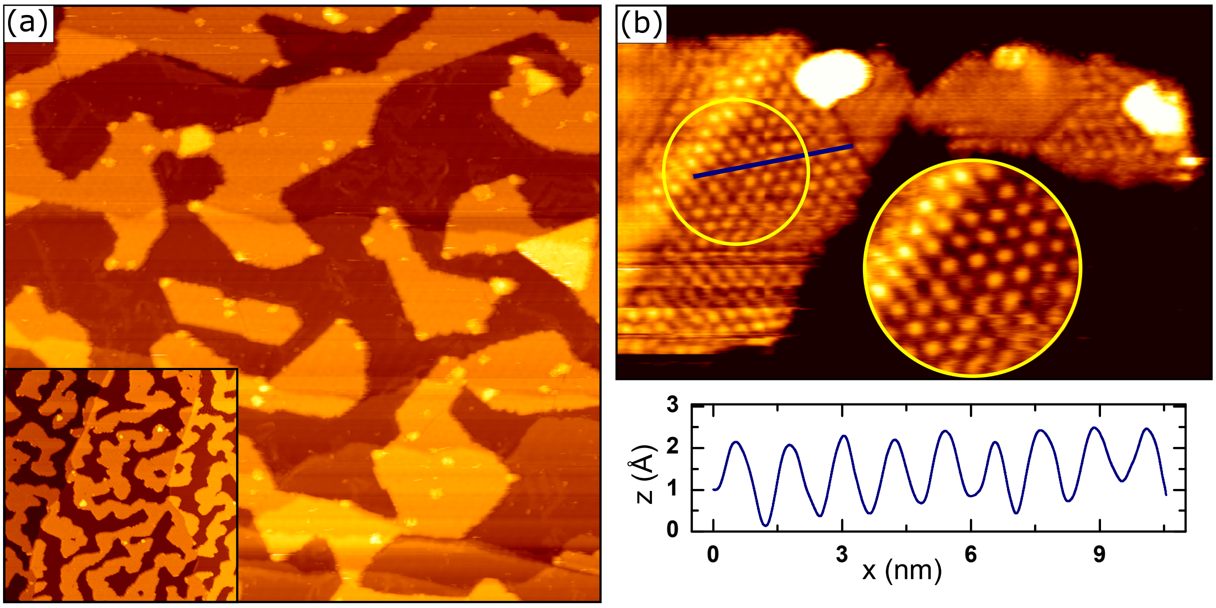

Figure 6.14: Polytype transition of 2H-TaS$_2$ to 1T-TaS$_2$: (a) STM topograph before (inset) and after (main panel) annealing 2H-TaS$_2$ to 1100 K in 5×10^{-8} mbar S vapour background. After the high temperature, the islands partially decompose and the island edges favour epitaxial orientation. (b) Room temperature STM close-up of an island showing a superstructure of periodicity (12.10 ± 0.05) Å. The structure is enhanced in the yellow circle. The line profile along the blue line shows a high corrugation of about 2 Å. Please note the different scaling compared to the 3 × 3 CDW amplitude in Fig. 6.1 (c).
Image information (image size, sample bias, tunnelling current): (a) 160×160 nm^2, 1 V, 20 pA, inset: 160×160 nm^2, 0.9 V, 0.2 nA, (b) 40×25 nm^2, 0.5 V, 0.2 nA.

to convert a sample which is entirely present in the 2H structure to the 1T structure through annealing at high temperature. In panel (a) overview STM topographs are shown. The sample was first grown using the usual recipe and reference parameters, *i.e.* growth step at room temperature and annealing at 1000 K in sulphur background. The inset of panel (a) shows the resulting network of coverage about 0.6 ML dominantly at monolayer height. When then annealing the sample at 1100 K in a high sulphur background of 5×10^{-8} mbar (to compensate for island decomposition), the sample morphology changes as shown in (a). As visible, the lateral island size increases and the islands develop hexagonal shapes. Though the high sulphur pressure prevents a severe decomposition of the islands and is possibly the cause for the bilayer islands (compare Fig. 4.2), additional signs of decomposition are present.

Furthermore, while a large part of the islands are preserved in the 2H structure (the 3 × 3 CDW is visible at low temperatures, not shown), a small part of the islands show a characteristically changed structure. Figure 6.14 (b) shows an STM topograph of a representative island. The superstructure which is present at room temperature shows a periodicity of (12.10 ± 0.05) Å and is rotated by roughly 15° with respect to the epitaxially oriented island edges. The line profile along the blue line indicates a high corrugation amplitude of about 2 Å. These observations are in agreement with the 1T structure [18, 404].

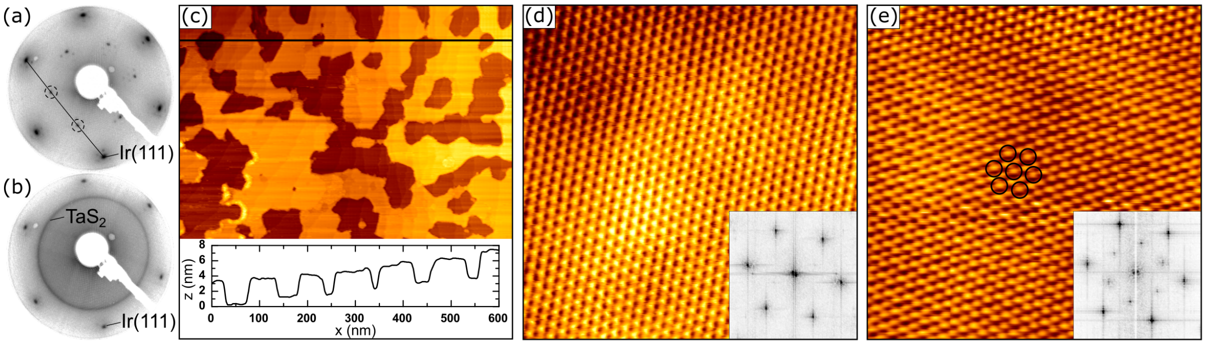

Figure 6.15: Effect of Eu intercalation below Gr on the growth morphology of TaS_2: (a) LEED pattern at 84 eV of Gr/Eu/Ir(111) showing a $(\sqrt{3} \times \sqrt{3})R30^\circ$ intercalation phase with respect to Ir(111). (b) LEED data at 84 eV after growth of TaS_2 on top. (c) STM topograph of the sample morphology. The large area shows multiple step edges. (d) STM close-up of the TaS_2 surface at room temperature. Inset: corresponding FT. (e) STM close-up of the TaS_2 surface at 40 K. Inset: corresponding FT.
Image information (image size, sample bias, tunnelling current): (c) 600×450 nm^2, 1.8 V, 50 pA, (d) 10×10 nm^2, -0.005 V, 1 nA, (e) 10×10 nm^2, 0.03 V, 0.1 nA.

We conclude that though the two-step synthesis, with a growth step at comparably lower temperatures, clearly favours the 2H phase in TaS_2, this can principally be manipulated by annealing to very high temperatures. This, however, comes at the expense of a high decomposition rate and thus requires high S fluxes.

Changing the Morphology *via* the Substrate Interaction

As the substrate interaction is a very important aspect in epitaxy, we explore how doping affects the system TaS_2/Gr/Ir(111). In an elegant approach, a suitable dopant can be inserted between Gr and Ir(111), which leaves the TMDC in its pristine chemical environment.

We here prepare Eu intercalated Gr/Ir(111) and afterwards grow TaS_2 on top, which shows a severe change in morphology, as Fig. 6.15 documents. In panel (a), a LEED pattern firstly illustrates the structure of Eu under Gr *via* a $(\sqrt{3} \times \sqrt{3})R30^\circ$ intercalation phase [254]. The intercalated Eu acts twofold on Gr: it firstly decouples Gr from Ir, which is evident by the decreased intensity of the moiré in LEED. Secondly, it strongly *n* dopes Gr by about 1.4 eV [254]. The effect of the decoupling on the on top grown TaS_2 is readily seen in LEED. Fig. 6.15 (b) indicates the nearly complete loss of any epitaxial relation between TaS_2 and its substrate *via* a full circle corresponding to the lattice parameter of TaS_2. The large scale STM topograph in (c) illustrates the effect of the strong doping: the entire growth morphology changed and ML TaS_2 is no longer present on the sample. The line profile verifies this through an average island height of about 3 Å at which a fringed network spans over the sample surface. Locally, the stained surface appearance of the islands is indicative of charge inhomogeneities, which however do not affect the room temperature appearance on the atomic level in panel (d) strongly. Both the STM topograph and the FT in the inset indicate pure hexagonal order, without any moiré or superstructure.

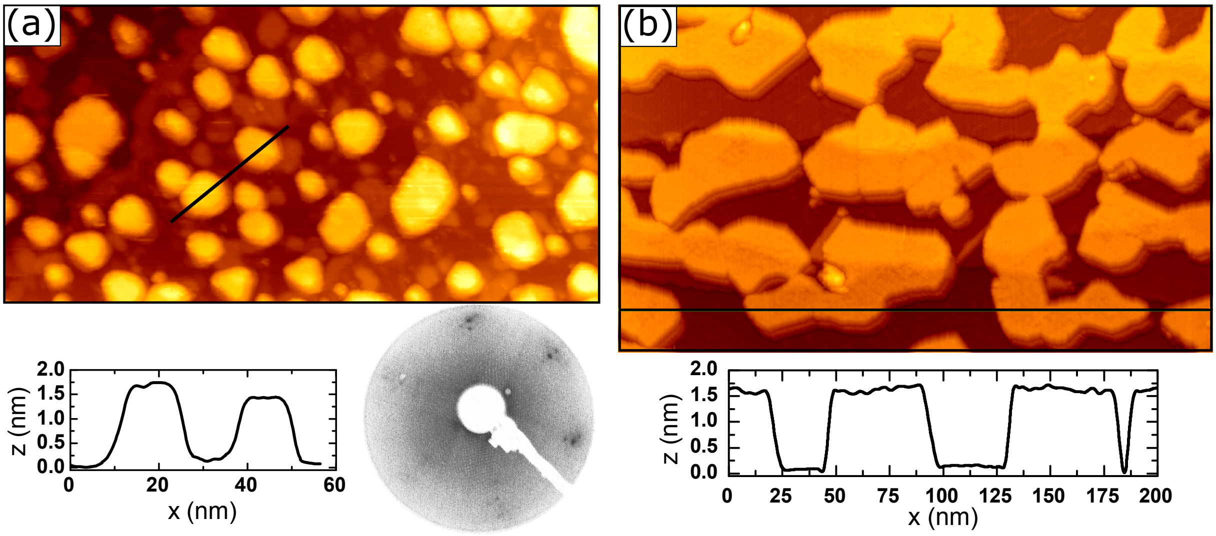

Figure 6.16: Changed morphology after exposing doped TaS_2 to high temperatures. (a) STM topograph of TaS_2 grown on Li intercalated Gr. Gr was exposed to Li at 500 K till weakening of moiré reflections in LEED is achieved. Afterwards, TaS_2 is grown on top. For synthesis reference parameters were chosen except of $F_{\mathrm{Ta}} = 0.5\,F_{\mathrm{Ta}}^{\mathrm{ref}} = 8.3 \times 10^{15}$ atoms m^{-2} s^{-1}, $t^{g} = 780\,\mathrm{s}$ and $T^{a} = 800\,\mathrm{K}$. The line profile along the black line indicates the absence of monolayer islands. LEED data at 90 eV hardly display TaS_2 reflections. (b) Sample morphology after a sample with partial bilayer coverage [cf. Fig. 6.7 (a)] was exposed to Li [cf. Fig. 6.10 (a)] and subsequently exposed to 800 K. The line profile along the black line indicates the absence of monolayer islands.
Image information (image size, sample bias, tunnelling current: (a) $200 \times 100\,\mathrm{nm}^2$, -1 V, 50 pA, (b) $200 \times 120\,\mathrm{nm}^2$, -0.8 V, 50 pA.

It is interesting to investigate the influence of this change on the CDW in TaS_2. Panel (e) shows an STM topograph of the TaS_2 multilayer surface at 40 K, far below the bulk transition temperature of 75 K [56]. Though the STM topograph does not present the superstructure easily, it is visible in the FT (inset). As a guide to the eye, the $(\sqrt{3} \times \sqrt{3})\mathrm{R}30^\circ$ superstructure is indicated by the black circles in real space. It is important to mention that in the course of our investigations on TaS_2, $(\sqrt{3} \times \sqrt{3})\mathrm{R}30^\circ$ superstructures have been observed also at room temperature and only in multilayer systems. We, therefore, rule out electronic origins such as a CDW but consider the possibility of intercalant Ta atom ordering between the two vdW layers. Here, the important note is the absence of a 3×3 or a 2×2 CDW at low temperatures. This may either relate to a too high doping level [similar to case of TaS_2 on Au(111) discussed in Section 6.5] or to an non-stoichiometric compound $Ta_{1+x}S_2$ not favouring CDW formation.

Before discussing possible reasons for the change in growth mode, we show that this behaviour is not unique to intercalation with Eu. Similar observations are made, when intercalating Gr with Li and then growing TaS_2 or when a sample that was doped by Li evaporation after its growth is exposed to high temperatures. This is shown in Fig. 6.16.

Panel (a) of Fig. 6.16 shows the result of TaS_2 growth on Li doped Gr. To begin with, it is important to note that this sample was not annealed to 1000 K as usually used for TaS_2, but only to

800 K. This decision is based on thermal desorption studies we performed, which indicated Li to be stable under Gr up to 900 K, whereafter it quickly deintercalates. Panel (a) shows that although the growth morphology has again entirely changed (compared to Fig. 6.15), still only multilayer heights are present. TaS_2 now aggregates in very compact islands (without fringed edges) that seem to show preferred heights of either 14 nm or 16 nm, which is indicated by the line profile along the black line. A precise height distribution determination, however, is hampered by a mixture of intercalation structures and possible ghost islands which are drawn into the image by a double STM tip. The LEED pattern is also ambiguous: the strong background noise indicates a high level of disorder and even the TaS_2 spots are questionable.

For a sample grown following the usual recipe [the morphology is presented in Fig. 6.7 (a)], then doped by Li [cf. Fig. 6.10 (a)] and afterwards exposed to 800 K, the result is again a clean multilayer network, as shown in panel (b). The line profile indicates an average height of about 1.6 nm, which is slightly higher than the bilayer height presented in Fig. 6.1. The nature of these morphology changes is unclear and will be discussed below.

In conclusion, STM measurements revealed metastability related to the growth of TaS_2. When grown on a doped but otherwise inert substrate a sudden change in growth mode drives the system to multilayer regime.

6.7 Discussion

Our investigations reveal that ML 2H-TaS_2 shows very similar characteristics to the bulk counterpart. This may be based on the fact that both QPI (Fig. 6.5) and ARPES (Fig. 6.6) indicate the decoupling from the substrate *via* only small doping of 0.1 excess electrons and the absence of hybridisation, which is strongly corroborated by the occurrence of standing wave patterns of the DOS visible close to defects. Since the overall band shape of the Ta *d* band crossing E_F in the monolayer case is in stark similarity to the bulk case, the observation of a 3×3 CDW state at low temperatures is in line with the expectation. Further corroboration is given by DFT calculations that reveal a Kohn anomaly at the CDW periodicity corresponding wave vector. The only deviation from previous bulk measurements is the size of the CDW gap, which we measure to be $2\Delta = (32 \pm 9)$ meV. A comparison of our pristine dI/dV spectrum (cf. Appendix A.6) with a spectrum from the literature [383] reveals this discrepancy to arise substantially from the two different analysis methods. While in Ref. [383] the gap is merely estimated, Ref. [47] points out that in STS on TMDCs the partial CDW gap may be located very near to features related to the flat *d* band of the transition metal. These may be assigned falsely to the CDW gap edge and artificially increase the gap size. The normalisation by I/V helps to disentangle these effects and puts the gap determination on reproducible grounds.

When interpreting the CDW phase transition from 3×3 to 2×2 in going from the ML to the BL, the different environment of the BL compared to the ML has to be taken into account. To specify, the first layer TaS_2 growing on Gr/Ir(111) has a different substrate (*i.e.* Gr) than the second layer, which grows on TaS_2 as a substrate. Considering the system ML TaS_2/Gr it can be stated that the

interaction between the two layers (and therefore the hybridisation) seems negligible, because:
(i) In constant current dI/dV maps standing wave patterns can be observed (cf. Fig. 6.5).
(ii) ARPES data are not indicative of any band hybridisation, Fig. 6.6.
In contrast to this, we assume stronger binding (and therefore stronger hybridisation) of the second TaS_2 layer to the first one:
(I) Standing wave patterns are hardly visible in the BL and are strongly distorted, see Fig. 6.9.
(II) The epitaxial relation between the second layer and the first layer is strict, while the ML TaS_2 islands display orientation scatter with respect to graphene.

Our investigations on Li doped ML 2H-TaS_2 further indicate that a change in doping level stabilises the CDW at a different wave vector to which DFT yields insight: the doping level causes a renormalisation of the phonon band structure, which shifts the Kohn anomaly - the instability region that is associated with the periodic lattice distortion of the CDW - towards the M point and consequently shorter CDW periodicities.

In the case of BL 2H-TaS_2, the origin of possible additional doping may be speculated to arise from a surplus of Ta atoms being present in the vdW gap between the two TaS_2 layers. This phenomenon of self-intercalation has been observed in bulk TaS_2 [394, 405], and may provide additional charge.

The shift of the Kohn anomaly, however, may not only arise from charge transfer due to external stimuli such as doping but also follows within DFT from an effective interlayer bias, that may naturally occur in the BL case due to the asymmetric environment of the top and bottom layer.

Though it should be mentioned that evidence for a 2×2 ordering has been found in isostructural and -electronic pristine 2H-$NbSe_2$ [406], this structure has not yet been observed in TaS_2. Finally, whether additional doping or interlayer asymmetries are the cause for the switching from 3×3 to 2×2 CDW in the bilayer case in our experiments remains speculative.

Regarding the investigated growth properties of 2H-TaS_2 on Gr/Ir(111), the results are twofold: firstly, the influence of the growth substrate temperature and the deposition rate on the growth morphology is strongly in line with the expectations and literature [206, 210, 281]. Both parameters are key to enabling large uniform grain sizes. While we observe the substrate temperature to be more efficient in suppressing second layer nucleation, the growth rate facilitates enlarging lateral dimensions.

Secondly, the effect of doping the substrate *prior* to TaS_2 growth is non-intuitive. When *n* doping 2H-TaS_2, subsequent exposure to high temperatures induces a transition to multilayer regime revealing the monolayer to be energetically costly. While it seems reasonable to relate the additional charge transferred from the dopant to the change in morphology, the microscopic mechanisms behind this transition are not yet understood. It appears that the doped surface influences the competition on the thermodynamic stability between the single-layer and the multilayer and apparently weakens the adhesion of TaS_2 on Gr. Furthermore, in a general approach, the resulting morphology – monolayer or multilayer – can be interpreted as a consequence of the competition of minimising the formation of destabilising island edges and maximising the van der Waals stacks that stabilise the system [407]. However, the substrate plays an additional role that also has to be taken into account [210], and

Coloumb repulsion and screening effects of the intercalate ions by the host electrons may affect the energetics. The role of subtle effects such as band filling and the effective d electron count that are known to affect morphologies in TMDCs [408, 409], will have to remain topics of future investigations.

6.8 Conclusion

Quasi-freestanding monolayer 1H-TaS$_2$ on Gr/Ir(111) displays a 3×3 CDW, while bilayer 2H-TaS$_2$ on the same substrate exhibits a less well ordered 2×2 CDW. The CDW gaps measured are $2\Delta = (32 \pm 9)$ meV and $2\Delta = (18 \pm 9)$ meV, respectively. For the ML the band structure and the Fermi surface were determined with ARPES. No indication of hybridisation between Gr and TaS$_2$ is present. Using a TB fit to the ARPES data and the dispersion of states near Γ obtained from standing wave patterns in STS maps, doping of 0.10 ± 0.02 additional electrons per unit cell is deduced.

Exposure to Li vapour causes a $(\sqrt{7} \times \sqrt{7})$R19.1° adatom superstructure on top of monolayer 1H-TaS$_2$, presumably accompanied by intercalation. A 2×2 periodicity measured after removal of the adatom phase together with a partial gap of $2\Delta = (18 \pm 9)$ meV imply the presence of a 2×2 CDW.

Our theoretical analysis reveals the microscopic contributors behind CDW (de-)stabilisation and the experimentally observed changes in periodicity. It emphasizes the importance of environmental embedding in the study of 2D materials: the theoretically derived CDW phase diagram of TaS$_2$ as a function of doping and hybridisation shows that both can suppress CDW order. The critical wave vectors $\mathbf{q}_c$ of the associated quantum phase transition from the CDW to the undistorted lattice depend on the stimulus driving CDW destabilisation and are $\mathbf{q}_c = 2/3\,\Gamma\mathrm{M}$, and $\mathbf{q}_c = \Gamma\mathrm{M}$ in the doping and hybridisation driven case, respectively.

In the BL TaS$_2$ case the experimental finding of 2×2 charge order is surprising given that the phonon dispersion of freestanding pristine BL TaS$_2$ is very similar to that of the ML. Our analysis shows that an interlayer potential can push the preferential CDW ordering vector towards ΓM, which could explain the observed 2×2 order. Additional charge from self-intercalated Ta in the vdW gap could also be responsible for this phonon renormalisation, but this remains speculative.

Additionally, the growth study performed supports high substrate temperature and slow deposition rate to be important to enable large grain sizes. A morphology transition towards the multilayer regime can be induced when exposing doped 2H-TaS$_2$ to elevated temperatures.

Quite generally, our results demonstrate that phase diagrams of van der Waals heterostructures are high-dimensional due to the all surface nature of the constituents. Every interface, either between van der Waals bound 2D layers or between 2D layers and a three-dimensional substrate allows additional control parameters to enter the stage – control parameters that could be made operative in heterostructure based devices.

PART IV

Summary and Outlook

Growing Transition Metal Disulphides on Inert Substrates

This thesis investigates the growth of sulphur based TMDCs *via* MBE. We demonstrate the synthesis of single to few-layer TMDCs on weakly interacting substrates *via* a simple yet versatile two-step technique. It consists of a low-temperature growth step, where the metal is deposited in a background sulphur pressure, and an annealing step, which is again performed under sulphur supply. In the first step, the low temperature and use of elemental S vapour from the solid-state compound FeS_2 allow to keep the background S pressure needed to a minimum and ensure clean samples. In the annealing step at high temperatures, epitaxial orientation, and large and compact island shapes are achieved.

The quasi-freestanding nature of the thin layers on Gr on Ir(111) is indicated by several surface science techniques. Considering semiconducting 2H-MoS_2, the MBE-grown single layers display a large band gap of (2.53 ± 0.08) eV in tunnelling spectroscopy and may even be moved and picked up by the STM tip. The absence of hybridisation of electronic states from the epilayer with the substrate is shown by ARPES, which furthermore highlights the 2H structure through a valence band maximum that is clearly found at the spin-split K valleys. The splitting amounts to 144 meV. Raman spectroscopy indicates independent thermal expansion and, finally, PL with a narrow peak width of 18 meV is observed.

We show the synthesis method to be versatile by demonstrating both the synthesis of three other TMDSs and by changing the substrate to h-BN on Ir(111).

Though the proof-of-principle demonstration of MoS_2 growth on h-BN has been given, it would be very interesting to expand the investigations on h-BN. The large band gap of h-BN could decouple the semiconductor MoS_2 even further and field-effect transistors based on MoS_2 and h-BN promise to be of high performance [410, 411]. However, the corrugation of h-BN on Ir(111) may become a challenge. On the one hand, the corrugation can lead to spatially modulated interaction strength with the substrate that may serve as an interesting laboratory concerning the effect on the TMDC. On the other hand, this inherently brings along a non-homogeneous environment that can be detrimental for applications. Suitable intercalants that reduce the corrugation of h-BN on Ir(111) are not tried and tested yet. However, as the interaction of h-BN with metals like Cu, Ag, Pt or Au is comparably weak, these promise to be a good starting point [412].

Understanding van der Waals Epitaxy

We, furthermore, provide detailed insight into the growth and annealing mechanisms in vdWE using MoS_2 as an example. While LEED indicates the TMDC to form already at room temperature, at this stage, the islands display dendritic forms and low alignment with the crystallographic axes of the substrate. During the annealing step, the structures reshape and reorient through island and edge diffusion and eventually form compact epitaxially aligned islands. The island decomposition, which happens at high temperatures can be partially counterbalanced by an applied S background, although this can also affect the growth morphology.

We investigate the influence of repeated growth cycles and find two effects. Firstly, repeated cycles improve the overall alignment and secondly, they promote multilayer morphologies. Building on this knowledge, we employ a seeding technique. Here, only a small amount of material is deposited in the first cycle to minimise second layer formation, which facilitates maintaining epitaxial order at high monolayer coverages.

The effect of inadvertently intercalated S under Gr was studied and found to lower the quality of the on top grown TMDC. Firstly, as doping of Gr by S is indicated to be small, an effect on the doping level of MoS_2 is not apparent. Secondly, S decouples Gr from Ir(111) and therefore reduces the epitaxial alignment of the TMDC. Thirdly, the intercalation introduces thin island morphologies and an increased density of point defects.

In the last part, we classify the typical kind of defects encountered in MBE-grown MoS_2. We use this topic to introduce experimental progress enabled through the newly developed technique, which concerns the electronic structure inside and around MoS_2 MTBs and the reversible amorphisation through defect production.

Stoichiometric VS_2 and Sulphur Depleted Phases

Regarding the system V-S, our investigations underline the complexity of the system and add novel phases to its phase diagram. In the monolayer regime, three different phases have been synthesised, once stoichiometric 1T-VS_2 and two sulphur deficient ones.

The investigate layers of stoichiometric monolayer 1T-VS_2 do not show indications for a CDW or magnetism. Since systematic studies on the monolayer 1T-VS_2 and possible correlation induced phases have remained elusive so far, a mechanism which fosters monolayer growth is needed. Here, we propose three approaches: (i) Slow growth at high S excess at around $350 - 400$ K could enable to grow larger area monolayer islands of higher quality. (ii) A stronger substrate interaction as, for example, in the system Gr/Ir(110) could facilitate monolayer stabilisation. (iii) Since substrate doping has been shown to influence the growth morphology in 2H-TaS_2, a similar mechanism could be studied for 1T-VS_2. As *n*-dopant, intercalated Eu could be readily tested. Though suitable *p* dopants are rare, the low temperatures used for growth of pristine VS_2 may allow O intercalation. This approach, however, is highly speculative and a better understanding of the monolayer-multilayer morphology change through *n* doping in TaS_2 is needed.

We also present two novel 2D phases. The first shows a regular $\sqrt{3} \times 7$ superstructure and the second has striped appearance. The nature of the first phase remains ambiguous and needs further investigations. Spectroscopic data could indicate an energy gap around the Fermi energy, and clear the possibility of CDW nature to the superstructure. The second phase forms through a reconstruction of the lattice as a consequence of the high amount of S depletion and is reproducibly formed at elevated temperatures. It would be interesting to support its structural stability through theoretical calculations, which could even indicate possible magnetic behaviour.

In the multilayer regime, our investigations firstly show clear indications for a CDW phase. Since the islands are locally self-intercalated, the $V_{1+x}S_2$ islands serve as an interesting platform to investigate the influence of local doping on the $(\sqrt{3} \times \sqrt{3})R30^\circ$ CDW. Low-temperature STS would be able to measure the local CDW gap and yield information on the size of the FS gapping. It is, however, necessary to achieve enhanced control over the V-S system to reliably control the self-intercalation rate at will.

Environmental Control of Charge Density Wave Order

Our investigations on TaS_2 give unambiguous results that the CDW phase persists in the monolayer. The 3×3 periodicity is visible in STM topographs and a CDW energy gap of (32 ± 9) meV is measured around the Fermi energy. DFT calculations of the phonon dispersion indicate a Kohn anomaly at the CDW wave vector that is associated with the instability.

The CDW persistence is interpreted as a consequence of the low interaction of TaS_2 with the substrate. This, in turn, is illustrated through standing wave QPI patterns in the LDOS of the TaS_2 surface in low-temperature STS. Analysing those together with ARPES gives a TB fit to the band structure, which indicates a carrier concentration of 1.10 ± 0.02 electrons per unit cell. In addition, ARPES again highlights the absence of hybridisation between TaS_2 and the substrate.

When exposing TaS_2 to Li vapour, $(\sqrt{7} \times \sqrt{7})R19.1^\circ$ Li adatom ordering is observed and presumably accompanied by intercalation. On top of this phase, we measure a (18 ± 9) meV energy gap. After removal of Li with the STM tip a 2×2 superstructure is indicative of a CDW phase transition. Similar behaviour is found on the bilayer TaS_2, which shows a disturbed 2×2 CDW and an energy gap of (18 ± 9) meV.

Employing DFT calculations, we infer the role of doping and hybridisation on the CDW transitions and offer a phase diagram with respect to these parameters. We find that phonon renormalisation can explain the change in periodicity and both are able to stabilise the lattice above critical values.

Possible reasons for this unexpected phase transition in the bilayer are discussed in terms of an interlayer potential and possible self-intercalation of TaS_2.

Since the reason for the phase transition remains speculative, further investigations on the system BL TaS_2/Gr/Ir(111) are imperative. XPS could give insight on the possibility of Ta self-intercalation and would be needed to be corroborated by ARPES showing a higher doping level in the BL.

Finally, using TaS_2 as an example, we demonstrate the influence of the growth substrate temperature and the deposition rate during the two-step synthesis. Since the high substrate temperature causes S to desorb at a high rate, increased S background pressures are needed to prevent severe intercalation. We show that the elevated growth temperature is an efficient lever to suppress second layer nucleation and that a slow deposition rate is beneficial for enlarging grain sizes.

Summarising the overall growth study results, we consider the following route to be promising for larger-scale TMDS synthesis: a three-step technique including a first low coverage seeding step in which a small amount is deposited and quickly annealed to ensure highly ordered islands. In a second step, using low-rate deposition at elevated temperatures the residual material is deposited. The temperature should enable thorough suppression of second layer nucleation, but not imply the need for excessive S pressure. Afterwards, a quick annealing step to the usual annealing temperature will ensure optimal epitaxial order.

PART V

Appendix

APPENDIX A

Scientific Appendix

The scientific appendix contains contributions from ***J. Hall****, N. Ehlen, J. Berges, W. Jolie, M. Rolf, T. Wekking, B. Pielić, C. Murray, C. van Efferen, C. Speckmann, B. V. Senkovskiy, M. Hell, E. van Loon, G. Di Santo, L. Petaccia, C. Busse, , M. Kralj, T. Wehling, A. Grüneis and T. Michely.*
A.1 *T. Wekking measured the mass spectra of the S vapour from* FeS_2 *under* ***my*** *supervision.* ***A.2 I*** *investigated the behaviour and thermal stability of Mo on Gr/Ir(111).* ***A.3 I*** *investigated the Gr/S(*$\sqrt{3}\times\sqrt{3}$*)R30°/Ir(111) and Gr/S(*4×2*)/Ir(111) phase, where W. Jolie took part of the STM data on Gr/S(*4×2*)/Ir(111).* ***A.4*** *ARPES on BL* MoS_2 *was taken by N. Ehlen,* ***me****, and B.V. Senkovskiy, who were instructed by G. Di Santo and L. Petaccia how to use the system at the BaDElPh beamline at ELETTRA synchrotron, Trieste. N. Ehlen, B. V. Senkovskiy, analysed ARPES.* ***A.5 I*** *investigated the thermal stability of* MoS_2 *on Gr/Ir(111) with the help of B. Pielić .* ***A.6 I*** *took and analysed the STS spectra with the assistance of M. Rolf.* ***A.7*** *J. Berges performed the DFT calculations on Li doping of* TaS_2*.* ***A.8*** *J. Berges and E. van Loon performed the DFT calculations of the phonon dispersion.* ***A.9 I*** *investigated high temperature MBE growth. A. Grüneis supervised optical measurements, T. Wehling supervised theoretical calculations and STM/STS measurements were supervised by T. Michely.*

A.1 The S Vapour From FeS_2

We measure the composition of vapour from FeS_2 by direct evaporation into a mass spectrometer inside a small test chamber. The background pressure in the test chamber is 3×10^{-9} mbar. At a distance of 8 cm between Knudsen cell and mass spectrometer and a chamber pressure of 5×10^{-8} mbar due to thermal decomposition of FeS_2, we measure the spectra shown in Fig. A.1. The spectrum is dominated by the signal at 64 amu, which we interpret as diatomic sulphur S_2 and a possible fraction of SO_2. We interpret the second highest signal at 32 amu as

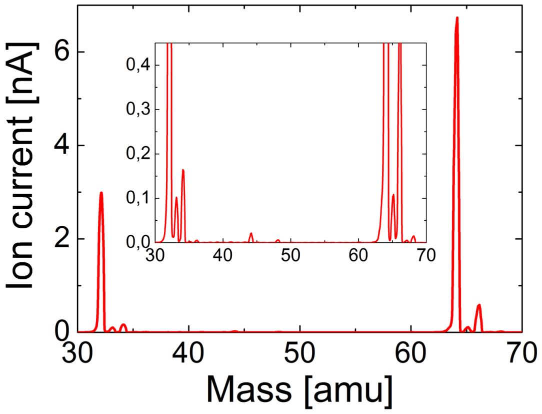

Figure A.1: Mass spectrum of FeS_2 vapour at a chamber pressure of 5×10^{-8} mbar. Inset: spectrum at increased resolution for small ion currents.

arising predominantly from doubly ionised S_2, with possible contributions from O_2 and atomic sulphur S. Besides high signals for masses 32 amu and 64 amu, the spectrum shows a well measurable signal for mass (33) 34 amu, which we interpret as (ionised) hydrogen sulphide H_2S. The peak at (65) 66 amu is interpreted as (ionised) hydrogen disulfide H_2S_2, which readily decomposed to H_2S and elemental S and may then contribute to the aforementioned peaks. It is worthwhile to mention that the spectrum shows no iron evaporation at an expectable mass of 56 amu.

A.2 Mo on Gr/Ir(111)

In Fig. 3.2 (d), bright bumps up to 50 Å height are observed and attributed to Mo clusters *on* Gr. This assignment is based on experiments that show the same features for experiments after Mo deposition on Gr/Ir(111), shown in figure A.2. Please note that in this experiment no sulphur was used. In figure A.2 (a), an STM topograph of Mo deposited on Gr/Ir(111) at room temperature is shown. As Mo does not wet Gr, clusters of several nm height are observable. Upon annealing to 1000 K, the topograph in figure A.2 (b) develops. Here, we identify four features, marked with numbered arrows in the figure. (1) Mo clusters on Gr, which may be compared to the ones in (a). (2) Mo intercalation islands, which are easily identifiable as under Gr by their moiré on top. (3) Mo islands on Ir(111), which do not show any moiré on top. We assume Mo has reacted with Gr and removed large areas. (4) Bare Ir(111) which has been laid open by Gr removal through Mo etching, but has not been fully covered by Mo successively.

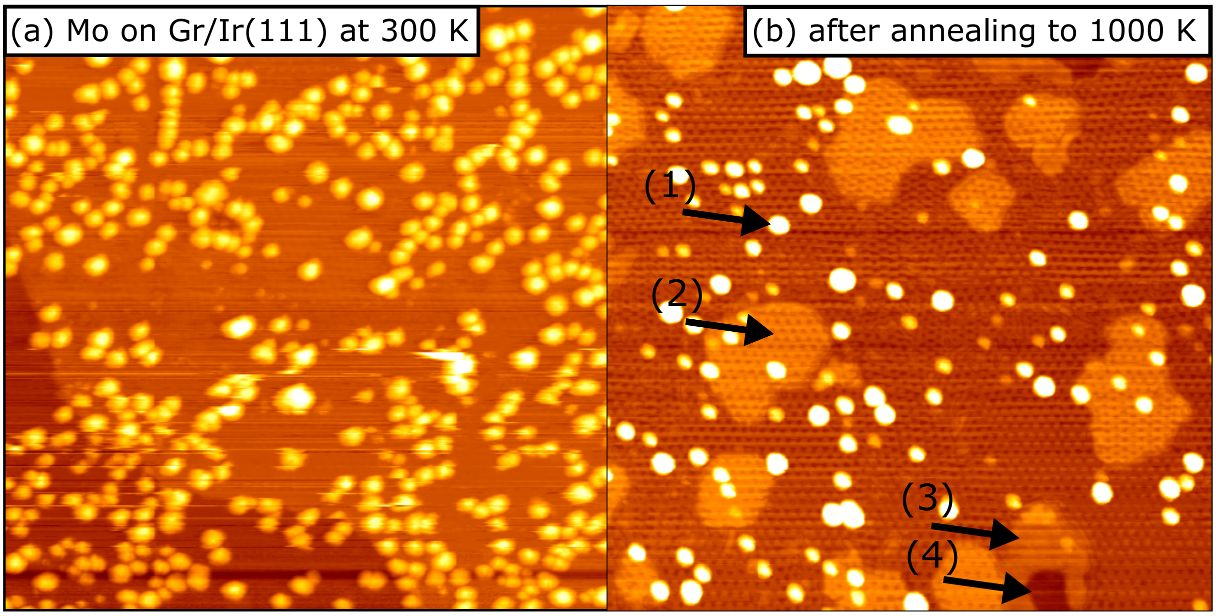

Figure A.2: STM topographs of Mo on Gr/Ir(111): (a) directly after deposition at 300 K. (b) after annealing to 1000 K. (1) Mo clusters on Gr. (2) Mo intercalated islands under Gr. (3) Mo islands without Gr on top. (4) bare Ir(111). Image sizes: 150 × 150 nm^2.

A.3 S Intercalation Underneath Gr/Ir(111)

In the literature, sulphur intercalation under Gr - also including other substrates than Ir(111) - is not numerously studied. In the system Gr/S/SiC(0001) it has been pointed out that charge transfer between sulphur and the graphene layer reduces the natural *n*-doping of Gr/6H-SiC(0001) shifting the Dirac point slightly upwards [413]. A simultaneous depletion of states at E_F at low temperatures has been interpreted as a gap opening caused by magnetic ordering that might be induced due to the interaction of intercalated sulphur with the buffer layer on top of SiC. Similar findings have been made in graphite-sulphur composites [414]. Exposing the system Gr/Ru(0001) to H_2S gas has been shown to result in a 4×2 superlattice intercalation phase of S [415], lifting the moiré corrugation and also reducing the strong *n*-doping. Surprisingly, the two more dilute $S(\sqrt{3} \times \sqrt{3})R30^\circ$ and $S(2 \times 2)$ phases, which are known to exist on bare Ru(0001) [416] were not possible to achieve.

Before discussing the observed intercalation phases of S underneath Gr/Ir(111), we first briefly introduce S adsorbate phases on Ir(111). Previous studies investigated the interaction of sulphur with the Ir(111) surface through H_2S adsorption and found the following key features: The dissociation of H_2S takes place already at room temperature and leads to the formation of an ordered $(\sqrt{3}\times\sqrt{3})R30^\circ$ sulphur adlayer phase [417], where S atoms are sitting in fcc hollow sites. Annealing the sample to 800 K ensures the complete desorption of hydrogen, whereas sulphur desorbs only near 1600 K. Additionally, first principle studies support the fcc site being the energetically most favourable site and indicate a high adsorption energy of $E_{\text{ads}} > -5$ eV per S atom [418, 419].

Another phase that is known to form is $S(4\times2)$, though this has not yet been published [420]. Due to structural similarity, we mention other fcc(111) or hcp(0001) systems where S adsorption results in a $S(4\times2)$ ordering $S(4\times2)$/Mo(111) [421], $S(4\times2)$/Rh(111) [422] and $S(4\times2)$/Ru(0001) [423]. In this phase, S atoms sit both in fcc and hcp sites and form a rectangular unit cell, which results in the possible formation of three domains on the Ir(111) surface, each being rotated by 60° with respect to each other.

Towards the intercalation of Gr, as a reference, we prepare a completely closed layer of Gr and investigate the intercalation of S. As indicated by LEED, after growing a fully closed layer of Gr/Ir(111) it has not been possible to intercalate S, neither using H_2S nor S_2 from FeS_2 as a sulphur source. This is summarised in Fig. A.3.

Growing only partially covered Gr/Ir(111), thus leaving bare Ir(111) where either H_2S or S_2 can dissociate, two intercalation phases $[(\sqrt{3} \times \sqrt{3})R30^\circ$ and $4 \times 2]$ have been observed.

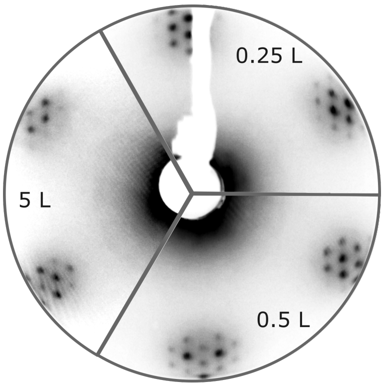

Figure A.3: No sulphur intercalation underneath perfectly closed Gr: The tripartite LEED data show the absence of S intercalation after subsequent dosing of 0.25 L, 0.5 L, and 5 L S at $T = 850$ K.

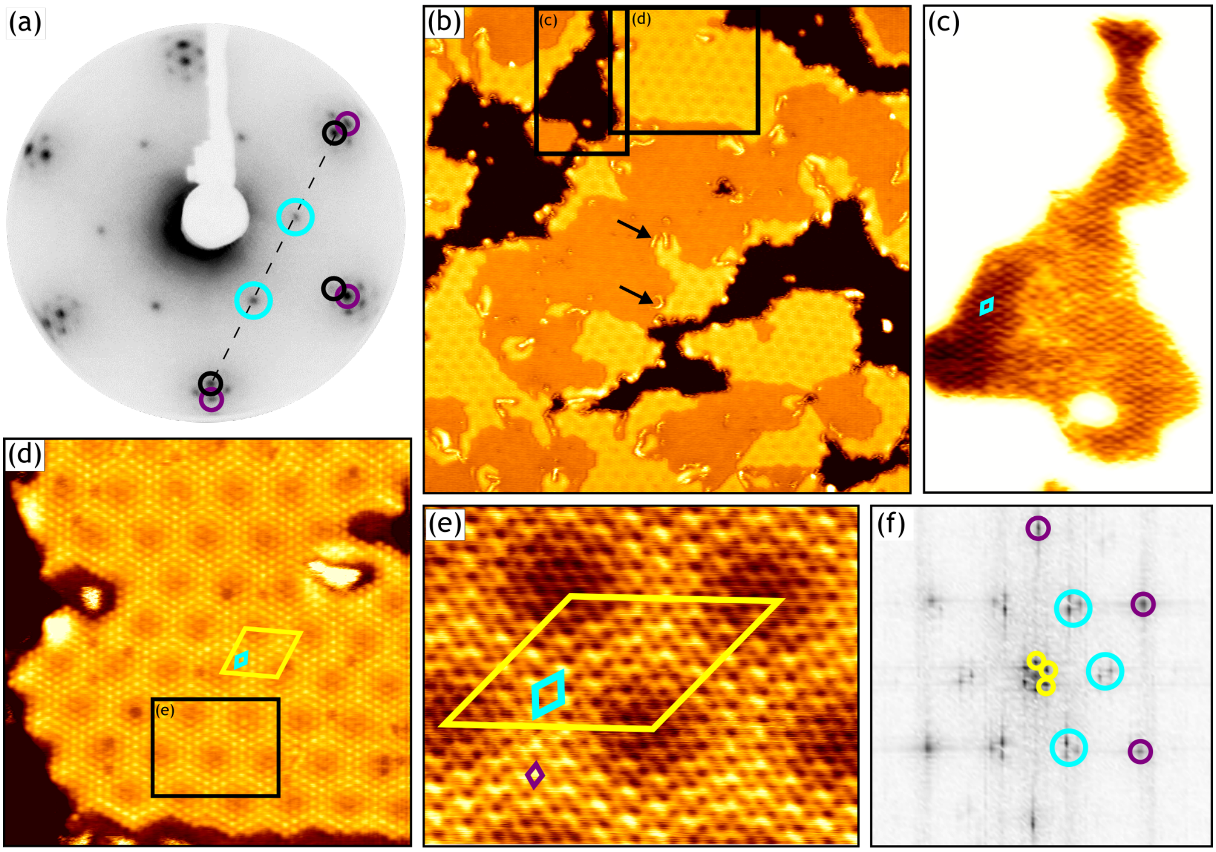

Figure A.4: $(\sqrt{3} \times \sqrt{3})$R30° intercalation under Gr: (a) LEED pattern at 70 eV of partial Gr/Ir(111) after dosage of 0.5 L H_2S at 850 K. The purple, black and turquoise circles indicate the position of the Gr, Ir and S diffraction spot, respectively. (b) STM topograph of the sample surface. The lowest, middle and highest level show Gr free areas, unintercalated Gr and intercalated Gr areas, respectively. The black boxes indicate the position of panel (c) and (d). Arrows indicate elongated structures of unknown origin. (c) Gr free area showing S$(\sqrt{3} \times \sqrt{3})$R30°/Ir(111). The turquoise rhomboid shows the $(\sqrt{3} \times \sqrt{3})$R30° unit cell. (d) Gr intercalated by S$(\sqrt{3} \times \sqrt{3})$R30°. Dark dots are S vacancies, yellow and turquoise rhomboid show moiré and S$(\sqrt{3} \times \sqrt{3})$R30° unit cell, respectively. Position of (e) is indicated by black box. (e) Close-up of (d) showing moiré (yellow), $(\sqrt{3} \times \sqrt{3})$R30° (turquoise), and Gr (purple) atomic lattice each indicated with their respective unit cell. (f) Corresponding Fourier transform with peaks related to the periodicities being circled in same colour as unit cell rhomboids.
Image information: (a) LEED 70 eV, STM (image size, tunnelling voltage, tunnelling current): (b) 90×90 nm^2, -0.9 V, 0.4 nA, (c) 13×23 nm^2, -0.9 V, 0.4 nA, (d) 20×20 nm^2, -1.0 V, 0.4 nA, (e) 6×5 nm^2, -0.5 V, 0.4 nA.

Gr/S$(\sqrt{3} \times \sqrt{3})$R30°/Ir(111)

Fig. A.4 summarises the S$(\sqrt{3} \times \sqrt{3})$R30° intercalated phase underneath Gr/Ir(111), which was achieved through dosing of 0.5 L H_2S at 850 K. Already in LEED in (a), a clear $(\sqrt{3} \times \sqrt{3})$R30° superstructure w.r.t. Ir(111) is visible, alongside weakening of the Gr/Ir(111) moiré. The STM overview topograph in (b) illustrates the sample morphology: the lowest level are Ir areas free of Gr, which are covered by S arranging in a $(\sqrt{3} \times \sqrt{3})$R30°superstructure. In STM these areas appear noisy as visible in (c). The sample is covered by roughly 75 % sample coverage of Gr, which in turn is partially intercalated by an area fraction of 40 % S indicated by the greater apparent height in STM. The unintercalated Gr has an apparent height of 2.3 ± 0.1 Å over the base level, which is S/Ir(111), while the intercalated shows a height of 3.0 ± 0.1 Å. As the fraction of unintercalated areas to intercalated ones is uniform throughout the sample surface and does not increase e.g. at step edges we speculate intercalation to proceed predominantly from island edges to under Gr. This is supported by the fact that larger islands are comparably lesser intercalated and by the aforementioned experiment, where S did not intercalate under perfectly closed Gr. Furthermore, the sample displays small elongated structures [see arrows in (b)] often enclosing the S intercalated areas, which are of yet unknown origin. Zooming in onto the surface allows uniformly scattered S vacancies to become visible under Gr which is displayed in (d). At last, also the atomic lattice of Gr becomes visible as shown in STM in (e) and its corresponding Fourier transform in (f).

Gr/S(4 × 2)/Ir(111)

After exposure of a sample with partial Gr/Ir(111) coverage to 10 L S from FeS_2 at 800 K, LEED shows a comparably complicated diffraction pattern illustrated in Fig. A.5 (a). To understand the pattern, we first note the well-known spots arising from Gr/Ir(111) and their moiré, which are marked in (a). It should be noted that in LEED the moiré is nearly completely suppressed, indicating the decoupling of the Gr from its substrate. The inner star-like diffraction pattern arises from the three different S(4 × 2) domains, which are rotated with respect to each other. To illustrate this, in (b) we mark those spots turquoise, which belong to one domain and in (c) overlay in a scheme all three rotational domains marked by distinct colours and reproduce the original LEED pattern.

Fig A.5 (d) shows an STM image of a partially Gr covered area. In the Gr free area, 4 × 2 S adsorption is indicated by a disordered network of domain boundaries. In the lower half of the image, a Gr flake with a wrinkle running through is visible. The strain which is partially released by the wrinkle is indicated *via* the local distortion of the moiré.

The region of disordered domain boundaries is enlarged in (e), where it is noted that a boundary does not necessarily separate rotational domains, as two domains can also be shifted by one Ir row. Here, we find the bottom domain to be rotated related to the upper four domains, which in turn are shifted to one another. Boundaries, however, do not need to be disordered, but also appear in straight lines as highlighted in (f). Here, the mismatch between the domains results in a domain boundary which has an apparent superstructure. In both (e) and (f), vacancies can be found plentiful.

Turning to Gr covered regions, we note similar findings, which are illustrated in the STM topograph in (g) and its Fourier transform in (h). Firstly, the S(4×2) phase can be found beneath Gr as indicated by the simultaneous observation of the superstructure and moiré. The fact that the 4 × 2 forms w.r.t. Ir and therefore is intercalated under Gr (and not on top) is apparent from the FT. Secondly, separated domains are visible, with either disordered or straight domain boundaries. The observation of point defects at the meeting point of boundaries leads us to infer those as nucleation sites. At last, in (i) the 4 × 2 is clearly identified and the atomic Gr lattice is faintly visible in the background.

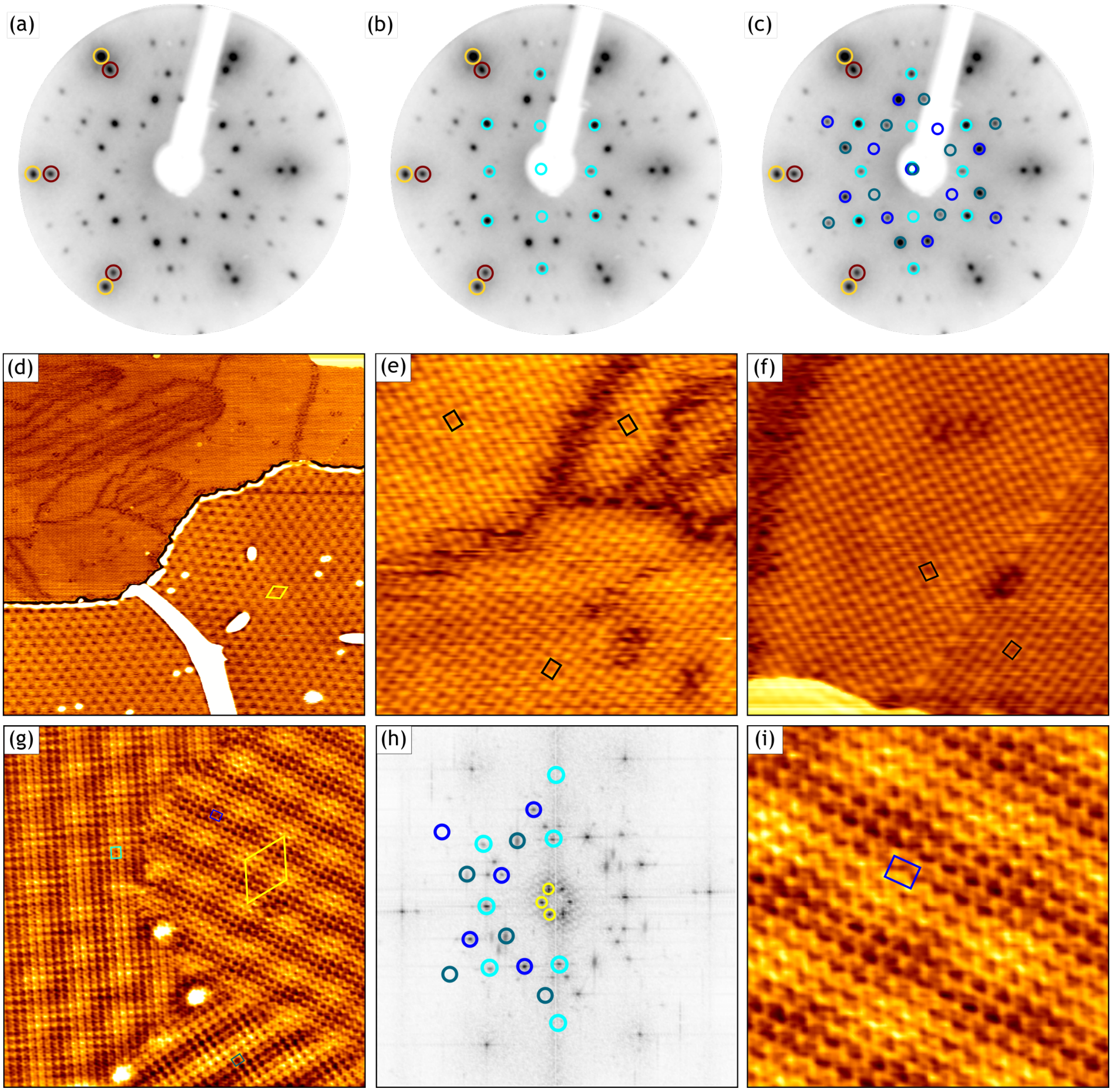

Figure A.5: 4 × 2 intercalation under Gr: (a) - (c) LEED pattern at 137 eV of partial Gr/Ir(111) after dosage of 2 L S from FeS_2 at 800 K. The orange and red circles indicate the position of the Gr and Ir spots, respectively. The turquoise, blue and mint-green circles of one colour indicate the spots which belong to a given domain of the 4×2 superstructure in real space, where in (a) there is no domain, in (b) one domain and in (c) three domains indicated. (d) STM topograph illustrating the partially Gr covered sample morphology and 4 × 2 S intercalation. The yellow rhomboid marks the moiré unit cell. Please note that the contrast is separately adjusted for the Ir terrace and Gr. (e) STM topograph illustrating an irregular network of domain boundaries on bare Ir(111). The 4 × 2 unit cells are indicated. (f) Regular domain boundary on bare Ir(111). (g) Three differently oriented 4×2 domains meeting under Gr/Ir(111), each being indicated with their respective unit cells. (h) Corresponding FT with circles indicating peaks that correspond to the same coloured domain in (g). (i) Close-up of 4×2 under Gr/Ir(111) with the unit cell indicated.
Images (a) – (f) are taken at 300 K, images (g) – (i) at 5 K. Image information: (a) LEED 137 eV, STM (image size, tunnelling voltage, tunnelling current): (d) 80 × 80 nm^2, −1 V, 0.2 nA, (e), (f) zoom of (d), (g) 20 × 20 nm^2, −0.5 V, 0.1 nA, (i) zoom of (g).

We interpret these findings twofold: Firstly, the weakening of the moiré in both intercalation structures is a sign for a decoupling of Gr from Ir(111). This behaviour is in line with many studies on intercalating Gr. Secondly, we interpret the formation of S superstructures specifically only with respect to Ir as a consequence of both a strong binding of S to the metal and a weak binding of S to Gr.

Additionally, preliminary experiments on estimating the doping level of Gr/S/Ir(111) by STS indicate only weak doping shifting the Dirac point less than 100 meV upward [424]. In ARPES, experiments designated to test the possibility of intercalated S doping Gr/Ir(111) even did not find an increase in hole concentration in Gr [44]. These findings all make plain that interaction between S and Gr is not strong and S may only decouple the on top grown system further from Ir(111).

A.4 ARPES of BL MoS_2

Figure A.6 shows ARPES spectra of 1.4 ML BL MoS_2. Growth conditions were specifically tuned to induce BL growth via high sulphur pressure annealing and cycled growth. It is clear from ARPES that the valence band maximum is not at the K point but at the Γ point (note the splitting of the band at Γ into two subbands, one with a higher binding energy of approximately 1.9 eV and one with a lower binding energy of approximately 1.3 eV). Furthermore, the splitting of the K point valleys has vanished.

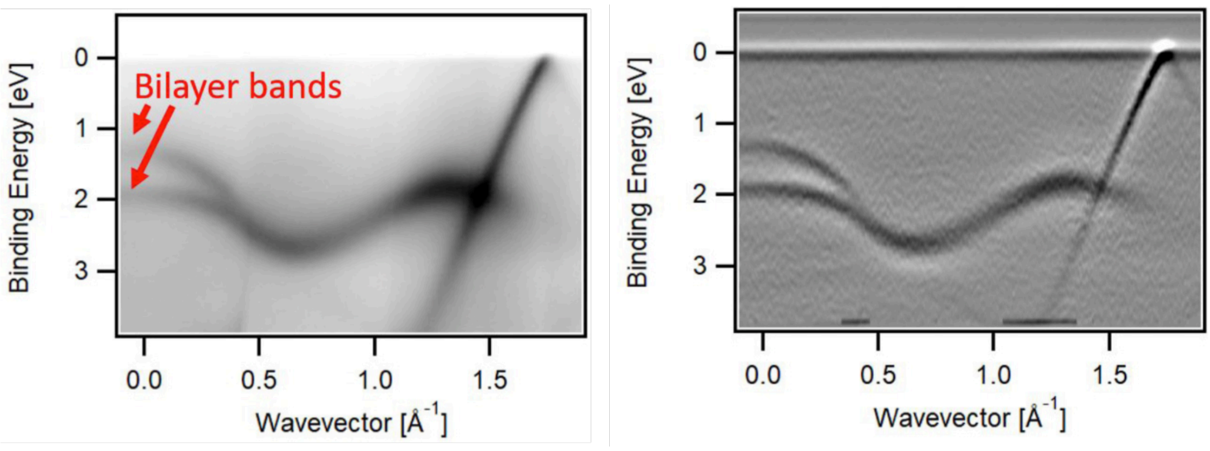

Figure A.6: ARPES of bilayer MoS2/Gr. Left: raw data, right: second derivative for enhancing spectral features.

A.5 Thermal Decomposition of MoS_2 Islands

When exposing the TMDC layers to high temperature thermal decomposition is observed. At the usual annealing temperatures of about 1000 K this is reasonably well compensated by a sulphur pressure of 2×10^{-9} mbar. In Fig. A.7 it is illustrated that at higher annealing temperatures this is no longer the case. As a reference, panel (a) shows the sample before high temperature annealing. The surface is covered by very roughly 50 % MoS_2 coverage. The straight edges and bright bumbs are results of a comparably long time annealing step of 20 min at 1050 K and 2×10^{-9} mbar S pressure, during which the sulphur pressure obviously was a little bit to low. However, after only 5 min of high temperature annealing at 1150 K in the usual same 2×10^{-9} mbar S pressure, the situation has severely changed: panel (b) documents a MoS_2 coverage of mostly $5 - 10$ %, but additional morphological features. The arrows mark very high clusters of height up to 12 nm, for which the contrast has been adjusted separately. These are interpreted as metallic Mo clusters which form due to the thermal decomposition of the MoS_2. Under one of the clusters a typical Mo intercalation structure is visible. In essence, the high temperature has quickly degraded the MoS_2 islands and due to too little S loss compensation, very high Mo clusters are left on the surface.

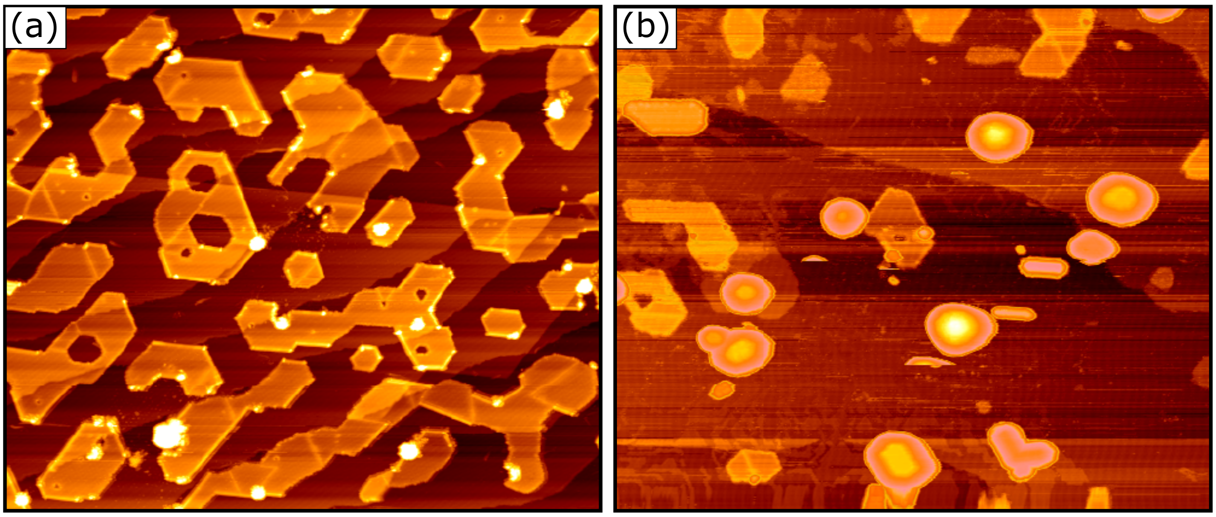

Figure A.7: Thermal decomposition of MoS_2 islands: (a) STM topographs before high temperature annealing. See text. (b) Sample morphology after annealing at 1150 K. See text. Note that the contrast has been adjusted separately for MoS_2 and Mo clusters (marked by arrows).
Image information (image size, tunnelling bias, tunnelling current): (a) 330×280 nm^2, -2 V, 30 pA, (b) 150×300 nm^2, -2 V, 40 pA.

A.6 Normalising dI/dV Spectra

Following Ref. [47,396], we normalise dI/dV spectra to enhance the visibility of spectral features of the STS. Below a theoretical derivation following Feenstra *et al.* [396] is given. Recalling the transmission probability $T(E, eU) = \exp(-2\kappa d)$ to be exponentially depending on the tip-sample distance, this dependency is also found in the analytical expression of the differential conductance [see Eqn. (A.2)]. Dividing by I/V yields T(E, eU) and T(eU, eU) to appear as ratio, which tends to cancel their exponential dependence.

In Fig. A.8, we demonstrate the full analysis of the constant height dI/dV spectra using the spectrum shown in Fig. 6.4 (c). The top panel shows the as-measured dI/dV. While a partial gap around the Fermi energy is clear and evident, its edge is hard to determine unambiguously. The middle panel illustrates the spectrum after division by I/V. The gap edges are now more clearly pronounced and allow reproducible determination of the FWHM after background subtraction in the bottom panel.

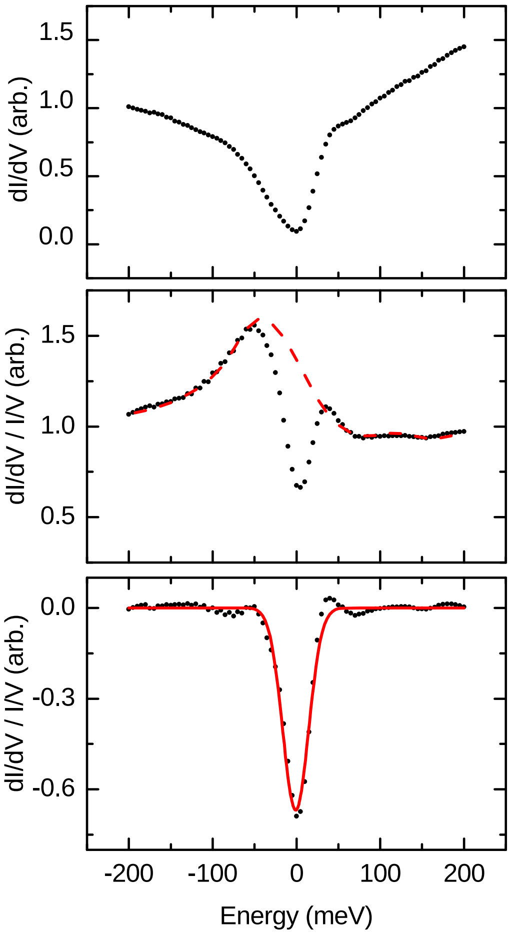

Figure A.8: Measured constant height dI/dV and analysis: (a) Raw dI/dV at 5 K with standard lock-in technique. (b) normalised $dI/dV/I/V$ to enhance visibility of dI/dV features. (c) normalised spectrum after background substraction. Image information constant height STS: $T = 5$ K, $U_{\text{stab}} = -0.3$ V, $I_{\text{stab}} = 0.5$ nA.

In the derivation, following Feenstra *et al.* [396], we assume the tunnelling current to read (see Section 2.1):

$$I \propto \int_0^{eU} T(E, eU)\rho_s(E)\, dE, \tag{A.1}$$

with $\rho_s(E)$ the DOS of the sample and $T(E, eU)$ the transmission probability, the differential conductance follows as

$$dI/dV \propto e\rho_s(eU)T(eU, eU) + e\int_0^{eU} \rho_s(E)\frac{d}{d(eU)}[T(E, eU)]\, dE. \tag{A.2}$$

Dividing by I/V thus yields

$$\frac{dI/dV}{I/V} \propto \frac{\rho_s(eU) + \int_0^{eU} \frac{\rho_s(E)}{T(eU,eU)} \frac{d}{d(eU)}[T(E, eU)]\, dE}{\frac{1}{eU}\int_0^{eU} \rho_s(E)\frac{T(E,eU)}{T(eU,eU)}}. \tag{A.3}$$

A.7 Estimating Li Doping by DFT

We estimate the doping level introduced by Li adsorption on TaS_2 by performing supercell calculations for freestanding TaS_2 and for Li-doped TaS_2 with DFT, see Fig. A.9.

Fig. A.9 (a) shows the band structure of pristine TaS_2. To facilitate comparison, we also unfold the (slightly reconstructed) metallic band from the supercell calculations onto the Brillouin zone of the simple unit cell. The linewidth in the corresponding plots is related to the overlap of corresponding states from both calculations, evaluated in the basis of Wannier functions.

To model Li doping, we assume that one adatom is positioned on top of every fourth Ta atom. The calculated Ta-Li distance amounts to 2.9 Å. As apparent in Fig. A.9 (b), there are now-unoccupied Li states just above the energy gap around 2 eV which provide an additional electron for TaS_2. The resulting doping level of $x = -0.240$ is close to the value of $x = -\frac{1}{4}$ expected from the stoichiometry of the system.

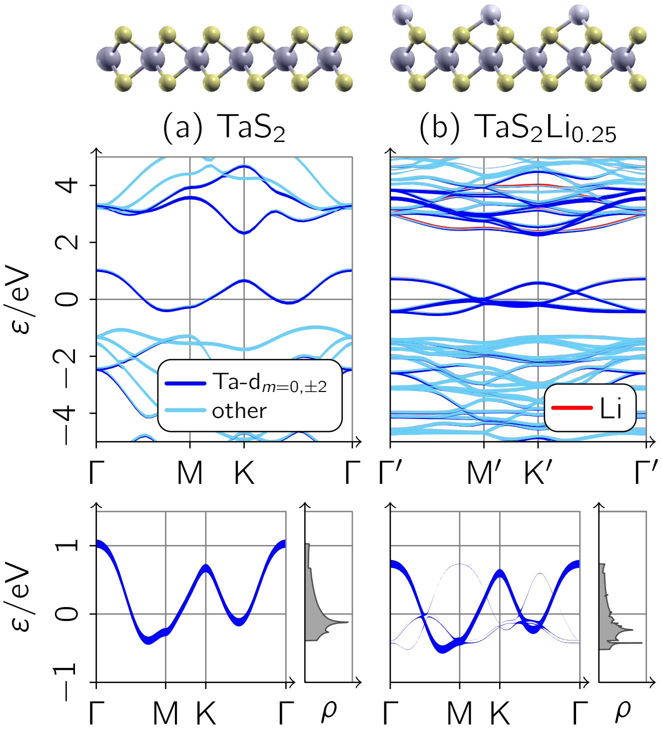

Figure A.9: Influence of Li adsorption on TaS_2: (a) Band structure of freestanding TaS_2, and (b) with one Li adatom per four Ta atoms. The upper panels show the dispersion along a path around the irreducible wedge of the Brillouin zone of the respective supercell. Line widths and colours visualise the projections onto (pseudo-) atomic orbitals. The lower panels show the low-energy band of TaS_2, unfolded onto the larger Brillouin zone of the unit cell. The effective doping levels and average shifts of the chemical potential are (b) $x = -0.240$ and $\Delta\mu = 133$ meV.

A.8 Calculations of the Phonon Dispersion

The goal of our theoretical modelling is to understand the influence of different external stimuli such as *e.g.* hybridization with substrates or electron doping on the TaS_2 phonon dispersion and thereby on the lattice instabilities which emerge from the softening of longitudinal-acoustic phonons due to metallic screening. To this end, we downfold the electronic structure and lattice dynamics of 2H-TaS_2 to a material-realistic low-energy model containing all phonons and the partially filled electronic conduction band. The phonons entering this model are bare (or more precisely partially screened) in the sense that they have to be renormalised due to interactions with electrons from the conduction band [266]. The corresponding bare phonons and the corresponding bare dynamical matrix D are obtained from constrained DFPT [266], where *constrained* means that screening within the low-energy electronic subspace is excluded in the determination of the phononic properties. The final experimentally observable phonon dispersion results from the renormalised dynamical matrix $\widetilde{D} = D + \Pi$, which accounts for mutual coupling of the lattice vibrations and the low-energy electronic degrees of freedom through the phonon "self-energy":

$$\Pi_{\tilde{q}\alpha\beta} = \frac{2}{N} \sum_{\tilde{k}nm} \widetilde{g}_{\tilde{q}\alpha\tilde{k}nm} \frac{f(\epsilon_{\tilde{k}+\tilde{q}m}) - f(\epsilon_{\tilde{k}n})}{\epsilon_{\tilde{k}+\tilde{q}m} - \epsilon_{\tilde{k}n}} g^{*}_{\tilde{q}\beta\tilde{k}nm}. \tag{A.4}$$

Here, $\epsilon_{\tilde{k}}$ is the electronic energy relative to the Fermi level, n and m label the bands of the low-energy subspace, and $\widetilde{g}$ and g are the fully and partially screened electron-phonon couplings from DFPT and constrained DFPT, respectively. $f(\epsilon_{\tilde{k}n})$ is the occupation number of the electronic state at $\tilde{k}$ in band n.

Based on Eq. (A.4), we analyze the influence of charge doping, hybridization with substrates, and interlayer bias potentials (BL case) on the phonon dispersions and particularly lattice instabilities of TaS_2.

Doping is accounted for, here, in a rigid band model by shifting the band energies $\epsilon_{\tilde{k}}$ relative to the Fermi level. Without the substrate, f is the Fermi function which reduces to a step function at $T = 0$. hybridization with the substrate leads to a Lorentzian broadening of the electronic levels and the occupation function at $T = 0$ becomes $f(\epsilon) = \frac{1}{2} - \frac{1}{\pi} \arctan(\frac{\epsilon}{\Gamma})$, where Γ is the half-width at half-maximum (HWHM) of the broadening. This result can be derived under the assumption that the hybridization does not depend on the energy. Note that the arctan decays only polynomially, contrary to the exponential decay of the Fermi-Dirac distribution. This means that states further away from the Fermi level are more relevant for hybridization than for temperature effects.

Our low-energy model is set up in the localised basis of Wannier functions and atomic displacements. This allows us to also manipulate the model on the level of hopping parameters and on-site energies, which helps us study the bilayer. In the same way as the rigid energy shift described above can be seen as adding a constant to all on-site energies of the monolayer, an interlayer-bias potential $\Delta\epsilon_0$ is introduced to the bilayer by adding $\Delta\epsilon_0/2$ to all on-site energies of one layer, while subtracting the same value from all on-site energies of the other layer.

For the monolayer TaS_2, assuming a fixed unit cell height of 15 Å (25 Å), minimizing the total energy and forces to below 10 µRy/Bohr yields a lattice constant of 3.34 Å (3.33 Å for the bilayer and a distance of 6.10 Å between the two Ta layers).

For the calculation of the phonon renormalization in the framework of Eq. (A.4), the $\tilde{k}$ resolution is increased to 216×216 points *via* Wannier/Fourier interpolation of the electronic dispersions and the electron-phonon coupling matrix elements. This ensures convergence also for small values of the broadening.

A.9 Synthesis at Very High Substrate Temperature

Since a very high substrate temperature enables enlarging grain sizes and suppresses second layer nucleation, we conducted a growth experiment directly at the annealing temperature of 1000 K, *i.e.* a one-step synthesis. The result is shown in Fig. A.10 with the synthesis parameters stated in the figure caption. The very high S pressure used allows a successful growth at very high substrate temperature resulting in about 70 % surface ML coverage with very good epitaxial orientation. The lateral grain sizes of up to 70 nm may even further be increased if the growth rate is lowered.

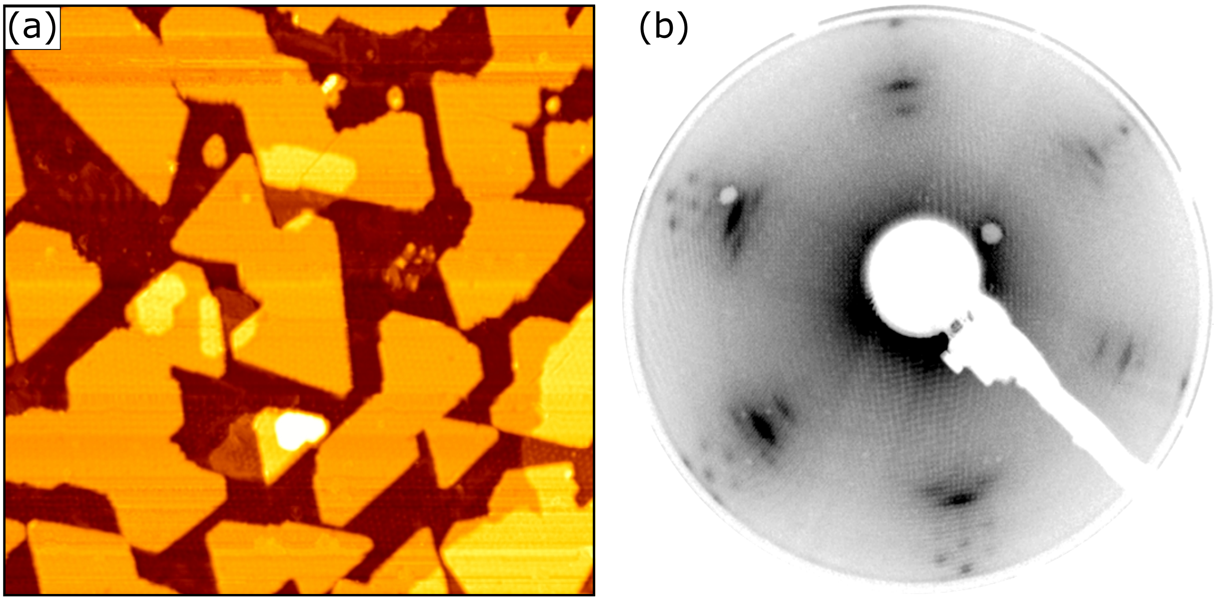

Figure A.10: Growth at very high substrate temperatures of 1000 K: For synthesis reference parameters were used, except for $t^{\mathrm{g}} = 240\,\mathrm{s}$, $F_{\mathrm{Ta}} = 1.5\,F_{\mathrm{Ta}}^{\mathrm{ref}} = 2.9 \times 10^{16}$ atoms $\mathrm{m}^{-2}\,\mathrm{s}^{-1}$ and $P_{\mathrm{sulphur}}^{\mathrm{g}} = 10\,P_{\mathrm{sulphur}}^{\mathrm{g,ref}} = 5 \times 10^{-8}$ mbar. (a) STM topographs of $\mathrm{TaS_2}$ on Gr/Ir(111). The high growth temperature results in large lateral grain sizes and the absence of second layer islands. (b) LEED at 84 eV. Even at a high coverage a well defined epitaxial relation is present.
Image information (image size, tunnelling bias, tunnelling current): (a) 200 × 200 nm^2, 1 V, 20 pA.

APPENDIX B

Liste der Teilpublikationen
(List of Publications)

Teile dieser Arbeit wurden als Bestandteil der folgenden Artikel in Fachzeitschriften bereits veröffentlicht:
Parts of the results presented in this thesis can be found in the following publications:

[43] **J. Hall**, B. Pielić, C. Murray, W. Jolie, T. Wekking, C. Busse, M. Kralj, and T. Michely
Molecular beam epitaxy of quasi-freestanding transition metal disulphide monolayers on van der Waals substrates: a growth study
2D Mater., **5** (2018), 025005

[44] N. Ehlen, **J. Hall**, B. Senkovskiy, M. Hell, J. Li, A. Herman, D. Smirnov, A. Fedorov, V. Y. Voroshnin, G. di Santo, L. Petaccia, T. Michely, and A. Grüneis
Narrow photoluminescence and Raman peaks of epitaxial MoS_2 *on graphene/Ir(111)*
2D Mater., **6** (2019), 011006

[45] C. Murray, W. Jolie, J. A. Fischer, **J. Hall**, C. van Efferen, N. Ehlen, A. Grüneis, C. Busse, and T. Michely
Comprehensive tunneling spectroscopy of quasifreestanding MoS_2 *on graphene on Ir(111)*
Phys. Rev. B, **99** (2019), 115434

[374] **J. Hall**, N. Ehlen, J. Berges, E. van Loon, C. van Efferen, C. Murray, M. Rösner, J. Li, B. V. Senkovskiy, M. Hell, M. Rolf, T. Heider, M. C. Asensio, J. Avila, L. Plucinski, T. Wehling, A. Grüneis, and T. Michely
Environmental Control of Charge Density Wave Order in Monolayer 2H-TaS_2
submitted to ACS Nano, under review

Weitere Publikationen:

Further publications:

[306] W. Jolie, C. Murray, P. S. Weiß, **J. Hall**, F. Portner, N. Atodiresei, A. V. Krasheninnikov, C. Busse, H.-P. Komsa, A. Rosch, and T. Michely
Tomonaga-Luttinger Liquid in a Box: Electrons Confined within MoS_2 *Mirror-Twin Boundaries*
Phys. Rev. X, **9** (2019), 011055

[322] C. Murray, C. van Efferen, W. Jolie, **J. Hall**, A. V. Krasheninnikov, C. Busse, H. P. Komsa, and T. Michely
Locally Confined 1D Hole Gas Caused by Band Bending in MoS_2 *on Gr/Ir(111)*
in preparation

[347] P. Valerius, **J. Hall**, A. Herman, S. Kretschmer, M. Ghorbani-Asl, A. Krasheninnikov, A. Grüneis, and T. Michely
Reversible crystalline-to-amorphous phase transition in MoS_2 *on Gr/Ir(111) by* Xe^+ *ion irradiation*
in preparation

[420] B. Pielić, **J. Hall**, V. Despoja, I. Š. Rakić, M. Petrović, A. Sohani, C. Busse, T. Michely, and M. Kralj
Sulfur structures on bare and graphene-covered Ir(111)
in preparation

Konferenzbeiträge als präsentierender Autor:
Conference contributions as presenting author:

2016/10 SFB1238 workshop, Essen (DE), talk, *Epitaxial growth of transition metal dichalcogenides on graphene on Ir(111)*

2016/10 SFB1238 student workshop, Koblenz (DE), talk, *Epitaxial growth of transition metal dichalcogenides on graphene on Ir(111)*

2017/03 DPG Frühjahrstagung Sektion Kondensierte Materie, Dresden (DE), talk, *Epitaxial growth of transition metal dichalcogenides*

2017/08 Conference Flatlands, École polytechnique fédérale de Lausanne, Lausanne (CH), talk, *Van der Waals epitaxy of single layer transition metal dichalcogenides*

2018/03 DPG Frühjahrstagung Sektion Kondensierte Materie, Berlin (DE), poster, *Growth and structure of mono- to few-layer* VS_2 *on graphene on Ir(111)*

2018/04 European Workshop on Epitaxial Graphene and 2D Materials, Salamanca (ES), poster, *Growth and structure of mono- to few-layer* VS_2 *on graphene on Ir(111)*

2019/03 DPG Frühjahrstagung Sektion Kondensierte Materie, Regensburg (DE), talk, *The* 3×3 *charge density wave in* 2H-TaS_2

2019/04 PDI Topical Workshop on 2D Materials Grown by MBE, Paul Drude Institut, Berlin (DE), invited talk, *Environmetal control of charge density wave order in* 2H-TaS_2

2019/05 Atomic structure of nanosystems from first-principles simulations and microscopy experiments, Aalto University, Helsinki (FI), talk, *The* 3×3 *charge density wave in* 2H-TaS_2

Seminarbeiträge als präsentierender Autor:
Seminar contributions as presenting author:

2017/03 institute seminar, Cologne (DE), talk, *Van der Waals Epitaxy of single layer transition metal dichalcogenides*

2018/05 conference title, Jülich (DE), invited talk, *Molecular beam epitaxy of single layer transition metal disulfides*

Bibliography

[1] K. S. Novoselov, A. K. Geim, S. V. Morozov, D. Jiang, Y. Zhang, S. V. Dubonos, I. V. Grigorieva and A. A. Firsov, 'Electric field in atomically thin carbon films', *Science* **306**, 666 (2004). Cited on page(s) 3 and 23

[2] A. K. Geim and K. S. Novoselov, 'The Rise of Graphene', *Nat. Mater.* **6**, 183 (2007). Cited on page(s) 3

[3] 'Physics and Chemistry of Materials with Layered Structures: Preparation and Crystal Growth of Materials with Layered Structures', 1 ed., edited by R. M. A. Lieth (Springer Netherlands, Dordrecht, 1977), 280. Cited on page(s) 3

[4] 'Physics and Chemistry of Materials with Layered Structures: Crystallography and Crystal Chemistry of Materials with Layered Structures', 2 ed., edited by F. Lévy (Springer Netherlands, Dordrecht, 1976), 378. Cited on page(s) 3

[5] 'Physics and Chemistry of Materials with Layered Structures: Electrons and Phonons in Layered Crystal Structures', 3 ed., edited by T. J. Wieting and M. Schlüter (Springer Netherlands, Dordrecht, 1979), 474. Cited on page(s) 3

[6] 'Physics and Chemistry of Materials with Layered Structures: Optical and Electrical Properties', 4 ed., edited by P. A. Lee (Springer Netherlands, Dordrecht, 1976), 476. Cited on page(s) 3

[7] 'Physics and Chemistry of Materials with Layered Structures: Structural Chemistry of Layer-Type Phases', 5 ed., edited by F. Hulliger and F. Lévy (Springer Netherlands, Dordrecht, 1977), 404. Cited on page(s) 3

[8] F. Lévy, in 'Physics and Chemistry of Materials with Layered Structures: Intercalated Layered Materials', 6 ed., edited by F. Lévy (Springer Netherlands, Dordrecht, 1979), 592. Cited on page(s) 3

[9] 'Physics and Chemistry of Materials with Layered Structures: Structural Phase Transitions in Layered Transition Metal Compounds', 8 ed., edited by K. Motizuki (Springer Netherlands, Dordrecht, 1986), 300. Cited on page(s) 3 and 13

[10] 'Physics and Chemistry of Materials with Layered Structures: Electronic Structure and Electronic Transitions in Layered Materials', 7 ed., edited by V. Grasso (Springer Netherlands, Dordrecht, 1986), 517. Cited on page(s) 3 and 11

[11] A. V. Kolobov and J. Tominaga, 'Two-Dimensional Transition-Metal Dichalcogenides', 239 ed. (Springer International Publishing, Switzerland, 2016), 538. Cited on page(s) 3, 9, 10, 11, and 12

[12] M. Van Maaren and G. Schaeffer, 'Some New Superconducting Group Va Dichalcogenides', *Phys. Lett. A* **24**, 645 (1967). Cited on page(s) 3

[13] E. Navarro-Moratalla, J. O. Island, S. Mañas-Valero, E. Pinilla-Cienfuegos, A. Castellanos-Gomez, J. Quereda, G. Rubio-Bollinger, L. Chirolli, J. A. Silva-Guillén, N. Agrait, G. A. Steele, F. Guinea, H. S. J. van der Zant and E. Coronado, 'Enhanced Superconductivity in Atomically Thin TaS_2', *Nat. Commun.* **7**, 11043 (2016). Cited on page(s) 3, 5, 19, and 94

[14] Y. Yang, S. Fang, V. Fatemi, J. Ruhman, E. Navarro-Moratalla, K. Watanabe, T. Taniguchi, E. Kaxiras and P. Jarillo-Herrero, 'Enhanced Superconductivity Upon Weakening of Charge Density Wave Transport in 2H-TaS_2 in the Two-Dimensional Limit', *Phys. Rev. B* **98**, 35203 (2018). Cited on page(s) 3, 5, and 94

[15] S. C. De La Barrera, M. R. Sinko, D. P. Gopalan, N. Sivadas, K. L. Seyler, K. Watanabe, T. Taniguchi, A. W. Tsen, X. Xu, D. Xiao and B. M. Hunt, 'Tuning Ising Superconductivity With Layer and Spin-Orbit Coupling in Two-Dimensional Transition-Metal Bichalcogenides', *Nat. Commun.* **9**, 1427 (2018). Cited on page(s) 3 and 94

[16] X. Xi, L. Zhao, Z. Wang, H. Berger, L. Forró, J. Shan and K. F. Mak, 'Strongly Enhanced Charge-Density-Wave Order in Monolayer $NbSe_2$', *Nat. Nanotechnol.* **10**, 765 (2015). Cited on page(s) 3, 19, and 94

[17] M. M. Ugeda *et al.*, 'Characterization of Collective Ground States in Single-Layer $NbSe_2$', *Nat. Phys.* **12**, 92 (2016). Cited on page(s) 3, 19, and 94

[18] L. Ma, C. Ye, Y. Yu, X. F. Lu, X. Niu, S. Kim, D. Feng, D. Tománek, Y.-W. Son, X. H. Chen and Y. Zhang, 'A Metallic Mosaic Phase and the Origin of Mott-Insulating State in 1T-TaS_2', *Nat. Commun.* **7**, 10956 (2016). Cited on page(s) 3 and 114

[19] Y. Nakata, K. Sugawara, R. Shimizu, Y. Okada, P. Han, T. Hitosugi, K. Ueno, T. Sato and T. Takahashi, 'Monolayer 1T-$NbSe_2$ as a Mott insulator', *NPG Asia Mater.* **8**, e321 (2016). Cited on page(s) 3, 19, and 20

[20] K. T. Law and P. A. Lee, '1T-TaS_2 as a Quantum Spin Liquid', *Proc. Natl. Acad. Sci.* **114**, 6996 (2017). Cited on page(s) 3 and 20

[21] A. A. Soluyanov, D. Gresch, Z. Wang, Q. Wu, M. Troyer, X. Dai and B. A. Bernevig, 'Type-II Weyl Semimetals', *Nature* **527**, 495 (2015). Cited on page(s) 3

[22] X. Qian, J. Liu, L. Fu and J. Li, 'Quantum Spin Hall Effect in Two-Dimensional Transition Metal Dichalcogenides.', *Science* **346**, 1344 (2014). Cited on page(s) 3

[23] Y. Zhang *et al.*, 'Direct observation of the transition from indirect to direct bandgap in atomically thin epitaxial $MoSe_2$', *Nat. Nanotechnol.* **9**, 111 (2014). Cited on page(s) 3 and 13

[24] B. Radisavljevic, A. Radenovic, J. Brivio, V. Giacometti and A. Kis, 'Single-Layer MoS_2 Transistors', *Nat. Nanotechnol.* **6**, 147 (2011). Cited on page(s) 3 and 52

[25] G. Froehlicher, E. Lorchat and S. Berciaud, 'Charge Versus Energy Transfer in Atomically Thin Graphene-Transition Metal Dichalcogenide van der Waals Heterostructures', *Phys. Rev. X* **8**, 011007 (2018). Cited on page(s) 3

[26] R. F. Frindt, 'Superconductivity in Ultrathin $NbSe_2$ Layers', *Phys. Rev. Lett.* **28**, 299 (1972). Cited on page(s) 3 and 19

[27] B. Huang, G. Clark, E. Navarro-Moratalla, D. R. Klein, R. Cheng, K. L. Seyler, D. Zhong, E. Schmidgall, M. A. McGuire, D. H. Cobden, W. Yao, D. Xiao, P. Jarillo-Herrero and X. Xu, 'Layer-Dependent Ferromagnetism in a van der Waals Crystal Down to the Monolayer Limit', *Nature* **546**, 270 (2017). Cited on page(s) 3 and 20

[28] C. Gong, L. Li, Z. Li, H. Ji, A. Stern, Y. Xia, T. Cao, W. Bao, C. Wang, Y. Wang, Z. Q. Qiu, R. J. Cava, S. G. Louie, J. Xia and X. Zhang, 'Discovery of Intrinsic Ferromagnetism in Two-Dimensional van der Waals Crystals', *Nature* **546**, 265 (2017). Cited on page(s) 3, 20, and 21

[29] Y. Ma, Y. Dai, M. Guo, C. Niu, Y. Zhu and B. Huang, 'Evidence of the Existence of Magnetism in Pristine VX_2 Monolayers ($X = S$, Se) and Their Strain-Induced Tunable Magnetic Properties', *ACS Nano* **6**, 1695 (2012). Cited on page(s) 3, 5, 21, and 22

[30] M. Yoshida, Y. Zhang, J. Ye, R. Suzuki, Y. Imai, S. Kimura, A. Fujiwara and Y. Iwasa, 'Controlling charge-density-wave states in nano-thick crystals of 1T-TaS_2', *Sci. Rep.* **4**, 7302 (2014). Cited on page(s) 3

[31] Y. Yu, F. Yang, X. F. Lu, Y. J. Yan, Y.-H. Cho, L. Ma, X. Niu, S. Kim, Y.-W. Son, D. Feng, S. Li, S.-W. Cheong, X. H. Chen and Y. Zhang, 'Gate-Tunable Phase Transitions in Thin Flakes of 1T-TaS_2', *Nat. Nanotechnol.* **10**, 270 (2015). Cited on page(s) 3 and 94

[32] G. Liu, B. Debnath, T. R. Pope, T. T. Salguero, R. K. Lake and A. A. Balandin, ‘A Charge-Density-Wave Oscillator Based on an Integrated Tantalum Disulfide-Boron Nitride-Graphene Device Operating at Room Temperature’, *Nat. Nanotechnol.* **11**, 845 (2016). Cited on page(s) 3

[33] J. A. Miwa, S. Ulstrup, S. G. Sørensen, M. Dendzik, A. Grubišić Čabo, M. Bianchi, J. V. Lauritsen and P. Hofmann, ‘Electronic Structure of Epitaxial Single-Layer MoS_2’, *Phys. Rev. Lett.* **114**, 46802 (2015). Cited on page(s) 4 and 23

[34] M. Dendzik, M. Michiardi, C. Sanders, M. Bianchi, J. A. Miwa, S. S. Grønborg, J. V. Lauritsen, A. Bruix, B. Hammer and P. Hofmann, ‘Growth and Electronic Structure of Epitaxial Single-Layer WS_2 on Au(111)’, *Phys. Rev. B* **92**, 245442 (2015). Cited on page(s) 4 and 23

[35] C. E. Sanders, M. Dendzik, A. S. Ngankeu, A. Eich, A. Bruix, M. Bianchi, J. A. Miwa, B. Hammer, A. A. Khajetoorians and P. Hofmann, ‘Crystalline and Electronic Structure of Single-Layer TaS_2’, *Phys. Rev. B* **94**, 81404 (2016). Cited on page(s) 4, 23, 94, 108, and 109

[36] R. M. Stan, S. K. Mahatha, M. Bianchi, C. E. Sanders, D. Curcio, P. Hofmann and J. A. Miwa, ‘Epitaxial single-layer NbS_2 on Au(111): Synthesis, structure, and electronic properties’, *Phys. Rev. Mater.* **3**, 44003 (2019). Cited on page(s) 4 and 23

[37] A. Koma, K. Sunouchi and T. Miyajima, ‘Fabrication and Characterization of Heterostructures with Subnanometer Thickness’, *Microelectron. Eng.* **2**, 129 (1984). Cited on page(s) 4, 24, and 39

[38] A. Koma and K. Yoshimura, ‘Ultrasharp Interfaces Grown with Van der Waals Epitaxy’, *Surf. Sci.* **174**, 556 (1986). Cited on page(s) 4, 24, and 39

[39] F. S. Ohuchi, B. A. Parkinson, K. Ueno and A. Koma, ‘van der Waals epitaxial growth and characterization of $MoSe_2$ thin films on SnS_2’, *J. Appl. Phys.* **68**, 2168 (1990). Cited on page(s) 4 and 24

[40] A. Koma, ‘Van der Waals Epitaxy - a New Epitaxial Growth Method for a Highly Lattice-Mismatched System’, *Thin Solid Films* **216**, 72 (1992). Cited on page(s) 4, 24, and 39

[41] J. Coraux, A. T. N’Diaye, M. Engler, C. Busse, D. Wall, N. Buckanie, F.-J. M. zu Heringdorf, R. van Gastel, B. Poelsema and T. Michely, ‘Growth of Graphene on Ir(111)’, *New J. Phys.* **11**, 23006 (2009). Cited on page(s) 4 and 40

[42] R. van Gastel, A. T. N’Diaye, D. Wall, J. Coraux, C. Busse, N. M. Buckanie, F.-J. zu Heringdorf, M. von Hoegen, T. Michely and B. Poelsema, ‘Selecting a Single Orientation for Millimeter Sized Graphene Sheets’, *Appl. Phys. Lett.* **95**, 121901 (2009). Cited on page(s) 4, 33, and 40

[43] J. Hall, B. Pielić, C. Murray, W. Jolie, T. Wekking, C. Busse, M. Kralj and T. Michely, ‘Molecular Beam Epitaxy of Quasi-Freestanding Transition Metal Disulphide Monolayers on van der Waals Substrates: A Growth Study’, *2D Mater.* **5**, 025005 (2018). Cited on page(s) 4, 39, 51, and 141

[44] N. Ehlen, J. Hall, B. V. Senkovskiy, M. Hell, J. Li, A. Herman, D. Smirnov, A. Fedorov, V. Y. Voroshnin, G. Di Santo, L. Petaccia, A. Grüneis and T. Michely, ‘Narrow Photoluminescence and Raman Peaks of Epitaxial MoS_2 on Graphene/Ir(111)’, *2D Mater.* **6**, 11006 (2018). Cited on page(s) 4, 39, 47, 48, 135, and 141

[45] C. Murray, W. Jolie, J. A. Fischer, J. Hall, C. van Efferen, N. Ehlen, A. Grüneis, C. Busse and T. Michely, ‘Comprehensive Tunneling Spectroscopy of Quasifreestanding MoS_2 on Graphene on Ir(111)’, *Phys. Rev. B* **99**, 115434 (2019). Cited on page(s) 4, 39, 46, 52, and 141

[46] L. A. Walsh and C. L. Hinkle, ‘van der Waals epitaxy: 2D materials and topological insulators’, *Appl. Mater. Today* **9**, 504 (2017). Cited on page(s) 5, 24, and 105

[47] W. Jolie, T. Knispel, N. Ehlen, K. Nikonov, C. Busse, A. Grüneis and T. Michely, ‘The Charge Density Wave in VSe_2 Revisited’, *Phys. Rev. B* **99**, 115417 (2019). Cited on page(s) 5, 19, 24, 72, 99, 103, 107, 117, and 137

[48] E. B. Isaacs and C. A. Marianetti, ‘Electronic Correlations in Monolayer VS_2’, *Phys. Rev. B* **94**, 35120 (2016). Cited on page(s) 5, 21, and 72

[49] T. Tsuda, H. Yasuoka, Y. Kitaoka and F. J. Di Salvo, '^{51}V NMR study of the phase transition in 1T-VS_2', *J. Magn. Magn. Mater.* **31-34**, 1101 (1983). Cited on page(s) 5 and 72

[50] M. Mulazzi, A. Chainani, N. Katayama, R. Eguchi, M. Matsunami, H. Ohashi, Y. Senba, M. Nohara, M. Uchida, H. Takagi and S. Shin, 'Absence of nesting in the charge-density-wave system 1T-VS_2 as seen by photoelectron spectroscopy', *Phys. Rev. B* **82**, 75130 (2010). Cited on page(s) 5, 19, 72, 77, and 89

[51] H. L. Zhuang and R. G. Hennig, 'Stability and magnetism of strongly correlated single-layer VS_2', *Phys. Rev. B* **93**, 54429 (2016). Cited on page(s) 5, 21, and 72

[52] H. Zhang, L.-M. Liu and W.-M. Lau, 'Dimension-dependent phase transition and magnetic properties of VS_2', *J. Mater. Chem. A* **1**, 10821 (2013). Cited on page(s) 5, 21, and 72

[53] D. W. Murphy, C. Cros, F. J. Di Salvo and J. V. Waszczak, 'Preparation and Properties of Li_xVS_2', *Inorg. Chem.* **16**, 3027 (1977). Cited on page(s) 5 and 72

[54] A. Gauzzi, A. Sellam, G. Rousse, Y. Klein, D. Taverna, P. Giura, M. Calandra, G. Loupias, F. Gozzo, E. Gilioli, F. Bolzoni, G. Allodi, R. De Renzi, G. L. Calestani and P. Roy, 'Possible Phase Separation and Weak Localization in the Absence of a Charge-Density Wave in Single-Phase 1T-VS_2', *Phys. Rev. B* **89**, 235125 (2014). Cited on page(s) 5 and 72

[55] F. Arnold *et al.*, 'Novel Single-Layer Vanadium Sulphide Phases', *2D Mater.* **5**, 045009 (2018). Cited on page(s) 5, 23, 73, 77, 82, and 92

[56] J. P. Tidman, O. Singh, A. E. Curzon and R. F. Frindt, 'The Phase Transition in 2H-TaS_2 at 75 K', *Philos. Mag.* **30**, 1191 (1974). Cited on page(s) 5, 19, 94, and 115

[57] G. A. Scholz, O. Singh, R. F. Frindt and A. E. Curzon, 'Charge Density Wave Commensurability in 2H-TaS_2 and Ag_xTaS_2', *Solid State Commun.* **44**, 1455 (1982). Cited on page(s) 5, 19, 94, and 98

[58] H. Lin, W. Huang, K. Zhao, C. Lian, W. Duan, X. Chen and S.-H. Ji, 'Growth of Atomically Thick Transition Metal Sulfide Films on Graphene/6H-SiC(0001) by Molecular Beam Epitaxy', *Nano Res.* **11**, 4722 (2018). Cited on page(s) 5, 19, and 94

[59] J. A. Wilson and A. D. Yoffe, 'The transition metal dichalcogenides discussion and interpretation of the observed optical, electrical and structural properties.', *Adv. Phys.* **18**, 193 (1969). Cited on page(s) 9, 10, 11, 12, 43, and 48

[60] M. Chhowalla, H. S. Shin, G. Eda, L.-J. Li, K. P. Loh and H. Zhang, 'The Chemistry of Two-Dimensional Layered Transition Metal Dichalcogenide Nanosheets.', *Nat. Chem.* **5**, 263 (2013). Cited on page(s) 9

[61] S. Manzeli, D. Ovchinnikov, D. Pasquier, O. V. Yazyev and A. Kis, '2D transition metal dichalcogenides', *Nat. Rev. Mater.* **2**, 17033 (2017). Cited on page(s) 9 and 10

[62] Q. H. Wang, K. Kalantar-Zadeh, A. Kis, J. N. Coleman and M. S. Strano, 'Electronics and optoelectronics of two-dimensional transition metal dichalcogenides', *Nat. Nanotechnol.* **7**, 699 (2012). Cited on page(s) 9

[63] D. Voiry, A. Mohite and M. Chhowalla, 'Phase Engineering of Transition Metal Dichalcogenides', *Chem. Soc. Rev.* **44**, 2702 (2015). Cited on page(s) 9

[64] G. H. Han, D. L. Duong, D. H. Keum, S. J. Yun and Y. H. Lee, 'van der Waals Metallic Transition Metal Dichalcogenides', *Chem. Rev.* **118**, 6297 (2018). Cited on page(s) 9

[65] H. Katzke, P. Tolédano and W. Depmeier, 'Phase Transitions Between Polytypes and Intralayer Superstructures in Transition Metal Dichalcogenides', *Phys. Rev. B* **69**, 134111 (2004). Cited on page(s) 11 and 12

[66] R. H. Friend and A. D. Yoffe, 'Electronic Properties of Intercalation Complexes of the Transition Metal Dichalcogenides', *Adv. Phys.* **36**, 1 (1987). Cited on page(s) 11 and 107

[67] E. Morosan, H. W. Zandbergen, B. S. Dennis, J. W. G. Bos, Y. Onose, T. Klimczuk, A. P. Ramirez, N. P. Ong and R. J. Cava, 'Superconductivity in Cu_xTiSe_2', *Nat. Phys.* **2**, 544 (2006). Cited on page(s) 11

[68] E. Morosan, K. E. Wagner, L. L. Zhao, Y. Hor, A. J. Williams, J. Tao, Y. Zhu and R. J. Cava, 'Multiple electronic transitions and superconductivity in Pd_xTiSe_2', *Phys. Rev. B* **81**, 094524 (2010). Cited on page(s) 11

[69] J. S. Chen, J. K. Wang, S. V. Carr, S. C. Vogel, O. Gourdon, P. Dai and E. Morosan, 'Chemical Tuning of Electrical Transport in $Ti_{1-x}Pt_xSe_{2-y}$', *Phys. Rev. B* **91**, 045125 (2015). Cited on page(s) 11

[70] K. E. Wagner, E. Morosan, Y. S. Hor, J. Tao, Y. Zhu, T. Sanders, T. M. McQueen, H. W. Zandbergen, A. J. Williams, D. V. West and R. J. Cava, 'Tuning the charge density wave and superconductivity in CuxTaS2', *Phys. Rev. B* **78**, 104520 (2008). Cited on page(s) 11

[71] S. S. P. Parkin and R. H. Friend, '3 d Transition-Metal Intercalates of the Niobium and Tantalum Dichalcogenides. I. Magnetic Properties', *Philos. Mag. B* **41**, 65 (1980). Cited on page(s) 11

[72] J. Choe, K. Lee, C.-L. Huang, N. Trivedi and E. Morosan, 'Magnetotransport in Fe-Intercalated TS_2: Comparison between $T = Ti$ and Ta', *Phys. Rev. B* **99**, 064420 (2019). Cited on page(s) 11

[73] C. Zhang, C. Gong, Y. Nie, K. A. Min, C. Liang, Y. J. Oh, H. Zhang, W. Wang, S. Hong, L. Colombo, R. M. Wallace and K. Cho, 'Systematic study of electronic structure and band alignment of monolayer transition metal dichalcogenides in Van der Waals heterostructures', *2D Mater.* **4**, 015026 (2017). Cited on page(s) 11

[74] R. Huisman, R. de Jonge, C. Haas and F. Jellinek, 'Trigonal-Prismatic Coordination in Solid Compounds of Transition Metals', *J. Solid State Chem.* **3**, 56 (1971). Cited on page(s) 11

[75] N. Ehlen, 'Privat Communication', *II. Phys. Institut, Univ. zu Köln* **2019**, (2019). Cited on page(s) 12

[76] D. Xiao, G.-B. Liu, W. Feng, X. Xu and W. Yao, 'Coupled Spin and Valley Physics in Monolayers of MoS_2 and Other Group-VI Dichalcogenides', *Phys. Rev. Lett.* **108**, 196802 (2012). Cited on page(s) 12, 13, and 52

[77] T. Kanazawa, T. Amemiya, A. Ishikawa, V. Upadhyaya, K. Tsuruta, T. Tanaka and Y. Miyamoto, 'Few-layer HfS_2 Transistors', *Sci. Rep.* **6**, 22277 (2016). Cited on page(s) 12

[78] K. F. Mak, C. Lee, J. Hone, J. Shan and T. F. Heinz, 'Atomically Thin MoS_2: A New Direct-Gap Semiconductor', *Phys. Rev. Lett.* **105**, 136805 (2010). Cited on page(s) 13

[79] A. Splendiani, L. Sun, Y. Zhang, T. Li, J. Kim, C.-Y. Chim, G. Galli and F. Wang, 'Emerging Photoluminescence in Monolayer MoS_2', *Nano Lett.* **10**, 1271 (2010). Cited on page(s) 13

[80] E. Ridolfi, D. Le, T. S. Rahman, E. R. Mucciolo and C. H. Lewenkopf, 'A Tight-Binding Model for MoS_2 Monolayers', *J. Phys. Condens. Matter* **27**, 365501 (2015). Cited on page(s) 13 and 102

[81] A. Klein, S. Tiefenbacher, V. Eyert, C. Pettenkofer and W. Jaegermann, 'Electronic Properties of WS_2 Monolayer Films', *Thin Solid Films* **380**, 221 (2000). Cited on page(s) 13

[82] A. Klein, S. Tiefenbacher, V. Eyert, C. Pettenkofer and W. Jaegermann, 'Electronic Band Structure of Single-Crystal and Single-Layer WS_2 : Influence of Interlayer van der Waals Interactions', *Phys. Rev. B* **64**, 205416 (2001). Cited on page(s) 13

[83] K. F. Mak, K. He, J. Shan and T. F. Heinz, 'Control of valley polarization in monolayer MoS_2 by optical helicity', *Nat. Nanotechnol.* **7**, 494 (2012). Cited on page(s) 13

[84] H. Zeng, J. Dai, W. Yao, D. Xiao and X. Cui, 'Valley polarization in MoS_2 monolayers by optical pumping', *Nat. Nanotechnol.* **7**, 490 (2012). Cited on page(s) 13

[85] X. Xu, W. Yao, D. Xiao and T. F. Heinz, 'Spin and Pseudospins in Layered Transition Metal Dichalcogenides', *Nat. Phys.* **10**, 343 (2014). Cited on page(s) 13

[86] A. Pulkin and O. V. Yazyev, ‘Spin- and valley-polarized transport across line defects in monolayer MoS_2’, *Phys. Rev. B* **93**, 41419 (2016). Cited on page(s) 13

[87] G. Eda, H. Yamaguchi, D. Voiry, T. Fujita, M. Chen and M. Chhowalla, ‘Photoluminescence From Chemically Exfoliated MoS_2’, *Nano Lett.* **11**, 5111 (2011). Cited on page(s) 13 and 23

[88] C. Lee, H. Yan, L. E. Brus, T. F. Heinz, J. Hone and S. Ryu, ‘Anomalous Lattice Vibrations of Single- and Few-Layer MoS_2’, *ACS Nano* **4**, 2695 (2010). Cited on page(s) 13

[89] H. Li, Q. Zhang, C. C. R. Yap, B. K. Tay, T. H. T. Edwin, A. Olivier and D. Baillargeat, ‘From Bulk to Monolayer MoS_2: Evolution of Raman Scattering’, *Adv. Funct. Mater.* **22**, 1385 (2012). Cited on page(s) 13

[90] G. Grüner, ‘Density Waves in Solids’ (CRC Press, Boca Raton, FL, 1994). Cited on page(s) 13, 15, and 17

[91] R. E. Peierls, ‘Quantum Theory of Solids’ (Clarendon Press, Oxford, 1955), 229. Cited on page(s) 13

[92] H. Fröhlich, ‘On the Theory of Superconductivity: The One-Dimensional Case’, *Proc. R. Soc. London. Ser. A.* **223**, 296 (1954). Cited on page(s) 13

[93] W. L. McMillan, ‘Electron-Phonon Interact. Phase Transitions’ (Springer US, Boston, MA, 1977), Pages 137–141. Cited on page(s) 13

[94] J. A. Wilson, F. J. Di Salvo and S. Mahajan, ‘Charge-Density Waves and Superlattices in the Metallic Layered Transition Metal Dichalcogenides’, *Adv. Phys.* **24**, 117 (1975). Cited on page(s) 13, 18, 20, and 93

[95] A. H. Castro Neto, ‘Charge Density Wave, Superconductivity, and Anomalous Metallic Behavior in 2D Transition Metal Dichalcogenides’, *Phys. Rev. Lett.* **86**, 4382 (2001). Cited on page(s) 13

[96] K. Rossnagel, ‘On the origin of charge-density waves in select layered transition-metal dichalcogenides’, *J. Phys. Condens. Matter* **23**, 213001 (2011). Cited on page(s) 13, 14, and 20

[97] C. Kittel, ‘Einführung in die Festkörperphysik’ (Oldenbourg, München Wien, 2002), 725. Cited on page(s) 14

[98] J. Lindhard, ‘On the Properties of a Gas of Charged Particles, by J. Lindhard’ (E. Munksgaard, Kopenhagen, 1954). Cited on page(s) 15

[99] S. M. Girvin and K. Yang, ‘Mod. Condens. Matter Phys.’ (Cambridge University Press, Cambridge, 2019). Cited on page(s) 15

[100] G. Giuliani and G. Vignale, ‘Quantum Theory of the Electron Liquid’ (Cambridge University Press, Cambridge, 2005), 777. Cited on page(s) 15

[101] W. Kohn, ‘Image of the Fermi Surface in the Vibration Spectrum of a Metal’, *Phys. Rev. Lett.* **2**, 393 (1959). Cited on page(s) 16

[102] S. K. Chan and V. Heine, ‘Spin Density Wave and Soft Phonon Mode from Nesting Fermi Surfaces’, *J. Phys. F* **3**, 795 (1973). Cited on page(s) 17

[103] X. Zhu, J. Guo, J. Zhang and E. W. Plummer, ‘Misconceptions associated with the origin of charge density waves’, *Adv. Phys. X* **2**, 622 (2017). Cited on page(s) 18

[104] X. Zhu, Y. Cao, J. Zhang, E. W. Plummer and J. Guo, ‘Classification of charge density waves based on their nature’, *Proc. Natl. Acad. Sci.* **112**, 2367 (2015). Cited on page(s) 18

[105] P. B. Littlewood and V. Heine, ‘The Effect of Electron-Electron Interactions on the Peierls Transition in Metals with Strong Nesting of Fermi Surfaces.’, *J. Phys. C* **14**, 2943 (1981). Cited on page(s) 18

[106] K. Tsutsumi, Y. Ishihara and H. Suzuki, ‘Adv. Supercond. II’ (Springer Japan, Tokyo, 1990), Pages 533–536. Cited on page(s) 19

[107] J. Feng *et al.*, 'Electronic Structure and Enhanced Charge-Density Wave Order of Monolayer VSe_2', *Nano Lett.* **18**, 4493 (2018). Cited on page(s) 19 and 72

[108] M. Bonilla, S. Kolekar, Y. Ma, H. C. Diaz, V. Kalappattil, R. Das, T. Eggers, H. R. Gutierrez, M. H. Phan and M. Batzill, 'Strong Roomerature Ferromagnetism in VSe_2 Monolayers on van der Waals Substrates', *Nat. Nanotechnol.* **13**, 289 (2018). Cited on page(s) 19, 21, 24, and 72

[109] G. Duvjir *et al.*, 'Emergence of a Metal–Insulator Transition and High-Temperature Charge-Density Waves in VSe_2 at the Monolayer Limit', *Nano Lett.* **18**, 5432 (2018). Cited on page(s) 19 and 91

[110] M. Leroux, L. Cario, A. Bosak and P. Rodière, 'Traces of Charge Density Waves in NbS_2', *Phys. Rev. B* **97**, 195140 (2018). Cited on page(s) 19

[111] M. Naito and S. Tanaka, 'Electrical Transport Properties in 2H-NbS_2, -$NbSe_2$, -TaS_2 and -$TaSe_2$', *J. Phys. Soc. Japan* **51**, 219 (1982). Cited on page(s) 19

[112] I. Guillamón, H. Suderow, S. Vieira, L. Cario, P. Diener and P. Rodière, 'Superconducting Density of States and Vortex Cores of 2H-NbS_2', *Phys. Rev. Lett.* **101**, 166407 (2008). Cited on page(s) 19

[113] C. Tresca and M. Calandra, 'Charge density wave and spin 1/2 insulating state in single layer 1T-NbS_2', *2D Mater.* **6**, 035041 (2019). Cited on page(s) 19 and 20

[114] N. Ramšak, H. J. P. van Midden, A. Prodan, V. Marinković, F. W. Boswell and J. C. Bennett, 'Defect-Induced Room-Temperature Modulation in NbS_2', *Phys. Rev. B* **60**, 4513 (1999). Cited on page(s) 19

[115] D. E. Moncton, J. D. Axe and F. J. Disalvo, 'Study of Superlattice Formation in 2H-$NbSe_2$ and 2H-$TaSe_2$ by Neutron Scattering', *Phys. Rev. Lett.* **34**, 734 (1975). Cited on page(s) 18 and 19

[116] E. Revolinsky, G. A. Spiering and D. J. Beerntsen, 'Superconductivity in the Niobium-Selenium System', *J. Phys. Chem. Solids* **26**, 1029 (1965). Cited on page(s) 18 and 19

[117] L. Li, W. Lu, Y. Liu, Z. Qu, L. Ling and Y. Sun, 'Influence of Defects on Charge-Density-Wave and Superconductivity in 1T-TaS_2 and 2H-TaS_2 systems', *Phys. C Supercond.* **492**, 64 (2013). Cited on page(s) 19

[118] Y.-F. Cao, K.-M. Cai, L.-J. Li, W.-J. Lu, Y.-P. Sun and K.-Y. Wang, 'Transport and Capacitance Properties of Charge Density Wave in Few-Layer 2H-TaS_2 Devices', *Chinese Phys. Lett.* **31**, 077203 (2014). Cited on page(s) 19

[119] X. Wang, H. Liu, J. Wu, J. Lin, W. He, H. Wang, X. Shi, K. Suenaga and L. Xie, 'Chemical Growth of 1T-TaS_2 Monolayer and Thin Films: Robust Charge Density Wave Transitions and High Bolometric Responsivity', *Adv. Mater.* **30**, 1800074 (2018). Cited on page(s) 19

[120] K. I. Yokota, G. Kurata, T. Matsui and H. Fukuyama, 'Superconductivity in the Quasi-Two-Dimensional Conductor 2H-$TaSe_2$', *Phys. B* **284-288**, 551 (2000). Cited on page(s) 18 and 19

[121] P. C. Börner, M. K. Kinyanjui, T. Björkman, T. Lehnert, A. V. Krasheninnikov and U. Kaiser, 'Observation of Charge Density Waves in Free-Standing 1T-$TaSe_2$ Monolayers by Transmission Electron Microscopy', *Appl. Phys. Lett.* **113**, 173103 (2018). Cited on page(s) 19

[122] R. Samnakay, D. Wickramaratne, T. R. Pope, R. K. Lake, T. T. Salguero and A. A. Balandin, 'Zone-Folded Phonons and the Commensurate–Incommensurate Charge-Density-Wave Transition in 1T-$TaSe_2$ Thin Films', *Nano Lett.* **15**, 2965 (2015). Cited on page(s) 19

[123] H. Ryu *et al.*, 'Persistent Charge-Density-Wave Order in Single-Layer $TaSe_2$', *Nano Lett.* **18**, 689 (2018). Cited on page(s) 18 and 19

[124] T. Kumakura, H. Tan, T. Handa, M. Morishita and H. Fukuyama, 'Charge Density Waves and Superconductivity in 2H-$TaSe_2$', *Czechoslov. J. Phys.* **46**, 2611 (1996). Cited on page(s) 18

[125] D. J. Eaglesham, S. McKernan and J. W. Steeds, 'A Double Honeycomb of Discommensurations in the Triply-Incommensurate State of 2H-$NbSe_2$', *J. Phys. C* **18**, L27 (1985). Cited on page(s) 18

[126] K. Ghoshray, B. Pahari, A. Ghoshray, V. V. Eremenko, V. A. Sirenko and B. H. Suits, '^{93}Nb NMR Study of the Charge Density Wave State in $NbSe_2$', *J. Phys. Condens. Matter* **21**, 155701 (2009). Cited on page(s) 18

[127] A. Soumyanarayanan, M. M. Yee, Y. He, J. van Wezel, D. J. Rahn, K. Rossnagel, E. W. Hudson, M. R. Norman and J. E. Hoffman, 'Quantum phase transition from triangular to stripe charge order in $NbSe_2$', *Proc. Natl. Acad. Sci.* **110**, 1623 (2013). Cited on page(s) 18

[128] N. E. Staley, J. Wu, P. Eklund, Y. Liu, L. Li and Z. Xu, 'Electric field effect on superconductivity in atomically thin flakes of $NbSe_2$', *Phys. Rev. B* **80**, 184505 (2009). Cited on page(s) 19

[129] M. Remškar, A. Prodan and V. Marinković, 'Charge-density wave modulation in surface layers of TaS_2 and NbS_2', *Surf. Sci.* **287-288**, 409 (1993). Cited on page(s) 19

[130] M. F. Bianco Raffaello, Errea Ion, Monacelli Lorenzo, Calandra Matteo, 'Quantum Enhancement of Charge Density Wave in NbS_2 in the 2D Limit', *Nano Lett.* **3**, 1 (2019). Cited on page(s) 19 and 94

[131] F. Güller, V. L. Vildosola and A. M. Llois, 'Spin Density Wave Instabilities in the NbS_2 Monolayer', *Phys. Rev. B* **93**, 94434 (2016). Cited on page(s) 19

[132] M. D. Johannes, I. I. Mazin and C. A. Howells, 'Fermi-Surface Nesting and the Origin of the Charge-Density Wave in $NbSe_2$', *Phys. Rev. B* **73**, 205102 (2006). Cited on page(s) 20

[133] M. D. Johannes and I. I. Mazin, 'Fermi Surface Nesting and the Origin of Charge Density Waves in Metals', *Phys. Rev. B* **77**, 165135 (2008). Cited on page(s) 20

[134] C. J. Arguello, S. P. Chockalingam, E. P. Rosenthal, L. Zhao, C. Gutiérrez, J. H. Kang, W. C. Chung, R. M. Fernandes, S. Jia, A. J. Millis, R. J. Cava and A. N. Pasupathy, 'Visualizing the Charge Density Wave Transition in 2H - NbSe2 in Real Space', *Phys. Rev. B* **89**, 235115 (2014). Cited on page(s) 20

[135] W. R. Fehlner and P. D. Loly, 'Nearly Flat Fermi Surfaces and the Static Wavenumber Dependent Susceptibility of Metals', *Solid State Commun.* **14**, 653 (1974). Cited on page(s) 20

[136] F. Weber, S. Rosenkranz, J. P. Castellan, R. Osborn, R. Hott, R. Heid, K. P. Bohnen, T. Egami, A. H. Said and D. Reznik, 'Extended phonon collapse and the origin of the charge-density wave in 2H-$NbSe_2$', *Phys. Rev. Lett.* **107**, 107403 (2011). Cited on page(s) 20

[137] F. Weber, R. Hott, R. Heid, K. P. Bohnen, S. Rosenkranz, J. P. Castellan, R. Osborn, A. H. Said, B. M. Leu and D. Reznik, 'Optical phonons and the soft mode in 2H-$NbSe_2$', *Phys. Rev. B* **87**, 245111 (2013). Cited on page(s) 20

[138] P. Darancet, A. J. Millis and C. A. Marianetti, 'Three-Dimensional Metallic and Two-Dimensional Insulating Behavior in Octahedral Tantalum Dichalcogenides', *Phys. Rev. B* **90**, 045134 (2014). Cited on page(s) 20

[139] P. Fazekas and E. Tosatti, 'Electrical, Structural and Magnetic Properties of Pure and Doped 1T-TaS_2', *Philos. Mag. B* **39**, 229 (1979). Cited on page(s) 20

[140] M. Calandra, 'Phonon-Assisted Magnetic Mott-Insulating State in the Charge Density Wave Phase of Single-Layer 1T-$NbSe_2$', *Phys. Rev. Lett.* **121**, 26401 (2018). Cited on page(s) 20

[141] R. Brouwer and F. Jellinek, 'The Low-Temperature Superstructures of 1T-$TaSe_2$ and 2H-$TaSe_2$', *Phys. B+C* **99**, 51 (1980). Cited on page(s) 20

[142] F. Bischoff, W. Auwärter, J. V. Barth, A. Schiffrin, M. Fuhrer and B. Weber, 'Nanoscale Phase Engineering of Niobium Diselenide', *Chem. Mater.* **29**, 9907 (2017). Cited on page(s) 20

[143] L. J. De Jongh and A. R. Miedema, 'Experiments on Simple Magnetic Model Systems', *Adv. Phys.* **23**, 1 (1974). Cited on page(s) 20

[144] 'Magnetic Properties of Layered Transition Metal Compounds', Vol. 9 of 'Physics and Chemistry of Meterials with Low-Dimensional Structures', edited by L. J. de Jongh (Springer Netherlands, Dordrecht, 1990). Cited on page(s) 20

[145] M. Gibertini, M. Koperski, A. F. Morpurgo and K. S. Novoselov, 'Magnetic 2D Materials and Heterostructures', *Nat. Nanotechnol.* **14**, 408 (2019). Cited on page(s) 20, 21, and 22

[146] R. Peierls, 'On Ising's model of ferromagnetism', *Math. Proc. Cambridge Philos. Soc.* **32**, 477 (1936). Cited on page(s) 20

[147] N. D. Mermin and H. Wagner, 'Absence of ferromagnetism or antiferromagnetism in one- or two-dimensional isotropic Heisenberg models', *Phys. Rev. Lett.* **17**, 1133 (1966). Cited on page(s) 21

[148] P. C. Hohenberg, 'Existence of Long-Range Order in One and Two Dimensions', *Phys. Rev.* **158**, 383 (1967). Cited on page(s) 21

[149] J. L. Lado and J. Fernández-Rossier, 'On the Origin of Magnetic Anisotropy in two Dimensional $\mathrm{CrI_3}$', *2D Mater.* **4**, 35002 (2017). Cited on page(s) 21

[150] S. Tongay, S. S. Varnoosfaderani, B. R. Appleton, J. Wu and A. F. Hebard, 'Magnetic properties of $\mathrm{MoS_2}$: Existence of ferromagnetism', *Appl. Phys. Lett.* **101**, 123105 (2012). Cited on page(s) 21

[151] Z. Yang, D. Gao, J. Zhang, Q. Xu, S. Shi, K. Tao and D. Xue, 'Realization of high Curie temperature ferromagnetism in atomically thin $\mathrm{MoS_2}$ and WS_2 nanosheets with uniform and flower-like morphology', *Nanoscale* **7**, 650 (2015). Cited on page(s) 21

[152] X. Mao, Y. Xu, Q. Xue, W. Wang and D. Gao, 'Ferromagnetism in exfoliated tungsten disulfide nanosheets', *Nanoscale Res. Lett.* **8**, 1 (2013). Cited on page(s) 21

[153] Z. Zhang, X. Zou, V. H. Crespi and B. I. Yakobson, 'Intrinsic Magnetism of Grain Boundaries in Two-Dimensional Metal Dichalcogenides', *ACS Nano* **7**, 10475 (2013). Cited on page(s) 21

[154] R. Shidpour and M. Manteghian, 'A density functional study of strong local magnetism creation on $\mathrm{MoS_2}$ nanoribbon by sulfur vacancy', *Nanoscale* **2**, 1429 (2010). Cited on page(s) 21

[155] M. Kan, B. Wang, Y. H. Lee and Q. Sun, 'A Density Functional Theory Study of the Tunable Structure, Magnetism and Metal-Insulator Phase Transition in $\mathrm{VS_2}$ Monolayers Induced by In-Plane Biaxial Strain', *Nano Res.* **8**, 1348 (2015). Cited on page(s) 21

[156] B. Liu, L. J. Wu, Y. Q. Zhao, L. Z. Wang and M. Q. Cai, 'A First-Principles Study of Magnetic Variation via Doping Vacancy in Monolayer $\mathrm{VS_2}$', *J. Magn. Magn. Mater.* **420**, 218 (2016). Cited on page(s) 21

[157] D. Gao, Q. Xue, X. Mao, W. Wang, Q. Xu and D. Xue, 'Ferromagnetism in Ultrathin $\mathrm{VS_2}$ Nanosheets', *J. Mater. Chem. C* **1**, 5909 (2013). Cited on page(s) 21 and 72

[158] M. Zhong, Y. Li, Q. Xia, X. Meng, F. Wu and J. Li, 'Ferromagnetism in $\mathrm{VS_2}$ nanostructures: Nanoflowers versus ultrathin nanosheets', *Mater. Lett.* **124**, 282 (2014). Cited on page(s) 21 and 72

[159] Z. L. Liu, X. Wu, Y. Shao, J. Qi, Y. Cao, L. Huang, C. Liu, J. O. Wang, Q. Zheng, Z. L. Zhu, K. Ibrahim, Y. L. Wang and H. J. Gao, 'Epitaxially Grown Monolayer $\mathrm{VSe_2}$ - an Air-Stable Magnetic Two-Dimensional Material with Low Work Function at Edges', *Sci. Bull.* **63**, 419 (2018). Cited on page(s) 21 and 72

[160] C. F. van Bruggen and C. Haas, 'Magnetic susceptibility and electrical properties of $\mathrm{VSe_2}$ single crystals', *Solid State Commun.* **20**, 251 (1976). Cited on page(s) 21 and 72

[161] E. C. Stoner, 'Atomic moments in ferromagnetic metals and alloys with non-ferromagnetic elements', *London, Edinburgh, Dublin Philos. Mag. J. Sci.* **15**, 1018 (1933). Cited on page(s) 22

[162] A. O. Fumega and V. Pardo, 'Absence of Ferromagnetism in $\mathrm{VSe_2}$ Caused by its Charge Density Wave Phase', *arXiv Prepr. arXiv1804.07102* **2018**, (2018). Cited on page(s) 22 and 72

[163] J. Zhou, J. Qiao, C.-G. Duan, A. Bournel, K. L. Wang and W. Zhao, 'Large tunneling magnetoresistance in $\mathrm{VSe_2/MoS_2}$ magnetic tunnel junction', *ACS Appl. Mater. Interfaces* **11**, 17647 (2019). Cited on page(s) 22

[164] L.-Y. Gan, Q. Zhang, Y. Cheng and U. Schwingenschlögl, 'Two-Dimensional Ferromagnet/Semiconductor Transition Metal Dichalcogenide Contacts: *p*-Type Schottky Barrier and Spin-Injection Control', *Phys. Rev. B* **88**, 235310 (2013). Cited on page(s) 22

[165] E. Gao, S. Z. Lin, Z. Qin, M. J. Buehler, X. Q. Feng and Z. Xu, 'Mechanical Exfoliation of Two-Dimensional Materials', *J. Mech. Phys. Solids* **115**, 248 (2018). Cited on page(s) 22

[166] Y. Shi, H. Li and L. J. Li, 'Recent advances in controlled synthesis of two-dimensional transition metal dichalcogenides via vapour deposition techniques', *Chem. Soc. Rev.* **44**, 2744 (2015). Cited on page(s) 22

[167] P. Schmidt, M. Binnewies, R. Glaum and M. Schmidt, 'Adv. Top. Cryst. Growth' (IntechOpen, www.intechopen.de, 2013). Cited on page(s) 22

[168] S. Das, J. A. Robinson, M. Dubey, H. Terrones and M. Terrones, 'Beyond Graphene: Progress in Novel Two-Dimensional Materials and van der Waals Solids', *Annu. Rev. Mater. Res.* **45**, 1 (2015). Cited on page(s) 22

[169] T. Moldt, A. Eckmann, P. Klar, S. V. Morozov, A. A. Zhukov, K. S. Novoselov and C. Casiraghi, 'High-yield production and transfer of graphene flakes obtained by anodic bonding', *ACS Nano* **5**, 7700 (2011). Cited on page(s) 23

[170] M. Velický, P. S. Toth, A. M. Rakowski, A. P. Rooney, A. Kozikov, C. R. Woods, A. Mishchenko, L. Fumagalli, J. Yin, V. Zólyomi, T. Georgiou, S. J. Haigh, K. S. Novoselov and R. A. Dryfe, 'Exfoliation of Natural van der Waals Heterostructures to a Single Unit Cell Thickness', *Nat. Commun.* **8**, 14410 (2017). Cited on page(s) 23

[171] A. Jawaid, D. Nepal, K. Park, M. Jespersen, A. Qualley, P. Mirau, L. F. Drummy and R. A. Vaia, 'Mechanism for Liquid Phase Exfoliation of MoS_2', *Chem. Mater.* **28**, 337 (2016). Cited on page(s) 23

[172] Q. Du, M. Zheng, L. Zhang, Y. Wang, J. Chen, L. Xue, W. Dai, G. Ji and J. Cao, 'Preparation of Functionalized Graphene Sheets by a Low-Temperature Thermal Exfoliation Approach and Their Electrochemical Supercapacitive Behaviors', *Electrochim. Acta* **55**, 3897 (2010). Cited on page(s) 23

[173] C. R. Wu, X. R. Chang, C. H. Wu and S. Y. Lin, 'The Growth Mechanism of Transition Metal Dichalcogenides by using Sulfurization of Pre-deposited Transition Metals and the 2D Crystal Hetero-structure Establishment', *Sci. Rep.* **7**, 42146 (2017). Cited on page(s) 23

[174] Y.-H. Lee, X.-Q. Zhang, W. Zhang, M.-T. Chang, C.-T. Lin, K.-D. Chang, Y.-C. Yu, J. T.-W. Wang, C.-S. Chang, L.-J. Li and Others, 'Synthesis of Large-Area MoS_2 Atomic Layers with Chemical Vapor Deposition', *Adv. Mater.* **24**, 2320 (2012). Cited on page(s) 23

[175] Q. Li, Q. Zhou, L. Shi, Q. Chen and J. Wang, 'Recent Advances in Oxidation and Degradation Mechanisms of Ultrathin 2D Materials Under Ambient Conditions and Their Passivation Strategies', *J. Mater. Chem. A* **7**, 4291 (2019). Cited on page(s) 23

[176] Y. Wang *et al.*, 'Monolayer $PtSe_2$, a new semiconducting transition-metal-dichalcogenide, epitaxially grown by direct selenization of Pt', *Nano Lett.* **15**, 4013 (2015). Cited on page(s) 23

[177] S. Helveg, J. V. Lauritsen, E. Lægsgaard, I. Stensgaard, J. K. Nørskov, B. S. Clausen, H. Topsøe and F. Besenbacher, 'Atomic-Scale Structure of Single-Layer MoS_2 Nanoclusters', *Phys. Rev. Lett.* **84**, 951 (2000). Cited on page(s) 23 and 43

[178] J. V. Lauritsen, J. Kibsgaard, S. Helveg, H. Topsøe, B. S. Clausen, E. Lægsgaard and F. Besenbacher, 'Size-Dependent Structure of MoS_2 Nanocrystals', *Nat. Nanotechnol.* **2**, 53 (2007). Cited on page(s) 23

[179] S. G. Sørensen, H. G. Fuchtbauer, A. K. Tuxen, A. S. Walton and J. V. Lauritsen, 'Structure and Electronic Properties of In Situ Synthesized Single-Layer MoS_2 on a Gold Surface', *ACS Nano* **8**, 6788 (2014). Cited on page(s) 23

[180] S. S. Grønborg, S. Ulstrup, M. Bianchi, M. Dendzik, C. E. Sanders, J. V. Lauritsen, P. Hofmann and J. A. Miwa, 'Synthesis of Epitaxial Single-Layer MoS_2 on Au(111)', *Langmuir* **31**, 9700 (2015). Cited on page(s) 23

[181] H. Bana *et al.*, 'Epitaxial Growth of Single-Orientation High-Quality MoS_2 Monolayers', *2D Mater.* **5**, 35012 (2018). Cited on page(s) 23

[182] J. A. Miwa, M. Dendzik, S. S. Grønborg, M. Bianchi, J. V. Lauritsen, P. Hofmann and S. Ulstrup, 'Van der Waals Epitaxy of Two-Dimensional MoS_2/Graphene Heterostructures in Ultrahigh Vacuum', *ACS Nano* **9**, 6502 (2015). Cited on page(s) 23, 40, and 43

[183] A. Grubišić Čabo, J. A. Miwa, S. S. Grønborg, J. M. Riley, J. C. Johannsen, C. Cacho, O. Alexander, R. T. Chapman, E. Springate, M. Grioni, J. V. Lauritsen, P. D. C. King, P. Hofmann and S. Ulstrup, 'Observation of Ultrafast Free Carrier Dynamics in Single Layer MoS_2', *Nano Lett.* **15**, 5883 (2015). Cited on page(s) 23

[184] A. Bruix, J. A. Miwa, N. Hauptmann, D. Wegner, S. Ulstrup, S. S. Grønborg, C. E. Sanders, M. Dendzik, A. Grubišić Čabo, M. Bianchi, J. V. Lauritsen, A. A. Khajetoorians, B. Hammer and P. Hofmann, 'Single-layer MoS_2 on Au(111): Band Gap Renormalization and Substrate Interaction', *Phys. Rev. B* **93**, 165422 (2016). Cited on page(s) 23 and 46

[185] S. K. Mahatha *et al.*, 'Electron-Phonon Coupling in Single-Layer MoS_2', *Surf. Sci.* **681**, 64 (2019). Cited on page(s) 24

[186] L. A. Walsh, R. Addou, R. M. Wallace and C. L. Hinkle, 'Molecular Beam Epitaxy' (Elsevier, Waltham, MA, 2018), Pages 515–531. Cited on page(s) 24

[187] D. Tsoutsou, K. E. Aretouli, P. Tsipas, J. Marquez-Velasco, E. Xenogiannopoulou, N. Kelaidis, S. Aminalragia Giamini and A. Dimoulas, 'Epitaxial 2D $MoSe_2$ ($HfSe_2$) semiconductor/2D $TaSe_2$ metal van der Waals heterostructures', *ACS Appl. Mater. & Interfaces* **8**, 1836 (2016). Cited on page(s) 24

[188] H. C. Diaz, R. Chaghi, Y. Ma and M. Batzill, 'Molecular Beam Epitaxy of the van der Waals Heterostructure $MoTe_2$ on MoS_2 : Phase, Thermal, and Chemical Stability', *2D Mater.* **2**, 44010 (2015). Cited on page(s) 24, 40, and 52

[189] A. Koma, 'Van der Waals Epitaxy for Highly Lattice-Mismatched Systems', *J. Cryst. Growth* **201**, 236 (1999). Cited on page(s) 24

[190] L. A. Walsh, R. Yue, Q. Wang, A. T. Barton, R. Addou, C. M. Smyth, H. Zhu, J. Kim, L. Colombo, M. J. Kim, R. M. Wallace and C. L. Hinkle, 'WTe_2 thin films grown by beam-interrupted molecular beam epitaxy', *2D Mater.* **4**, 025044 (2017). Cited on page(s) 24

[191] R. Yue *et al.*, '$HfSe_2$ thin films: 2D transition metal dichalcogenides grown by molecular beam epitaxy', *ACS Nano* **9**, 474 (2015). Cited on page(s) 24

[192] A. Roy, H. C. P. Movva, B. Satpati, K. Kim, R. Dey, A. Rai, T. Pramanik, S. Guchhait, E. Tutuc and S. K. Banerjee, 'Structural and Electrical Properties of $MoTe_2$ and $MoSe_2$ Grown by Molecular Beam Epitaxy', *ACS Appl. Mater. & Interfaces* **8**, 7396 (2016). Cited on page(s) 24

[193] Y. Yu, G. Wang, S. Qin, N. Wu, Z. Wang, K. He and X. A. Zhang, 'Molecular beam epitaxy growth of atomically ultrathin $MoTe_2$ lateral heterophase homojunctions on graphene substrates', *Carbon* **115**, 526 (2017). Cited on page(s) 24

[194] X. Liu, I. Balla, H. Bergeron, G. P. Campbell, M. J. Bedzyk and M. C. Hersam, 'Rotationally Commensurate Growth of MoS_2 on Epitaxial Graphene', *ACS Nano* **10**, 1067 (2016). Cited on page(s) 24, 43, and 46

[195] K. E. Aretouli, P. Tsipas, D. Tsoutsou, J. Marquez-Velasco, E. Xenogiannopoulou, S. A. Giamini, E. Vassalou, N. Kelaidis and A. Dimoulas, 'Two-Dimensional Semiconductor $HfSe_2$ and $MoSe_2$/$HfSe_2$ van der Waals Heterostructures by Molecular Beam Epitaxy', *Appl. Phys. Lett.* **106**, 143105 (2015). Cited on page(s) 24

[196] K. E. Aretouli, D. Tsoutsou, P. Tsipas, J. Marquez-Velasco, S. Aminalragia Giamini, N. Kelaidis, V. Psycharis and A. Dimoulas, 'Epitaxial 2D $SnSe_2$/ 2D WSe_2 van der Waals Heterostructures', *ACS Appl. Mater. & Interfaces* **8**, 23222 (2016). Cited on page(s) 24

[197] K. Kobayashi, 'Moiré Pattern In Scanning Tunneling Microscopy: Mechanism in Observation of Subsurface Nanostructures', *Phys. Rev. B* **53**, 11091 (1996). Cited on page(s) 24

[198] C. Zhang, C. P. Chuu, X. Ren, M. Y. Li, L. J. Li, C. Jin, M. Y. Chou and C. K. Shih, 'Interlayer couplings, Moiré patterns, and 2D electronic superlattices in MoS_2/WSe_2 hetero-bilayers', *Sci. Adv.* **3**, e1601459 (2017). Cited on page(s) 24

[199] H. J. Liu, L. Jiao, L. Xie, F. Yang, J. L. Chen, W. K. Ho, C. L. Gao, J. F. Jia, X. D. Cui and M. H. Xie, 'Molecular-Beam Epitaxy of Monolayer and Bilayer WSe_2: A Scanning Tunneling Microscopy/Spectroscopy Study and Deduction of Exciton Binding Energy', *2D Mater.* **2**, 34004 (2015). Cited on page(s) 24

[200] Y. Zhang *et al.*, 'Electronic structure, surface doping, and optical response in epitaxial WSe_2 thin films', *Nano Lett.* **16**, 2485 (2016). Cited on page(s) 24

[201] S. Tiefenbacher, C. Pettenkofer and W. Jaegermann, 'Moiré pattern in LEED obtained by van der Waals epitaxy of lattice mismatched $WS_2/MoTe_2(0001)$ heterointerfaces', *Surf. Sci.* **450**, 181 (2000). Cited on page(s) 24

[202] M. M. Ugeda, A. J. Bradley, S.-F. Shi, F. H. da Jornada, Y. Zhang, D. Y. Qiu, W. Ruan, S.-K. Mo, Z. Hussain, Z.-X. Shen, F. Wang, S. G. Louie and M. F. Crommie, 'Giant bandgap renormalization and excitonic effects in a monolayer transition metal dichalcogenide semiconductor', *Nat. Mater.* **13**, 1091 (2014). Cited on page(s) 24, 25, and 40

[203] P. Pochet, B. C. McGuigan, J. Coraux and H. T. Johnson, 'Toward Moiré engineering in 2D materials via dislocation theory', *Appl. Mater. Today* **9**, 240 (2017). Cited on page(s) 24

[204] S. Barja *et al.*, 'Charge Density Wave Order in 1D Mirror Twin Boundaries of Single-Layer $MoSe_2$', *Nat. Phys.* **12**, 751 (2016). Cited on page(s) 24, 40, 44, and 67

[205] Y. Ma, H. C. Diaz, J. Avila, C. Chen, V. Kalappattil, R. Das, M.-H. Phan, T. Čadež, J. M. P. Carmelo, M. C. Asensio and M. Batzill, 'Angle resolved photoemission spectroscopy reveals spin charge separation in metallic $MoSe_2$ grain boundary', *Nat. Commun.* **8**, 14231 (2017). Cited on page(s) 24, 40, 44, and 67

[206] R. Yue *et al.*, 'Nucleation and growth of WSe_2: enabling large grain transition metal dichalcogenides', *2D Mater.* **4**, 45019 (2017). Cited on page(s) 25, 52, and 118

[207] V. I. Artyukhov, Z. Hu, Z. Zhang and B. I. Yakobson, 'Topochemistry of Bowtie- and Star-Shaped Metal Dichalcogenide Nanoisland Formation', *Nano Lett.* **16**, 3696 (2016). Cited on page(s) 25

[208] A. Govind Rajan, J. H. Warner, D. Blankschtein and M. S. Strano, 'Generalized Mechanistic Model for the Chemical Vapor Deposition of 2D Transition Metal Dichalcogenide Monolayers', *ACS Nano* **10**, 4330 (2016). Cited on page(s) 25

[209] Y. Nie, C. Liang, K. Zhang, R. Zhao, S. M. Eichfeld, P. R. Cha, L. Colombo, J. A. Robinson, R. M. Wallace and K. Cho, 'First principles kinetic Monte Carlo study on the growth patterns of WSe_2 monolayer', *2D Mater.* **3**, 25029 (2016). Cited on page(s) 25

[210] Y. Nie, C. Liang, P.-R. Cha, L. Colombo, R. M. Wallace and K. Cho, 'A kinetic Monte Carlo simulation method of van der Waals epitaxy for atomistic nucleation-growth processes of transition metal dichalcogenides', *Sci. Rep.* **7**, 2977 (2017). Cited on page(s) 25 and 118

[211] L. Wu, W. Yang and G. Wang, 'Mechanism of substrate-induced anisotropic growth of monolayer WS_2 by kinetic Monte Carlo simulations', *npj 2D Mater. Appl.* **3**, 6 (2019). Cited on page(s) 25

[212] H. C. Diaz, Y. Ma, S. Kolekar, J. Avila, C. Chen, M. C. Asensio and M. Batzill, 'Substrate Dependent Electronic Structure Variations of van der Waals Heterostructures of $MoSe_2$ or $MoSe_{2(1-x)}Ta_{2x}$ Grown by van der Waals Epitaxy', *2D Mater.* **4**, 025094 (2017). Cited on page(s) 25

[213] N. R. Wilson, P. V. Nguyen, K. Seyler, P. Rivera, A. J. Marsden, Z. P. Laker, G. C. Constantinescu, V. Kandyba, A. Barinov, N. D. Hine, X. Xu and D. H. Cobden, 'Determination of Band Offsets, Hybridization, and Exciton Binding in 2D Semiconductor Heterostructures', *Sci. Adv.* **3**, e1601832 (2017). Cited on page(s) 25

[214] A. H. Castro Neto, F. Guinea, N. M. R. Peres, K. S. Novoselov and A. K. Geim, 'The Electronic Properties of Graphene', *Rev. Mod. Phys.* **81**, 109 (2009). Cited on page(s) 25

[215] A. Eftekhari and H. Garcia, 'The Necessity of Structural Irregularities for the Chemical Applications of Graphene', *Mater. Today Chem.* **4**, 1 (2017). Cited on page(s) 25

[216] O. Leenaerts, B. Partoens and F. M. Peeters, 'Adsorption ofH_2O , NH_3, CO, NO_2 and NO on Graphene: A First-Principles Study', *Phys. Rev. B* **77**, 125416 (2008). Cited on page(s) 25

[217] A. T. N'Diaye, J. Coraux, T. N. Plasa, C. Busse and T. Michely, 'Structure of epitaxial graphene on Ir(111)', *New J. Phys.* **10**, 43033 (2008). Cited on page(s) 25 and 43

[218] P. Eckerlin and H. Kandler, in 'Group III: Condensed Matter (Landolt–Brönstein: Numerical Data and Functional Relationships in Science and Technology—New Series)', 6 ed., edited by P. Eckerlin and H. Kandler (Berlin: Springer, Berlin, 1971). Cited on page(s) 25

[219] C. Busse, P. Lazić, R. Djemour, J. Coraux, T. Gerber, N. Atodiresei, V. Caciuc, R. Brako, A. T. N'Diaye, S. Blügel, J. Zegenhagen and T. Michely, 'Graphene on Ir(111): Physisorption with Chemical Modulation', *Phys. Rev. Lett.* **107**, 036101 (2011). Cited on page(s) 26

[220] I. Pletikosić, M. Kralj, P. Pervan, R. Brako, J. Coraux, A. T. N'Diaye, C. Busse and T. Michely, 'Dirac Cones and Minigaps for Graphene on Ir(111)', *Phys. Rev. Lett.* **102**, 056808 (2009). Cited on page(s) 26

[221] F. H. zum Hagen *et al.*, 'Structure and Growth of Hexagonal Boron Nitride on Ir(111)', *ACS Nano* **10**, 11012 (2016). Cited on page(s) 26, 34, and 49

[222] J. Gómez Díaz, Y. Ding, R. Koitz, A. P. Seitsonen, M. Iannuzzi and J. Hutter, 'Hexagonal Boron Nitride on Transition Metal Surfaces', *Theor. Chem. Acc.* **132**, 1350 (2013). Cited on page(s) 26

[223] Nobelprize.org, 'The Nobel Prize 1986', *https://www.nobelprize.org/prizes/physics/1986/summary/* **1986**, (1986). Cited on page(s) 27

[224] C. J. Chen, 'Introduction to Scanning Tunneling Microscopy' (Oxford University Press, Oxford, 1993), 423. Cited on page(s) 27

[225] B. Voigtländer, 'Scanning Probe Microscopy', 'NanoScience and Technology' (Springer Berlin Heidelberg, Berlin, Heidelberg, 2015). Cited on page(s) 27 and 28

[226] J. Bardeen, 'Tunnelling from a Many-Particle Point of View', *Phys. Rev. Lett.* **6**, 57 (1961). Cited on page(s) 27

[227] J. Tersoff and D. R. Hamann, 'Theory and Application for the Scanning Tunneling Microscope', *Phys. Rev. Lett.* **50**, 1998 (1983). Cited on page(s) 28

[228] J. Tersoff and D. R. Hamann, 'Theory of the Scanning Tunneling Microscope', *Phys. Rev. B* **31**, 805 (1985). Cited on page(s) 28

[229] M. F. Crommie, C. P. Lutz and D. M. Eigler, 'Imaging Standing Waves in a Two-Dimensional Electron Gas', *Nature* **363**, 524 (1993). Cited on page(s) 29 and 101

[230] Y. Hasegawa and P. Avouris, 'Direct Observation of Standing Wave Formation at Surface Steps Using Scanning Tunneling Spectroscopy', *Phys. Rev. Lett.* **71**, 1071 (1993). Cited on page(s) 29

[231] M. Yankowitz, D. McKenzie and B. J. LeRoy, 'Local Spectroscopic Characterization of Spin and Layer Polarization in WSe_2', *Phys. Rev. Lett.* **115**, 136803 (2015). Cited on page(s) 29

[232] H. Liu, J. Chen, H. Yu, F. Yang, L. Jiao, G.-B. Liu, W. Ho, C. Gao, J. Jia, W. Yao and M. Xie, 'Observation of Intervalley Quantum Interference in Epitaxial Monolayer Tungsten Diselenide', *Nat. Commun.* **6**, 8180 (2015). Cited on page(s) 29

[233] K. Kaasbjerg, J. H. J. Martiny, T. Low and A.-P. Jauho, 'Symmetry-Forbidden Intervalley Scattering by Atomic Defects in Monolayer Transition-Metal Dichalcogenides', *Phys. Rev. B* **96**, 241411 (2017). Cited on page(s) 29

[234] C. J. Arguello, E. P. Rosenthal, E. F. Andrade, W. Jin, P. C. Yeh, N. Zaki, S. Jia, R. J. Cava, R. M. Fernandes, A. J. Millis, T. Valla, R. M. Osgood and A. N. Pasupathy, 'Quasiparticle Interference, Quasiparticle Interactions, and the Origin of the Charge Density Wave in 2H-NbSe$_2$', *Phys. Rev. Lett.* **114**, 037001 (2015). Cited on page(s) 29

[235] L. Chen, P. Cheng and K. Wu, 'Quasiparticle Interference in Unconventional 2D Systems', *J. Phys. Condens. Matter* **29**, 103001 (2017). Cited on page(s) 29

[236] L. Simon, C. Bena, F. Vonau, M. Cranney and D. Aubel, 'Fourier-Transform Scanning Tunnelling Spectroscopy: the Possibility to Obtain Constant-Energy Maps and Band Dispersion Using a Local Measurement', *J. Phys. D.* **44**, 464010 (2011). Cited on page(s) 29

[237] J. Friedel, 'Metallic Alloys', *Nuovo Cim.* **7**, 287 (1958). Cited on page(s) 29

[238] J. E. Hoffman, 'Spectroscopic Scanning Tunneling Microscopy Insights into Fe-Based Superconductors', *Reports Prog. Phys.* **74**, 124513 (2011). Cited on page(s) 29

[239] N. W. Ashcroft, N. D. Mermin and J. Gress, 'Festkoörperphysik' (Oldenbourg, München Wien, 2001). Cited on page(s) 29

[240] L. Petersen, P. Hofmann, E. Plummer and F. Besenbacher, 'Fourier Transform–STM: Determining the Surface Fermi Contour', *J. Electron Spectros. Relat. Phenomena* **109**, 97 (2000). Cited on page(s) 29 and 101

[241] T. Hänke, S. Sykora, R. Schlegel, D. Baumann, L. Harnagea, S. Wurmehl, M. Daghofer, B. Büchner, J. van den Brink and C. Hess, 'Probing the Unconventional Superconducting State of LiFeAs by Quasiparticle Interference', *Phys. Rev. Lett.* **108**, 127001 (2012). Cited on page(s) 30

[242] C. Davisson and L. H. Germer, 'The Scattering of Electrons by a Single Crystal of Nickel', *Nature* **119**, 558 (1927). Cited on page(s) 30

[243] K. R. Mitchell, 'Low-Energy Electron Diffraction', *Contemp. Phys.* **14**, 251 (1973). Cited on page(s) 30

[244] D. Woodruff, 'Ref. Modul. Mater. Sci. Mater. Eng.' (Elsevier, Waltham, MA, 2016). Cited on page(s) 30

[245] H. Hertz, 'Ueber einen Einfluss des ultravioletten Lichtes auf die electrische Entladung', *Ann. der Phys. und Chemie* **267**, 983 (1887). Cited on page(s) 30

[246] A. Einstein, 'Über einen die Erzeugung und Verwandlung des Lichtes betreffenden heuristischen Gesichtspunkt', *Ann. Phys.* **322**, 132 (1905). Cited on page(s) 30

[247] H. Yang, A. Liang, C. Chen, C. Zhang, N. B. M. Schroeter and Y. Chen, 'Visualizing Electronic Structures of Quantum Materials by Angle-Resolved Photoemission Spectroscopy', *Nat. Rev. Mater.* **3**, 341 (2018). Cited on page(s) 30

[248] A. Damascelli, 'Probing the Electronic Structure of Complex Systems by ARPES', *Phys. Scr.* **T109**, 61 (2004). Cited on page(s) 31

[249] G. van der Laan and A. I. Figueroa, 'X-ray Magnetic Circular Dichroism – A Versatile Tool to Study Magnetism', *Coord. Chem. Rev.* **277-278**, 95 (2014). Cited on page(s) 31

[250] S. Standop, Dissertation, Universität zu Köln, 2013. Cited on page(s) 32

[251] S. Runte, Dissertation, Universität zu Köln, 2013. Cited on page(s) 32

[252] I. Horcas, R. Fernández, J. M. Gómez-Rodríguez, J. Colchero, J. Gómez-Herrero and A. M. Baro, 'WSXM: A Software for Scanning Probe Microscopy and a Tool for Nanotechnology', *Rev. Sci. Instrum.* **78**, 13705 (2007). Cited on page(s) 32

[253] L. Petaccia, P. Vilmercati, S. Gorovikov, M. Barnaba, A. Bianco, D. Cocco, C. Masciovecchio and A. Goldoni, 'BaD ElPh: A 4 m Normal-Incidence Monochromator Beamline at Elettra', *Nucl. Instruments Methods Phys. Res. Sect. A* **606**, 780 (2009). Cited on page(s) 33

[254] S. Schumacher *et al.*, 'Europium underneath graphene on Ir(111): Intercalation mechanism, magnetism, and band structure', *Phys. Rev. B* **90**, 235437 (2014). Cited on page(s) 34, 45, and 115

[255] P. Pervan, P. Lazić, M. Petrović, I. Šrut Rakić, I. Pletikosić, M. Kralj, M. Milun and T. Valla, 'Li Adsorption Versus Graphene Intercalation on Ir(111): From Quenching to Restoration of the Ir Surface State', *Phys. Rev. B* **92**, 245415 (2015). Cited on page(s) 34

[256] K. W. Nebesny, G. E. Collins, P. A. Lee, L. K. Chau, J. Danziger, E. Osburn and N. R. Armstrong, 'Organic/inorganic-molecular beam epitaxy: formation of an ordered phthalocyanine/tin (IV) sulfide heterojunction', *Chem. Mater.* **3**, 829 (1991). Cited on page(s) 34 and 40

[257] J. M. Lambert, G. Simkovich and P. L. Walker, 'The Kinetics and Mechanism of the Pyrite-to-Pyrrhotite Transformation', *Metall. Mater. Trans. B* **29**, 385 (1998). Cited on page(s) 34

[258] L. Charpentier and P. J. Masset, in 'Mater. Sci. Forum', Vol. 654-656 of 'Materials Science Forum', edited by J.-F. Nie and A. Morton (Trans Tech Publications, Trans Tech Publication, Switzerland, 2010), Pages 2398–2401. Cited on page(s) 34

[259] P. Giannozzi *et al.*, 'QUANTUM ESPRESSO: a Modular and Open-Source Software Project for Quantum Simulations of Materials', *J. Phys. Condens. Matter* **21**, 395502 (2009). Cited on page(s) 35

[260] P. Giannozzi *et al.*, 'Advanced Capabilities for Materials Modelling with QUANTUM ESPRESSO', *J. Phys. Condens. Matter* **29**, 465901 (2017). Cited on page(s) 35

[261] J. P. Perdew, K. Burke and M. Ernzerhof, 'Generalized Gradient Approximation Made Simple', *Phys. Rev. Lett.* **77**, 3865 (1996). Cited on page(s) 35

[262] J. P. Perdew, K. Burke and M. Ernzerhof, 'Generalized Gradient Approximation Made Simple', *Phys. Rev. Lett.* **78**, 1396 (1997). Cited on page(s) 35

[263] D. R. Hamann, 'Optimized Norm-Conserving Vanderbilt Pseudopotentials', *Phys. Rev. B* **88**, 85117 (2013). Cited on page(s) 35

[264] M. J. van Setten, M. Giantomassi, E. Bousquet, M. J. Verstraete, D. R. Hamann, X. Gonze and G.-M. Rignanese, 'The PseudoDojo: Training and Grading a 85 Element Optimized Norm-Conserving Pseudopotential Table', *Comput. Phys. Commun.* **226**, 39 (2018). Cited on page(s) 35

[265] S. Grimme, J. Antony, S. Ehrlich and H. Krieg, 'A Consistent and Accurate *Ab Initio* Parametrization of Density Functional Dispersion Correction (DFT-D) for the 94 Elements H-Pu', *J. Chem. Phys.* **132**, 154104 (2010). Cited on page(s) 35

[266] Y. Nomura and R. Arita, '*Ab Initio* Downfolding for Electron-Phonon-Coupled Systems: Constrained Density-Functional Perturbation Theory', *Phys. Rev. B* **92**, 245108 (2015). Cited on page(s) 35, 107, and 138

[267] A. A. Mostofi, J. R. Yates, G. Pizzi, Y.-S. Lee, I. Souza, D. Vanderbilt and N. Marzari, 'An Updated Version of wannier90: A Tool for Obtaining Maximally-Localised Wannier Functions', *Comput. Phys. Commun.* **185**, 2309 (2014). Cited on page(s) 35

[268] F. Giustino, M. L. Cohen and S. G. Louie, 'Electron-Phonon Interaction Using Wannier Functions', *Phys. Rev. B* **76**, 165108 (2007). Cited on page(s) 35

[269] S. Poncé, E. R. Margine, C. Verdi and F. Giustino, ‘EPW: Electron-Phonon Coupling, Transport and Superconducting Properties Using Maximally Localized Wannier Functions’, *Comput. Phys. Commun.* **209**, 116 (2016). Cited on page(s) 35

[270] C. Zhang, A. Johnson, C.-L. Hsu, L.-J. Li and C.-K. Shih, ‘Direct Imaging of Band Profile in Single Layer MoS_2 on Graphite: Quasiparticle Energy Gap, Metallic Edge States, and Edge Band Bending’, *Nano Lett.* **14**, 2443 (2014). Cited on page(s) 40 and 46

[271] H. Liu, L. Jiao, F. Yang, Y. Cai, X. Wu, W. Ho, C. Gao, J. Jia, N. Wang, H. Fan, W. Yao and M. Xie, ‘Dense Network of One-Dimensional Midgap Metallic Modes in Monolayer $MoSe_2$ and Their Spatial Undulations’, *Phys. Rev. Lett.* **113**, 66105 (2014). Cited on page(s) 40 and 67

[272] H. Liu, H. Zheng, F. Yang, L. Jiao, J. Chen, W. Ho, C. Gao, J. Jia and M. Xie, ‘Line and Point Defects in $MoSe_2$ Bilayer Studied by Scanning Tunneling Microscopy and Spectroscopy’, *ACS Nano* **9**, 6619 (2015). Cited on page(s) 40

[273] A. J. Bradley, M. M. Ugeda, F. H. da Jornada, D. Y. Qiu, W. Ruan, Y. Zhang, S. Wickenburg, A. Riss, J. Lu, S.-K. Mo, Z. Hussain, Z.-X. Shen, S. G. Louie and M. F. Crommie, ‘Probing the Role of Interlayer Coupling and Coulomb Interactions on Electronic Structure in Few-Layer $MoSe_2$ Nanostructures’, *Nano Lett.* **15**, 2594 (2015). Cited on page(s) 40

[274] H. C. Diaz, Y. Ma, R. Chaghi and M. Batzill, ‘High Density of (Pseudo) Periodic Twin-Grain Boundaries in Molecular Beam Epitaxy-Grown van der Waals Heterostructure: $MoTe_2/MoS_2$’, *Appl. Phys. Lett.* **108**, 191606 (2016). Cited on page(s) 40

[275] H. Zheng *et al.*, ‘Atomic-Scale Visualization of Quasiparticle Interference on a Type-II Weyl Semimetal Surface’, *Phys. Rev. Lett.* **117**, 266804 (2016). Cited on page(s) 40

[276] X. Ma *et al.*, ‘Charge Density Wave Phase Transitions in Large-Scale Few-Layer 1T-VTe_2 Grown by Molecular Beam Epitaxy’, *ACS Appl. Mater. & Interfaces* **11**, 10729 (2019). Cited on page(s) 40

[277] Q. He, P. Li, Z. Wu, B. Yuan, Z. Luo, W. Yang, J. Liu, G. Cao, W. Zhang, Y. Shen, P. Zhang, S. Liu, G. Shao and Z. Yao, ‘Molecular Beam Epitaxy Scalable Growth of Wafer-Scale Continuous Semiconducting Monolayer $MoTe_2$ on Inert Amorphous Dielectrics’, *Adv. Mater.* **2019**, 1901578 (2019). Cited on page(s) 40

[278] W. A. West and A. W. C. Menzies, ‘The Vapor Pressures of Sulphur between 100 C and 550 C with related Thermal Data’, *J. Phys. Chem.* **33**, 1880 (1928). Cited on page(s) 40

[279] J. Kibsgaard, J. V. Lauritsen, E. Lægsgaard, B. S. Clausen, H. Topsøe and F. Besenbacher, ‘Cluster-Support Interactions and Morphology of MoS_2 Nanoclusters in a Graphite-Supported Hydrotreating Model Catalyst’, *J. Am. Chem. Soc.* **128**, 13950 (2006). Cited on page(s) 40

[280] S. Ulstrup, A. G. Cabo, J. A. Miwa, J. M. Riley, S. S. Grønborg, J. C. Johannsen, C. Cacho, O. Alexander, R. T. Chapman, E. Springate, M. Bianchi, M. Dendzik, J. V. Lauritsen, P. D. C. King and P. Hofmann, ‘Ultrafast Band Structure Control of a Two-Dimensional Heterostructure’, *ACS Nano* **10**, 6315 (2016). Cited on page(s) 40 and 46

[281] D. Fu *et al.*, ‘Molecular Beam Epitaxy of Highly Crystalline Monolayer Molybdenum Disulfide on Hexagonal Boron Nitride’, *J. Am. Chem. Soc.* **139**, 9392 (2017). Cited on page(s) 40, 52, and 118

[282] T. Shimada, F. S. Ohuchi and B. A. Parkinson, ‘Thermal decomposition of SnS 2 and SnSe 2 : Novel molecular-beam epitaxy sources for sulfur and selenium’, *J. Vac. Sci. & Technol. A* **10**, 539 (1992). Cited on page(s) 40

[283] S. Tiefenbacher, H. Sehnert, C. Pettenkofer and W. Jaegermann, ‘Epitaxial films of WS_2 by metal organic van der Waals epitaxy (MO-VDWE)’, *Surf. Sci.* **318**, L1161 (1994). Cited on page(s) 40

[284] R. Schlaf, N. R. Armstrong, B. A. Parkinson, C. Pettenkofer and W. Jaegermann, ‘Van der Waals epitaxy of the layered semiconductors $SnSe_2$ and SnS_2: morphology and growth modes’, *Surf. Sci.* **385**, 1 (1997). Cited on page(s) 40

[285] O. Faye, A. Raj, V. Mittal and A. C. Beye, ‘H_2S Adsorption on Graphene in the Presence of Sulfur: A Density Functional Theory Study’, *Comput. Mater. Sci.* **117**, 110 (2016). Cited on page(s) 41

[286] M. V. Bollinger, J. V. Lauritsen, K. W. Jacobsen, J. K. Nørskov, S. Helveg and F. Besenbacher, ‘One-Dimensional Metallic Edge States in MoS_2’, *Phys. Rev. Lett.* **87**, 196803 (2001). Cited on page(s) 43

[287] P. A. Young, ‘Lattice parameter measurements on molybdenum disulphide’, *J. Phys. D.* **1**, 936 (1968). Cited on page(s) 43

[288] J. V. Lauritsen, M. V. Bollinger, E. Lægsgaard, K. W. Jacobsen, J. K. Nørskov, B. S. Clausen, H. Topsøe and F. Besenbacher, ‘Atomic-Scale Insight into Structure and Morphology Changes of MoS_2 Nanoclusters in Hydrotreating Catalysts’, *J. Catal.* **221**, 510 (2004). Cited on page(s) 43

[289] H. Schweiger, P. Raybaud, G. Kresse and H. Toulhoat, ‘Shape and Edge Sites Modifications of MoS_2 Catalytic Nanoparticles Induced by Working Conditions: A Theoretical Study’, *J. Catal.* **207**, 76 (2002). Cited on page(s) 43

[290] Y. Cao *et al.*, ‘Quality Heterostructures from Two-Dimensional Crystals Unstable in Air by Their Assembly in Inert Atmosphere’, *Nano Lett.* **15**, 4914 (2015). Cited on page(s) 43 and 94

[291] Y. Ma, S. Kolekar, H. Coy Diaz, J. Aprojanz, I. Miccoli, C. Tegenkamp and M. Batzill, ‘Metallic Twin Grain Boundaries Embedded in $MoSe_2$ Monolayers Grown by Molecular Beam Epitaxy’, *ACS Nano* **11**, 5130 (2017). Cited on page(s) 44

[292] H.-P. Komsa and A. V. Krasheninnikov, ‘Engineering the Electronic Properties of Two-Dimensional Transition Metal Dichalcogenides by Introducing Mirror Twin Boundaries’, *Adv. Electron. Mater.* **3**, 1600468 (2017). Cited on page(s) 44 and 66

[293] M. Sicot, P. Leicht, A. Zusan, S. Bouvron, O. Zander, M. Weser, Y. S. Dedkov, K. Horn and M. Fonin, ‘Size-Selected Epitaxial Nanoislands Underneath Graphene Moire on Rh(111)’, *ACS Nano* **6**, 151 (2012). Cited on page(s) 45

[294] D. W. Boukhvalov and M. I. Katsnelson, ‘Destruction of Graphene by Metal Ddatoms’, *Appl. Phys. Lett.* **95**, 23109 (2009). Cited on page(s) 45

[295] T. Cheiwchanchamnangij and W. R. L. Lambrecht, ‘Quasiparticle Band Structure Calculation of Monolayer, Bilayer, and Bulk MoS_2’, *Phys. Rev. B* **85**, 205302 (2012). Cited on page(s) 46

[296] A. Ramasubramaniam, ‘Large Excitonic Effects in Monolayers of Molybdenum and Tungsten Dichalcogenides’, *Phys. Rev. B* **86**, 115409 (2012). Cited on page(s) 46

[297] H.-P. Komsa and A. V. Krasheninnikov, ‘Effects of Confinement and Cnvironment on the Clectronic Structure and Exciton Binding Energy of MoS_2 from First Principles’, *Phys. Rev. B* **86**, 241201 (2012). Cited on page(s) 46

[298] Y. L. Huang, Y. Chen, W. Zhang, S. Y. Quek, C.-H. Chen, L.-J. Li, W.-T. Hsu, W.-H. Chang, Y. J. Zheng, W. Chen and A. T. S. Wee, ‘Bandgap Tunability at Single-Layer Molybdenum Disulphide Grain Boundaries’, *Nat. Commun.* **6**, 6298 (2015). Cited on page(s) 46, 52, and 68

[299] A. F. Rigosi, H. M. Hill, K. T. Rim, G. W. Flynn and T. F. Heinz, ‘Electronic band gaps and exciton binding energies in monolayer $Mo_xW_{1-x}S_2$ transition metal dichalcogenide alloys probed by scanning tunneling and optical spectroscopy’, *Phys. Rev. B* **94**, 75440 (2016). Cited on page(s) 46

[300] J. Shi, X. Zhou, G.-F. Han, M. Liu, D. Ma, J. Sun, C. Li, Q. Ji, Y. Zhang, X. Song, X.-Y. Lang, Q. Jiang, Z. Liu and Y. Zhang, ‘Narrow-Gap Quantum Wires Arising from the Edges of Monolayer MoS_2 Synthesized on Graphene’, *Adv. Mater. Interfaces* **3**, 1600332 (2016). Cited on page(s) 46

[301] M. Hong, P. Yang, X. Zhou, S. Zhao, C. Xie, J. Shi, Z. Zhang, Q. Fu and Y. Zhang, ‘Decoupling the Interaction between Wet-Transferred MoS_2 and Graphite Substrate by an Interfacial Water Layer’, *Adv. Mater. Interfaces* **5**, 1800641 (2018). Cited on page(s) 46

[302] N. Krane, C. Lotze, J. M. Läger, G. Reecht and K. J. Franke, 'Electronic Structure and Luminescence of Quasi-Freestanding MoS_2 Nanopatches on Au(111)', *Nano Lett.* **16**, 5163 (2016). Cited on page(s) 46

[303] T. Förster, 'Zwischenmolekulare Energiewanderung und Fluoreszenz', *Ann. Phys.* **437**, 55 (1948). Cited on page(s) 47

[304] D. L. Dexter, 'A Theory of Sensitized Luminescence in Solids', *J. Chem. Phys.* **21**, 836 (1953). Cited on page(s) 47

[305] F. Schulz, R. Drost, S. K. Hämäläinen, T. Demonchaux, A. P. Seitsonen and P. Liljeroth, 'Epitaxial hexagonal boron nitride on Ir(111): A work function template', *Phys. Rev. B* **89**, 235429 (2014). Cited on page(s) 49

[306] W. Jolie, C. Murray, P. S. Weiß, J. Hall, F. Portner, N. Atodiresei, A. V. Krasheninnikov, C. Busse, H.-P. Komsa, A. Rosch and T. Michely, 'Tomonaga-Luttinger Liquid in a Box: Electrons Confined within MoS_2 Mirror-Twin Boundaries', *Phys. Rev. X* **9**, 011055 (2019). Cited on page(s) 51, 65, 67, and 142

[307] P. Joensen, R. Frindt and S. Morrison, 'Single-Layer MoS_2', *Mater. Res. Bull.* **21**, 457 (1986). Cited on page(s) 51

[308] J. Ryou, Y.-S. Kim, S. KC and K. Cho, 'Monolayer MoS_2 Bandgap Modulation by Dielectric Environments and Tunable Bandgap Transistors', *Sci. Rep.* **6**, 29184 (2016). Cited on page(s) 52

[309] R. Suzuki, M. Sakano, Y. J. Zhang, R. Akashi, D. Morikawa, A. Harasawa, K. Yaji, K. Kuroda, K. Miyamoto, T. Okuda, K. Ishizaka, R. Arita and Y. Iwasa, 'Valley-dependent spin polarization in bulk MoS_2 with broken inversion symmetry', *Nat. Nanotechnol.* **9**, 611 (2014). Cited on page(s) 52

[310] S. KC, R. C. Longo, R. M. Wallace and K. Cho, 'Surface Oxidation Energetics and Kinetics on MoS_2 Monolayer', *J. Appl. Phys.* **117**, 135301 (2015). Cited on page(s) 52

[311] B. Zhao, C. Shang, N. Qi, Z. Chen and Z. Chen, 'Stability of Defects in Monolayer MoS_2 and Their Interaction with O_2 Molecule: A First-Principles Study', *Appl. Surf. Sci.* **412**, 385 (2017). Cited on page(s) 52

[312] J. Martincová, M. Otyepka and P. Lazar, 'Is Single Layer MoS_2 Stable in the Air?', *Chem. - A Eur. J.* **23**, 13233 (2017). Cited on page(s) 52

[313] J.-H. Ahn, W. M. Parkin, C. H. Naylor, A. T. C. Johnson and M. Drndić, 'Ambient Effects on Electrical Characteristics of CVD-Grown Monolayer MoS_2 Field-Effect Transistors', *Sci. Rep.* **7**, 4075 (2017). Cited on page(s) 52

[314] J. Pető, T. Ollár, P. Vancsó, Z. I. Popov, G. Z. Magda, G. Dobrik, C. Hwang, P. B. Sorokin and L. Tapasztó, 'Spontaneous Doping of the Basal Plane of MoS_2 Single Layers Through Oxygen Substitution Under Ambient Conditions', *Nat. Chem.* **10**, 1246 (2018). Cited on page(s) 52

[315] P. Han, E. R. Adler, Y. Liu, L. St Marie, A. El Fatimy, S. Melis, E. Van Keuren and P. Barbara, 'Ambient Effects on Photogating in MoS_2 Photodetectors', *Nanotechnology* **30**, 284004 (2019). Cited on page(s) 52

[316] J.-Y. Noh, H. Kim and Y.-S. Kim, 'Stability and Electronic Structures of Native Defects in Single-Layer MoS_2', *Phys. Rev. B* **89**, 205417 (2014). Cited on page(s) 65

[317] H.-P. Komsa and A. V. Krasheninnikov, 'Native Defects in Bulk and Monolayer MoS_2 from First Principles', *Phys. Rev. B* **91**, 125304 (2015). Cited on page(s) 65

[318] S. Haldar, H. Vovusha, M. K. Yadav, O. Eriksson and B. Sanyal, 'Systematic Study of Structural, Electronic, and Optical Properties of Atomic-Scale Defects in the Two-Dimensional Transition Metal DKichalcogenides MX_2 (M = Mo, W, X = S, Se, Te)', *Phys. Rev. B* **92**, 235408 (2015). Cited on page(s) 65

[319] Y.-C. Lin, D. O. Dumcenco, H.-P. Komsa, Y. Niimi, A. V. Krasheninnikov, Y.-S. Huang and K. Suenaga, ‘Properties of Individual Dopant Atoms in Single-Layer MoS_2: Atomic Structure, Migration, and Enhanced Reactivity’, *Adv. Mater.* **26**, 2857 (2014). Cited on page(s) 65

[320] S. McDonnell, R. Addou, C. Buie, R. M. Wallace and C. L. Hinkle, ‘Defect-Dominated Doping and Contact Resistance in MoS_2’, *ACS Nano* **8**, 2880 (2014). Cited on page(s) 65

[321] Z. Lin, B. R. Carvalho, E. Kahn, R. Lv, R. Rao, H. Terrones, M. A. Pimenta and M. Terrones, ‘Defect Engineering of Two-Dimensional Transition Metal Dichalcogenides’, *2D Mater.* **3**, 022002 (2016). Cited on page(s) 65

[322] C. Murray, C. van Efferen, W. Jolie, J. Hall, A. V. Krasheninnikov, C. Busse, H.-P. Komsa and T. Michely, ‘Locally Confined 1D Hole Gas Caused by Band Bending in MoS_2 on Gr/Ir(111)’, *In. Preparation* **2019**, (2019). Cited on page(s) 65, 68, and 142

[323] W. Zhou, X. Zou, S. Najmaei, Z. Liu, Y. Shi, J. Kong, J. Lou, P. M. Ajayan, B. I. Yakobson and J.-C. Idrobo, ‘Intrinsic Structural Defects in Monolayer Molybdenum Disulfide’, *Nano Lett.* **13**, 2615 (2013). Cited on page(s) 65

[324] S. Najmaei, Z. Liu, W. Zhou, X. Zou, G. Shi, S. Lei, B. I. Yakobson, J.-C. Idrobo, P. M. Ajayan and J. Lou, ‘Vapour Phase Growth and Grain Boundary Structure of Molybdenum Disulphide Atomic Layers’, *Nat. Mater.* **12**, 754 (2013). Cited on page(s) 65

[325] A. M. van der Zande, P. Y. Huang, D. A. Chenet, T. C. Berkelbach, Y. You, G.-H. Lee, T. F. Heinz, D. R. Reichman, D. A. Muller and J. C. Hone, ‘Grains and Grain Boundaries in Highly Crystalline Monolayer Molybdenum Disulphide’, *Nat. Mater.* **12**, 554 (2013). Cited on page(s) 65

[326] Y.-C. Lin, T. Björkman, H.-P. Komsa, P.-Y. Teng, C.-H. Yeh, F.-S. Huang, K.-H. Lin, J. Jadczak, Y.-S. Huang, P.-W. Chiu, A. V. Krasheninnikov and K. Suenaga, ‘Three-Fold Rotational Defects in Two-Dimensional Transition Metal Dichalcogenides’, *Nat. Commun.* **6**, 6736 (2015). Cited on page(s) 65

[327] J. Hong *et al.*, ‘Exploring Atomic Defects in Molybdenum Disulphide Monolayers’, *Nat. Commun.* **6**, 6293 (2015). Cited on page(s) 65

[328] H.-P. Komsa, S. Kurasch, O. Lehtinen, U. Kaiser and A. V. Krasheninnikov, ‘From Point to Extended Defects in Two-Dimensional MoS_2: Evolution of Atomic Structure Under Electron Irradiation’, *Phys. Rev. B* **88**, 035301 (2013). Cited on page(s) 65

[329] R. Addou, L. Colombo and R. M. Wallace, ‘Surface Defects on Natural MoS_2’, *ACS Appl. Mater. & Interfaces* **7**, 11921 (2015). Cited on page(s) 65 and 66

[330] P. Vancsó, G. Z. Magda, J. Pető, J.-Y. Noh, Y.-S. Kim, C. Hwang, L. P. Biró and L. Tapasztó, ‘The Intrinsic Defect Structure of Exfoliated MoS_2 Single Layers Revealed by Scanning Tunneling Microscopy’, *Sci. Rep.* **6**, 29726 (2016). Cited on page(s) 65

[331] X. Liu, I. Balla, H. Bergeron and M. C. Hersam, ‘Point Defects and Grain Boundaries in Rotationally Commensurate MoS_2 on Epitaxial Graphene’, *J. Phys. Chem. C* **120**, 20798 (2016). Cited on page(s) 65, 66, and 68

[332] S. Zhang, C.-G. Wang, M.-Y. Li, D. Huang, L.-J. Li, W. Ji and S. Wu, ‘Defect Structure of Localized Excitons in a WSe_2 Monolayer’, *Phys. Rev. Lett.* **119**, 046101 (2017). Cited on page(s) 65

[333] M. Precner, T. Polaković, D. J. Trainer, A. V. Putilov, C. Di Giorgio, I. Cone, X. X. Xi, M. Iavarone and G. Karapetrov, in ‘AIP Conf. Proc.’ (AIP Publishing LLC, Melville, NY, 2018), No. 1, 020004. Cited on page(s) 65 and 66

[334] I. Delač Marion, D. Čapeta, B. Pielić, F. Faraguna, A. Gallardo, P. Pou, B. Biel, N. Vujičić and M. Kralj, ‘Atomic-Scale Defects and Electronic Properties of a Transferred Synthesized MoS_2 Monolayer’, *Nanotechnology* **29**, 305703 (2018). Cited on page(s) 65 and 66

[335] C. González, B. Biel and Y. J. Dappe, 'Theoretical Characterisation of Point Defects on a MoS_2 Monolayer by Scanning Tunnelling Microscopy', *Nanotechnology* **27**, 105702 (2016). Cited on page(s) 65 and 66

[336] J.-P. Peng, J.-Q. Guan, H.-M. Zhang, C.-L. Song, L. Wang, K. He, Q.-K. Xue and X.-C. Ma, 'Molecular Beam Epitaxy Growth and Scanning Tunneling Microscopy Study of $TiSe_2$ ultrathin films', *Phys. Rev. B* **91**, 121113 (2015). Cited on page(s) 66

[337] S. Barja *et al.*, 'Identifying Substitutional Oxygen as a Prolific Point Defect in Monolayer Transition Metal Dichalcogenides with Experiment and Theory', *arXiv Prepr. arXiv1810.03364* **2018**, (2018). Cited on page(s) 66

[338] Y. J. Zheng and S. Y. Quek, 'First Principles Study of Intrinsic and Extrinsic Point Defects in Monolayer WSe_2', *arXiv Prepr. arXiv1901.05238* **2019**, (2019). Cited on page(s) 66

[339] M. Batzill, 'Mirror Twin Grain Boundaries in Molybdenum Dichalcogenides', *J. Phys. Condens. Matter* **30**, 493001 (2018). Cited on page(s) 66

[340] O. Lehtinen, H.-P. Komsa, A. Pulkin, M. B. Whitwick, M.-W. Chen, T. Lehnert, M. J. Mohn, O. V. Yazyev, A. Kis, U. Kaiser and A. V. Krasheninnikov, 'Atomic Scale Microstructure and Properties of Se-Deficient Two-Dimensional $MoSe_2$', *ACS Nano* **9**, 3274 (2015). Cited on page(s) 66

[341] S.-i. Tomonaga, 'Remarks on Bloch's Method of Sound Waves applied to Many-Fermion Problems', *Prog. Theor. Phys.* **5**, 544 (1950). Cited on page(s) 67

[342] J. M. Luttinger, 'An Exactly Soluble Model of a Many-Fermion System', *J. Math. Phys.* **4**, 1154 (1963). Cited on page(s) 67

[343] F. D. M. Haldane, ''Luttinger Liquid Theory' of One-Dimensional Quantum Fluids. I. Properties of the Luttinger Model and their Extension to the General 1D Interacting Spinless Fermi Gas', *J. Phys. C* **14**, 2585 (1981). Cited on page(s) 67

[344] T. Kaneko and R. Saito, 'Origin of Band Bending at Domain Boundaries of MoS_2: First-Principles Study', *Jpn. J. Appl. Phys.* **57**, 04FP09 (2018). Cited on page(s) 68

[345] D. Wang, H. Yu, L. Tao, W. Xiao, P. Fan, T. Zhang, M. Liao, W. Guo, D. Shi, S. Du, G. Zhang and H. Gao, 'Bandgap Broadening at Grain Boundaries in Single-Layer MoS_2', *Nano Res.* **11**, 6102 (2018). Cited on page(s) 68

[346] M. Ghorbani-Asl, S. Kretschmer, D. E. Spearot and A. V. Krasheninnikov, 'Two-Dimensional MoS_2 Under Ion Irradiation: From Controlled Defect Production to Electronic Structure Engineering', *2D Mater.* **4**, 025078 (2017). Cited on page(s) 68

[347] P. Valerius, J. Hall, A. Herman, S. Kretschmer, M. Ghorbani-Asl, A. V. Krasheninnikov, A. Grüneis and T. Michely, 'Reversible Crystalline-to-Amorphous Phase Transition in MoS_2 on Gr/Ir(111) by Xe^+ Ion Irradiation', *In. Preparation* **2019**, (2019). Cited on page(s) 68 and 142

[348] W. Jolie, Dissertation, Universität zu Köln, 2017. Cited on page(s) 70

[349] C.-W. Chen, J. Choe and E. Morosan, 'Charge Density Waves in Strongly Correlated Electron Systems', *Reports Prog. Phys.* **79**, 084505 (2016). Cited on page(s) 71

[350] 'High T_c Superconductors and Related Transition Metal Oxides', edited by A. Bussmann-Holder and H. Keller (Springer Berlin Heidelberg, Berlin, Heidelberg, 2007). Cited on page(s) 71

[351] M. Uehara, S. Mori, C. H. Chen and S. W. Cheong, 'Percolative phase separation underlies colossal magnetoresistance in mixed-valent manganites', *Nature* **399**, 560 (1999). Cited on page(s) 71

[352] N. Luo, C. Si and W. Duan, 'Structural and Electronic Phase Transitions in Ferromagnetic Monolayer VS_2 Induced by Charge Doping', *Phys. Rev. B* **95**, 205432 (2017). Cited on page(s) 72

[353] J. Feng, X. Sun, C. Wu, L. Peng, C. Lin, S. Hu, J. Yang and Y. Xie, ‘Metallic Few-Layered VS_2 Ultrathin Nanosheets: High Two-Dimensional Conductivity for In-Plane Supercapacitors’, *J. Am. Chem. Soc.* **133**, 17832 (2011). Cited on page(s) 72, 75, and 92

[354] D. J. Eaglesham, R. L. Withers and D. M. Bird, ‘Charge-Density-Wave Transitions in 1T-VSe_2’, *J. Phys. C* **19**, 359 (1986). Cited on page(s) 72

[355] K. Terashima, T. Sato, H. Komatsu, T. Takahashi, N. Maeda and K. Hayashi, ‘Charge-density wave transition of 1T-VSe_2 studied by angle-resolved photoemission spectroscopy’, *Phys. Rev. B* **68**, 155108 (2003). Cited on page(s) 72

[356] V. N. Strocov, M. Shi, M. Kobayashi, C. Monney, X. Wang, J. Krempasky, T. Schmitt, L. Patthey, H. Berger and P. Blaha, ‘Three-dimensional electron realm in VSe_2 by soft-x-ray photoelectron spectroscopy: Origin of charge-density waves’, *Phys. Rev. Lett.* **109**, 86401 (2012). Cited on page(s) 72

[357] J. Yang, W. Wang, Y. Liu, H. Du, W. Ning, G. Zheng, C. Jin, Y. Han, N. Wang, Z. Yang, M. Tian and Y. Zhang, ‘Thickness dependence of the charge-density-wave transition temperature in VSe_2’, *Appl. Phys. Lett.* **105**, 63109 (2014). Cited on page(s) 72

[358] P. Chen, W. W. Pai, Y. H. Chan, V. Madhavan, M. Y. Chou, S. K. Mo, A. V. Fedorov and T. C. Chiang, ‘Unique Gap Structure and Symmetry of the Charge Density Wave in Single-Layer VSe_2’, *Phys. Rev. Lett.* **121**, 196402 (2018). Cited on page(s) 72

[359] S. Magonov, H.-J. Contow, H. Hillebrecht, M. Drechlser and W. Rotter, ‘Atomic structure and superstructure of vanadium disulfide by scanning tunneling microscopy’, *Optik* **83**, 60 (1989). Cited on page(s) 72

[360] X. Sun, T. Yao, Z. Hu, Y. Guo, Q. Liu, S. Wei and C. Wu, ‘In Situ Unravelling Structural Modulation Across the Charge-Density-Wave Transition in Vanadium Disulfide’, *Phys. Chem. Chem. Phys.* **17**, 13333 (2015). Cited on page(s) 72

[361] N. Katayama, M. Uchida, D. Hashizume, S. Niitaka, J. Matsuno, D. Matsumura, Y. Nishihata, J. Mizuki, N. Takeshita, A. Gauzzi, M. Nohara and H. Takagi, ‘Anomalous Metallic State in the Vicinity of Metal to Valence-Bond Solid Insulator Transition in $LiVS_2$’, *Phys. Rev. Lett.* **103**, 146405 (2009). Cited on page(s) 72

[362] M. Hossain, J. Wu, W. Wen, H. Liu, X. Wang and L. Xie, ‘Chemical Vapor Deposition of 2D Vanadium Disulfide and Diselenide and Raman Characterization of the Phase Transitions’, *Adv. Mater. Interfaces* **5**, 1800528 (2018). Cited on page(s) 72

[363] B. Predel, in ‘Pu-Re – Zn-Zr’, Vol. 5 J of ‘Landolt-Börnstein - Group IV Physical Chemistry’, edited by O. Madelung (Springer-Verlag, Berlin/Heidelberg, 1998), Chap. Sulf.-Van. Cited on page(s) 72

[364] P. Poddar and A. K. Rastogi, ‘Metastability and disorder effects in nonstoichiometric VS_2’, *J. Phys. Condens. Matter* **14**, 2677 (2002). Cited on page(s) 72

[365] Y. Oka, K. Kosuge and S. Kachi, ‘Order-disorder transition of the metal vacancies in the vanadium-sulfur system. I. An experimental study’, *J. Solid State Chem.* **23**, 11 (1978). Cited on page(s) 72

[366] Q. Ji, C. Li, J. Wang, J. Niu, Y. Gong, Z. Zhang, Q. Fang, Y. Zhang, J. Shi, L. Liao, X. Wu, L. Gu, Z. Liu and Y. Zhang, ‘Metallic Vanadium Disulfide Nanosheets as a Platform Material for Multifunctional Electrode Applications’, *Nano Lett.* **17**, 4908 (2017). Cited on page(s) 72 and 75

[367] H. Moutaabbid, Y. Le Godec, D. Taverna, B. Baptiste, Y. Klein, G. Loupias and A. Gauzzi, ‘High-Pressure Control of Vanadium Self-Intercalation and Enhanced Metallic Properties in 1T-$V_{1+x}S_2$ Single Crystals’, *Inorg. Chem.* **55**, 6481 (2016). Cited on page(s) 72, 89, and 92

[368] S. Barua, M. C. Hatnean, M. R. Lees and G. Balakrishnan, ‘Signatures of the Kondo effect in VSe_2’, *Sci. Rep.* **7**, 10964 (2017). Cited on page(s) 72

[369] Q. Cao, F. F. Yun, L. Sang, F. Xiang, G. Liu and X. Wang, 'Defect Introduced Paramagnetism and Weak Localization in Two-Dimensional Metal VSe_2', *Nanotechnology* **28**, 475703 (2017). Cited on page(s) 72

[370] F. J. Owens, 'Phys. Low Dimens. Mater.' (World Scientific, Singapore, 2017), 172. Cited on page(s) 72

[371] Z. L. Liu, B. Lei, Z. L. Zhu, L. Tao, J. Qi, D. L. Bao, X. Wu, L. Huang, Y. Y. Zhang, X. Lin, Y. L. Wang, S. Du, S. T. Pantelides and H. J. Gao, 'Spontaneous Formation of 1D Pattern in Monolayer VSe_2 with Dispersive Adsorption of Pt Atoms for HER Catalysis', *Nano Lett.* **XXXX**, XXXX (2019). Cited on page(s) 73, 80, and 82

[372] Z. I. Popov, N. S. Mikhaleva, M. A. Visotin, A. A. Kuzubov, S. Entani, H. Naramoto, S. Sakai, P. B. Sorokin and P. V. Avramov, 'The electronic structure and spin states of 2D graphene/VX_2 ($X = S, Se$) heterostructures', *Phys. Chem. Chem. Phys.* **18**, 33047 (2016). Cited on page(s) 77

[373] I. Kawada, M. Nakano-Onoda, M. Ishii, M. Saeki and M. Nakahira, 'Crystal Structures of V_3S_4 and V_5S_8', *J. Solid State Chem.* **15**, 246 (1975). Cited on page(s) 86

[374] J. Hall *et al.*, 'Environmental Control of Charge Density Wave Order in Monolayer 2H-TaS_2', *In. Preparation* **2019**, (2019). Cited on page(s) 93 and 141

[375] J. G. Bednorz and K. A. Müller, 'Possible High T_c Superconductivity in the Ba-La-Cu-O System', *Zeitschrift für Phys. B Condens. Matter* **64**, 189 (1986). Cited on page(s) 93

[376] Y. Kamihara, H. Hiramatsu, M. Hirano, R. Kawamura, H. Yanagi, T. Kamiya and H. Hosono, 'Iron-Based Layered Superconductor: LaOFeP', *J. Am. Chem. Soc.* **128**, 10012 (2006). Cited on page(s) 93

[377] Y. Cao, V. Fatemi, A. Demir, S. Fang, S. L. Tomarken, J. Y. Luo, J. D. Sanchez-Yamagishi, K. Watanabe, T. Taniguchi, E. Kaxiras, R. C. Ashoori and P. Jarillo-Herrero, 'Correlated Insulator Behaviour at Half-Filling in Magic-Angle Graphene Superlattices', *Nature* **556**, 80 (2018). Cited on page(s) 93

[378] A. K. Geim and I. V. Grigorieva, 'Van der Waals Heterostructures', *Nature* **499**, 419 (2013). Cited on page(s) 93

[379] K. S. Novoselov, A. Mishchenko, A. Carvalho and A. H. C. Neto, '2D Materials and van der Waals Heterostructures', *Science* **353**, 461 (2016). Cited on page(s) 93

[380] D. N. Basov, R. D. Averitt and D. Hsieh, 'Towards Properties on Demand in Quantum Materials', *Nat. Mater.* **16**, 1077 (2017). Cited on page(s) 93

[381] Q. Wang *et al.*, 'Interface-Induced High-Temperature Superconductivity in Single Unit-Cell FeSe Films on $SrTiO_3$', *Chin. Phys. Lett.* **29**, 37402 (2012). Cited on page(s) 94

[382] R. V. Coleman, B. Giambattista, P. K. Hansma, A. Johnson, W. W. McNairy and C. G. Slough, 'Scanning Tunnelling Microscopy of Charge-Density Waves in Transition Metal Chalcogenides', *Adv. Phys.* **37**, 559 (1988). Cited on page(s) 94

[383] C. Wang, B. Giambattista, C. G. Slough, R. V. Coleman and M. A. Subramanian, 'Energy Gaps Measured by Scanning Tunneling Microscopy', *Phys. Rev. B* **42**, 8890 (1990). Cited on page(s) 94, 99, and 117

[384] C. Wang, C. G. Slough and R. V. Coleman, 'Spectroscopy of Dichalcogenides and Trichalcogenides Using Scanning Tunneling Microscopy', *J. Vac. Sci. Technol. B* **9**, 1048 (1991). Cited on page(s) 94 and 99

[385] W. C. Tonjes, V. A. Greanya, R. Liu, C. G. Olson and P. Molinié, 'Charge-Density-Wave Mechanism in the 2H-$NbSe_2$ Family: Angle-Resolved Photoemission Studies', *Phys. Rev. B* **63**, 235101 (2001). Cited on page(s) 94 and 102

[386] S. Nagata, T. Aochi, T. Abe, S. Ebisu, T. Hagino, Y. Seki and K. Tsutsumi, 'Superconductivity in the Layered Compound 2H-TaS_2', *J. Phys. Chem. Solids* **53**, 1259 (1992). Cited on page(s) 94

[387] J. Peng, Z. Yu, J. Wu, Y. Zhou, Y. Guo, Z. Li, J. Zhao, C. Wu and Y. Xie, 'Disorder Enhanced Superconductivity Toward TaS_2 Monolayer', *ACS Nano* **12**, 9461 (2018). Cited on page(s) 94

[388] Z. Wang, Y.-Y. Sun, I. Abdelwahab, L. Cao, W. Yu, H. Ju, J. Zhu, W. Fu, L. Chu and H. Xu, 'Surface-Limited Superconducting Phase Transition on 1T-TaS_2', *ACS Nano* **12**, 12619 (2018). Cited on page(s) 94

[389] O. R. Albertini, A. Y. Liu and M. Calandra, 'Effect of Doping on Lattice Instabilities of Single-Layer 1H-TaS_2', *Phys. Rev. B* **95**, 235121 (2017). Cited on page(s) 94 and 109

[390] H. M. Lefcochilos-Fogelquist, O. R. Albertini and A. Y. Liu, 'Substrate-Induced Suppression of Charge Density Wave Phase in Monolayer 1H-TaS_2 on Au(111)', *Phys. Rev. B* **99**, 174113 (2019). Cited on page(s) 94 and 109

[391] B. Shao, A. Eich, C. Sanders, A. S. Ngankeu, M. Bianchi, P. Hofmann, A. A. Khajetoorians and T. O. Wehling, 'Pseudodoping of a Metallic Two-Dimensional Material by the Supporting Substrate', *Nat. Commun.* **10**, 180 (2019). Cited on page(s) 94, 108, and 109

[392] L. F. Mattheiss, 'Band Structures of Transition-Metal-Dichalcogenide Layer Compounds', *Phys. Rev. B* **8**, 3719 (1973). Cited on page(s) 96

[393] A. Meetsma, G. A. Wiegers, R. J. Haange and J. L. De Boer, 'Structure of 2H-TaS_2', *Acta Crystallogr. C* **46**, 1598 (1990). Cited on page(s) 96 and 97

[394] F. Jellinek, 'The System Tantalum-Sulfur', *J. Alloy. Compd.* **4**, 9 (1962). Cited on page(s) 97 and 118

[395] M. K. Kinyanjui, T. Björkman, T. Lehnert, J. Köster, A. Krasheninnikov and U. Kaiser, 'Effects of Electron Beam Generated Lattice Defects on the Periodic Lattice Distortion Structure in 1T-TaS_2 and 1T-$TaSe_2$ Thin Layers', *Phys. Rev. B* **99**, 024101 (2019). Cited on page(s) 98

[396] R. Feenstra, J. A. Stroscio and A. Fein, 'Tunneling Spectroscopy of the Si(111) 2 × 1 Surface', *Surf. Sci.* **181**, 295 (1987). Cited on page(s) 99 and 137

[397] L. Petersen, P. T. Sprunger, P. Hofmann, E. Lægsgaard, B. G. Briner, M. Doering, H.-P. Rust, A. M. Bradshaw, F. Besenbacher and E. W. Plummer, 'Direct Imaging of the Two-Dimensional Fermi Contour: Fourier-Transform STM', *Phys. Rev. B* **57**, R6858 (1998). Cited on page(s) 101

[398] D. W. Shen, B. P. Xie, J. F. Zhao, L. X. Yang, L. Fang, J. Shi, R. H. He, D. H. Lu, H. H. Wen and D. L. Feng, 'Novel mechanism of a Charge Density Wave in a Transition Metal Dichalcogenide', *Phys. Rev. Lett.* **99**, 216404 (2007). Cited on page(s) 102

[399] K. Wijayaratne, J. Zhao, C. Malliakas, D. Young Chung, M. G. Kanatzidis and U. Chatterjee, 'Spectroscopic Signature of Moment-Dependent Electron-Phonon Coupling in 2H-TaS_2', *J. Mater. Chem. C* **5**, 11310 (2017). Cited on page(s) 102

[400] D. C. Liu and J. Nocedal, 'On the Limited Memory BFGS Method for Large Scale Optimization', *Math. Program.* **45**, 503 (1989). Cited on page(s) 102

[401] A. H. Thompson, 'Electrochemical Studies of Lithium Intercalation in Titanium and Tantalum Dichalcogenides', *Phys. B+C* **99**, 100 (1980). Cited on page(s) 107

[402] J. R. Dahn and W. R. McKinnon, 'Lithium Intercalation in 2H-Li_xTaS_2', *J. Phys. Condens. Matter* **17**, 4231 (1984). Cited on page(s) 107

[403] S. Baroni, S. De Gironcoli, A. Dal Corso and P. Giannozzi, 'Phonons and Related Crystal Properties from Density-Functional Perturbation Theory', *Rev. Mod. Phys.* **73**, 515 (2001). Cited on page(s) 107

[404] C. G. Slough, W. W. McNairy, R. V. Coleman, J. Garnaes, C. B. Prater and P. K. Hansma, 'Atomic Force Microscopy and Scanning Tunneling Microscopy of Charge-Density Waves in 1T-$TaSe_2$ and 1T-TaS_2', *Phys. Rev. B* **42**, 9255 (1990). Cited on page(s) 114

[405] K. Sakamaki, A. Funshima and Y. Onuki, ‘Definitive Structure of a Stacking Boundary of Charge Density Waves in 1T-TaS_2 Using a Scanning Tunneling Microscope’, *J. Phys. Chem. Solids* **52**, 409 (1991). Cited on page(s) 118

[406] C. H. Chen, ‘Electron Diffraction Study of the Charge-Density Wave Superlattice in 2H-$NbSe_2$’, *Solid State Commun.* **49**, 645 (1984). Cited on page(s) 118

[407] M. J. Cuddy, K. P. Arkill, Z. W. Wang, H.-P. Komsa, A. V. Krasheninnikov and R. E. Palmer, ‘Fabrication and Atomic Structure of Size-Selected, Layered MoS_2 Clusters for Catalysis’, *Nanoscale* **6**, 12463 (2014). Cited on page(s) 118

[408] M. A. Py and R. R. Haering, ‘Structural Destabilization Induced by Lithium Intercalation in MoS_2 and Related Compounds’, *Can. J. Phys.* **61**, 76 (1983). Cited on page(s) 118

[409] M. Kertesz and R. Hoffmann, ‘Octahedral vs. Trigonal-Prismatic Coordination and Clustering in Transition-Metal Dichalcogenides’, *J. Am. Chem. Soc.* **106**, 3453 (1984). Cited on page(s) 118

[410] G.-H. Lee, Y.-J. Yu, X. Cui, N. Petrone, C.-H. Lee, M. S. Choi, D.-Y. Lee, C. Lee, W. J. Yoo, K. Watanabe, T. Taniguchi, C. Nuckolls, P. Kim and J. Hone, ‘Flexible and Transparent MoS_2 Field-Effect Transistors on Hexagonal Boron Nitride-Graphene Heterostructures’, *ACS Nano* **7**, 7931 (2013). Cited on page(s) 123

[411] Y. Y. Illarionov, G. Rzepa, M. Waltl, T. Knobloch, A. Grill, M. M. Furchi, T. Mueller and T. Grasser, ‘The Role of Charge Trapping in MoS_2/SiO_2 and MoS_2/hBN Field-Effect Transistors’, *2D Mater.* **3**, 035004 (2016). Cited on page(s) 123

[412] W. Auwärter, ‘Hexagonal Boron Nitride Monolayers on Metal Supports: Versatile Templates for Atoms, Molecules and Nanostructures’, *Surf. Sci. Rep.* **74**, 1 (2019). Cited on page(s) 123

[413] C. Hwang *et al.*, ‘Magnetic Effects in Sulfur-Decorated Graphene’, *Sci. Rep.* **6**, 21460 (2016). Cited on page(s) 131

[414] R. R. da Silva, J. H. S. Torres and Y. Kopelevich, ‘Indication of Superconductivity at 35 K in Graphite-Sulfur Composites’, *Phys. Rev. Lett.* **87**, 147001 (2001). Cited on page(s) 131

[415] R. Bernardo-Gavito, Dissertation, Universidad Autónoma de Madrid, 2016. Cited on page(s) 131

[416] M. Pisarra, R. Bernardo-Gavito, J. Navarro, A. Black, C. Díaz, F. Calleja, D. Granados, R. Miranda, F. Martín and A. Vázquez de Parga, ‘Coverage Evolution of the Unoccupied Density of States in Sulfur Superstructures on Ru(0001)’, *Appl. Surf. Sci.* **433**, 300 (2018). Cited on page(s) 131

[417] C. M. Chan and W. H. Weinberg, ‘The Structure of the $(\sqrt{3}\times\sqrt{3})R30^\circ$ Sulfur Overlayer on the Iridium (111) Surface’, *J. Chem. Phys.* **71**, 3988 (1979). Cited on page(s) 131

[418] W. P. Krekelberg, J. Greeley and M. Mavrikakis, ‘Atomic and Molecular Adsorption on Ir(111)’, *J. Phys. Chem. B* **108**, 987 (2003). Cited on page(s) 131

[419] D. R. Alfonso, ‘First-Principles Studies of H_2S Adsorption and Dissociation on Metal Surfaces’, *Surf. Sci.* **602**, 2758 (2008). Cited on page(s) 131

[420] B. Pielić, J. Hall, V. Despoja, I. Rakić, M. Petrović, A. Sohani, C. Busse, T. Michely and M. Kralj, ‘Sulfur Structures on Bare and Graphene-Covered Ir(111)’, *In. Preparation* **2019**, (2019). Cited on page(s) 131 and 142

[421] J. Wilson, ‘Growth of Sulphide Films on Mo(111)’, *Surf. Sci.* **59**, 315 (1976). Cited on page(s) 131

[422] J. Foord and A. Reynolds, ‘Sulphur Adsorption and Sulphide Growth on Rh(111)’, *Surf. Sci.* **164**, 640 (1985). Cited on page(s) 131

[423] S. Kelemen and T. Fischer, ‘Interaction of H_2S with the Ru(001) Surface’, *Surf. Sci.* **87**, 53 (1979). Cited on page(s) 131

[424] C. Murray, ‘Privat Communication’, *II. Phys. Institut, Univ. zu Köln* **2019**, (2019). Cited on page(s) 135

Danksagung

Zum Gelingen dieser Arbeit haben viele Personen auf unterschiedliche Weise beigetragen. Diesen möchte ich abschließend meinen Dank aussprechen.

An erster Stelle möchte ich Prof. Dr. Thomas Michely danken. Hierbei gilt mein Dank einerseits auf fachlicher Ebene allen Erklärungen, Ratschlägen und stundenlagen 'eine-Minute-Gesprächen'. Andererseits möchte ich Dir ebenso für persönlichen Rat und unterstützende Stellungsnahmen danken.

Ich danke Priv. Doz. Daniel Bürgler für das Interesse an meiner Arbeit und die Übernahme des Zweitgutachtens. Herrn Prof. Dr. Klas Lindfors gilt mein Dank für die Übernahme des Vorsitzes meiner Prüfungskommission. Dr. Jens Brede möchte ich für die Übernahme des Beisitzes danken.

Des Weiteren möchte ich mich bei allen Personen bedanken, die durch ihre Kooperationen zu dieser Arbeit einen großen Teil beigetragen haben. Hier gilt mein Dank Alexander Grüneis, Niels Ehlen, Boris Senkovskiy, Jun Li und Martin Hell, welche sowohl in den Forschungen an MoS_2, als auch an TaS_2 mir einerseits die Möglichkeit gegeben haben neue Messmethoden kennenzulernen, und andererseits durch viele Diskussionen zum Erfolg der Projekte beigetragen haben. Darüber hinaus möchte ich Tim Wehling, Jan Berges und Erik van Loon danken, welche von der theoretischer Seite einen großen Beitrag zu den Untersuchungen an TaS_2 geleistet haben. In diesem Bereich gilt mein Dank zuletzt auch Carsten Busse, Caio Silva, Jiaqi Cai und Daniela Dombrowski für die Zusammenarbeit während XSW Messungen.

Ich möchte ebenso den Menschen danken, die auf technischer Seite zum Gelingen dieser Arbeit beigetragen haben. Hier gilt mein Dank Norbert Henn und Pascal Hurth und allen Mitarbeiter*innen der Mechanik- und Elektronikwerkstätten.

Ich danke Tobias Hartl, Tobias Wekking, Matthias Rolf und Camiel van Efferen, die durch ihre jeweiligen Bachelor- und Masterarbeiten zu einem Teil meines Promotionsprojektes beigetragen haben (und es teilweise auch maßgeblich – wenn auch unbeabsichtigt – beeinflusst haben). Des Weiteren bedanke ich mich für das Korrekturlesen der geschriebenen Arbeit bei Clifford Murray, Stefan Kraus, Moritz Will, Philipp Valerius, Pantelis Bampoulis, Jeison Fischer, Carsten Speckmann und Florian Peißker. Generell möchte ich mich bei den Mitglieder*innen der AG Michely bedanken – für Gespräche, Anteilnahme, Tipps und Hilfe.

Zuletzt gilt mein Dank den Menschen, die mich ohne fachliche Kenntnis durch die Promotion begleitet haben und mir zeigen, dass die Welt noch mehr als Wissenschaft offen hält; meiner Familie und meinen Freunden.

Erklärung gemäß Promotionsordnung

Ich versichere, dass ich die von mir vorgelegte Dissertation selbstständig angefertigt, die benutzten Quellen und Hilfsmittel vollständig angegeben und die Stellen der Arbeit - einschließlich Tabellen, Karten und Abbildungen -, die anderen Werken im Wortlaut oder dem Sinn nach entnommen sind, in jedem Einzelfall als Entlehnung kenntlich gemacht habe; dass diese Dissertation noch keiner anderen Fakultät oder Universität zur Prüfung vorgelegen hat; dass sie - abgesehen von den angegebenen Teilpublikationen - noch nicht veröffentlicht worden ist, sowie, dass ich eine solche Veröffentlichung vor Abschluss des Promotionsverfahrens nicht vornehmen werde. Die Bestimmungen der Promotionsordnung sind mir bekannt. Die von mir vorgelegte Dissertation ist von Prof. Dr. Thomas Michely betreut worden.

Köln, den 22.07.2019

Joshua Hall

Lebenslauf *(Curriculum Vitae)*

Persönliche Daten

Name	Hall
Vorname	Joshua
Geburtstag	30.08.1989
Geburtsort	Emmerich
Staatsangehörigkeit	deutsch

Ausbildung

01/2016 – 07/2019	Promotionsstudium II. Physikalisches Institut, Universität zu Köln Arbeitsgruppe Prof. Dr. T. Michely
10/2011 – 11/2014	M. Sc. Physik, Universität zu Köln Durchschnittsnote: 1,6 Masterarbeit "Towards *In Situ* Investigations of MoS_2 with Scanning Electron and Four-Tip Scanning Probe Microscopy" (Note: 1,3) angefertigt am PGI-6, Forschungszentrum Jülich
10/2008 – 09/2011	B. Sc in Physik, RWTH Aachen Durchschnittsnote: 1,9 Bachelorarbeit "Zeitaufgelöste elektrische Untersuchungen der Temparaturabhängigkeit des Spintransports an $Ni_{80}Fe_{20}/Al_2O_3/Si$-Hybridstrukturen" (Note: sehr gut) angefertigt am II. Physikalischen Institut, RWTH Aachen
06/2008	Allgemeine Hochschulreife, Konrad-Adenauer-Gymnasium Kleve Durchschnittsnote: 1,9